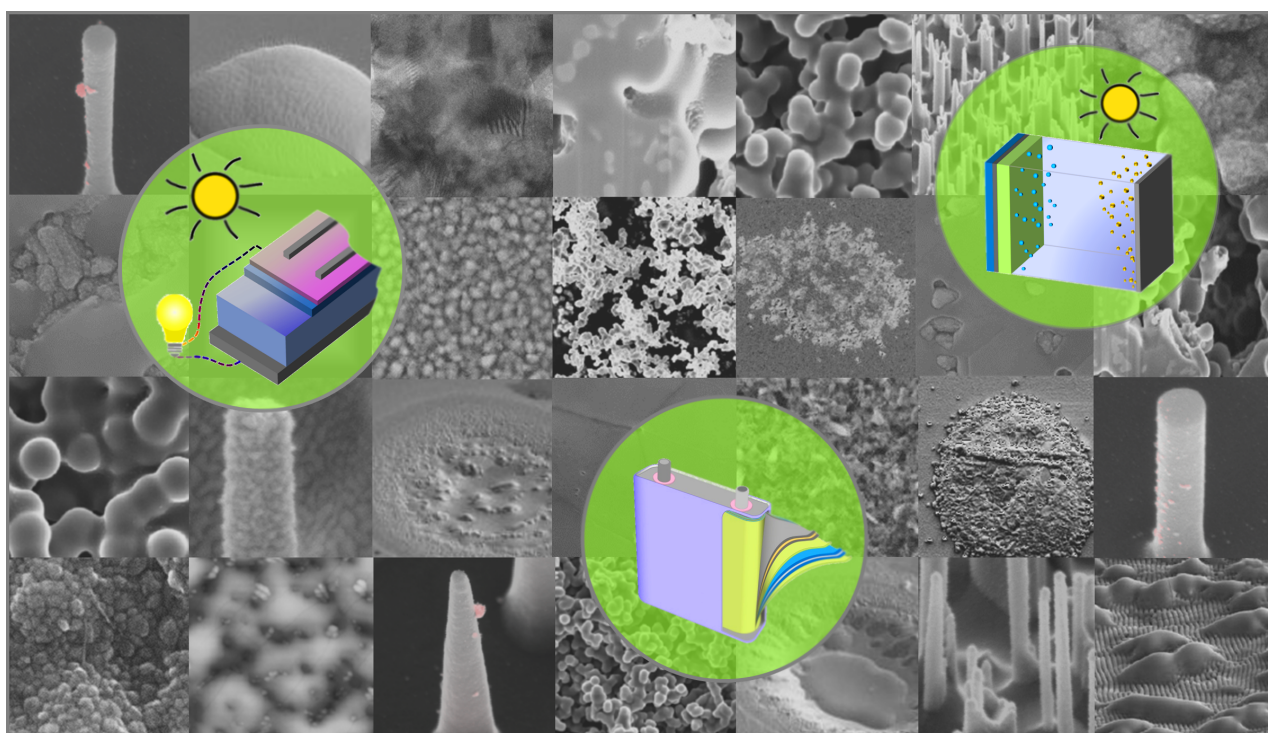# Nano- and microstructures for energy conversion: materials and devices

Edited by Martina Schmid and Harry Mönig

Imprint

Renewable energy conversion using nano- and microstructured materials

Harry Mönig[*1] and Martina Schmid[2]

The imposing environmental and economic challenges due to climate change have become a major topic of discussion on the global political agenda. Effectively reducing greenhouse gases in the atmosphere and decreasing air pollution in metropolitan areas requires a paradigm shift away from the conventional practise of fossil fuel combustion. Therefore, the development of new technologies based on renewable energy conversion should be one of the major goals of the global society. The *Beilstein Journal of Nanotechnology* thematic issue "Nano- and microstructures for energy conversion: materials and devices" provides insights into the latest developments in the related fields. Besides a focus on solar-cell concepts [1-5], it also addresses light harvesting by solar fuel production [6,7], and energy storage by batteries [8].

Nanostructured materials can be synthesized by a huge variety of approaches, extending from self-assembled structures [9], over various lithographic techniques [10] and imprinting methods [11], to different crystallization routes [12]. The thematic issue "Nano- and microstructures for energy conversion: materials and devices" covers the photo-electrochemical growth of platinum catalysts at plasmonic hot spots [6], the laser-assisted local growth of chalcopyrite absorbers [4], the preferential reactive ion etching of silicon by morphological anisotropies [5], the oxidation of copper nanoparticles resulting in nanoporous cobalt oxide photocathodes [7], and an approach in which silicon nanoparticles are embedded in an amorphous carbon matrix [8].

In terms of material saving, nano- and microstructured absorbers offer great potential, e.g., via ultrathin absorbers as highlighted for Sb_2S_3 hybrid solar cells [1] or via microabsorbers as shown for $Cu(In,Ga)Se_2$ [4] in this thematic issue. At the same time, material reduction demands for optical concepts that support efficient collection of the incident solar radiation. In this regard, nanotexturing is of interest, where optical resonances and light scattering can be tailored to give rise to field enhancement, path-length enhancement and finally increased absorption. Nano- and microtextures in Si heterojunction solar cells are addressed from a theoretical point of view in [3], whereas [5] additionally presents an experimental verification of the benefits arising from core–shell nanowire arrays for Si

heterojunction solar cells. Contacts with a high surface-to-volume ratio can clearly be seen. Particularly in photovoltaics, they may be prone to increased recombination losses. For other applications, such as water splitting, porous materials may however be desired as the example of Co_3O_4 photocathodes in [7] shows.

In general, the nanostructure of any material will strongly affect the corresponding optical and electronic properties by controlling the surface-to-volume ratio and the related morphological characteristics. Besides the concepts for increasing the absorption or the area of a chemically reactive surface, a very established approach concerns bandgap engineering by varying the size and shape of nanoparticles, which enables, for instance, the optimization of the optoelectronic material properties to the solar spectrum [13]. Furthermore, nanostructures can be used to embed sensitive photoactive materials in order to protect them from oxidation or photochemical processes due to exposure to moisture [14].

The mentioned examples of nanoscale materials and device concepts highlight the huge possibilities to tailor the corresponding functional properties in order to optimize the processes involved in energy conversion and storage. Yet, it is important to keep in mind that from an economic point of view, boosting efficiencies alone is not sufficient to establish a certain technology on the market. Rather, efficiencies must be related to the device lifetime and the production cost in order to compete with conventional approaches. It is particularly important whether upscaling by large-area deposition techniques is possible and whether the used precursor substances are available in sufficient quantities at reasonable cost. Therefore, it is highly desirable to use raw materials from cheap earth-abundant elements [15] or to minimize the amount of absorber materials by a combination with optics for efficient light collection [4,16] in order to achieve environmentally friendly production and recycling cycles. This also implies that substances with a high degree of toxicity should be avoided as far as possible [17]. The use of such toxic substances not only leads to a considerable increase in the fabrication cost (due to expensive security measures to meet the health and safety requirements in workspace) but also leads to indirect costs incurred during recycling or disposal of the materials [18,19].

To further establish the various technological approaches using nano- and microstructured materials for energy conversion, several challenges have to be overcome. Besides efficiency, device stability is a major concern, which particularly holds for cases in which organic or hybrid materials are involved [20]. For example protection against device degradation by advanced encapsulation techniques can help to further develop such tech-nologies [21]. As it is the case for conventional materials, interface engineering is also a major factor for device optimization. Due to the significantly increased surface-to-volume ratio of nanostructured materials, the development of interface passivation strategies is one of the major challenges in the case of photovoltaic devices where recombination losses are most harmful at the photoactive interfaces. To a large extent, the difficulties in this endeavour originate from the complexity of interfaces nanostructured in three dimensions [22]. Relating the morphology to results from defect-spectroscopy experiments, theoretical models and device performance could be a valuable approach to comprehensively address such issues.

Despite these challenges, nano- and microstructured materials will certainly play a dominant role in the development of next generation devices for energy conversion. At the same time, the huge variety of devices and material concepts also require massive efforts from the research community together with the related scientific discussions. In this sense, the present thematic issue provides a platform for a contemporary cross-section of topics in this broad field of research.

The *Beilstein Journal of Nanotechnology* is a unique medium for scientific exchange across the traditional disciplines. It is based on a non-profit organization, making it independent from commercial interests, while following the highest standards of open-access publishing. It was a pleasure to work closely with the editorial office and all the authors and reviewers contributing to the present thematic issue.

Harry Mönig and Martina Schmid

Münster and Duisburg, February 2019

ORCID® iDs

Harry Mönig - https://orcid.org/0000-0003-2639-9198
Martina Schmid - https://orcid.org/0000-0001-5103-0750

References

1. Kaienburg, P.; Klingebiel, B.; Kirchartz, T. *Beilstein J. Nanotechnol.* **2018**, *9,* 2114–2124. doi:10.3762/bjnano.9.200
2. Stroyuk, O. *Beilstein J. Nanotechnol.* **2018**, *9,* 2209–2235. doi:10.3762/bjnano.9.207
3. Lokar, Z.; Lipovsek, B.; Topic, M.; Krc, J. *Beilstein J. Nanotechnol.* **2018**, *9,* 2315–2329. doi:10.3762/bjnano.9.216
4. Ringleb, F.; Andree, S.; Heidmann, B.; Bonse, J.; Eylers, K.; Ernst, O.; Boeck, T.; Schmid, M.; Krüger, J. *Beilstein J. Nanotechnol.* **2018**, *9,* 3025–3038. doi:10.3762/bjnano.9.281
5. Vismara, R.; Isabella, O.; Ingenito, A.; Si, F. T.; Zeman, M. *Beilstein J. Nanotechnol.* **2019**, *10,* 322–331. doi:10.3762/bjnano.10.31
6. Kontoleta, E.; Askes, S. H. C.; Lai, L.-H.; Garnett, E. C. *Beilstein J. Nanotechnol.* **2018**, *9,* 2097–2105. doi:10.3762/bjnano.9.198

7. Patel, M.; Kim, J. *Beilstein J. Nanotechnol.* **2018,** *9,* 2432–2442. doi:10.3762/bjnano.9.228

8. Ruttert, M.; Holtstiege, F.; Hüsker, J.; Börner, M.; Winter, M.; Placke, T. *Beilstein J. Nanotechnol.* **2018,** *9,* 2381–2395. doi:10.3762/bjnano.9.223

9. Gröschel, A. H.; Müller, A. H. E. *Nanoscale* **2015,** *7,* 11841–11876. doi:10.1039/c5nr02448j

10. Feldmann, M., Ed. *Nanolithography: The Art of Fabricating Nanoelectronic and Nanophotonic Devices and Systems;* Woodhead Publishing, 2014.

11. Kooy, N.; Mohamed, K.; Pin, L.; Guan, O. *Nanoscale Res. Lett.* **2014,** *9,* 320. doi:10.1186/1556-276x-9-320

12. Bai, R.; Pandya, D. K.; Chaudhary, S.; Dhaka, V.; Khayrudinov, V.; Lemettinen, J.; Kauppinen, C.; Lipsanen, H. *Beilstein J. Nanotechnol.* **2019,** *10,* 274–280. doi:10.3762/bjnano.10.26

13. Khan, M. M.; Ansari, S. A.; Pradhan, D.; Ansari, M. O.; Han, D. H.; Lee, J.; Cho, M. H. *J. Mater. Chem. A* **2014,** *2,* 637–644. doi:10.1039/c3ta14052k

14. Waleed, A.; Tavakoli, M. M.; Gu, L.; Wang, Z.; Zhang, D.; Manikandan, A.; Zhang, Q.; Zhang, R.; Chueh, Y.-L.; Fan, Z. *Nano Lett.* **2017,** *17,* 523–530. doi:10.1021/acs.nanolett.6b04587

15. Shin, D.; Saparov, B.; Mitzi, D. B. *Adv. Energy Mater.* **2017,** *7,* 1602366. doi:10.1002/aenm.201602366

16. Schmid, M.; Manley, P.; Ott, A.; Song, M.; Yin, G. *J. Mater. Res.* **2016,** *31,* 3273–3289. doi:10.1557/jmr.2016.382

17. Fthenakis, V. M.; Moskowitz, P. D. *Prog. Photovoltaics* **1995,** *3,* 295–306. doi:10.1002/pip.4670030504

18. Binek, A.; Petrus, M. L.; Huber, N.; Bristow, H.; Hu, Y.; Bein, T.; Docampo, P. *ACS Appl. Mater. Interfaces* **2016,** *8,* 12881–12886. doi:10.1021/acsami.6b03767

19. Tao, J.; Yu, S. *Sol. Energy Mater. Sol. Cells* **2015,** *141,* 108–124. doi:10.1016/j.solmat.2015.05.005

20. Christians, J. A.; Habisreutinger, S. N.; Berry, J. J.; Luther, J. M. *ACS Energy Lett.* **2018,** *3,* 2136–2143. doi:10.1021/acsenergylett.8b00914

21. Shi, L.; Young, T. L.; Kim, J.; Sheng, Y.; Wang, L.; Chen, Y.; Feng, Z.; Keevers, M. J.; Hao, X.; Verlinden, P. J.; Green, M. A.; Ho-Baillie, A. W. Y. *ACS Appl. Mater. Interfaces* **2017,** *9,* 25073–25081. doi:10.1021/acsami.7b07625

22. Zielke, L.; Vierrath, S.; Moroni, R.; Mondon, A.; Zengerle, R.; Thiele, S. *RSC Adv.* **2016,** *6,* 80700–80705. doi:10.1039/c6ra16560e

BEILSTEIN JOURNAL OF NANOTECHNOLOGY

Localized photodeposition of catalysts using nanophotonic resonances in silicon photocathodes

Evgenia Kontoleta, Sven H. C. Askes, Lai-Hung Lai and Erik C. Garnett[*]

Abstract

Nanostructured semiconductors feature resonant optical modes that confine light absorption in specific areas called "hot spots". These areas can be used for localized extraction of the photogenerated charges, which in turn could drive chemical reactions for synthesis of catalytic materials. In this work, we use these nanophotonic hot spots in vertical silicon nanowires to locally deposit platinum nanoparticles in a photo-electrochemical system. The tapering angle of the silicon nanowires as well as the excitation wavelength are used to control the location of the hot spots together with the deposition sites of the platinum catalyst. A combination of finite difference time domain (FDTD) simulations with scanning electron microscopy image analysis showed a reasonable correlation between the simulated hot spots and the actual experimental localization and quantity of platinum atoms. This nanophotonic approach of driving chemical reactions at the nanoscale using the optical properties of the photo-electrode, can be very promising for the design of lithography-free and efficient hierarchical nanostructures for the generation of solar fuels.

Introduction

The relentless rise of CO_2 levels in the atmosphere as well as the growth of the world population remind us of the importance of finding new, clean pathways to cover our energy needs. Fuel generation from renewable energy resources could be one of the "clean" approaches for meeting our energy requirements. Although, sunlight is the most abundant source of green energy, its long-term storage is required, due to daily and yearly fluctu-

ations. The most promising medium for stable, high-density storage is in the form of chemical energy, such as H_2 or organic compounds, by using photochemical fuel generators [1-4].

In the center of a photochemical fuel generator are the photo-electrodes, where light absorption and conversion to chemical energy take place. The photo-electrodes are in contact with an

electrolyte that is the primary source of fuel together with the sunlight. In such a system, light absorption by the electrodes leads to the creation of electron–hole pairs, which after their separation participate in chemical reactions in the electrolyte to make fuels. One example is water splitting for H_2 generation [5,6]. Carefully designed photo-electrodes are necessary for low cost and high efficiency, which are both needed to make solar fuels competitive with fossil fuels as an energy carrier. Nanostructuring the main photoactive material, e.g., a semiconductor, has proven to be a promising method for increasing the efficiency of solar fuel generation [7,8]. The higher surface to volume ratio in nanostructured semiconductors ensures the use of less material, reduces the requirements on current density and often increases light absorption. This increased light absorption comes from optical resonances in nanomaterials, which have been studied extensively in both metallic (plasmonic) and dielectric material systems [9-13]. One hallmark of resonant absorption is the appearance of localized "hot spots". In particular, semiconducting nanostructures can sustain Mie-like leaky modes due to their high refractive index and the occurrence of multiple internal light reflections from the boundaries of the structure [9,13]. However, in vertical nanowires under normal-incidence illumination, Mie modes cannot be excited and instead coupling to waveguide modes (e.g., the HE_{11}) and subsequent Fabry–Perot cavity interference play the dominant role in creating these hot spots [14,15]. The highly concentrated electric fields at the hot spots lead to elevated concentrations of photogenerated charge carriers that can be used to drive solar fuel reactions [16-19]. Additionally, photochemical fuel generators require a catalyst, such as platinum, to lower the overpotential to drive the chemical reaction [2,7,20-24]. The catalyst would be ideally located at the semiconductor–solution interface, directly at the location of the hot spots.

Placing the catalyst exclusively at the hot spots would reduce both the catalyst loading (lowering the cost) and the average time between charge generation and chemical reaction (increasing the efficiency). However, current catalysts are simply randomly placed on semiconductor photo-electrodes with an optimized average density [20,24,25]. Photodeposition of the catalytic material with photogenerated charges from excited semiconductors has been also achieved but without a good control over the deposition sites [26-31]. An exception is the work of Li et al. [27], where charge separation was achieved at different crystal facets of $BiVO_4$ nanocrystals for selective photodeposition of metal and metal oxide catalytic nanoparticles. Nevertheless, this method for the moment is limited to this specific material and structure.

Here we present a different approach in which localized nanophotonic resonances in semiconductors are used to place cata-

lyst particles exactly where they are needed. We show that the location of catalyst deposition on vertical silicon nanowires can be tuned by adjusting their shape (tapering angle) or changing the excitation wavelength. The experimentally observed deposition profiles match reasonably well with optical simulations of the photogenerated charge carrier distribution for each shape and wavelength. Most notably, deposition profiles far from those expected from a simple Beer–Lambert law have been obtained, in contrast to previous related work on silicon microwires [32,33]. Our results provide the first step for rationally designed catalyst positioning using the underlying resonant properties of nanoscale photocatalysts, tunable simply by altering the shape, size or excitation wavelength. The extensive literature on such nanophotonic tuning makes this an exciting approach for lithography-free nanoscale control over catalyst positioning [34-38].

We have chosen vertical silicon nanowires as a model nanophotonic system because of their ease of fabrication, known optical constants and broad spectral absorption range. In presence of a Pt-catalyst precursor (H_2PtCl_6) in a three-electrode photo-electrochemical system (Figure 1), photogenerated electrons reach the surface of the silicon nanowires, reducing the precursor to form metallic platinum nanoparticles (Pt(0)). The position of the Pt deposition can be controlled by adjusting the tapering angle or the incident wavelength. The platinum photodeposition results are observed with a scanning electron microscope (SEM) and compared with the output of finite difference time domain (FDTD) simulations of the density distribution of the photogenerated carriers within the silicon nanostructures.
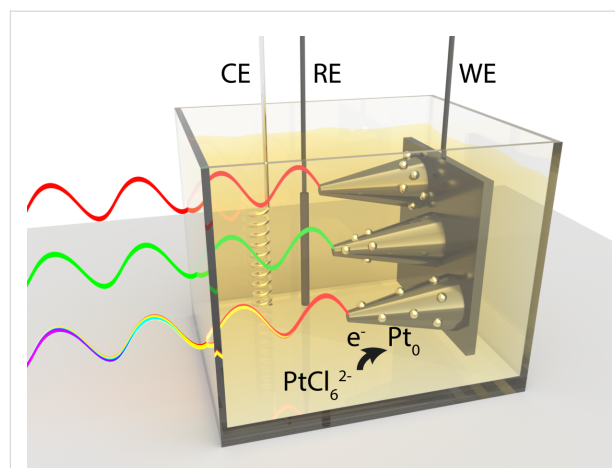
Figure 1: Schematic illustration of the photo-electrochemical deposition of metallic Pt on silicon nanostructures from hexachloroplatinate ($PtCl_6^{2-}$) in a three-electrode photo-electrochemical cell with counter electrode (CE), reference electrode (RE) and working electrode (WE). The location of catalyst deposition can be tuned by adjusting the excitation wavelength from red to green to white, or (not shown) the nanostructure shape.

Results and Discussion

## Fabrication of silicon nanostructures and calculation of their optical modes

Silicon nanostructures were fabricated by etching a p-type silicon substrate using a combination of Cl_2 and HBr/O_2 plasmas with 110 nm diameter SiO_2 spheres being used as etch mask. Tuning the ratio of the HBr/O_2 plasmas allowed for vertical nanowires with variable sidewall tapering angle (see details in Experimental section and Figure S1, Supporting Information File 1). Vertical nanocones (height ≈ 720 nm, top diameter ≈ 60 nm, bottom diameter ≈ 160 nm, angle ≈ 15°), inverted nanocones (height ≈ 1 µm, top diameter ≈ 70 nm, base diameter ≈ 120 nm and smallest diameter ≈ 60 nm) and nanowires (height ≈ 790 nm, diameter ≈ 80 nm) were fabricated here and subsequently used to tune the distribution of photogenerated carriers (Figure 2). An 18 nm amorphous TiO_2 layer was conformally deposited on the silicon nanostructures by using atomic layer deposition (ALD). This layer assists with charge separation, stabilizes the silicon surface and helps to passivate trap states, leading to well-known improvements in photo-electrochemical performance [39-41]. The amorphous TiO_2 layer was further annealed at 350 °C for 3 h to form crystalline anatase TiO_2, which led to an improved performance. The final TiO_2 layers were characterized with X-ray diffraction (XRD) (Figure S2, Supporting Information File 1) and ellipsometry

(Figure S3, Supporting Information File 1) to verify their quality. Both the XRD pattern and optical constants (*n* and *k* values) matched the literature values for thin anatase TiO_2 films [42].

The photocarrier density distribution under monochromatic illumination (532 or 638 nm) in the Si–TiO_2 nanostructures was simulated using the FDTD method. It was assumed that every absorbed photon was converted to an electron–hole pair and only the optical effects were taken into account in the simulations. The dimensions of the average silicon nanostructures extracted from SEM images were used for the simulations, while the *n* and *k* values measured with ellipsometry were used for the TiO_2 coating. Every structure was simulated on a thick silicon substrate, also coated with 18 nm TiO_2, and the surrounding refractive index was set to 1.33 to resemble the aqueous conditions of the reaction environment. The simulations show the cross-sectional absorbed power profiles (normalized to the maximum value per plot) of the three different silicon nanostructures, for excitation at 532 nm (Figure 2b) and 638 nm (Figure 2c). The location of the hot spots depends on the excitation wavelength and the shape of the nanostructure. Silicon nanocones confine light mostly at the top of the structure at 532 nm (Figure 2b) in contrast to an excitation at 638 nm, where most of the light is absorbed at the bottom of the cone (Figure 2c). In the case of inverted nanocones, light is concentrated primarily at the bottom for both wavelengths, although at 532 nm there are also additional hot spots along the height. In silicon nanowires, hot spots are present at the top and the middle of the structure for 532 nm but for excitation at 638 nm, more hot spots appear. Overall, the results of these simulations confirm the presence of distinct hot spots in the nanostructures and enable us to investigate whether the simulated hot spots match the location of the deposited catalytic material after illumination.

Photodeposition of platinum

A three-electrode photo-electrochemical cell, electrically connected with a potentiostat, was used for deposition of the platinum catalyst on the nanostructures. The sample served as the working electrode (WE) with a platinum wire counter electrode (CE) and Ag/AgCl reference electrode (RE) (Figure 1). During a typical photo-electrodeposition experiment, the sample was mounted in direct contact with a Pt-precursor electrolyte (4 mM H_2PtCl_6, pH 11) and the current flow to the working electrode was recorded as a function of time at a constant electrochemical potential, i.e., in the chronoamperometry mode. The samples had an open-circuit voltage potential of around −0.1 V (vs Ag/AgCl) and were biased by 700 mV to a more reducing potential of −0.8 V (vs Ag/AgCl) during deposition, to efficiently extract the photogenerated charges from the
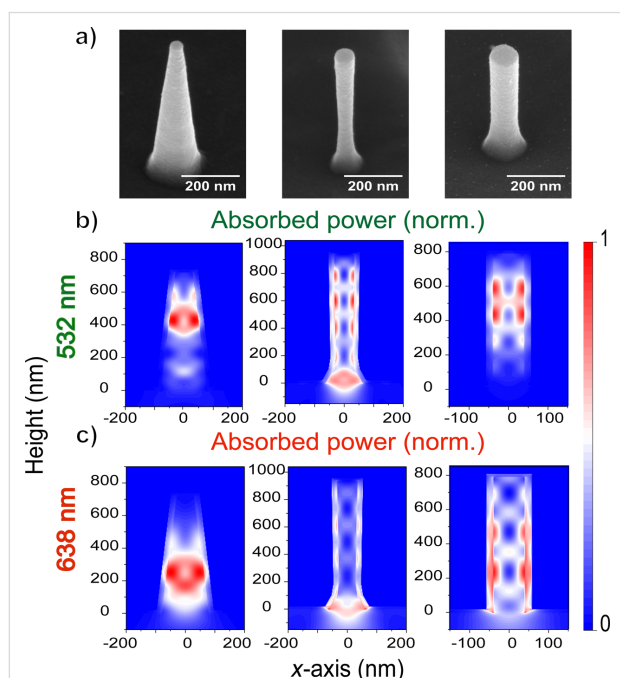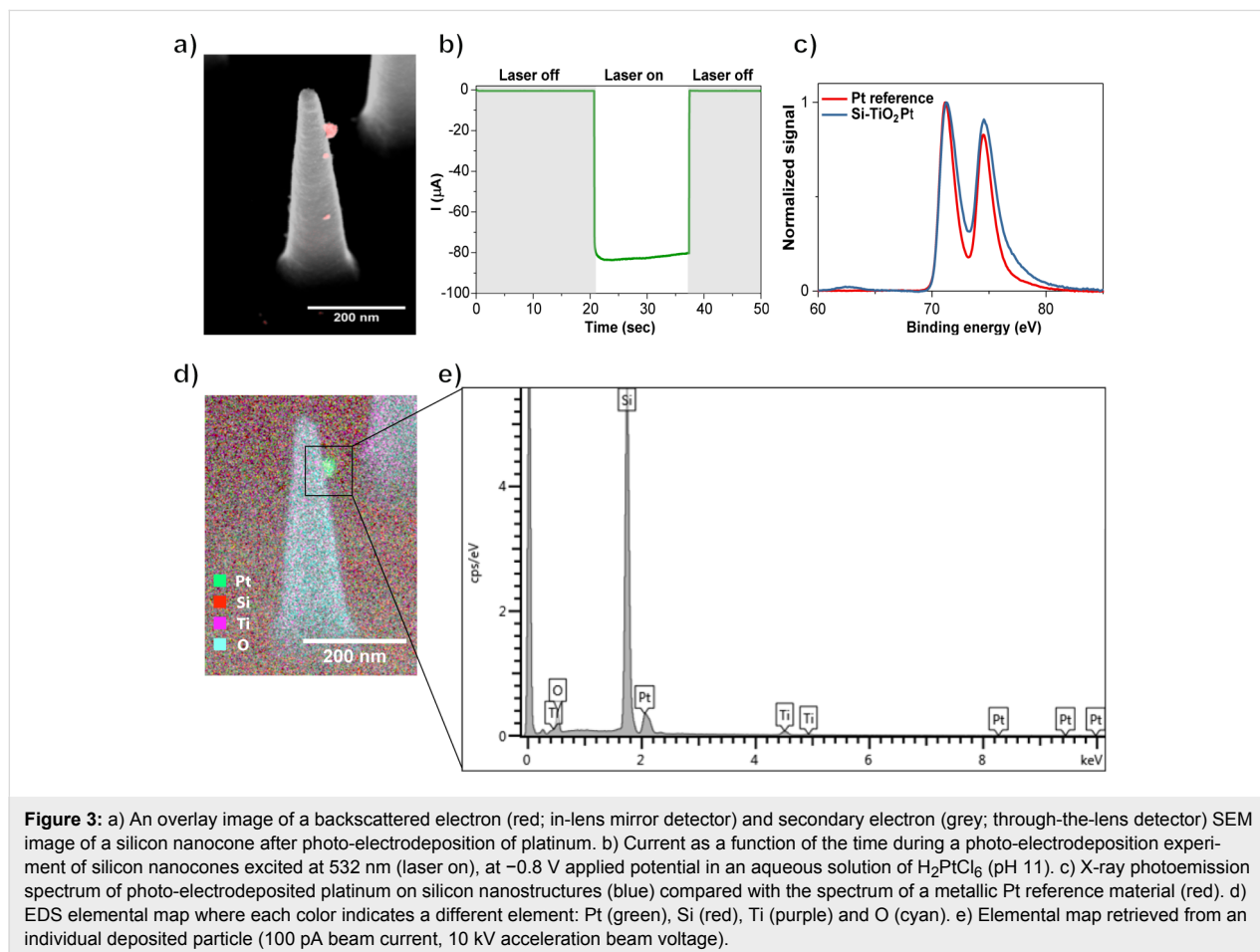

Figure 2: (a) SEM images of a silicon nanocone (left), an inverted nanocone (middle) and a nanowire (right) coated with an 18 nm TiO_2 layer. The tapering angle was controlled by varying the Cl_2 and HBr/O_2 flow rates during plasma etching. (b, c) FDTD simulations of absorbed power in each nanostructure at (b) 532 nm and (c) 638 nm normalized to the maximum value.

Si nanostructures into the electrolyte and enhance the kinetics of the reaction. The flat-band potential of TiO_2 at pH 11 is above the conduction band edge of p-type silicon, so TiO_2 acts as an electron blocking layer here [5,43,44]. Therefore, the presence of TiO_2 offers a control over the potential we could apply to selectively promote photodeposition while avoiding electrodeposition. In the absence of a TiO_2 layer the recorded dark current is much higher than the corresponding photocurrent (Figure S4a, Supporting Information File 1), which means that the electrons reaching the electrolyte by biasing the samples dominate over the photogenerated ones. SEM images (Figure S5, Supporting Information File 1) show the homogenous formation of platinum nanoparticles both on the Si nanostructures and on the substrate, when the samples were illuminated without the TiO_2 layer but still under biased conditions. The final potential value (−0.8 V) for photo-electrodeposition of platinum nanoparticles in the presence of a TiO_2 layer was chosen because it yields a high current ratio between illumination and dark conditions (Figure S6, Supporting Information File 1). Even more negative potentials than −0.8 V could be used here, but it was not necessary since the kinetics of the reaction were fast enough to drive the photo-electrodeposition

in a few seconds. Typically, the current was 75–200 times greater with illumination than without. As shown in Figure 3b, during the first 20 s of a typical photo-electrodeposition experiment using 532 nm light, the laser beam was blocked and the current was recorded. As soon as the laser beam hit the sample, a current increase was observed due to the contribution of the photogenerated charges. After an electrical charge of around 1.35 mC was passed to the illuminated sample, the laser beam was blocked again and the measurement was stopped.

The area of the laser beam (0.06 mm^2 for 532 nm and 0.35 mm^2 for 638 nm) was much smaller than the surface of the samples in contact with the electrolyte (0.3 cm^2), which allowed straightforward identification of the illuminated area and discrimination of platinum deposition under light and dark conditions in the same experiment (Figure S7, Supporting Information File 1). SEM images (Figure 3a and Figure S8, Supporting Information File 1) taken from the illuminated region revealed the presence of new nanoparticles on the silicon nanostructures and substrate. These were not observed far from the illuminated region (Figure S9, Supporting Information File 1), which confirmed that the irradiation had caused the formation of nano-

Figure 3: a) An overlay image of a backscattered electron (red; in-lens mirror detector) and secondary electron (grey; through-the-lens detector) SEM image of a silicon nanocone after photo-electrodeposition of platinum. b) Current as a function of the time during a photo-electrodeposition experiment of silicon nanocones excited at 532 nm (laser on), at −0.8 V applied potential in an aqueous solution of H_2PtCl_6 (pH 11). c) X-ray photoemission spectrum of photo-electrodeposited platinum on silicon nanostructures (blue) compared with the spectrum of a metallic Pt reference material (red). d) EDS elemental map where each color indicates a different element: Pt (green), Si (red), Ti (purple) and O (cyan). e) Elemental map retrieved from an individual deposited particle (100 pA beam current, 10 kV acceleration beam voltage).

particles. Energy-dispersive X-ray spectrometry (EDS) mapping clearly confirmed the presence of platinum, when an individual newly formed particle was analyzed (Figure 3d and Figure 3e). Furthermore, the oxidation state of platinum was investigated with X-ray photo-electron spectroscopy (XPS) on a sample with a higher amount of photo-electrodeposited platinum (ca. 2 mC). The observed platinum $4f_{7/2}$ and $4f_{5/2}$ binding energy peaks corresponded very well to those of a metallic Pt reference material (Figure 3c). Overall, these results demonstrate that light can be used as an external stimulus for the formation of catalytic Pt(0) material on Si nanostructures.

Correlation of hot spots and Pt deposition sites

Next, a comparison was made between the Pt deposition sites and the simulated optical hot spots of the Si nanostructures with an SEM image analysis approach, as follows: First, preliminary chronoamperometric experiments were conducted to indicate the conditions in which we could easily identify the location of the platinum particles on each nanostructure without the total overgrowth of the latter. A total amount of around 1 mC was needed to obtain well separated Pt particles with a diameter of 11 nm, which typically corresponded to 15–20 s of illumination at 532 or 638 nm with a light intensity of 1.2 W/cm^2 or 0.35 W/cm^2, respectively. The size of the deposited platinum nanoparticles was selected only for particle identification purposes and further optimization of the photo-electrodeposition process is necessary for the fabrication of efficient photo-catalytic samples. For each Si nanostructure morphology, overlays of secondary-electron and backscattered-electron (collected with an in-lens mirror detector) SEM images were acquired. This overlay method facilitates the identification of platinum nanoparticles based on the high electron backscattering efficiency of this heavy element (Figure 4a and Figures S10–S12, Supporting Information File 1). Images were collected from 100 individual nanostructures of each morphology while exclusively considering structures with dimensions within half a standard deviation of the average structure. Furthermore, platinum particles with a diameter below 6 nm were excluded, as they could also originate from electrodeposition (Figure S9, Supporting Information File 1). The volume of each Pt nanoparticle was estimated and converted to the corresponding number of platinum atoms. Finally, histograms were made to visualize the deposited amount of Pt as a function of the Si nanostructure height (Figure 4b and Figure 4c). The results are presented together with the simulated integrated absorbed power (normalized to the maximum value per plot) along the height of every structure at 532 and 638 nm.

Comparison of the platinum deposition distribution on the silicon nanostructures and the integrated absorbed power
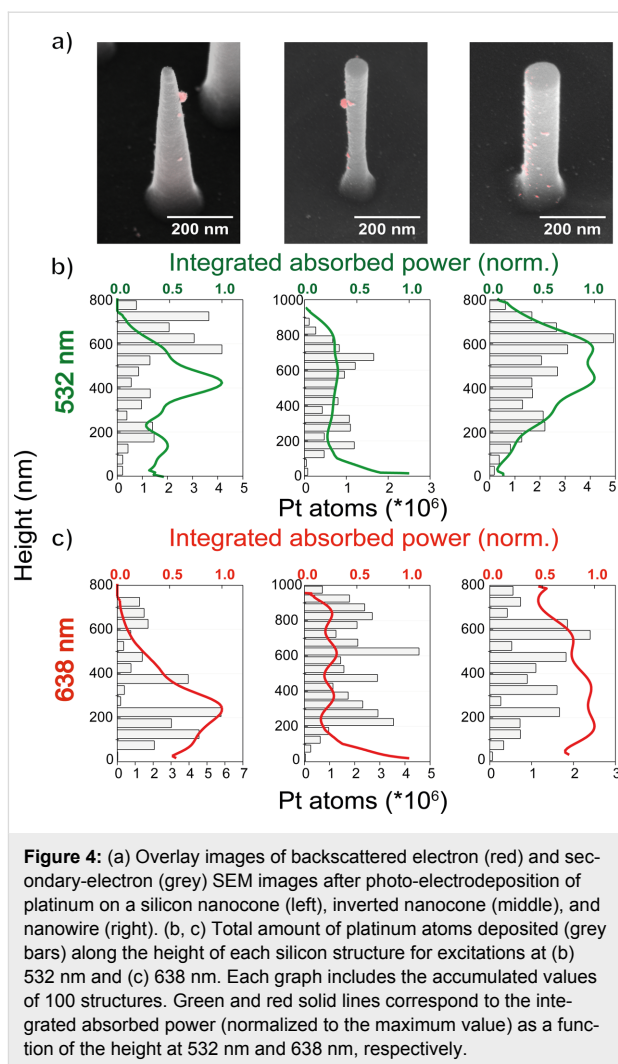
Figure 4: (a) Overlay images of backscattered electron (red) and secondary-electron (grey) SEM images after photo-electrodeposition of platinum on a silicon nanocone (left), inverted nanocone (middle), and nanowire (right). (b, c) Total amount of platinum atoms deposited (grey bars) along the height of each silicon structure for excitations at (b) 532 nm and (c) 638 nm. Each graph includes the accumulated values of 100 structures. Green and red solid lines correspond to the integrated absorbed power (normalized to the maximum value) as a function of the height at 532 nm and 638 nm, respectively.

profiles reveals that they match reasonably. Specifically, for silicon nanocones a correlation of the platinum deposition sites and the optical modes is shown for both excitation wavelengths with some deviations. At 532 nm, the two peaks of the platinum distribution are slightly shifted towards larger heights, while at 638 nm deposition of platinum is also observed in locations not expected from the absorbed power simulations, i.e., at the top of the nanostructure. In the case of inverted nanocones, the platinum deposition profiles seem to follow the profiles of the integrated absorbed power. However, simulations showed that most of the light is absorbed at the bottom of the nanostructure, where no platinum is observed in the experiments. In contrast, deposition of the catalytic material occurs primarily at a height of around 200–300 nm from the bottom. This discrepancy may be explained by the fact that both nanocones and inverted nanocones exhibit structural diameter differences along their height, which could lead to differences in carrier collection efficiency if the diffusion length is of the order of, or smaller than, the diameter. Such variations in carrier collection

efficiency would naturally alter the final deposition distribution in a manner qualitatively consistent with our observations. Finally, silicon nanowires excited at 532 nm concentrate the incident light mostly at the top or the middle of the structure, corresponding well with the platinum deposition analysis. For 638 nm excitation, the same structures exhibited multiple deposition sites along their height, which is also correlated to the integrated absorbed power peaks.

Instead of the formation of new small particles of platinum on the silicon nanostructures, overgrowth of the already deposited ones was noticed from the SEM images (Figures S10–S12, Supporting Information File 1). This effect could be explained by the fact that platinum nanoparticles act as electron-trapping centers on the surface of TiO_2 [45,46]. After the formation of the very first platinum nanoparticles, photogenerated electrons from the silicon nanostructures are transferred to TiO_2 and in sequence to the already formed platinum. The Schottky barrier between TiO_2 and platinum nanoparticles does not allow for a "back" transfer of electrons. Hence, charge separation is promoted, which allows further reduction of hexachloroplatinate to Pt(0) on one of the existing platinum nanoparticles rather than in new locations. As a result, the initial platinum nanoparticle formation may alter the final deposition profile from the simulated one by prohibiting the deposition at other parts of the nanostructrure. As mentioned earlier, an external electric field is applied to the samples for more efficient extraction of the photogenerated charges. This electric field is not taken into account in the simulated distribution of the charges along the height of the Si nanostructures (Figure 2), and this is another factor that could affect the localization of the photo-electrodeposition. The platinum deposition could also be broadened compared to the simulated profile due to our method of measuring the height of each particle, which extracts 3D distances from a 2D image. Noise could also be introduced by the TiO_2 layer itself. Although TiO_2 has a shorter electron diffusion length compared to silicon [47,48], the TiO_2 surface could also have randomly distributed surface sites with higher catalytic activity, leading to preferential deposition, or traps that capture carriers preventing deposition.

Conclusion

We show that the optical modes of silicon nanostructures can be used for lithography-free patterning of catalytic nanoparticles. Tuning of the photo-electrochemical formation of platinum nanoparticles along the height of silicon nanostructures was achieved by changing either the shape (tapering angle) of the silicon nanostructures or the excitation wavelength (red or green light). This method utilizing the optical modes of semiconducting nanostructures to pattern catalytic materials with nanoscale control can be a very promising method for an easy and low-cost fabrication of efficient photo-electrodes. It provides a lot of flexibility on the materials involved and on the design of the final structure. Further research should be focused on improving the positioning precision and implementing the approach in a state-of-the art photo-electrode/catalyst system in order to demonstrate the potential for solar fuel production enhancement.

Experimental
General
Chemicals were purchased from major chemical suppliers and used as received. Scanning electron microscopy (SEM) was performed on a FEI Verios 460 with a typical acceleration beam voltage of 5 kV and 100 pA beam current. Secondary-electron images were collected with a through-the-lens detector (TLD) and backscattered-electron images were collected with an in-lens mirror detector. Energy dispersive X-ray spectrometry (EDS) was performed with an Oxford Instruments device with an acceleration beam voltage of 10 kV and beam current of 100 pA. X-ray diffraction was done with a Bruker D2 Phaser with Cu Kα radiation (λ = 1.5418 Å).

Simulations
Lumerical FDTD Solutions was used for simulations of single silicon nanostructures on a $3.5 \times 3.5 \times 2$ μm silicon substrate. Absorbed power simulations were conducted with an 18 nm TiO_2 layer, with refractive index values (*n* and *k*) retrieved from ellipsometry (Figure S3, Supporting Information File 1). An example of the simulation environment can be found in Figure S13 (Supporting Information File 1) in which the case of inverted nanocones is presented. The structures were excited with a plane wave source with wavelengths of 400–1100 nm and the absorbed power was retrieved from an absorption per unit volume monitor with wavelength selection option. The refractive index of the surrounding medium was set to 1.33. The mesh size in the FDTD simulations was equal to $2 \times 2 \times 2$ nm for all the structures.

Fabrication of silicon nanostructures
Silicon p-type samples (Active Business Company GmbH, <100> orientation) 12 × 12 mm, with 1–10 Ω·cm resistivity, were used as substrates for the fabrication of the three different types of silicon nanostructures. First, the samples were cleaned with soap and consecutively rinsed with copious amounts of water, acetone and isopropanol. After that, the samples were submerged in hot piranha solution (120 °C, 3:1 concentrated H_2SO_4/30% H_2O_2) for 20 min and rinsed with deionized water. Then 2–3 μL of 110 nm diameter SiO_2 spheres dispersed in ethanol were drop-cast on the clean silicon samples and annealed for 1 min at 60 °C on a hot plate. The samples were etched with a combination of plasmas (PlasmaPro 100 Cobra

ICP Etch). First Cl$_2$ (20 sec, 50 sccm, HF forward power 40 W, 7 mTorr) was used for removal of the native oxide and then HBr/O$_2$ (5 min for nanocones and 11 min for nanowires and inverted nanocones, HF forward power 30 W, 7 mTorr) was used for etching the silicon to the desired structures. Before the etching steps an oxygen cleaning step was used (1 min and 30 sec, 50 sccm O$_2$, HF forward power 60 W, ICP forward power 100 W, 6 mTorr). The temperature used for all the steps of the plasma etching was 20 °C. The ratio of HBr/O$_2$ was very crucial for the control of the shape of the silicon structures. For the nanocones a ratio of 48.2:1.8 sccm (HBr/O$_2$) was chosen, 49.5:0.5 for inverted nanocones and 49:1 for stand-up nanowires. The ICP forward power during Cl$_2$ and HBr/O$_2$ etching was 750 W for silicon nanocones and nanowires, and 600 W for inverted nanocones. After etching, the samples were treated with 7 vol % HF solution for the removal of SiO$_2$ formed during the etching procedure, rinsed with water, dipped in hot piranha solution for 20 min and rinsed one more time with water. The last step (hot piranha solution) proved necessary to obtain a smooth coating of the structures with TiO$_2$, probably due to the increase of the hydrophilicity.

Formation of TiO$_2$ using atomic layer deposition

A custom-built atomic layer deposition system was used for the deposition of thin and compact TiO$_2$ layers on the silicon nanostructures. For 18 nm TiO$_2$ layers, subsequent injection of MilliQ water (18.2 MΩ·cm) and 99.995 % TiCl$_4$ (for 10 ms each) took place in a vacuum chamber with a delay of 18 s between each injection. The samples were heated by a copper stage at 100 °C. The base pressure of the system was below 5·10^{-2} mbar. The pressure during deposition was adjusted to 1.1 mbar using an N$_2$ purging flow to remove the formed gases and excess precursors. Post-annealing of the samples in a tube oven, in air, at 350 °C for 3 h with a ramp of 11 °C/min was needed for the formation of anatase TiO$_2$ (Figure S2, Supporting Information File 1).

Photo-electrochemical deposition

For the deposition of platinum nanoparticles, a photo-electrochemical cell (Zahner Scientific Instruments, PECC-1, slightly modified) made from Teflon was used (Figure S14, Supporting Information File 1). The cell has three inputs for the three different electrodes (working, reference and counter). Only a small area (0.3 cm^2) of the working electrode (i.e., the sample) was in contact with the electrolyte, which was illuminated through a quartz window. The electrolyte consisted of an aqueous solution of chloroplatinic acid (4 mM) and Na$_2$SO$_4$ (0.1 M), with the pH value adjusted to 11 with 2 M NaOH. The back contact of the sample consisted of 4 nm of chromium and 50 nm of gold deposited with a double-target sputter coater (Leica EM

ACE600). The electrical connections of the sample with the potentiostat (BioLogic Science Instruments, SP-200) were made using conductive aluminum tape (Advance Tapes AT521) adhered to the back metal contact of the sample, which was not in contact with the electrolyte.

X-ray photoemission spectroscopy (XPS)

X-ray photoemission spectroscopy (XPS) was performed in a custom-built ultrahigh-vacuum chamber, operating at a base pressure below 5 × 10^{-9} mbar. A XM1200 monochromatic X-ray source (Al Kα line, Scienta Omicron) was used for X-ray excitation of the sample under a 45° angle. Photoemitted electrons were collected using a HIPP-3 analyzer (Scienta Omicron). A polished platinum pellet (99.99%, Kurt J. Lesker Company) was used for acquiring a Pt reference spectrum. Spectra were charge-corrected using the binding energy of C 1s (284.8 eV).

Supporting Information

Schematic description of the experimental process step by step for the Si nanostructures fabrication; XRD and ellipsometry data of the TiO$_2$ layer; chronoamperometry measurements of Si nanocones with and without TiO$_2$ layer; SEM image of Si nanocone after illumination without the TiO$_2$ layer; current-vs-potential measurement on silicon nanocones; SEM images in and out of the illumination spot and of the illumination spot itself; representation of the photo-electrochemical cell; schematic diagram of the FDTD simulations and SEM images of more silicon nanostructures after photo-electrodeposition of platinum for verification of the effect.

Supporting Information File 1
Additional experimental data.
[https://www.beilstein-journals.org/bjnano/content/supplementary/2190-4286-9-198-S1.pdf]

ORCID® iDs
Evgenia Kontoleta - https://orcid.org/0000-0002-3327-1523
Sven H. C. Askes - https://orcid.org/0000-0001-6538-3645
Erik C. Garnett - https://orcid.org/0000-0002-9158-8326

References

1. Landman, A.; Dotan, H.; Shter, G. E.; Wullenkord, M.; Houaijia, A.; Maljusch, A.; Grader, G. S.; Rothschild, A. *Nat. Mater.* **2017,** *16,* 646–651. doi:10.1038/nmat4876
2. Shi, Z.; Wen, X.; Guan, Z.; Cao, D.; Luo, W.; Zou, Z. *Ann. Phys.* **2015,** *358,* 236–247. doi:10.1016/j.aop.2015.04.005
3. Joya, K. S.; Joya, Y. F.; Ocakoglu, K.; van de Krol, R. *Angew. Chem., Int. Ed.* **2013,** *52,* 10426–10437. doi:10.1002/anie.201300136
4. Benson, E. E.; Kubiak, C. P.; Sathrum, A. J.; Smieja, J. M. *Chem. Soc. Rev.* **2009,** *38,* 89–99. doi:10.1039/B804323J
5. Li, J.; Wu, N. *Catal. Sci. Technol.* **2015,** *5,* 1360–1384. doi:10.1039/C4CY00974F
6. Bak, T.; Nowotny, J.; Rekas, M.; Sorrell, C. C. *Int. J. Hydrogen Energy* **2002,** *27,* 991–1022. doi:10.1016/s0360-3199(02)00022-8
7. Li, Z.; Feng, J.; Yan, S.; Zou, Z. *Nano Today* **2015,** *10,* 468–486. doi:10.1016/j.nantod.2015.06.001
8. Kamat, P. V. *J. Phys. Chem. C* **2007,** *111,* 2834–2860. doi:10.1021/jp066952u
9. Brongersma, M. L.; Cui, Y.; Fan, S. *Nat. Mater.* **2014,** *13,* 451–460. doi:10.1038/nmat3921
10. Atwater, H. A.; Polman, A. *Nat. Mater.* **2010,** *9,* 205–213. doi:10.1038/nmat2629
11. Wang, W.; Ramezani, M.; Väkeväinen, A. I.; Törmä, P.; Rivas, J. G.; Odom, T. W. *Mater. Today* **2018,** *21,* 303–314. doi:10.1016/j.mattod.2017.09.002
12. Landreman, P. E.; Chalabi, H.; Park, J.; Brongersma, M. L. *Opt. Express* **2016,** *24,* 29760. doi:10.1364/oe.24.029760
13. Cao, L.; Fan, P.; Vasudev, A. P.; White, J. S.; Yu, Z.; Cai, W.; Schuller, J. A.; Fan, S.; Brongersma, M. L. *Nano Lett.* **2010,** *10,* 439–445. doi:10.1021/nl9036627
14. Wells, S. M.; Merkulov, I. A.; Kravchenko, I. I.; Lavrik, N. V.; Sepaniak, M. J. *ACS Nano* **2012,** *6,* 2948–2959. doi:10.1021/nn204110z
15. Grzela, G.; Paniagua-Domínguez, R.; Barten, T.; van Dam, D.; Sánchez-Gil, J. A.; Rivas, J. G. *Nano Lett.* **2014,** *14,* 3227–3234. doi:10.1021/nl5005948
16. Boriskina, S. V.; Ghasemi, H.; Chen, G. *Mater. Today* **2013,** *16,* 375–386. doi:10.1016/j.mattod.2013.09.003
17. Zheng, X.; Zhang, L. *Energy Environ. Sci.* **2016,** *9,* 2511–2532. doi:10.1039/C6EE01182A
18. Zhang, X.; Li, X.; Zhang, D.; Su, N. Q.; Yang, W.; Everitt, H. O.; Liu, J. *Nat. Commun.* **2017,** *8,* 14542. doi:10.1038/ncomms14542
19. Wang, P.; Huang, B.; Dai, Y.; Whangbo, M.-H. *Phys. Chem. Chem. Phys.* **2012,** *14,* 9813. doi:10.1039/c2cp40823f
20. Zhang, Z.; Wang, Z.; Cao, S.-W.; Xue, C. *J. Phys. Chem. C* **2013,** *117,* 25939–25947. doi:10.1021/jp409311x
21. Lu, Y.-C.; Xu, Z.; Gasteiger, H. A.; Chen, S.; Hamad-Schifferli, K.; Shao-Horn, Y. *J. Am. Chem. Soc.* **2010,** *132,* 12170–12171. doi:10.1021/ja1036572
22. Kim, H. J.; Kearney, K. L.; Le, L. H.; Haber, Z. J.; Rockett, A. A.; Rose, M. J. *J. Phys. Chem. C* **2016,** *120,* 25697–25708. doi:10.1021/acs.jpcc.6b08096
23. Zhou, L.; Zhang, C.; McClain, M. J.; Manjavacas, A.; Krauter, C. M.; Tian, S.; Berg, F.; Everitt, H. O.; Carter, E. A.; Nordlander, P.; Halas, N. J. *Nano Lett.* **2016,** *16,* 1478–1484. doi:10.1021/acs.nanolett.5b05149
24. Jiang, Z.; Zhang, Z.; Shangguan, W.; Isaacs, M. A.; Durndell, L. J.; Parlett, C. M. A.; Lee, A. F. *Catal. Sci. Technol.* **2016,** *6,* 81–88. doi:10.1039/C5CY01364J
25. Zhong, Z.; Ho, J.; Teo, J.; Shen, S.; Gedanken, A. *Chem. Mater.* **2007,** *19,* 4776–4782. doi:10.1021/cm071165a
26. Han, K. N.; Li, C. A.; Bui, M. P. N.; Pham, X. H.; Kim, B. S.; Choa, Y. H.; Seong, G. H. *Sens. Actuators, B* **2012,** *174,* 406–413. doi:10.1016/j.snb.2012.08.066
27. Li, R.; Zhang, F.; Wang, D.; Yang, J.; Li, M.; Zhu, J.; Zhou, X.; Han, H.; Li, C. *Nat. Commun.* **2013,** *4,* 1432. doi:10.1038/ncomms2401
28. McDonald, K. J.; Choi, K.-S. *Chem. Mater.* **2011,** *23,* 1686–1693. doi:10.1021/cm1020614
29. Zhong, D. K.; Cornuz, M.; Sivula, K.; Grätzel, M.; Gamelin, D. R. *Energy Environ. Sci.* **2011,** *4,* 1759. doi:10.1039/c1ee01034d
30. Taing, J.; Cheng, M. H.; Hemminger, J. C. *ACS Nano* **2011,** *5,* 6325–6333. doi:10.1021/nn201396v
31. Fernando, J. F. S.; Shortell, M. P.; Noble, C. J.; Harmer, J. R.; Jaatinen, E. A.; Waclawik, E. R. *ACS Appl. Mater. Interfaces* **2016,** *8,* 14271–14283. doi:10.1021/acsami.6b03128
32. Dasog, M.; Carim, A. I.; Yalamanchili, S.; Atwater, H. A.; Lewis, N. S. *Nano Lett.* **2016,** *16,* 5015–5021. doi:10.1021/acs.nanolett.6b01782
33. Krogstrup, P.; Jørgensen, H. I.; Heiss, M.; Demichel, O.; Holm, J. V.; Aagesen, M.; Nygard, J.; Fontcuberta i Morral, A. *Nat. Photonics* **2013,** *7,* 306–310. doi:10.1038/nphoton.2013.32
34. Schmitt, S. W.; Sarau, G.; Christiansen, S. *Sci. Rep.* **2015,** *5,* 17089. doi:10.1038/srep17089
35. Coenen, T.; van de Groep, J.; Polman, A. *ACS Nano* **2013,** *7,* 1689–1698. doi:10.1021/nn3056862
36. Lin, C.; Povinelli, M. L. *Opt. Express* **2009,** *17,* 19371. doi:10.1364/oe.17.019371
37. Wang, Z. Y.; Zhang, R. J.; Wang, S. Y.; Lu, M.; Chen, X.; Zheng, Y. X.; Chen, L. Y.; Ye, Z.; Wang, C. Z.; Ho, K. M. *Sci. Rep.* **2015,** *5,* 7810. doi:10.1038/srep07810
38. Scheuermann, A. G.; Prange, J. D.; Gunji, M.; Chidsey, C. E. D.; McIntyre, P. C. *Energy Environ. Sci.* **2013,** *6,* 2487. doi:10.1039/c3ee41178h
39. Shaner, M. R.; Hu, S.; Sun, K.; Lewis, N. S. *Energy Environ. Sci.* **2015,** *8,* 203–207. doi:10.1039/C4EE03012E
40. Hu, S.; Shaner, M. R.; Beardslee, J. A.; Lichterman, M.; Brunschwig, B. S.; Lewis, N. S. *Science* **2014,** *344,* 1005–1009. doi:10.1126/science.1251428
41. Bezares, F. J.; Long, J. P.; Glembocki, O. J.; Guo, J.; Rendell, R. W.; Kasica, R.; Shirey, L.; Owrutsky, J. C.; Caldwell, J. D. *Opt. Express* **2013,** *21,* 27587. doi:10.1364/oe.21.027587
42. Siefke, T.; Kroker, S.; Pfeiffer, K.; Puffky, O.; Dietrich, K.; Franta, D.; Ohlídal, I.; Szeghalmi, A.; Kley, E.-B.; Tünnermann, A. *Adv. Opt. Mater.* **2016,** *4,* 1780–1786. doi:10.1002/adom.201600250
43. Lyon, L. A.; Hupp, J. T. *J. Phys. Chem. B* **1999,** *103,* 4623–4628. doi:10.1021/jp9908404
44. Kohtani, S.; Yoshida, K.; Maekawa, T.; Iwase, A.; Kudo, A.; Miyabe, H.; Nakagaki, R. *Phys. Chem. Chem. Phys.* **2008,** *10,* 2986. doi:10.1039/b719913a
45. Jiao, J.; Wei, Y.; Chi, K.; Zhao, Z.; Duan, A.; Liu, J.; Jiang, G.; Wang, Y.; Wang, X.; Han, C.; Zheng, P. *Energy Technol.* **2017,** *5,* 877–883. doi:10.1002/ente.201600572
46. Shuang, S.; Lv, R.; Xie, Z.; Zhang, Z. *Sci. Rep.* **2016,** *6,* 26670. doi:10.1038/srep26670
47. Hodes, G.; Kamat, P. V. *J. Phys. Chem. Lett.* **2015,** *6,* 4090–4092. doi:10.1021/acs.jpclett.5b02052
48. Chi, J. Y.; Gatos, H. C. *J. Appl. Phys.* **1979,** *50,* 3433–3440. doi:10.1063/1.326336

Spin-coated planar Sb$_2$S$_3$ hybrid solar cells approaching 5% efficiency

Pascal Kaienburg[*1], Benjamin Klingebiel[1] and Thomas Kirchartz[*1,2]

Address:
[1]IEK5-Photovoltaics, Forschungszentrum Jülich, 52425 Jülich, Germany and [2]Faculty of Engineering and CENIDE, University of Duisburg-Essen, Carl-Benz-Str. 199, 47057 Duisburg, Germany

Email:
Pascal Kaienburg[*] - paskai@posteo.de; Thomas Kirchartz[*] - t.kirchartz@fz-juelich.de

* Corresponding author

Keywords:
antimony sulfide; hole transport material; solar cell

Abstract

Antimony sulfide solar cells have demonstrated an efficiency exceeding 7% when assembled in an extremely thin absorber configuration deposited via chemical bath deposition. More recently, less complex, planar geometries were obtained from simple spin-coating approaches, but the device efficiency still lags behind. We compare two processing routes based on different precursors reported in the literature. By studying the film morphology, sub-bandgap absorption and solar cell performance, improved annealing procedures are found and the crystallization temperature is shown to be critical. In order to determine the optimized processing conditions, the role of the polymeric hole transport material is discussed. The efficiency of our best solar cells exceeds previous reports for each processing route, and our champion device displays one of the highest efficiencies reported for planar antimony sulfide solar cells.

Introduction

Antimony sulfide (Sb$_2$S$_3$) is a promising high band gap light absorber for solar cells [1-5]. The record efficiency of 7.5% [6] is comparable to that of other less investigated materials, such as the best lead-free perovskites [7], Cu$_2$O [8] and Sb$_2$Se$_3$ [9,10] and outperforms bismuth-halides [11,12], SnS [13] and Bi$_2$S$_3$ [14-16]. However, the efficiency of Sb$_2$S$_3$ trails behind the more thoroughly studied material systems such as lead-based perovskites [17], organic solar cells [18,19] or PbS [20], thus further technological investigation is needed. Two basic

factors that impact the solar cell performance of a given material are the device architecture, which defines the mechanism of charge separation, and the deposition method for the absorber, which affects the film and electronic material quality.

Sb$_2$S$_3$ is commonly applied in an extremely thin absorber (ETA) architecture, which is similar to that of dye-sensitized solar cells [21]. A thin absorber layer of around 10 nm [22] is deposited on a mesoporous TiO$_2$ scaffold and the pores are

subsequently filled with a hole transport material (HTM). Progress in terms of device efficiency can be attributed to more feasible HTMs [1-5] and improved properties of the Sb_2S_3 itself [6], which lead to a record efficiency of >7% as shown in Figure 1. The core idea behind the ETA concept is that thin inorganic absorber layers relax the requirements for electronic material quality [23-25] since charges are quickly extracted from the absorber. However, the benefits are restricted by recombination via trap-assisted tunneling [24] which must be compensated by increasing the absorber thickness for optimized performance. A major challenge in the processing of ETA solar cells is the improper infiltration of pores [22], which can give way to incomplete coverage of the TiO_2 scaffold and an interface between TiO_2 and HTM. From a conceptual perspective, planar geometries reduce the large interface area required in ETA cells for appreciable photocurrent generation and should better prevent direct contact between the electron and hole transport layers both of which should reduce recombination [26]. Indeed, despite the generally lower efficiencies, as depicted in Figure 1, planar geometries have reached slightly higher open-circuit voltages [27,28] than the best performing ETA cells [1,6] – especially when devices are compared that apply the same HTM and Sb_2S_3 deposition method [26,29-31].

Figure 1: Development of Sb_2S_3 technology. Solar cells with extremely thin absorber architecture [1-6,29] reach the highest efficiencies. Planar devices have been produced via various methods such as atomic layer deposition (ALD) [32], chemical bath deposition (CBD) [27] and (rapid) thermal evaporation (R)TE [33-35]. As the latest development, spin-coated planar solar cells [31,36-38] reached an efficiencies >4%. This work extends the progress to almost 5%.

Typically Sb_2S_3 is fabricated via chemical bath deposition (CBD) [2,39-41] with the drawback of a complex growth mechanism that includes heterogeneous nucleation and exponential growth which requires the precise control of processing conditions and eventually limits the process' reproducibility [29,32]. During chemical reactions in the water bath, various antimony

oxides, hydroxides and sulfates form [6,42-44] which could be detrimental to device performance. With respect to oxide formation a short air exposure was shown to increase device performance but longer exposure times deteriorated the solar cell [45]. In another study post-sulfurization reduced the Sb_2O_3 content and thereby the concentration of deep traps which improved solar cell performance [6].

As an alternative to CBD, spin-coating of different antimony- and sulfur-containing precursors was proposed [29,36,37]. A metal-organic complex is formed in solution which is then spin-coated and afterwards thermally decomposed. Just like for CBD [2,41] or ALD [22,32] the resulting amorphous film needs to be annealed at elevated temperatures to obtain crystalline Sb_2S_3. Choi and Il Seok reported an antimony–thiourea (Sb–TU) complex and demonstrated efficiencies above 5% in an ETA configuration with poly[2,6-(4,4-bis-(2-ethylhexyl)-4*H*-cyclopenta[2,1-b;3,4-b']-dithiophene)-*alt*-4,7-(2,1,3-benzothiadiazole)] PCPDTBT as the hole transport material and efficiencies above 6% when an organic bulk heterojunction was used instead of the pure polymer [29]. Gil et al. [38] applied the same precursor to a planar device configuration and found a strong correlation between TU content and film morphology. The best morphology and device efficiency of 2.7% was obtained for Sb/TU ratios that imply a strongly sulfur-deficient stoichiometry according to the previously mentioned study [29]. However, Gil et al. [38] performed crystallization in an H_2S atmosphere which could increase the sulfur content in the film. In a follow up work, Sung et al. [31] showed that rough substrates are beneficial for the formation of compact Sb_2S_3 films which relaxed the constraint that a good morphology requires low TU content. Molar ratios closer to stoichiometric conditions yielded relatively compact layers and enabled higher efficiencies up to 3.8%. Although the conditions to reach a good morphology were to some extent de-coupled from the film's chemical composition, voids can still be identified in the presented SEM images, which leaves room for further process improvement. Based on an antimony-butyldithiocarbamate (Sb-BDC) complex, Wang et al. [37] fabricated pinhole-free layers with large grains and the so-far highest reported efficiency of 4.3% for spin-coated planar Sb_2S_3 solar cells as can be seen from Figure 1. However, this route includes Sb_2O_3 as a precursor whose detrimental impact has been discussed above. While these initial results on spin-coated planar antimony sulfide solar cells are promising, many process parameters have not yet been discussed properly.

In this work, we follow the two depicted fabrication routes for spin-coated planar Sb_2S_3 solar cells based on different precursors [29,37]. For the Sb-TU precursor we introduce a slow annealing process that considerably improves substrate coverage. We compare both process routes in terms of morphology,

electronic defects and device performance with a focus on the crystallization step. For optimized annealing conditions, we vary the hole transport material and illustrate a qualitatively different impact on device performance for the two precursor process routes. For both precursor routes, the efficiency of the presented optimized devices exceeds that of previous reports.

Results and Discussion

In the process described in [29] antimony chloride $SbCl_3$ and thiourea $SC(NH_2)_2$, or short TU, are used to form an antimony-thiourea complex $[Sb(TU)_2]Cl_3$ in the high boiling point solvent *N,N*-dimethylformamide DMF. While [31,38] chose 2-methoxyethanol instead of DMF as the solvent, we stuck to the original recipe with DMF. The second process route applied in this work and described in [37] uses antimony oxide Sb_2O_3 and butyldithiocarbamic acid BDCA, formed by reacting *n*-butylamine with CS_2, to obtain an antimony-butyldithiocarbamate complex $Sb(S_2CNHC_4H_9)_3$ which is dissolved in ethanol. With reference to the formed Sb-complex and as indicated in the introduction, we will refer to the first process as Sb-TU route, and to the second process as Sb-BDC route. For both processes the spin-coated Sb-complex is thermally decomposed at around 200 °C leaving an amorphous film and then crystallized at higher temperatures in an inert atmosphere [29,37]. Details of the fabrication can be found in the Experimental section. It is noteworthy that both processes use an excess of the sulfur precursors. For the case of Sb-TU it was shown that stoichiometric crystalline Sb_2S_3 with an S/Sb ratio of $3/2 = 1.5$ in the resulting film, which showed the best performance in an ETA solar cell, requires this initial excess of sulfur in the precursor ($SbCl_3$/TU = 1.8) [29].

In a first step, the film morphology was studied. While the Sb-TU process allows the homogeneous deposition of Sb_2S_3 in a mesoporous TiO_2 scaffold which enables device efficiencies comparable to other deposition methods [29], direct thermal decomposition of the spin-coated solution at 180 °C leaves large parts of the planar substrate uncovered as can be seen in the scanning electron microscope (SEM) image in Figure 2a. Between smooth-looking domains of Sb_2S_3, the grains of the FTO (Pilkington TEC7) covered with spray-coated TiO_2 are clearly visible. For better comparison, SEM images of substrates without Sb_2S_3 can be found in Figure S1, Supporting Information File 1. The morphology is improved by annealing the films at 100 °C directly after spin-coating for approximately 60 minutes prior to thermal decomposition at 180 °C. Figure 2b shows that this slow annealing step drastically reduces the area of pinholes in the film. Both images in Figure 2a and 2b are taken after crystallization at 265 °C. The holes are already present in the amorphous films as can be seen in the corresponding images shown in Figure S1, Supporting Information File 1. The exis-
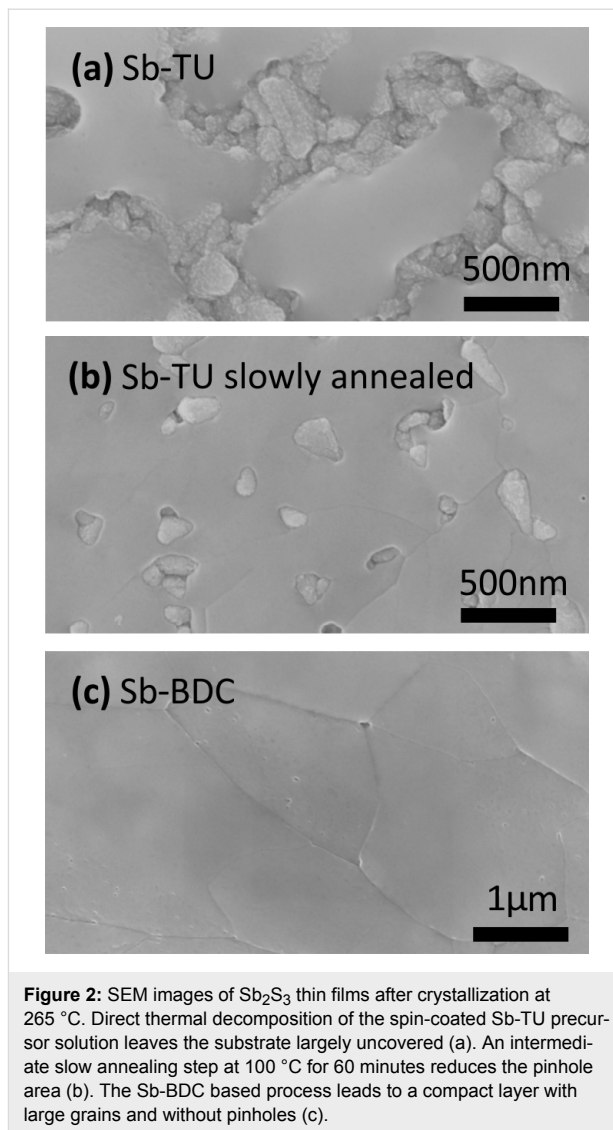
Figure 2: SEM images of Sb_2S_3 thin films after crystallization at 265 °C. Direct thermal decomposition of the spin-coated Sb-TU precursor solution leaves the substrate largely uncovered (a). An intermediate slow annealing step at 100 °C for 60 minutes reduces the pinhole area (b). The Sb-BDC based process leads to a compact layer with large grains and without pinholes (c).

tence of pinholes is thus not caused by crystallizing the film which emphasizes that the detailed procedure of thermal decomposition is crucial for the film morphology. Grain sizes are on the order of 500 nm. While even the optimized annealing procedure cannot fully avoid the presence of pinholes for the Sb-TU process, the Sb-BDC process leads to compact layers largely free of pinholes as shown in Figure 2c. Except for a lower crystallization temperature as will be discussed later, we closely followed the recipe reported in [37] and obtain a very similar film morphology, with grain sizes exceeding 1 μm but slightly smaller than the reported average of 6 μm. Note that the amorphous film has a porous structure as can be seen in Figure S1c, Supporting Information File 1. The compact and pinhole-free morphology is a result of crystallization during the Sb-BDC process which again underlines the apparently different mechanisms governing film formation in the Sb-BDC and Sb-TU processes.

Most deposition methods such as chemical bath deposition [2,41], atomic layer deposition [22,32], thermal evaporation [33,35,46] and the here-discussed spin-coating [29,37] produce amorphous films that are subsequently crystallized at temperatures above the minimum crystallization temperature of 250 °C for antimony sulfide [47-49]. The typical crystallization temperature is 300 °C [2,6,29,31,37] while values of 330 °C [4,5,32,50] and up to 400 °C [51] are reported. To gain insights into the crystallization behavior in terms of morphology, creation of defects and solar cell performance we produced samples crystallized on a hot plate at various temperatures in a nitrogen atmosphere. The hot plate temperature and homogeneity was confirmed by contact thermometer measurements. The lowest temperature was chosen to be 265 °C slightly above the minimum crystallization temperature of Sb_2S_3. The morphology was studied with SEM and atomic force microscopy (AFM). Possible changes in electronic quality with crystallization temperature were investigated via photothermal deflection spectroscopy (PDS) where the absorption coefficient of a thin-film is measured over several orders of magnitude [52,53] which cannot be achieved by standard transmission–reflection measurements using an UV–vis photospectrometer. The large dynamic range of PDS makes it a powerful tool for to study the density of states in the sub-bandgap region [53-56] including band tails that yield the Urbach energy as a measure of disorder as well as the detection of (optically active) defects in the band gap which can act as recombination centers in a solar cell.

The Sb-TU process shows a slight increase in uncovered substrate area for a crystallization temperature of 300 °C (Figure 3b) compared to a crystallization temperature of 265 °C (Figure 3a). This trend continues for higher crystallization temperatures as can be seen from AFM scans shown in Figure S2 where the corresponding SEM measurements are also presented. At 400 °C the film seems to disintegrate and macroscopic holes form. The small, bright, tapered features that are observed in the domains not covered by Sb_2S_3 can be attributed to the peaks of large FTO grains as can be seen from the comparison with the SEM images of the FTO in Figure S1, Supporting Information File 1. In the relevant temperature range of 265 °C to 300 °C, the Sb_2S_3 domains tend towards a droplet-like morphology with increasing temperature which can be interpreted as an on-going de-wetting of the substrate. The issue of de-wetting was reported for the transition from the amorphous to the crystalline phase of Sb_2S_3 for a thin layer on a mesoporous TiO_2 scaffold [22,57]. For PDS measurements of the Sb-TU process, a TiO_2 layer was spray-coated onto the glass before depositing the Sb_2S_3 layer because non-optimal adhesion prevents direct coating of glass with Sb-TU solution. The deposition conditions thus closely resemble those of the fabricated solar cells. The results for different crystallization temperatures in the Sb-TU process are shown in Figure 3c. For the sample crystallized at 265 °C and 300 °C, the measurement signal quickly saturates at energies above the band gap. At low energies the absorption strength of the substrate becomes comparable to that of the Sb_2S_3 film which is evident from the characteristic H_2O absorption peak of Corning glass below 1 eV. While the layer crystallized at 265 °C and 300 °C behave almost identical, the defect absorption of the layer crystallized at 350 °C is increased drastically. The same holds true for the

Figure 3: Crystallization in the Sb-TU (a–d) and Sb-BDC (e–h) process. AFM measurements of the Sb-TU route show a coarsening of the morphology at 300 °C (b) compared to 265 °C (a). Electronic defects detected with PDS (c) are created in the band gap for temperatures of 350 °C or above. Corresponding device performance (d). SEM images of the Sb-BDC process for higher crystallization temperatures (e) and longer crystallization times (f) compared to the standard (265 °C, 2 min). New features in the morphology come along with increased defect absorption (g) and deteriorated device performance (h) for conditions uncritical in the Sb-TU process.

400 °C sample. Due to the macroscopic holes in the film described earlier, the incoming light is still transmitted and not fully absorbed even at high energies which inhibits a proper analysis of the absorption coefficient. Therefore the 400 °C sample does not coincide with the other samples that match very well for energies above the band gap. The increased defect absorption for the crystallization at 350 °C or higher hints towards a lower cell performance because a higher defect density would cause increased recombination and eventually a lower open-circuit voltage V_{oc}. To confirm this hypothesis we produced solar cells in a standard configuration described in the experimental section with P3HT as the hole transport material. The results are shown in Figure 3d and Table S1, Supporting Information File 1 and the J_{sc} values obtained from solar simulator measurements are confirmed by external quantum efficiency (EQE) measurements shown in Figure S4, Supporting Information File 1. The cell from an Sb_2S_3 layer crystallized at 300 °C shows a lower V_{oc} and J_{sc} than the cell crystallized at 265 °C. At 350 °C, the V_{oc} drops drastically which is consistent with the increased defect absorption observed with PDS (Figure 3c). When the film morphology degenerates at 400 °C the cell performance decays further.

Next, a similar study was conducted for the Sb-BDC process with a focus on crystallization at 265 °C and 300 °C. The SEM image in Figure 3e of the layer crystallized at 300 °C shows a similar morphology as the one crystallized at 265 °C shown in Figure 2c except that small pyramidal structures appear on top of the grains. A sample crystallized at 265 °C for 30 minutes shown in Figure 3f instead of the standard 2 minutes shows similar structures (also see the zoomed-out SEM images in Figure S3, Supporting Information File 1). The nature of these features remains unclear. Similar structures were reported for chemical-bath-deposited and evaporated Sb_2S_3 [27,35,47,58] and seem to be present in [37] as well. The absorption coefficient of the Sb-BDC sample crystallized at 265 °C shown in Figure 3g is almost identical to that of the Sb-TU sample crystallized at the same temperature shown in Figure 3c and drawn again in Figure 3g for direct comparison. However, the defect absorption of Sb_2S_3 from the Sb-BDC route crystallized at 300 °C is strongly enhanced. A sample prepared at 265 °C but with a crystallization time of 30 minutes reveals a similar increase in defect absorption. For both samples with increased defect absorption the absorption behaves non-monotonous with energy. The maxima and minima can be most-likely attributed to interference in the smooth films – which did not fully cancel out during data analysis – instead of actual variations in the materials' density of states in the sub-bandgap region. The negative impact of the increased defect density on device performance is confirmed by comparing solar cells crystallized at 265 °C for 2 minutes and 30 minutes and at 300 °C for

2 minutes in Figure 3h and Table S2, Supporting Information File 1.

In summary, for both investigated process routes an optimized crystallization temperature of 265 °C was found which is lower than the commonly applied treatment at 300 °C. For the Sb-TU process, higher crystallization temperatures cause a de-wetting of the substrate. New features arise on top of the Sb_2S_3 film in the Sb-BDC process for longer crystallization times and crystallization at 300 °C. At the same time significantly increased defect formation was observed. The same conditions were uncritical in terms of defect formation for the Sb-TU process where similar degradation started only at crystallization temperatures of 350 °C. Possibly, the stoichiometry of Sb and S changes in different ways for the two process routes during crystallization. Residues from precursors used in the Sb-BDC process such as Sb_2O_3 whose negative impact on device performance was shown [6,45] might also lead to defect formation during crystallization. Further insights would require a correlation between electronic defect creation at higher crystallization temperatures with changes in the chemical composition and microstructure of the Sb_2S_3 layer.

With a focus on the two different hole transport materials P3HT and KP115 shown in Figure 4a, the $J-V$ curves and solar cell performance of the best devices for the two process routes are compared in Figure 4b and Table 1. The Sb-BDC process reaches higher device efficiencies compared to the Sb-TU process, mostly due to the approximately 30% higher J_{sc}. EQE measurements shown in Figure 4c and 4d confirm this result, which can be explained by a thicker Sb_2S_3 layer of 190 nm compared to 100 nm for the Sb-TU process. Since Sb_2S_3 absorbs up to longer wavelengths than both polymers as can be seen from Figure 4c, the falling edge of the EQE can be attributed to Sb_2S_3 absorption. The inflection point of the EQE [59] yields a band gap of 1.79 eV. Although fill factor (FF) and V_{oc} do not vary as much between the processes as the J_{sc}, it is noteworthy that despite a lower efficiency the highest V_{oc} of 650 mV is obtained for the Sb-TU process with KP115 as HTM. One possible reason would be a lower recombination rate due to fewer deep defects in the Sb-TU process. The shunt behavior caused by the pinholes in the Sb-TU process depends on the choice of HTM which could limit the V_{oc} in the case of P3HT. This explanation is consistent with the negligible V_{oc} difference between different HTMs in the case of the pinhole-free layers obtained from the Sb-BDC process.

The two semiconducting polymers poly(3-hexylthiophene) P3HT and poly[(4,4′-bis(2-ethylhexyl)dithieno[3,2-*b*:2′,3′-*d*]silole)-2,6-diyl-*alt*-(2,5-bis(3-tetradecylthiophen-2-yl)thiazolo[5,4-*d*]thiazole)-2,5-diyl] KP115 depicted in Figure 4a
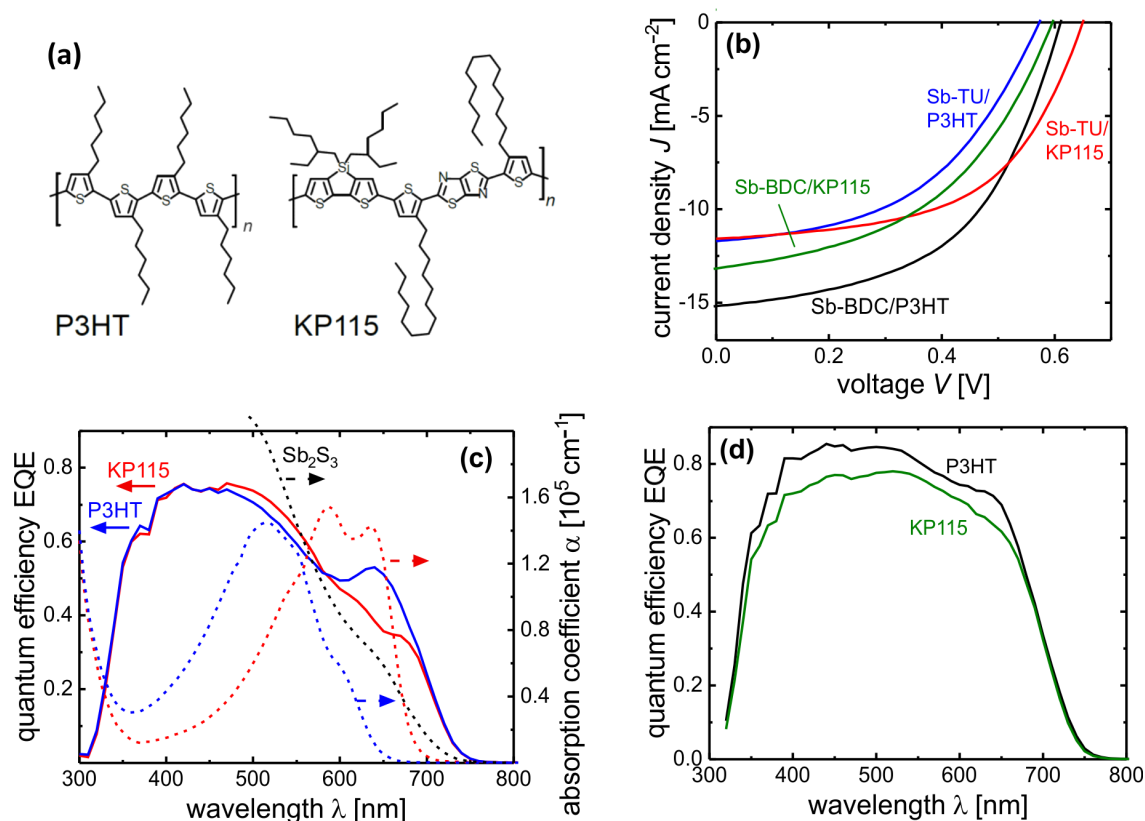
Figure 4: Chemical structure of the applied polymers (a). Sun simulator (b) and external quantum efficiency (c,d) measurements of FTO/TiO$_2$/Sb$_2$S$_3$/HTM/MoO$_x$/Ag samples. The EQE for Sb-TU samples are shown in (c) together with absorption coefficients of Sb$_2$S$_3$ and the two HTMs which absorb parasitically. EQE for Sb-BDC samples are shown in (d).

Table 1: Device performance of samples shown in Figure 4. The efficiency for EQE-corrected J_{sc} is given in the last column.

Process	HTM	V_{oc} [mV]	FF [%]	J_{sc} [mA cm^{-2}]	PCE [%]	$J_{sc,EQE}$ [mA cm^{-2}]	PCE$_{corr}$ [%]
Sb-TU	P3HT	573	47.8	11.7	3.20	12.1	3.31
Sb-TU	KP115	650	54.8	11.6	4.13	11.7	4.16
Sb-BDC	P3HT	611	52.1	15.2	4.83	15.6	4.97
Sb-BDC	KP115	596	46.6	13.2	3.65	14.4	3.98
Sb-BDC	P3HT[a]	597	49.0	13.9	4.06	14.4	4.22

[a]Fabricated on same day as Sb-BDC/KP115 device for direct comparison, graph shown in Figure S5, Supporting Information File 1.

allow high efficiencies at comparably thick layers when applied as absorbers in organic solar cells due to good transport properties [60-62]. Photons that are absorbed by the polymer generate excitons that can only diffuse up to around 10 nm before they recombine. While a photocurrent contribution from the polymer was demonstrated for certain Sb$_2$S$_3$ ETA cells [29] where the interface area is large and close-by, absorption in planar Sb$_2$S$_3$ cells by the polymer is to a large extent parasitic [27]. The applied polymers differ in band gap as can be seen from the measured absorption spectra in Figure 4c and the position of the highest occupied molecular orbital (HOMO). The HOMO of

Sb$_2$S$_3$ obtained from ultraviolet photon spectroscopy (UPS) measurements is reported to lie between 5.3 and 5.5 eV [30,51,63] with one report claiming 5.9 eV [32]. Reported HOMO values of the polymers are 4.9–5.1 eV for P3HT [64,65] and 5.3–5.4 eV for KP115 [61,66] and are obtained from cyclic voltammetry measurements, which yields lower lying HOMO levels than UPS measurements [67]. The HOMO of KP115 is thus better aligned with the valence band of Sb$_2$S$_3$ which could be beneficial for the V_{oc} and FF. Indeed, for the Sb-TU process both values are significantly larger for the better-matching KP115. However, this is not the case for the Sb-BDC process

where the Sb_2S_3/KP115 cell even shows a slightly lower V_{oc} and FF – also when compared to an Sb_2S_3/P3HT cell prepared on the same day as listed in Table 1 and shown in Figure S5, Supporting Information File 1. For the thinner Sb_2S_3 layers from the Sb-TU process the shape of the EQE spectra in Figure 4c differs significantly between the Sb_2S_3/P3HT and Sb_2S_3/KP115 cells for wavelengths above 500 nm. This can be explained by the different absorption spectra which are plotted together with the EQE data. P3HT has a larger band gap than KP115 so that P3HT does not absorb above approximately 650 nm. The incident light is instead transmitted to the metal back contact where it is reflected back through the P3HT into the Sb_2S_3 absorber where it contributes to the photocurrent. The decreased parasitic absorption above 650 nm causes a maximum in the EQE at roughly that wavelength. KP115 on the other hand still absorbs at 650 nm so that the EQE of the Sb_2S_3/KP115 device is decreased almost up to 700 nm. Since organic polymers have narrow absorption bands, the higher band gap P3HT continues to absorb parasitically further in the blue wavelengths than KP115. This could explain the enhanced EQE for the Sb_2S_3/KP115 device at wavelengths below 550 nm where the enhancement is however less pronounced because more light is already absorbed in the Sb_2S_3 than at longer wavelengths. Consequently, the J_{sc} of the Sb_2S_3/P3HT is 4% higher than that of Sb_2S_3/KP115. For the Sb-BDC process similar but less pronounced EQE features are observed as can be seen for the samples prepared on the same day and shown in Figure S5, Supporting Information File 1. One reason is that the HTM layer could be coated thinner (30 nm compared to 50 nm in the Sb-TU process) since the Sb-BDC route results in smoother and pinhole-free layers whereby the amount of parasitic absorption is decreased. Another reason is that the Sb-BDC process yields thicker Sb_2S_3 layers (190 nm vs 100 nm from the Sb-TU process) so that more light is absorbed in the Sb_2S_3 before it reaches the HTM.
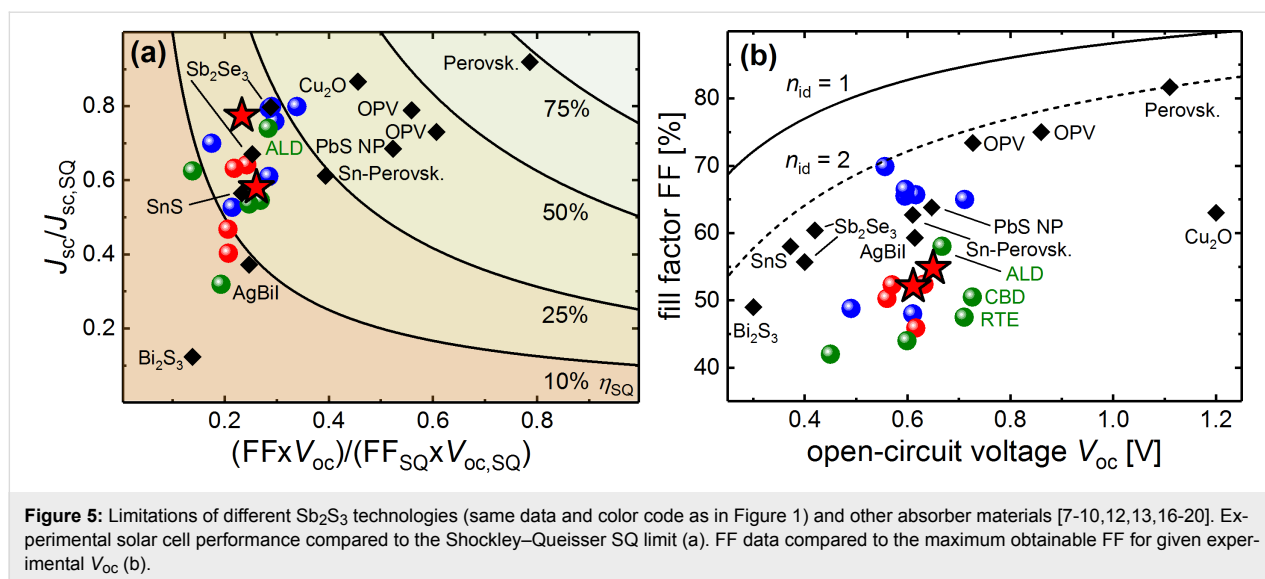
In summary, the investigated Sb_2S_3 process routes do not seem to be generally limited by an unmatched HOMO of the HTM. For the Sb-TU route, the best results are obtained with KP115, but for the Sb-BDC route, P3HT performs best. The positive effects for the films with pinholes from Sb-TU might be attributed to a better shunt blocking in the case of KP115, which is currently under further investigation. Another reason could be that the Sb_2S_3/HTM interface is limiting for the Sb-TU process, whereas the bulk of Sb_2S_3 becomes limiting for the thicker absorber layers from the Sb-BDC. The EQE spectra and corresponding J_{sc} values are clearly influenced by the absorption spectra of the applied polymer. Parasitic absorption is more pronounced for polymers with a band gap closer to that of Sb_2S_3, for thinner layers of Sb_2S_3 and for thicker polymer layers.

Conclusion and Outlook

We compared two spin-coating processes based on different precursors for Sb_2S_3 solar cells in a planar configuration. For both fabrication routes, an optimum crystallization temperature of 265 °C – slightly above the minimum crystallization temperature and lower than the typically reported 300 °C – was found. Depending on the process, the exact heating procedure with regard to intermediate temperature annealing or crystallization time is critical for morphology, defect density and device performance. The best choice of hole transport material depends on the precursor route and is likely related to whether pinholes are present or not. Optimized process parameters for both processing routes enabled increased device efficiencies with respect to the corresponding literature reports. The Sb-BDC process with P3HT as HTM marks one of the highest efficiencies for planar Sb_2S_3 solar cells and is only outdone by fabrication via cumbersome atomic layer deposition [32] as can be seen from Figure 1.

In analogy to [68] the losses relative to the Shockley–Queisser limit [69] in J_{sc} and FF-V_{oc} product is shown in Figure 5a. This work, as well as other reports on Sb_2S_3 solar cells, reaches relatively high J_{sc} values when compared to some less-established absorber materials mentioned in the Introduction. Electronic losses in FF and V_{oc} are more severe. Figure 5b further deconvolutes the critical parameters by comparing the FFs of the same solar cells to the theoretical maximum FF [70,71] which is a function of the V_{oc} and the ideality factor n_{id}. The Shockley–Queisser limit of the V_{oc} is almost 1.5 V for Sb_2S_3 so that V_{oc} losses clearly exceed losses in the FF which are nevertheless noticeable for all planar Sb_2S_3 solar cells as can be seen from Figure 5b. The high J_{sc} of Sb_2S_3 underlines the general suitability as an absorber but further improvements must tackle the deficient fill factor and especially the low open-circuit voltages obtained for all Sb_2S_3 solar cells up-to-date.

Regarding future technological progress, our study shows that for otherwise similarly processed samples the choice of precursor is crucial for the resulting film morphology and device efficiency. Complex chemistry offers versatile options for the design of new precursors that could further enhance the efficiency of solution processed Sb_2S_3. For any new process pinhole-free layers with tuneable thickness and control over stoichiometry are desirable and correlation to device performance is insightful. Post-processing, such as sulfurization from gas [32] or liquid [6] sulfur sources might reduce the density of electronic defects in Sb_2S_3 for certain deposition methods that leave sulfur deficient films [29,72]. Another aim in terms of fabrication is to exploit the anisotropic nature of Sb_2S_3 by aligning the 1D ribbons with the direction of charge transport between the contacts. A beneficial effect was demonstrated for the structurally identical Sb_2Se_3 [9]. A proper substrate choice

Figure 5: Limitations of different Sb_2S_3 technologies (same data and color code as in Figure 1) and other absorber materials [7-10,12,13,16-20]. Experimental solar cell performance compared to the Shockley–Queisser SQ limit (a). FF data compared to the maximum obtainable FF for given experimental V_{oc} (b).

or embedding a seed layer might be the key to directed growth in Sb_2S_3.

Experimental

Chemicals: All chemicals were purchased from Sigma-Aldrich except for KP115 which was purchased from 1-material. Dried solvents with analytical (p.a.) quality were used.

Sb_2S_3 layers from Sb-TU precursor: 1 mmol of $SbCl_3$ was dissolved in 1 mL of DMF and stirred for 30 min. The solution was then added to TU with an $SbCl_3$/TU molar ratio of 1:1.8, stirred again overnight and filtered before use. The solution was spin-coated at 70 rps for 40 s with 10 s of acceleration. The samples were then annealed for 60 min at 100 °C on a hot plate which was then heated up to 180 °C where the samples remained for another 10 min followed by crystallization on another hot plate for 30 min at the temperature indicated in the text with a standard crystallization temperature of 265 °C. We chose 265 °C slightly above the minimum crystallization temperature of Sb_2S_3 as the lowest temperature to account for minor temperature fluctuations across the hot plate and differences between the hot plate's surface temperature and the film temperature. Because of the inhomogeneous morphology of the Sb-TU process no single layer thickness can be given but an average thickness of 100 nm was determined from AFM measurements on glass/TiO_2/Sb_2S_3. Layers for SEM and AFM imaging were prepared on FTO TEC7 by Pilkington after spray-coating of TiO_2. Layers for PDS and UV-Vis measurements were coated on Corning glass after spray-coating of TiO_2. Sb_2S_3 was exclusively processed under an inert N_2-atmosphere.

Sb_2S_3 layers from Sb-BDC precursor: 1 mmol of Sb_2O_3 was dissolved in a solution of 1.5 mL CS_2 mixed with 2 mL ethanol

and stirred for 1 h. 2 mL *n*-butylamine were then added in a dropwise manner and the solution was allowed to cool down four times during the preparation since the formation reaction is exothermal and CS_2 has a boiling point of 46 °C. The solution was stirred again overnight and filtered before use. The solution was spin-coated at 133 rps for 30 s with 3 s of acceleration. The samples were then annealed for 1 min at 200 °C on a hot plate and then crystallized on another hot plate as indicated in the text with a standard crystallization temperature of 265 °C for 2 min. The resulting layer thickness is 190 nm. Layers for SEM and AFM imaging were prepared on FTO TEC7 substrates by Pilkington after spray-coating of TiO_2. Layers for PDS and UV–vis measurements were coated directly on Corning glass since – in contrast to the Sb-TU route – adhesion on glass was uncritical. Sb_2S_3 was exclusively processed under an inert N_2-atmosphere.

Solar cells: *N-i-p* stack of FTO/TiO_2/Sb_2S_3/HTM/MoO_x/Ag. FTO TEC7 substrates by Pilkington were structured by Kintec. A compact layer of TiO_2 was obtained by spray-coating a 0.2 M solution of titanium diisopropoxide bis(acetylacetonate) 75 wt % in ethanol on a hot plate at roughly 470 °C. After cooling down to about 200 °C, samples were transferred to a glovebox with N_2 where they were further processed on the next day. Sb_2S_3 layers were fabricated as described above. P3HT was dissolved in chlorobenzene (CB) and stirred overnight at 65 °C. The cooled solution was spin-coated at 6000 rpm for 120 s with an acceleration time of 3 s after which the samples were annealed at 130 °C for 15 min. For Sb-TU samples a 15 mg/mL solution was used and for Sb-BDC samples a 10 mg/mL solution was used. KP115 was dissolved in 1,2-dichlorobenzene (DCB) with a concentration of 10 mg/mL and stirred overnight at 110 °C. The hot solution was spin-

coated at for 120 s with an acceleration time of 3 s after which the samples were dried in a closed petri dish for 3 h. For Sb-TU samples the spin speed was 1500 rpm and for Sb-BDC samples 4000 rpm. Resulting polymer thicknesses were measured on a glass reference and adjusted to 50 nm for Sb-TU samples and 30 nm for Sb-BDC samples. The different optimized polymer layer thickness is due to the rougher and pinhole-containing Sb-TU films. Finally 30 nm of MoO_x and 200 nm of Ag were thermally evaporated. The metal contact configuration where MoO_x forms a tunneling junction with the HTM is typical for organic solar cells in an *n-i-p* configuration. The cell area was 0.16 cm^2.

Layer and device characterization: The scanning electron microscope was a Zeiss (Leo) Gemini 1550 with Shottky field-emission cathode and an in-lens detector. The lateral resolution equals approximately 1 nm at 20 kV and the measurement was performed under a vacuum base pressure of 10^{-6} mbar. UV–vis measurements were performed with a Lambda 950 spectrophotometer from PerkinElmer equipped with an integrating sphere in the UV–vis range from 300 nm to 1000 nm. Absorption coefficients were obtained from UV–vis (transmission–reflection) and PDS (absorptance) data by measuring the layer thickness. In the energy range of strong absorption the absorption coefficient obtained from PDS is compared and scaled to transmission–reflection measurements which give a more accurate absolute value of the absorption coefficient in this regime. PDS, EQE and *J–V* measurements were done before any exposure to air had occurred. Samples for PDS were mounted in a cuvette containing the liquid FC75 inside the glovebox. Solar simulator and EQE measurements were done under inert atmosphere by mounting the samples (while still inside a glovebox) in a closed holder with glass window. Current–voltage curves were performed with an AM1.5 spectrum on a grade AAA Solar Simulator. No masks were used for solar simulator measurements since the J_{sc} values were obtained from EQE measurements. The reflection from the glass lid of the sample holder (8–10% depending on wavelength) was measured and accounted for during EQE analysis.

Calculations for performance limitation: The band gap is the only parameter needed to calculate the Shockley–Queisser limit of a certain material. The inflection point IP of the falling edge of EQE data served as value for the band gap [59]. The EQE IP obtained from measurements within this work was taken for all Sb_2S_3 data points. Other material's IP were estimated from published EQE data. The FF is calculated by Green's approximation [70] which was shown to be accurate in the regimes depicted in Figure 5a and 5b [73]. In Figure 5a the SQ limit of the V_{oc} and $n_{id} = 1$ is assumed. In Figure 5b the FF–V_{oc} relation is shown for the boundary cases of $n_{id} = 1$ and $n_{id} = 2$.

Supporting Information

Supporting Information File 1
Additional Figures and Tables.
[https://www.beilstein-journals.org/bjnano/content/supplementary/2190-4286-9-200-S1.pdf]

ORCID® iDs
Pascal Kaienburg - https://orcid.org/0000-0003-3887-3395
Thomas Kirchartz - https://orcid.org/0000-0002-6954-8213

References

1. Im, S. H.; Lim, C.-S.; Chang, J. A.; Lee, Y. H.; Maiti, N.; Kim, H.-J.; Nazeeruddin, M. K.; Grätzel, M.; Seok, S. I. *Nano Lett.* **2011,** *11,* 4789–4793. doi:10.1021/nl2026184
2. Itzhaik, Y.; Niitsoo, O.; Page, M.; Hodes, G. *J. Phys. Chem. C* **2009,** *113,* 4254–4256. doi:10.1021/jp900302b
3. Moon, S.-J.; Itzhaik, Y.; Yum, J.-H.; Zakeeruddin, S. M.; Hodes, G.; Grätzel, M. *J. Phys. Chem. Lett.* **2010,** *1,* 1524–1527. doi:10.1021/jz100308q
4. Chang, J. A.; Rhee, J. H.; Im, S. H.; Lee, Y. H.; Kim, H.-j.; Seok, S. I.; Nazeeruddin, M. K.; Gratzel, M. *Nano Lett.* **2010,** *10,* 2609–2612. doi:10.1021/nl101322h
5. Chang, J. A.; Im, S. H.; Lee, Y. H.; Kim, H.-j.; Lim, C.-S.; Heo, J. H.; Seok, S. I. *Nano Lett.* **2012,** *12,* 1863–1867. doi:10.1021/nl204224v
6. Choi, Y. C.; Lee, D. U.; Noh, J. H.; Kim, E. K.; Seok, S. I. *Adv. Funct. Mater.* **2014,** *24,* 3587–3592. doi:10.1002/adfm.201304238
7. Zhao, Z.; Gu, F.; Li, Y.; Sun, W.; Ye, S.; Rao, H.; Liu, Z.; Bian, Z.; Huang, C. *Adv. Sci.* **2017,** *4,* 1700204. doi:10.1002/advs.201700204
8. Minami, T.; Nishi, Y.; Miyata, T. *Appl. Phys. Express* **2016,** *9,* 052301. doi:10.7567/APEX.9.052301
9. Zhou, Y.; Wang, L.; Chen, S.; Qin, S.; Liu, X.; Chen, J.; Xue, D.-J.; Luo, M.; Cao, Y.; Cheng, Y.; Sargent, E. H.; Tang, J. *Nat. Photonics* **2015,** *9,* 409–415. doi:10.1038/nphoton.2015.78
10. Wen, X.; Chen, C.; Lu, S.; Li, K.; Kondrotas, R.; Zhao, Y.; Chen, W.; Gao, L.; Wang, C.; Zhang, J.; Niu, G.; Tang, J. *Nat. Commun.* **2018,** *9,* 2179. doi:10.1038/s41467-018-04634-6
11. Kim, Y.; Yang, Z.; Jain, A.; Voznyy, O.; Kim, G.-H.; Liu, M.; Quan, L. N.; García de Arquer, F. P.; Comin, R.; Fan, J. Z.; Sargent, E. H. *Angew. Chem., Int. Ed.* **2016,** *55,* 9586–9590. doi:10.1002/anie.201603608
12. Jung, K. W.; Sohn, M. R.; Lee, H. M.; Yang, I. S.; Sung, S. D.; Kim, J.; Diau, E. W.-G.; Lee, W. I. *Sustainable Energy Fuels* **2018,** *2,* 294–302. doi:10.1039/c7se00477j
13. Sinsermsuksakul, P.; Sun, L.; Lee, S. W.; Park, H. H.; Kim, S. B.; Yang, C.; Gordon, R. G. *Adv. Energy Mater.* **2014,** *4,* 1400496. doi:10.1002/aenm.201400496
14. Whittaker-Brooks, L.; Gao, J.; Hailey, A. K.; Thomas, C. R.; Yao, N.; Loo, Y.-L. *J. Mater. Chem. C* **2015,** *3,* 2686–2692. doi:10.1039/C4TC02534B

15. Rath, A. K.; Bernechea, M.; Martinez, L.; de Arquer, F. P. G.; Osmond, J.; Konstantatos, G. *Nat. Photonics* **2012,** *6,* 529–534. doi:10.1038/nphoton.2012.139

16. Martinez, L.; Stavrinadis, A.; Higuchi, S.; Diedenhofen, S. L.; Bernechea, M.; Tajima, K.; Konstantatos, G. *Phys. Chem. Chem. Phys.* **2013,** *15,* 5482. doi:10.1039/c3cp50599e

17. Yang, W. S.; Park, B.-W.; Jung, E. H.; Jeon, N. J.; Kim, Y. C.; Lee, D. U.; Shin, S. S.; Seo, J.; Kim, E. K.; Noh, J. H.; Seok, S. I. *Science* **2017,** *356,* 1376–1379. doi:10.1126/science.aan2301

18. Zhang, S.; Qin, Y.; Zhu, J.; Hou, J. *Adv. Mater.* **2018,** *30,* 1800868. doi:10.1002/adma.201800868

19. Li, H.; Xiao, Z.; Ding, L.; Wang, J. *Sci. Bull.* **2018,** *63,* 340–342. doi:10.1016/j.scib.2018.02.015

20. Xu, J.; Voznyy, O.; Liu, M.; Kirmani, A. R.; Walters, G.; Munir, R.; Abdelsamie, M.; Proppe, A. H.; Sarkar, A.; García de Arquer, F. P.; Wei, M.; Sun, B.; Liu, M.; Ouellette, O.; Quintero-Bermudez, R.; Li, J.; Fan, J.; Quan, L.; Todorovic, P.; Tan, H.; Hoogland, S.; Kelley, S. O.; Stefik, M.; Amassian, A.; Sargent, E. H. *Nat. Nanotechnol.* **2018,** *13,* 456–462. doi:10.1038/s41565-018-0117-z

21. Albero, J.; Atienzar, P.; Corma, A.; Garcia, H. *Chem. Rec.* **2015,** *15,* 803–828. doi:10.1002/tcr.201500007

22. Wedemeyer, H.; Michels, J.; Chmielowski, R.; Bourdais, S.; Muto, T.; Sugiura, M.; Dennler, G.; Bachmann, J. *Energy Environ. Sci.* **2013,** *6,* 67–71. doi:10.1039/C2EE23205G

23. Kaiser, I.; Ernst, K.; Fischer, C.-H.; Könenkamp, R.; Rost, C.; Sieber, I.; Lux-Steiner, M. C. *Sol. Energy Mater. Sol. Cells* **2001,** *67,* 89–96. doi:10.1016/s0927-0248(00)00267-1

24. Taretto, K.; Rau, U. *Prog. Photovoltaics* **2004,** *12,* 573–591. doi:10.1002/pip.549

25. Kaienburg, P.; Rau, U.; Kirchartz, T. *Phys. Rev. Appl.* **2016,** *6,* 024001. doi:10.1103/PhysRevApplied.6.024001

26. Boix, P. P.; Lee, Y. H.; Fabregat-Santiago, F.; Im, S. H.; Mora-Sero, I.; Bisquert, J.; Seok, S. I. *ACS Nano* **2012,** *6,* 873–880. doi:10.1021/nn204382k

27. Zimmermann, E.; Pfadler, T.; Kalb, J.; Dorman, J. A.; Sommer, D.; Hahn, G.; Weickert, J.; Schmidt-Mende, L. *Adv. Sci.* **2015,** *2,* 1500059. doi:10.1002/advs.201500059

28. Savadogo, O. *J. Electrochem. Soc.* **1994,** *141,* 2871. doi:10.1149/1.2059248

29. Choi, Y. C.; Seok, S. I. *Adv. Funct. Mater.* **2015,** *25,* 2892–2898. doi:10.1002/adfm.201500296

30. Muto, T.; Larramona, G.; Dennler, G. *Appl. Phys. Express* **2013,** *6,* 072301. doi:10.7567/APEX.6.072301

31. Sung, S.-J.; Gil, E. K.; Lee, S.-J.; Choi, Y. C.; Yang, K.-J.; Kang, J.-K.; Cho, K. Y.; Kim, D.-H. *J. Ind. Eng. Chem.* **2017,** *56,* 196–202. doi:10.1016/j.jiec.2017.07.012

32. Kim, D.-H.; Lee, S.-J.; Park, M. S.; Kang, J.-K.; Heo, J. H.; Im, S. H.; Sung, S.-J. *Nanoscale* **2014,** *6,* 14549–14554. doi:10.1039/C4NR04148H

33. Osorio Mayon, Y.; White, T. P.; Wang, R.; Yang, Z.; Catchpole, K. R. *Phys. Status Solidi A* **2016,** *213,* 108–113. doi:10.1002/pssa.201532438

34. Yuan, S.; Deng, H.; Dong, D.; Yang, X.; Qiao, K.; Hu, C.; Song, H.; Song, H.; He, Z.; Tang, J. *Sol. Energy Mater. Sol. Cells* **2016,** *157,* 887–893. doi:10.1016/j.solmat.2016.07.050

35. Liu, C. P.; Chen, Z. H.; Wang, H. E.; Jha, S. K.; Zhang, W. J.; Bello, I.; Zapien, J. A. *Appl. Phys. Lett.* **2012,** *100,* 243102. doi:10.1063/1.4728985

36. You, M. S.; Lim, C.-S.; Kwon, D. H.; Heo, J. H.; Im, S. H.; Chae, K. J. *Org. Electron.* **2015,** *21,* 155–159. doi:10.1016/j.orgel.2015.02.015

37. Wang, X.; Li, J.; Liu, W.; Yang, S.; Zhu, C.; Chen, T. *Nanoscale* **2017,** *9,* 3386–3390. doi:10.1039/C7NR00154A

38. Gil, E. K.; Lee, S.-J.; Sung, S.-J.; Cho, K. Y.; Kim, D.-H. *J. Nanosci. Nanotechnol.* **2016,** *16,* 10763–10766. doi:10.1166/jnn.2016.13235

39. Messina, S.; Nair, M.; Nair, P. *Thin Solid Films* **2007,** *515,* 5777–5782. doi:10.1016/j.tsf.2006.12.155

40. Savadogo, O. *J. Electrochem. Soc.* **1992,** *139,* L16. doi:10.1149/1.2069211

41. Nair, M. T. S. *J. Electrochem. Soc.* **1998,** *145,* 2113. doi:10.1149/1.1838605

42. Gödel, K. C.; Choi, Y. C.; Roose, B.; Sadhanala, A.; Snaith, H. J.; Seok, S. I.; Steiner, U.; Pathak, S. K. *Chem. Commun.* **2015,** *51,* 8640–8643. doi:10.1039/C5CC01966D

43. Maiti, N.; Im, S. H.; Lim, C.-S.; Seok, S. I. *Dalton Trans.* **2012,** *41,* 11569. doi:10.1039/c2dt31348k

44. Pawar, S.; Pawar, B.; Kim, J.; Joo, O.-S.; Lokhande, C. *Curr. Appl. Phys.* **2011,** *11,* 117–161. doi:10.1016/j.cap.2010.07.007

45. Gödel, K. C.; Roose, B.; Sadhanala, A.; Vaynzof, Y.; Pathak, S. K.; Steiner, U. *Phys. Chem. Chem. Phys.* **2017,** *19,* 1425–1430. doi:10.1039/C6CP07559B

46. Escorcia-García, J.; Becerra, D.; Nair, M.; Nair, P. *Thin Solid Films* **2014,** *569,* 28–34. doi:10.1016/j.tsf.2014.08.024

47. Perales, F.; Lifante, G.; Agulló-Rueda, F.; de las Heras, C. *J. Phys. D: Appl. Phys.* **2007,** *40,* 2440–2444. doi:10.1088/0022-3727/40/8/005

48. Versavel, M. Y.; Haber, J. A. *Thin Solid Films* **2007,** *515,* 7171–7176. doi:10.1016/j.tsf.2007.03.043

49. Droichi, M.; Vaillant, F.; Bustarret, E.; Jousse, D. *J. Non-Cryst. Solids* **1988,** *101,* 151–155. doi:10.1016/0022-3093(88)90150-0

50. Lee, D. U.; Woo Pak, S.; Gook Cho, S.; Kyu Kim, E.; Il Seok, S. *Appl. Phys. Lett.* **2013,** *103,* 023901. doi:10.1063/1.4813272

51. Qiu, Z.; Liu, C.; Pan, G.; Meng, W.; Yue, W.; Chen, J.; Zhou, X.; Zhang, F.; Wang, M. *Phys. Chem. Chem. Phys.* **2015,** *17,* 12328–12339. doi:10.1039/c5cp00030k

52. Jackson, W. B.; Amer, N. M.; Boccara, A.; Fournier, D. *Appl. Opt.* **1981,** *20,* 1333–1344. doi:10.1364/ao.20.001333

53. Müller, T. C. M.; Kirchartz, T. In *Advanced Characterization Techniques for Thin Film Solar Cells;* Abou-Ras, D.; Kirchartz, T.; Rau, U., Eds.; Wiley-VCH Verlag GmbH & Co. KGaA: Weinheim, Germany, 2016; pp 189–214. doi:10.1002/9783527699025.ch8

54. Jackson, W. B.; Amer, N. M. *Phys. Rev. B* **1982,** *25,* 5559. doi:10.1103/physrevb.25.5559

55. Cody, G. D.; Tiedje, T.; Abeles, B.; Brooks, B.; Goldstein, Y. *Phys. Rev. Lett.* **1981,** *47,* 1480–1483. doi:10.1103/PhysRevLett.47.1480

56. Tiedje, T.; Cebulka, J. M.; Morel, D. L.; Abeles, B. *Phys. Rev. Lett.* **1981,** *46,* 1425–1428. doi:10.1103/PhysRevLett.46.1425

57. Yang, R. B.; Zakharov, N.; Moutanabbir, O.; Scheerschmidt, K.; Wu, L.-M.; Gösele, U.; Bachmann, J.; Nielsch, K. *J. Am. Chem. Soc.* **2010,** *132,* 7592–7594. doi:10.1021/ja102590v

58. Parize, R.; Cossuet, T.; Chaix-Pluchery, O.; Roussel, H.; Appert, E.; Consonni, V. *Mater. Des.* **2017,** *121,* 1–10. doi:10.1016/j.matdes.2017.02.034

59. Rau, U.; Blank, B.; Müller, T. C.; Kirchartz, T. *Phys. Rev. Appl.* **2017,** *7,* 044016. doi:10.1103/physrevapplied.7.044016

60. Li, G.; Shrotriya, V.; Huang, J.; Yao, Y.; Moriarty, T.; Emery, K.; Yang, Y. *Nat. Mater.* **2005,** *4,* 864–868. doi:10.1038/nmat1500

61. Peet, J.; Wen, L.; Byrne, P.; Rodman, S.; Forberich, K.; Shao, Y.; Drolet, N.; Gaudiana, R.; Dennler, G.; Waller, D. *Appl. Phys. Lett.* **2011,** *98,* 043301. doi:10.1063/1.3544940

62. Sweetnam, S.; Graham, K. R.; Ngongang Ndjawa, G. O.; Heumüller, T.; Bartelt, J. A.; Burke, T. M.; Li, W.; You, W.; Amassian, A.; McGehee, M. D. *J. Am. Chem. Soc.* **2014,** *136,* 14078–14088. doi:10.1021/ja505463r

63. Boix, P. P.; Larramona, G.; Jacob, A.; Delatouche, B.; Mora-Seró, I.; Bisquert, J. *J. Phys. Chem. C* **2012,** *116,* 1579–1587. doi:10.1021/jp210002c

64. Scharber, M.; Mühlbacher, D.; Koppe, M.; Denk, P.; Waldauf, C.; Heeger, A.; Brabec, C. *Adv. Mater.* **2006,** *18,* 789–794. doi:10.1002/adma.200501717

65. Zhou, E.; Cong, J.; Wei, Q.; Tajima, K.; Yang, C.; Hashimoto, K. *Angew. Chem., Int. Ed.* **2011,** *50,* 2799–2803. doi:10.1002/anie.201005408

66. Scharber, M. C. *Adv. Mater.* **2016,** *28,* 1994–2001. doi:10.1002/adma.201504914

67. Guan, Z.-L.; Kim, J. B.; Wang, H.; Jaye, C.; Fischer, D. A.; Loo, Y.-L.; Kahn, A. *Org. Electron.* **2010,** *11,* 1779–1785. doi:10.1016/j.orgel.2010.07.023

68. Polman, A.; Knight, M.; Garnett, E. C.; Ehrler, B.; Sinke, W. C. *Science* **2016,** *352,* aad4424. doi:10.1126/science.aad4424

69. Shockley, W.; Queisser, H. J. *J. Appl. Phys.* **1961,** *32,* 510–519. doi:10.1063/1.1736034

70. Green, M. A. *Sol. Cells* **1982,** *7,* 337–340. doi:10.1016/0379-6787(82)90057-6

71. Green, M. A. *Solid-State Electron.* **1981,** *24,* 788–789. doi:10.1016/0038-1101(81)90062-9

72. Tumelero, M. A.; Faccio, R.; Pasa, A. A. *J. Phys. Chem. C* **2016,** *120,* 1390–1399. doi:10.1021/acs.jpcc.5b10233

73. Neher, D.; Kniepert, J.; Elimelech, A.; Koster, L. J. A. *Sci. Rep.* **2016,** *6,* 24861. doi:10.1038/srep24861

License and Terms

Lead-free hybrid perovskites for photovoltaics

Oleksandr Stroyuk[§]

Abstract

This review covers the state-of-the-art in organo–inorganic lead-free hybrid perovskites (HPs) and applications of these exciting materials as light harvesters in photovoltaic systems. Special emphasis is placed on the influence of the spatial organization of HP materials both on the micro- and nanometer scale on the performance and stability of perovskite-based solar light converters. This review also discusses HP materials produced by isovalent lead(II) substitution with Sn^{2+} and other metal(II) ions, perovskite materials formed on the basis of M^{3+} cations (Sb^{3+}, Bi^{3+}) as well as on combinations of M^+/M^{3+} ions aliovalent to $2Pb^{2+}$ (Ag^+/Bi^{3+}, Ag^+/Sb^{3+}, etc.). The survey is concluded with an outlook highlighting the most promising strategies for future progress of photovoltaic systems based on lead-free perovskite compounds.

Review
Introduction

The field of photovoltaics and photochemical light harvesting using nanocrystalline semiconductor materials is a thriving field of research that intersects physics, physical and material chemistry, photonics and photochemistry. The investment in photovoltaic solar cells has increased among other sustainable sources of electricity, whereby the market is dominated by silicon solar cells with top light-to-current conversion efficiencies reaching ≈27% [1]. As an alternative to the Si-based cells requiring a relatively thick absorber layer due to the indirect character of electron transitions in Si, direct-bandgap metal chalcogenide semiconductors have been employed as nanome-

ter-thin-film light harvesters, such as $Cu(Ga)InS(Se)_2$ or CdTe, showing a light conversion efficiency of up to 21% [1,2]. Progress in dye-sensitized solar cells (reaching ≈12% efficiency [1,2]) has stimulated attempts in using metal chalcogenide nanocrystals (NCs) as sensitizers in liquid-junction solar cells [3,4]. These systems have shown remarkable progress, improving from 0.1% a decade ago to over 12% in 2018 [5].

Simultaneously, a new rising star in semiconductor photovoltaics – hybrid organo–inorganic lead-based perovskites ($MPbX_3$, where M = methylammonium (MA), formamidinium

(FA), Cs; X = Cl, Br, I) – first employed only several years ago are making a fast progress increasing from ≈2% in 2006 to more than 20% starting from 2015 (Figure 1a) [6-31].

The avalanche progress of the hybrid perovskite (HP) photovoltaic system was documented in detail by numerous review papers covering all aspects of the preparative chemistry and photophysics of lead-based HPs, solar cell design, challenges and pitfalls on the way to the HP cells competitive with the silicon counterparts, as well as issues of stability, environmental impact and possible recycling of the Pb-HP-based devices [11-13,16,23,26,27,29-50]. A tremendous amount of work has been performed in searching for the most efficient and stable compounds with mixed cations (e.g., MA^+/Cs^+, MA^+/FA^+) and mixed halide components [20,21,29,30,49,51].

It was recognized that Pb-HPs, especially with inorganic Cs^+ ions that have no asymmetry typical for organic MA or FA cations, also have an extremely high potential for application in other areas, in particular as light emitters for LEDs, laser applications and in photodetectors [28-31,35,43,47,50,52-54]. The versatility of the possible optoelectronic applications of Pb-HPs has stimulated an explosive progress in preparative chemistry and photophysics of HP nanocrystals (NCs) [16,24,28-30,43,50,53-56]. Recently, broad recognition was gained by 1D and 2D layered hybrid perovskite materials with strong anisotropy of electron properties. Such materials are currently treated as very promising light harvesters with highly tunable optical and charge transport characteristics [14,16,24,28-31,44,47,57,58].

In recent years, some saturation of the initial drastic growth of the power conversion efficiency (PCE) of lead-HP-based solar cells has been observed (Figure 1a). Simultaneously a number of critical challenges related to these materials were recognized as limiting their future broad implementation [29-31,36,39,40,42,48-50,57,59]. The unrivaled light-to-current conversion efficiency of lead-based HP absorbers is largely compromised by the hydrolytic and photochemical instability of Pb-HPs as well as the highly toxic character of the released Pb^{2+}, which requires the development of special recycling protocols [40,42]. While the first problem seems to be solvable, in particular by the encapsulation and a design of the cationic sublattice, the presence of Pb^{2+} cannot be avoided.

Lead is allowed for usage in the outdoor photovoltaic modules, but the utilization of alternative, less toxic metals is highly welcomed [40,42,54,57,59-61]. One of the promising routes to decrease the environmental burden of Pb-HP cells and to maintain reasonably high PCEs was to partially substitute Pb^{2+} with other double-charged cations, such as Sn^{2+}, Mn^{2+}, or Ge^{2+}, where the tin-based materials have gained the most attention and progress [10,16,18,29,30,38,44,54,59-65]. The Sn-based HPs ($CsSnX_3$, $MASnX_3$) show a high charge carrier mobility and diffusion length, comparable to the Pb-based analogs [16,18,57,59,60,62,63,65,66]. Despite large recombination losses reported for $CsSnX_3$ materials, solar cells based on these compounds showed a promising light conversion efficiency of ≈13% indicating a great potential for the lead-free HP [59,62,63]. Numerous attempts and probes have shown that photoactive perovskite compounds can be developed also for other metals, in particular for Bi^{3+}, Sb^{3+}, Cu^{2+}, and combinations of Ag^+/Bi^{3+}, Ag^+/Sb^{3+}, and In^+/Bi^{3+}.

A drastic growth of interest in lead-free HPs has been witnessed in the past three years, where the number of relevant publications has skyrocketed by more than an order of magnitude from 2014 to 2017 with the number of papers published in the first half of 2018 already exceeding the number in 2016 (Figure 1b). The fast progress in the area of lead-free HPs is also supported
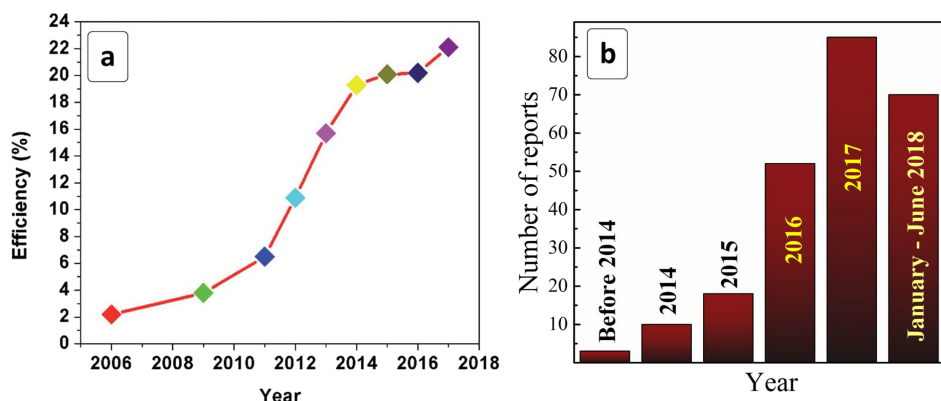
Figure 1: Temporal evolution of (a) the power conversion efficiency of lead-HP-based solar cells and (b) the number of publications on lead-free HPs. (a) Reprinted with permission from [27], copyright 2018 The Royal Society of Chemistry.

by an ever-growing number of review papers trying to distinguish the most promising venues and materials and to suggest outlines of further exploration [28-30,42,50,53,54,57,59-61,64,65].

Historically, the first HP cell was built basing on a "classic" design of the dye-sensitized solar cells with the HP layer acting as a sensitizer of a mesoporous metal oxide (TiO_2) scaffold [67]. Later, it was recognized that Pb-based HPs are incomparably more efficient when applied as light harvesters in photovoltaic planar or bulk heterojunction solar cells. Such cells have

two designs – a "conventional" n–i–p design with a HP layer deposited onto the metal oxide electron transport layer (ETL) and then covered with an organic hole transport layer (HTL) and an "inverted" p–i–n design, where an HP layer is formed on an HTL support and covered with an organic ETL, such as fullerene derivatives (see below in Figure 2). The conventional n–i–p scheme dominates in the studies of HPs with the typical ETLs being titania and various TiO_2-based composites [27]. The most efficient and frequently used HTLs are among the derivatives of spirobifluorene (Spiro-OMeTAD, see Table 1) and polythiophenes (PEDOT:PSS).

Table 1: Photovoltaic characteristics of selected mixed and lead-free HP-based solar cells.[a]

Perovskite	Cell configuration	J_{sc}, A/cm²	V_{oc}, V	FF	PCE, %	Ref.
Sn,Pb-HPs						
$MASn_{0.5}Pb_{0.5}I_3$	FTP/TiO_2/**HP**/P3HT/Au-Ag	20.04	0.42	0.50	4.18	[68]
$MASn_{0.1}Pb_{0.9}IBr_2$	FTO/TiO_2/**HP**/C	14.3	1.26	0.63	11.33	[69]
$MAPb_{0.5}Sn_{0.5}(I_{0.8}Br_{0.2})_3$	ITO/PEDOT:PSS/**HP**/ICBA/Ag	25.9	0.90	0.75	17.63	[70]
Sn-HPs						
$MASnI_3$	FTO/TiO_2/**HP**/PTAA/Au	24.28	0.429	0.64	6.63	[71]
$CsSnI_3$	ITO/TiO_2/HP/Spiro-MeOTAD/Au	23.2	0.86	0.65	12.96	[72]
$MASnIBr_{1.8}Cl_{0.2}$	FTO/TiO_2/**HP**/C	14.0	0.38	0.57	3.1	[73]
$MASnIBr_2$	FTO/TiO_2/**HP**/Spiro-MeOTAD/Au	12.30	0.82	0.57	5.73	[74]
$BA_2MA_3Sn_4I_{13}$	FTO/TiO_2/**HP**/PTAA/Au	24.1	0.229	0.46	2.53	[75]
$FASnI_3$	ITO/PEDOT/**HP**/C_{60}/BCP/Al	24.1	0.525	0.71	9.0	[76]
$FASnI_3$	ITO/SnO_2/C_{60}/HP/Spiro-MeOTAD/Ag	22.45	0.47	0.68	7.09	[77]
Ge-HPs						
$MAGeI_3$	FTO/TiO_2/**HP**/Spiro-MeOTAD/Au	4.0	0.150	0.30	0.20	[119]
$MAGeI_{2.7}Br_{0.3}$	ITO/PEDOT:PSS/**HP**/$PC_{70}BM$/Ag	2.43	0.460	0.51	0.57	[123]
Bi-HPs						
$MA_3Bi_2I_9$	FTO/TiO_2/**HP**/Spiro-MeOTAD/Au	0.798	0.486	0.42	0.164	[132]
$MA_3Bi_2I_9$	FTO/TiO_2/**HP**/Spiro-MeOTAD/Au	3.00	0.83	0.79	1.64	[64]
$MA_3Bi_2I_9$	FTO/TiO_2/**HP**/P3HT/Au	1.157	0.354	0.464	0.19	[65]
$Cs_2AgBiBr_6$	FTO/TiO_2/**HP**/Spiro-MeOTAD/Au	3.93	0.98	0.63	2.43	[170]
Sb-HPs						
$MA_3Sb_2I_9$	ITO/PEDOT:PSS/**HP**/$PC_{61}BM$/ZnO/Al	1.0	0.896	0.55	0.49	[130]
$MA_3Sb_2I_9$	ITO/PEDOT:PSS/**HP**/$PC_{71}BM$/C_{60}-BCP/Al	5.41	0.62	0.61	2.04	[70]
$MASbSI_2$	FTO/TiO_2/**HP**/PCPSTBT	8.12	0.65	0.59	3.08	[67]
$MA_3Sb_2Cl_xI_{9-x}$	FTO/TiO_2/**HP**/Spiro-MeOTAD/Au	5.04	0.69	0.63	2.19	[131]
$Rb_3Sb_2I_9$	FTO/TiO_2/**HP**/Poly-TPD/Au	2.11	0.55	0.57	0.66	[71]
$Cs_3Sb_2I_9$	ITO/PEDOT:PSS/**HP**/$PC_{70}BM$/Al	5.31	0.72	0.39	1.49	[69]

[a]The accuracy of values presented as reported, J_{sc} – short-circuit photocurrent density, V_{oc} – open-circuit photovoltage, FF – fill factor. Abbreviations: BA = $CH_3(CH_2)_3NH_3$; P3HT – poly(3-hexylthiophen-2,5-diyl); Spiro-MeOTAD – 2,2′,7,7′-tetrakis-(*N*,*N*-di-*p*-methoxyphenylamine)-9,9′-spirobifluorene; PCPSTBT –poly(2,6-(4,4-bis(2-ethylhexyl)-4*H*-cyclopenta[2,1-*b*;3,4-*b'*]dithiophene)-alt-4,7(2,1,3-benzothiadiazole)); poly-TPD – poly(*N*,*N*'-bis-4-butylphenyl-*N*,*N*'-bisphenyl)benzidine; PEDOT:PSS – poly(ethylenedioxythiophene):polystyrenesulfonate; PC_xBM – [6,6]-phenyl C_x butyric acid methyl ester; BCP – 2,9-dimethyl-4,7-diphenyl-1,10-phenanthroline; ICBA – indene–C_{60} adduct; PTAA – poly[bis(4-phenyl)(2,4,6-trimethylphenyl)-amine].

Recently, very good prospects were recognized for the cell design without organic HTL and back contacts, both roles played by a carbon layer. Panels (c) and (d) in Figure 2 show CB/VB levels of selected lead-free perovskites based on Sn^{2+}/Sn^{4+} (Figure 2c) and Sb^{3+}/Bi^{3+} (Figure 2d) with respect to the acceptor/donor levels of a series of typical ETL/HTL materials.
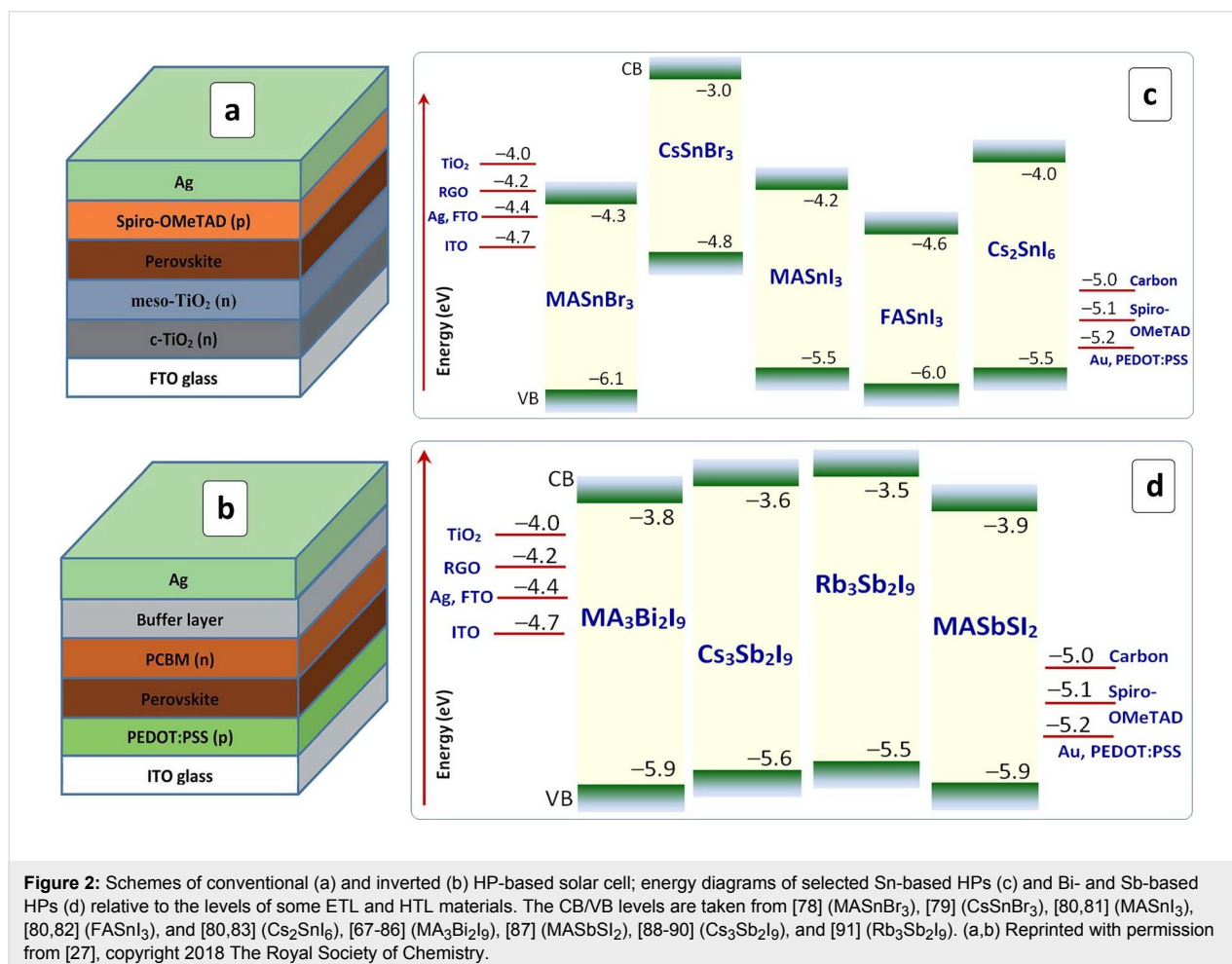
The present review aims to survey lead-free perovskites and closely related compounds reported in light of their possible applications as light harvesters in photovoltaic systems. Special focus is placed on the influence of the spatial organization of HP materials both on the micro- and nanoscale levels with respect to the performance and stability of perovskite-based solar light converters. The survey starts from HPs with lead ions partially substituted by isovalent cations of other less toxic metals, then focuses on lead-free HPs where the central metal ion is in the oxidation state of +2, predominantly, Sn^{2+} and Ge^{2+}. Then, hybrid perovskite materials formed on the basis of M^{3+} cations (Sb^{3+}, Bi^{3+}) as well as on combinations of M^{+}/M^{3+} ions aliovalent to $2Pb^{2+}$ (like Ag^{+}/Bi^{3+}, Ag^{+}/Sb^{3+}) are dis-

cussed as one of the most promising avenues to further progress in the research of lead-free perovskite light harvesters. The final Conclusion and Outlook section is focused on future strategies of the design of photovoltaic systems on lead-free perovskite compounds and the materials that have a high potential to be discovered.

Hybrid perovskites with partially/completely substituted Pb^{2+} cations

Hybrid perovskites with partially substituted lead ions

Using a small "tool kit" of two metals, Sn and Pb, and two organic cations, A = MA and FA, a broad variety of isostructural Pb-, Sn- and Pb–Sn-based $ASn_xPb_{1-x}I_3$ HPs can be synthesized with a bandgap varying from 1.25 to 1.75 eV depending on the HP composition [92]. By simultaneously tuning the composition of Pb–Sn and halide components, a solar light absorber was designed with a bandgap of 1.35 eV ideal for the solar light harvesting. The inverted cells based on $MAPb_{0.5}Sn_{0.5}(I_{0.8}Br_{0.2})_3$ demonstrated PCEs of up to 17.63% [70]. A suppressed lattice disorder of this HP results in a low

Figure 2: Schemes of conventional (a) and inverted (b) HP-based solar cell; energy diagrams of selected Sn-based HPs (c) and Bi- and Sb-based HPs (d) relative to the levels of some ETL and HTL materials. The CB/VB levels are taken from [78] (MASnBr$_3$), [79] (CsSnBr$_3$), [80,81] (MASnI$_3$), [80,82] (FASnI$_3$), and [80,83] (Cs$_2$SnI$_6$), [67-86] (MA$_3$Bi$_2$I$_9$), [87] (MASbSI$_2$), [88-90] (Cs$_3$Sb$_2$I$_9$), and [91] (Rb$_3$Sb$_2$I$_9$). (a,b) Reprinted with permission from [27], copyright 2018 The Royal Society of Chemistry.

density of traps and sub-bandgap states reflecting in a relatively small E_g–V_{oc} loss of 0.45 eV [70].

The bandgap of alloyed $FASn_xPb_{1-x}I_3$ HPs was found to vary in an unexpected way, that is, decreasing upon the introduction of Sn from ≈1.5 eV for MAPI to 1.24 eV for $x = 0.4$ and then increasing to ≈1.3 eV for the $FASnI_3$ perovskite [93]. The "bowing" of the $E_g(x)$ dependence may originate from a transition from cubic to orthorhombic lattice symmetry upon increasing tin content [93]. A similar anomalous variation of the bandgap, as well as the CB/VB level positions with the Sn content, was reported for $CH_3NH_3Sn_xPb_{1-x}I_{3-y}Cl_y$ HPs [94].

A study of alloyed $ASn_{1-x}Pb_xI_3$ (A = Cs^+, FA^+, MA^+ or their combinations) produced in the form of NCs showed the mixed compounds to be much more stable to ambient air as compared to both $ASnI_3$ and $APbI_3$ individually [95-97]. The cation-exchange approach applied to produce $FASn_{1-x}Pb_xI_3$ and

$FAPbI_3$ from $FASnI_3$ is expected to be a general one and appropriate for the introduction of other isovalent and aliovalent cations such as Mn^{2+}, Co^{2+}, Bi^{3+}, and Al^{3+} into the sites of Sn^{2+} or Pb^{2+} [97]. The chemical stability of mixed Sn–Pb perovskites can be further enhanced by the passivation with a C_{60} layer [98]. The fullerene was found to eliminate the surface trap states of $MAPb_{0.75}Sn_{0.25}I_3$ crystals suppressing the electron–hole recombination as well as shielding the HP layer from the ambient moisture and oxygen.

Solar cells with mixed $MASn_xPb_{1-x}I_3$ HPs and a P3HT HTL showed a dome-shaped PCE dependence on the lead content (Figure 3a), where a maximum η of 4.18% was achieved at an Sn/Pb atomic ratio of 1:1 [68]. The conventional MAPI HP displayed a much lower efficiency, while a pure Sn-based HP turned out to be inactive with this HTL material. A higher efficiency of mixed Sn,Pb-HPs stems largely from a broader absorption range extending to $\lambda_e = 1060$ nm as compared to
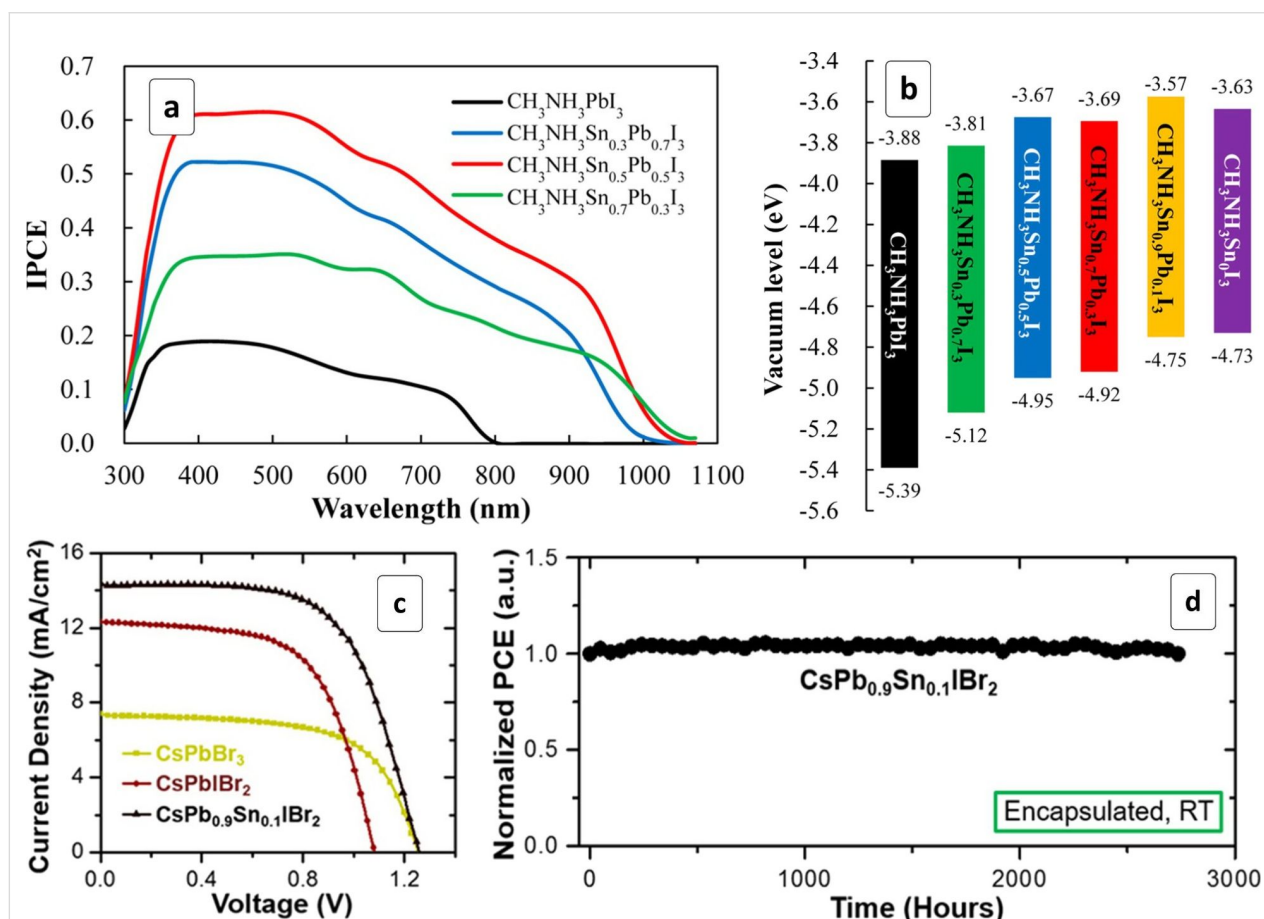
Figure 3: (a,b) Internal photon-to-current conversion efficiency (IPCE) spectra of solar cells comprising a series of Sn,Pb-based HPs with different Sn/Pb ratios (a) and energy diagram of the corresponding perovskites (b); (c) current–voltage curves for solar cells based on $CsPbBr_3$, $CsPbIBr_2$ and $CsPb_{0.9}Sn_{0.1}IBr_2$ HPs; (d) test of prolonged performance stability of a solar cell based on $CsPb_{0.9}Sn_{0.1}IBr_2$ HP, RT – room temperature. (a,b) Reprinted with permission from [68], copyright 2014 American Chemical Society and (c,d) Reprinted with permission from [69], copyright 2017 American Chemical Society.

only 800 nm for MAPI (Figure 3a). A partial substitution of the lead with tin was found to affect the VB position of the HP much stronger than the corresponding CB level (Figure 3b). This fact hints at the importance of the selection of an appropriate hole transport material for each particular HP composition to realize the potential of such materials to a full extent.

The introduction of 10% Sn into $CsPbIBr_2$ HP results in a bandgap narrowing from 1.90 to 1.79 eV and an increase of the solar cell performance (Figure 3c) from 8.25% for the undoped Pb-HP to 11.33% for the $CsSn_{0.1}Pb_{0.9}IBr_2$-based device [69]. The latter cell also exhibited a record V_{oc} of 1.26 V amounting to ≈70% of the optical bandgap and vividly showing a high potential of such photovoltaic materials. Additionally, the cell fitted with an encapsulating protective layer showed a remarkable stability with the PCE unchanged in a more than 2500 h test trial (Figure 3d) [69].

Manganese(II) ions were found to substitute Pb(II) in MA-Pb-Cl-Br HPs, the perovskite preserving the crystal structure up to 90% Mn [99]. Up to 46% Pb^{2+} ions can be exchanged with Mn^{2+} in $CsPbCl_3$ NCs produced by hot-injection, resulting in a highly increased photoluminescence (PL) efficiency [100]. Mixed $MAPb_xMn_{1-x}I_{1+2x}Cl_{2-2x}$ ($x = 0.1–1.0$) synthesized by a solid-state reaction displayed an unprecedentedly high open-circuit voltage of up to 1.19 V and fill factor (FF) of almost 90% when introduced into inverted solar cells with PEDOT:PSS and PCBM charge transport layers [101]. Despite the high V_{oc} and FF values, the cells showed quite a low efficiency of ≈0.3% indicating huge recombinational losses and leaving large room for further improvement of the structural quality of the perovskite absorber layer.

The substitution of a mere 2% lead with Sr(II) in $CsPbI_2Br$ HP was found to result in a spectacular PCE increase from 6.6% to 10.1% and an enhancement of the thermal HP stability [102]. Strontium ions accumulate in a surface layer of the HP film exerting a passivating effect and resulting in a longer charge carrier lifetime [102]. The introduction of Ca^{2+} on the Pb^{2+} sites of $CsPbI_3$ HP results in a more homogeneous a better contact between the HP and HTL, as well as the surface passivation by a Ca-enriched surface layer [103]. The best Ca-substituted $CsPbI_3$ HPs show a PCE of higher than 13% and maintain more than 85% of the initial efficiency for more than two months of testing with encapsulation [103].

A partial substitution of Pb(II) with In(III) yields HPs with a reduced lead content and a promising PCE exceeding 17.5% [104]. The introduction of Sb(III) during the growth of MAPI HP results in the substitution of lead with antimony and formation of a $MA_3Sb_2I_9$ layer on the surface of growing MAPI crys-

tals thus limiting their size to ≈50 nm [105]. An enhanced PL of the Sb-doped MAPI crystals indicates that the electron–hole recombination is efficiently suppressed by the surface antimony-rich layer [105].

Sn-based hybrid perovskites

The $MASnI_3$ perovskite displays a bandgap of ≈1.3 eV [74,81] corresponding to the absorption onset at $\lambda_e \approx 950$ nm, which is significantly shifted as compared to the MAPI counterpart ($E_g = 1.55$ eV, ≈800 nm) [74] and comparably high absorption coefficients of ≈10^5 cm^{-1} [106]. Thick $MASnI_3$ perovskite wafers synthesized by a temperature-reduction-induced crystallization showed an even narrower bandgap of ≈1.2 eV [107]. The $FASnI_3$ compound with a bulkier formamidinium cation displayed a larger bandgap of 1.41 eV [82]. A partial substitution of I with Br results in a controlled expansion of the bandgap up to 1.68 eV for $FASnI_2Br$ [108]. The reported bandgaps of selected Sn-based HPs are collected in Table 2.

Table 2: Bandgap and approximate absorption band edge position (λ_e) of selected Sn-based hybrid perovskites.

Perovskite	E_g, eV	λ_e, nm	Ref.
$MASnCl_3$	2.1	590	[109]
$MASnBr_3$	2.2	570	[78]
$CsSnBr_3$	1.80	690	[110]
$MASnI_3$	1.21–1.23	1010–1030	[111]
	1.3	960	[74,79,81]
$FASnI_3$	1.41	880	[82]
$FASnI_2Br$	1.68	740	[108]
Cs_2SnI_6	1.48	840	[83,112]
MA_2SnI_6	1.81	690	[54]

Similar to MAPI, the morphology of $MASnI_3$ plays an important role in the efficiency of the solar cells based on this light harvester. This fact stimulated a screening of suitable solvents and deposition conditions, revealing dimethylsulfoxide (DMSO) as one of the most promising candidates for spin-coating deposition technology [113,114], which produced uniform pin-hole-free $MASnI_3$ films due to the formation of an intermediate $SnI_2 \times DMSO$ phase [114]. Trimethylamine acts in a similar way forming intermediate complexes with SnI_2 (and SnF_2 as a stability-enhancing additive) and facilitating the formation of dense and uniform $MASnI_3$ and $FASnI_3$ films [77]. The simultaneous presence of the trimethylamine and SnF_2 was found to be crucial both for conventional and inverted solar cell configurations. For example, the modification of an inverted $FASnI_3$-based cell with SnF_2 resulted in a spectacular PCE increase from 0.52 to 4.20% with a further increase to 7.09% (Table 1) induced by the introduction of trimethylamine as a morphology-directing agent [77].

The quality of MASnI$_3$ films as components of solar cells can be ameliorated by introducing ethylenediamine (en) acting simultaneously as an additional organic cation in the HP lattice and as a morphology-directing agent [71]. The cells with such modified MASnI$_3$ absorbers showed a PCE of 6.63% (Table 1) with a relatively high FF of ≈64% (Figure 4a). High-quality MASnI$_3$ films yielding a PCE of 1.86% were prepared using a low-temperature vapor-assisted deposition [115].

The stability of MASnI$_3$- and CsSnI$_3$-based solar cells is largely compromised by a low HP stability to oxidation [80,116]. It was found that the Sn^{2+} state of the central ion can be stabilized by introducing an excess of SnI$_2$, with the best cells showing a

PCE of 4.81% (Figure 4b) and a prolonged stability of the photovoltaic parameters [80]. Calculations by the density functional theory (DFT) indicated that a partial substitution of Cs$^+$ with Rb$^+$ should considerably increase the stability of CsSnI$_3$ [117].

To avoid a partial conversion of Sn^{2+} into Sn^{4+}, the latter acting as charge carrier traps in ASnX$_3$ HPs, it was suggested to deposit the perovskite layer under a reductive atmosphere, for example, in the presence of hydrazine vapors [119]. The conversion of Sn^{4+} into Sn^{2+}, which can be described as $2SnI_6^{2-} + N_2H_4 = 2SnI_4^{2-} + N_2 + 2HI$, results in a reduction of the density of Sn^{2+} vacancies (Figure 5a) suppressing the unde-
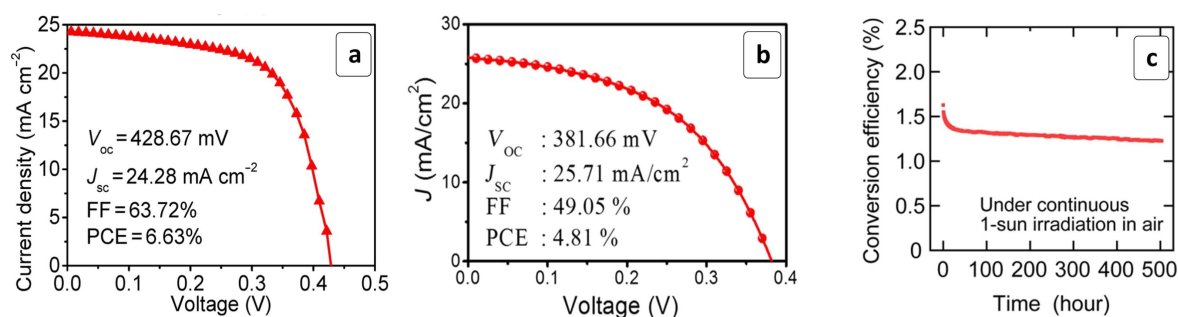
Figure 4: (a,b) Photocurrent density–voltage curves recorded for the solar cells based on MASnI$_3$ HPs (a) and CsSnI$_3$ HPs (b); (c) test of prolonged performance stability of a solar cell based on MASnI$_3$ HPs. (a) Reprinted with permission from [71], copyright 2017 American Chemical Society; (b) Reprinted with permission from [80], copyright 2017 American Chemical Society; (c) Reprinted with permission from [118], copyright 2017 American Chemical Society.
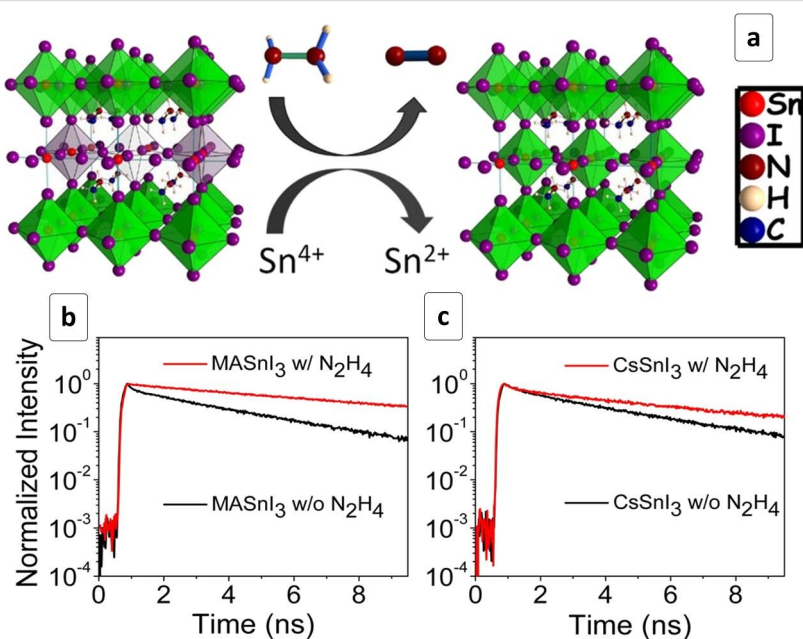
Figure 5: (a) Scheme of a possible mechanism of Sn-based HP transformation upon reaction with hydrazine; (b,c) kinetic photoluminescence decay curves for MASnI$_3$ (b) and CsSnI$_3$ (c) produced without treatment (black lines) and with an N$_2$H$_4$ vapor treatment (red lines). Reprinted and adapted with permission from [119], copyright, 2016 American Chemical Society.

sirable p-type conductivity and reverting the perovskites back to n-type semiconducting behavior [119]. The hydrazine treatment results in an appreciable increase of the radiative lifetime of ASnX$_3$ HPs irrespective of the type of cation A (Figure 5b,c) and halide component composition, clearly indicating a reduction of the trap-mediated non-radiative recombination losses.

The effect of elimination of Sn^{2+} vacancies in FASnI$_3$ HP resulting from tin(II) oxidation can also be achieved by a partial substitution of iodide with bromide [120]. The devices with a mixed Br/I halide component displayed a reduced dark current and lower recombination rate, resulting in an increased V_{oc} and FF and showed a PCE above 5%, whereby the cells retained stability over a 1000 h time trial span [120]. In a similar manner, the mixed CsSnIBr$_2$ HP revealed a higher stability and a lower density of Sn^{2+} vacancies which can be further decreased by growing the HP crystals in the presence of hypophosphoric acid as a tin(II) complexant [121]. The corresponding cells revealed the stable PCE for a 77 day trial at room temperature and during a 9 h test at 473 K [121].

An elegant way of simultaneously ordering MASnI$_3$ deposits and protecting them from exposure to air/moisture was suggested via the growth of HP nanowires in the pores of anodized alumina membranes [122]. The effective blockage of the diffusion of water and oxygen molecules to the alumina-incorporated MASnI$_3$ nanowires resulted in a three order of magnitude slower degradation of this material as compared to planar films of the same composition [122].

It was found that of the three "homologs" of CsSnX$_3$ HPs (X = Cl, Br, I) the bromide-based compound shows an exceptionally high photochemical and chemical stability, which can further be enhanced by doping with SnF$_2$ [110].

The stability of MASnI$_3$-based cells can also be strongly enhanced by doping with SnF$_2$ [118,123,124]. The doped materials showed a remarkable stability when illuminated under ambient air conditions without additional encapsulation (Figure 4c). Additionally, the SnF$_2$ doping results in a decrease of the HP bandgap down to 1.25 eV, which is highly beneficial for the cell performance. This redshift effect was attributed to the Burstein–Moss effect arising from a significant doping of the absorber material with holes [118]. The SnF$_2$ doping was found to almost double the radiative lifetime of charge carriers and considerably increase the carrier diffusion length [125]. A similar approach can be applied to increase the stability of FASnI$_3$ absorbers [82].

The quality and stability of FASnI$_3$ can be strongly enhanced by introducing trace amounts of 2D tin HPs comprising both FA and 2-phenylethylammonium cations [126]. The presence of 2D HP favors a more homogeneous growth of FASnI$_3$ crystals, resulting in a reduced number of grain boundaries and the suppression of the formation of Sn^{4+}. The high quality of such FASnI$_3$ films was evidenced by a strongly reduced background carrier density and a longer charge carrier lifetime [126]. The solar cells produced from these highly uniform HP layers revealed a negligible hysteresis and no light soaking effect, indicating a largely suppressed recombination. The best PCE was 9%, which is by 50% higher than for similar cells with the HP layer modified by SnF$_2$ [76].

A compositional variation of the halide component of CsSnX$_3$ HPs is a potent instrument allowing the bandgap and CB/VB energies to be changed, and therefore, to affect the spectral sensitivity range and V_{oc} of the CsSnX$_3$-based solar cells. The individual and mixed-halide Sn-HPs demonstrated a broad spectrum of bandgaps varying from 2.97 eV for CsSnCl$_3$ to 1.31 eV for CsSnI$_3$ with all possible intermediate values achievable by tailoring the type and relative content of halide ions (Figure 6a) [126].

By varying the bromide content in CsSnI$_{3-x}$Br$_x$ perovskite the HP bandgap can be smoothly increased from 1.27 eV (CsSnI$_3$) to 1.37 eV (CsSnI$_2$Br) to 1.65 eV (CsSnIBr$_2$) and up to 1.75 eV for CsSnBr$_3$ (Figure 6b) [127]. The open-circuit voltage of the corresponding solar cells increases from ≈200 meV to 410 meV. A combination of two tendencies – a bandgap increase resulting in a narrowing of the spectral sensitivity range and a V_{oc} increase contributing to a higher PCE – results in an optimal HP composition of CsSnI$_2$Br yielding the highest light harvesting efficiency [127].

Similar attempts of introducing chloride ions into Cs$_2$SnI$_6$ HP showed that single-phase compounds can exist only at compositions close to the individual I- and Cl-based compounds (Figure 6c), while at intermediate compositions a mixture of phases is typically produced [128]. In the case of I/Br-mixed Sn^{4+}-based HP a series of single-phase Cs$_2$SnI$_{6-x}$Br$_x$ compounds were prepared with a bandgap tuned from 1.3 eV to 2.9 eV [129]. The highest PCE of 2.1% was reported for an intermediate composition corresponding to $x = 2$ [129].

Similar to the Cs-containing HPs, the optoelectronic properties of MASnX$_3$ HPs can also be engineered by a partial substitution of halide anions. A gradual shift from MASnI$_3$ to MASnBr$_3$ via a series of intermediate solid-solution compounds (some illustrated by Figure 6d) results in an E_g expansion from 1.30 eV to 2.15 eV. Here the bandgap increment contributes mostly to a shift of the CB level to lower energies, while the VB level remains relatively unaffected [74]. For all
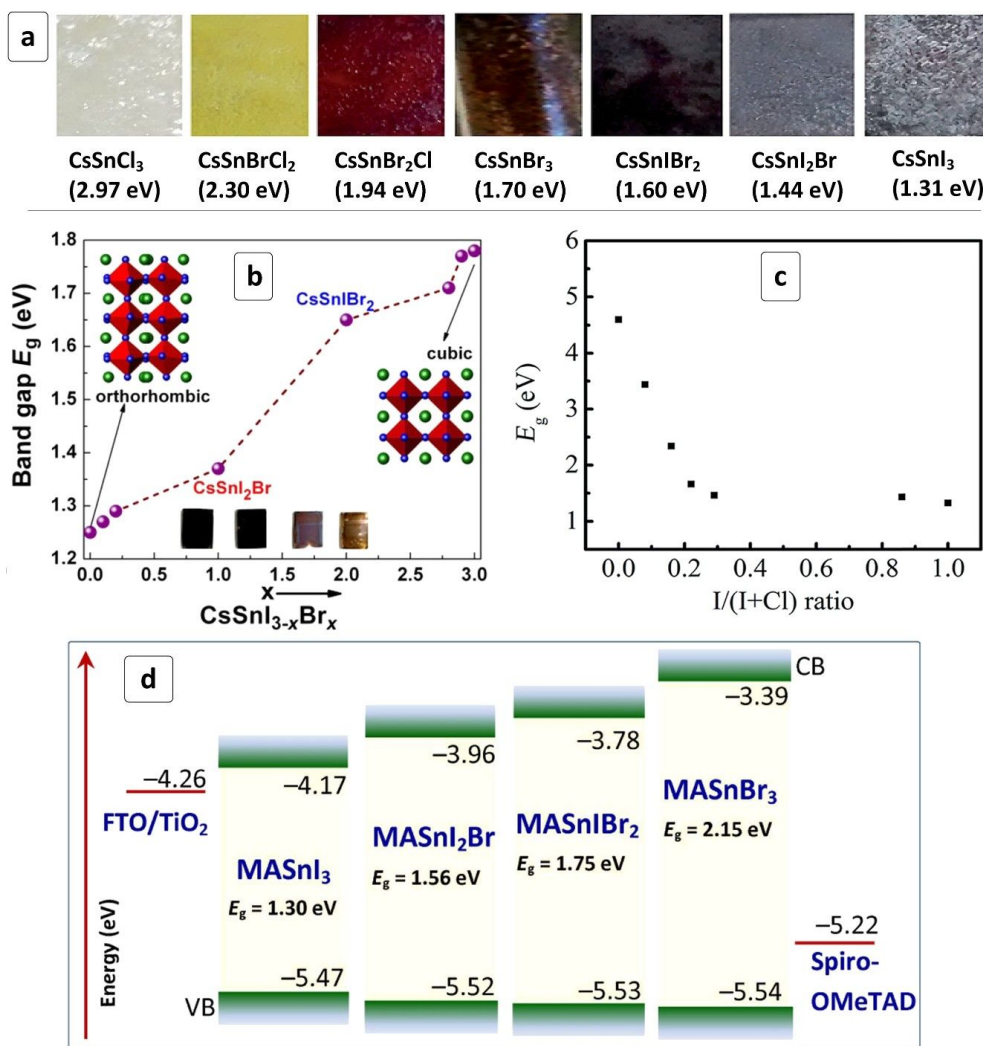
Figure 6: (a) Photographs of HP films produced from different $CsSnI_{3-x}Br_x$ and $CsSnBr_{3-x}Cl_3$ compounds (bandgaps are provided in parenthesis); (b,c) Bandgap as a function of the composition of $CsSnI_{3-x}Br_x$ HPs (b) and $Cs_2SnI_xCl_{6-x}$ HPs (c); (d) energy diagrams of solar cells based on $MASnI_{3-x}Br_x$ HPs, FTO/TiO$_2$ ETL and Spiro-OMeTAD HTL. The diagram is plotted using numerical data reported in [74]. (a) Reprinted and adapted from [126], copyright 2016 The Royal Society of Chemistry; (b) Reprinted and adapted from [127], copyright 2015 American Chemical Society; (c) Reprinted and adapted from [128], copyright 2018 The Royal Society of Chemistry.

compositions, the CB/VB positions are suitable for the construction of solar cells with a TiO$_2$ ETL and Spiro-OMeTAD HTL. The CB shift results in an increase in the efficiency of electron transfer to the titania scaffold. This tendency is, however, counter-balanced by a reduction of the spectral sensitivity range due to an increased E_g. Summarily, both trends result in the highest PCE observed for the intermediate MASnIBr$_2$ HP (Table 1).

A combination of all three halides within a single tin-HP is a promising route to efficient and stable solar cell absorbers as shown on the example of MASnIBr$_{1.8}$Cl$_{0.2}$ HP displaying PCEs higher than 3% in a HTL-free cell as well as a long-term operational stability [73].

The light-harvesting MASnBr$_3$ HP films were produced by evaporation of SnBr$_2$ and MABr [78]. The co-evaporation technique was found to be preferable over a sequential deposition in terms of the photovoltaic efficiency due to the surface oxidation of the evaporated SnBr$_2$ layer before the deposition of methylammonuim bromide [78].

The electron diffusion length in MASnI$_3$ perovskite was estimated to be around 20 nm in contrast to over a micrometer in the corresponding lead HPs [111]. In view of this finding, the task of the preparation of large-as-possible HP grains with a minimized grain boundary area and surface defects seems to be of much lower significance for the Sn-based HPs, than for their lead-based counterparts. We can, therefore, expect a similar

photovoltaic efficiency from micro- and nanometer Sn-HP crystals and try to affect the charge carrier transport through the HP/ETL and HP/HTL interfaces by tailoring the HP morphology on the nanometer scale. It was also found that the size-selected Cs_2SnI_6 NCs (12–49 nm) are characterized by a much smaller effective electron mass ($0.12m_0$) as compared to the bulk HP ($0.56m_0$) [130]. Therefore, one might expect a strong influence of the NC size on the CB level position favorable for the "band design" of the light absorber to fit the energy levels of various ETL materials.

The Sn-based HPs can be synthesized in a variety of nanoscale morphologies, including 0D NCs, nanorods, nanoplatelets, etc., allowing possible size/shape effects to be investigated with respect to the optical, luminescent and photovoltaic properties of such materials. For example, reasonably monodisperse ≈10 nm NCs of a variety of $CsSnX_3$ HPs (X = Cl, Br, I, Cl/Br, Br/I) can be produced (Figure 7a) by a general hot injection method using mildly reducing and coordinating tri-octylphosphine as a solvent for SnX_2 [131]. A similar approach was recently applied for the synthesis of $CsSnI_3$ nanoplates

with a thickness of less than 4 nm [132]. The formation of $CsSnX_3$ nanoscale phases requires the presence of toxic tri-octylphosphine, whereby the Sn(II)-based NCs are unstable and prone to oxidation in other high-boiling-point solvents [131,132].

Sn(IV)-based Cs_2SnI_6 HP was proposed as an alternative light absorber material that forms a variety of morphologies and can be synthesized in the more environmentally friendly oleic acid/oleylamine in octadecene [130,133,134]. The shape of nanoscale Cs_2SnI_6 can be tuned quite easily by varying the duration of crystal growth. The reaction between Sn(IV) oleate and CsI yields ≈2.5 nm NCs in a minute after cesium iodide injection (Figure 7b), where the NCs transform into HP nanorods after a 5 min ripening at 220 °C (Figure 7c) [133]. The Cs_2SnI_6 nanorods gradually transform into nanowires (Figure 7d) with the aspect ratio increasing from 3 to 28 after a 10 min reaction. At longer reaction times (30 min) nanowires transform into nanobelts (Figure 7e) that assemble into nanoplatelets with a thickness of ≈8 nm (Figure 7f) after a 60 min ripening at 220 °C.

Figure 7: TEM (a–h) and STEM (j) images of $CsSnI_3$ nanocrystals (NCs): (a) Cs_2SnI_6 in the form of NCs (b), nanorods (c,g), nanowires (d), nanobelts (e), and nanoplatelets (f); $CsSnBr_3$ nanocages (h,j). (a) Reproduced with permission from [131], copyright 2016 American Chemical Society; (b–f) Reprinted and adapted with permission from [133], copyright 2016 American Chemical Society; (g) Reprinted and adapted with permission from [72], copyright 2016 American Chemical Society and (h,j) Reprinted and adapted with permission from [135], copyright 2017 American Chemical Society.

When using Cs oleate as a precursor, the average size of the resulting Cs_2SnI_6 NCs can be smoothly varied from ≈12 to ≈40 nm by increasing the hot-injection synthesis temperature from 80 to 220 °C [130]. Such Cs_2SnI_6 NCs showed a size-dependent bandgap, decreasing from 1.47 nm for the smallest NCs to 1.36 eV to the largest ones. The NCs are free from any surface ligands and stable long enough for the preparation of solar cell electrodes [130].

The Cs_2SnI_6 HPs can be formed by in situ oxidizing unstable $CsSnI_3$ with air oxygen [112] or directly deposited from a chemical bath [64]. The Cs_2SnI_6 perovskite is characterized by a bandgap of 1.48 eV and absorption coefficients over 10^5 cm^{-1} above 1.7 eV [112].

$MASnI_3$ and Cs_2SnI_6 HPs can be conveniently synthesized by the electro-assisted oxidation of Pb^0 or Sn^0 films (produced by evaporation) in alcohol solutions of alkali metal or alkyl ammonium halides [136]. The method is perfect for the direct formation of Sn-based HPs with tailored morphology and composition avoiding the use of unstable Sn^{2+}/Sn^{4+} precursors and toxic solvents. Moreover, it was argued in [136] that the method allows for the thermodynamics-driven formation of HPs, resulting in a higher material quality and reproducibility as compared to the conventional kinetically quenched syntheses (solvent evaporation, spin or spray coating).

The shape control over $CsSnX_3$ nanoscale phases grown in the presence of tri-octylphosphine oxide can be exerted by introducing complexants preferentially directing the NC growth along certain lattice planes. For example, $CsSnX_3$ nanorods (X = Cl, Br, I) with a relatively homogeneous rod diameter distribution were synthesized in the presence of diethylenetriamine (Figure 7g) [72]. The $CsSnX_3$ nanorods applied as light

harvesters with TiO_2/SpiroMeOTAD ETL/HTL combination revealed relatively high PCEs increasing from 9.66% for X = Cl to 10.46% for X = Br to 12.96% for X = I (Table 1), all three devices demonstrating a high V_{oc} of 0.85–0.87 V [72].

A controlled self-assembly phenomenon reported in [135] resulted in the formation of hollow "nanocages" composed of $CsSnBr_3$ NCs (Figure 7h,j). The nanocages can be stabilized against decomposition caused by oxidation, hydrolysis or photochemical processes by a post-synthesis treatment with perfluorooctanoic acid.

A series of 2D $(CH_3(CH_2)_3NH_3)_2(CH_3NH_3)_{n-1}Sn_nI_{3n+1}$ perovskites was recently introduced as stable and promising alternatives of 3D $ASnX_3$ HPs for photovoltaic applications [75]. The 2D HPs revealed semiconductor properties with a bandgap decreasing from 1.83 eV for $n = 1$ to 1.2 eV at $n \to \infty$ (Figure 8a). The 2D HP layers can be selectively oriented parallel to the substrate when the HP is spin-coated from DMSO and perpendicular – if the deposition occurs from *N,N*-dimethylformamide (DMF). The CB energy position was found to strongly depend on the HP composition (Figure 8b).

This allows for the search of an optimum between the efficiency of the electron transfer to the TiO_2 scaffold and the spectral sensitivity range defined by E_g. The Sn_4I_{13} "isomer" with a "close-to-ideal" E_g of 1.42 eV was suggested as an optimal light harvester, displaying a promising PCE of 2.5% (Table 1) [75].

Along with the photovoltaic cells with an HP layer sandwiched between ETL and HTL, the photo-electrochemical HP-based systems are explored as well, where an electron-shutting redox-couple is used for the charge exchange between the light-absorbing electrode and a counter electrode. For example, a
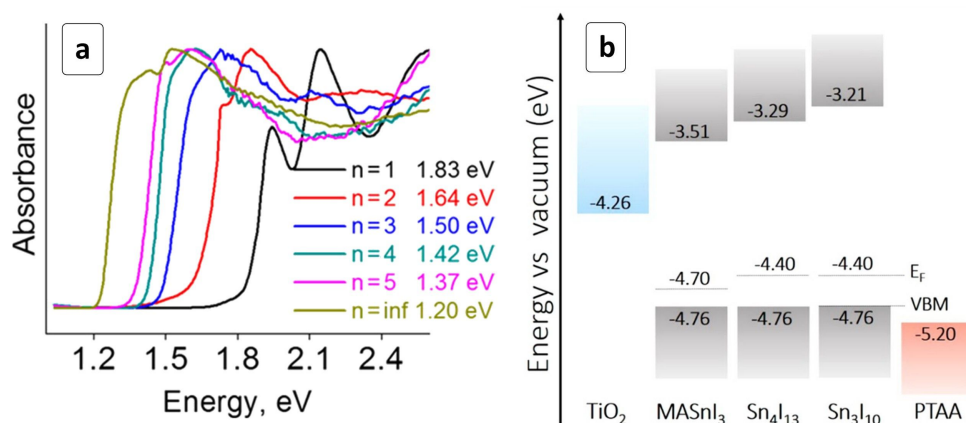
Figure 8: (a) Absorption spectra of $(CH_3(CH_2)_3NH_3)_2(CH_3NH_3)_{n-1}Sn_nI_{3n+1}$ homological HPs; (b) energy level alignment in solar cells with selected HPs. VBM is the valence band (VB) minimum, E_F is Fermi energy. Reprinted with permission from [75], copyright 2017 American Chemical Society.

solar cell based on a $MASnI_{3-x}Br_x$ film coupled to a carbon counter electron by a dissolved benzoquinone redox-couple BQ^0/BQ^- showed a PCE of 1.51% [137].

An $FTO/TiO_2/MASnCl_3$ photoanode (E_g = 2.1 eV) was combined with an FTO/Pt counter electrode and a solid/liquid electrolyte consisting of polyethylene oxide soaked with an acetonitrile solution of KI/I_2 into a solar cell displaying PCEs of up to 0.55% [109].

The mixed $CsSnI_{2.95}F_{0.05}$ was successfully tested as an efficient HTL for dye-sensitized solar cells operating with PCEs of up to ≈10% [138].

Other M^{2+}-based hybrid perovskites

Germanium(II) forms a series of perovskites isostructural to MAPI with a bandgap decreasing from 3.76 eV for $MAGeCl_3$ to 2.81 eV for $MAGeBr_3$ to 1.61 eV for $MAGeI_3$, the latter value close to E_g of MAPI (1.55 eV) [139]. Ge-based $AGeI_3$ HPs with A = Cs^+ (E_g = 1.63 eV), MA^+ (2.0 eV), and FA^+ (2.35 eV) were reported to be stable up to 150 °C but prone to the air oxidation [140]. The VB top and CB bottom of Ge-HPs are formed predominantly by Ge s- and p-orbitals, respectively, resulting in direct "intra-atomic"-like electron transitions. As the cation A size grows, the lattice constant increases, resulting in a further splitting between the Ge-related bonding and anti-bonding levels and, therefore, in an increase of the observed bandgap (Figure 9a) [140]. This behavior indicates favorable conditions for bandgap tuning by cationic substitutions. All three compounds have suitable CB/VB positions to be incorporated into the solar cells with typical ETL/HTL (Figure 9b) showing a PCE of 0.2% for $MAGeI_3$-based cells (Table 1).

A DFT study of $CsGeI_3$ HP showed that the iodide vacancy in this material can serve as a deep hole trap, in contrast to the corresponding Pb- and Sn-based HPs resulting in a reduction of the V_{oc} [141]. These results indicate that efforts should be applied for the synthesis of stoichiometric $CsGeI_3$ materials as well as on the development of post-synthesis HI treatment of iodide-deficient $CsGeI_3$ absorber layers.

Theoretical studies also showed a high susceptibility of the electron properties of $MAGeI_3$ perovskite to the strain. Application of a compressive or dilating stress is expected to switch the HP conductivity from p- to n-type and vary the bandgap within a range of 1.35–2.50 eV [142].

Typically, Ge HPs are prone to hydrolytic decomposition when coming in contact with a humid environment [144]. Possible mechanisms and pathways of the hydrolytic degradation of $MAGeI_3$ HP as a function of the crystal face were examined in detail in [145]. The stability of Ge-based HPs can be enhanced in mixed-halide HPs as well as by hydrophobic cations. In particular, by introducing cations that are more bulky than MA^+, such as phenylethylamine (PEA) cation $C_6H_5(CH_2)_2NH_3^+$, a layered structure can be formed with inorganic germanium iodide layers separated by organic PEA layers (Figure 9c) [143]. The $(PEA)_2GeI_4$ HP revealed a direct bandgap of 2.12 eV making it suitable for tandem solar cells. This layered perovskite was also found to be much more stable in humid air than $MAGeI_3$ because of its high hydrophobicity of the organic component [143].

The stability of $MAGeI_3$ HP and its performance as a light harvester of solar cells can also be enhanced by introducing bromide additives. By substituting 10% I^- with Br^- a PCE of 0.57% was achieved (Table 1) in an inverted cell with a fullerene ETL [144].

The combination of Sn^{2+} and Ge^{2+} in single HPs results in solid-solution $CH_3NH_3Sn_{(1-x)}Ge_xI_3$ compounds with a bandgap tunable from 1.3 eV (x = 0) to 2.0 eV (x = 1) [146].
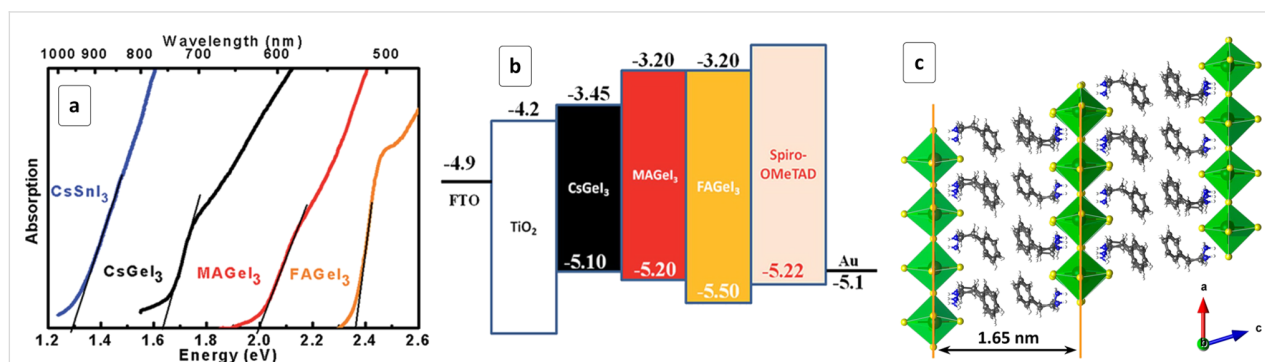
Figure 9: (a) Absorption spectra of $AGeI_3$ HPs with different cations; (b) energy level alignment in solar cells with $AGeI_3$ HPs; (c) structure of layered $(PEA)_2GeI_4$ HP. (a,b) Reprinted with permission from [140], copyright 2015 The Royal Society of Chemistry; (c) Reprinted with permission from [143], copyright 2017 American Chemical Society.

A Mn^{2+}-based analog of MAPI was produced by the spin-coating of a mixture of MnI$_2$ and MAI on mesoporous titania scaffolds [147]. After covering with a Spiro-MeOTAD HTL, the MAMnI$_3$-based device showed a response to the visible light illumination that was stable for at least 2000 s in an on/off cycling test [147]. A similar response to the UV light was observed for MA$_2$MnCl$_4$ perovskite incorporated into an FTO/TiO$_2$/HP/carbon device [148].

One of the first Cu^{2+}-based HPs (C$_4$H$_9$NH$_3$)$_2$CuCl$_4$ was synthesized as early as in 2005 by reacting buthylamine hydrochloride with CuCl$_2$ [149]. However, the potential of the hybrid perovskites was not yet realized at that time and this material was not tested as a potential light harvester.

A highly stable C$_6$H$_4$NH$_2$CuBr$_2$I compound was synthesized by reacting 2-iodaniline with CuBr$_2$ [150]. It displayed extraordinary hydrophobicity and retained stability even after a 4 h immersion in water. This stability is coupled with a high sensitivity to visible light and a bandgap of 1.64 eV. A solar cell trial of this material showed a PCE of ≈0.5% [150] indicating plenty of room for further studies. A two-dimensional layered (C$_6$H$_5$CH$_2$NH$_3$)$_2$CuBr$_4$ perovskite (E_g = 1.81 eV) demonstrated a high stability and the feasibility for future photovoltaic applications [151].

Recently, the first example of layered 2D copper-based (CH$_3$NH$_3$)$_2$CuCl$_x$Br$_{4-x}$ HPs has been reported [152] thereby demonstrating the appealing potential of such compounds for photovoltaic applications. The perovskite with x = 4 was studied

in detail and found to be formed by single layers of CuCl$_4$Br$_2$ octahedra separated by cation-filled galleries with a size of ≈1 nm (Figure 10a). The materials are characterized by strong absorbance below 650 nm with absorption coefficients of ≈10^5 cm^{-1} and a composition-dependent bandgap ranging from 2.48 eV for MA$_2$CuCl$_4$ to 1.80 eV for MA$_2$CuCl$_{0.5}$Br$_{3.5}$ [152] (Figure 10b) and resulting in a gamut of HP colors from yellow to dark brown (Figure 10c).

Sb- and Bi-based hybrid perovskites

In contrast to Sn^{2+}-based HPs that are prone to oxidation and hydrolysis, Bi- and Sb-based perovskites reveal a reasonable chemical/photochemical stability, retaining composition and structure in prolonged tests even without additional encapsulation. In the case of antimony, stable compounds of MA$_3$Sb$_2$I$_9$ [90,153], MASbSI$_2$ [87], and Cs$_3$Sb$_2$I$_9$ [88-90,154] were reported, while for bismuth, a larger array of compositions was studied, including MA$_3$Bi$_2$I$_9$ (MABI) [84,85,155-163], Cs$_3$Bi$_2$X$_9$ [164,165], and MA$_2$KBiCl$_6$ [166]. The reported bandgaps of selected Bi- and Sb-based HPs are collected in Table 3.

Bi-based HPs

The MABI perovskite is composed of Bi$_2$I$_9$ bi-octahedral units with two bismuth ions in the center of an octahedra connected via three iodine atoms. MABI shows two distinct electron transitions near the absorption band edge – an indirect transition with E_g^i = 1.99 eV and a direct one with E_g^d = 2.15 eV [155]. Both transitions contribute to the light-harvesting by the Bi-based HPs as indicated by detailed PL studies on lumines-
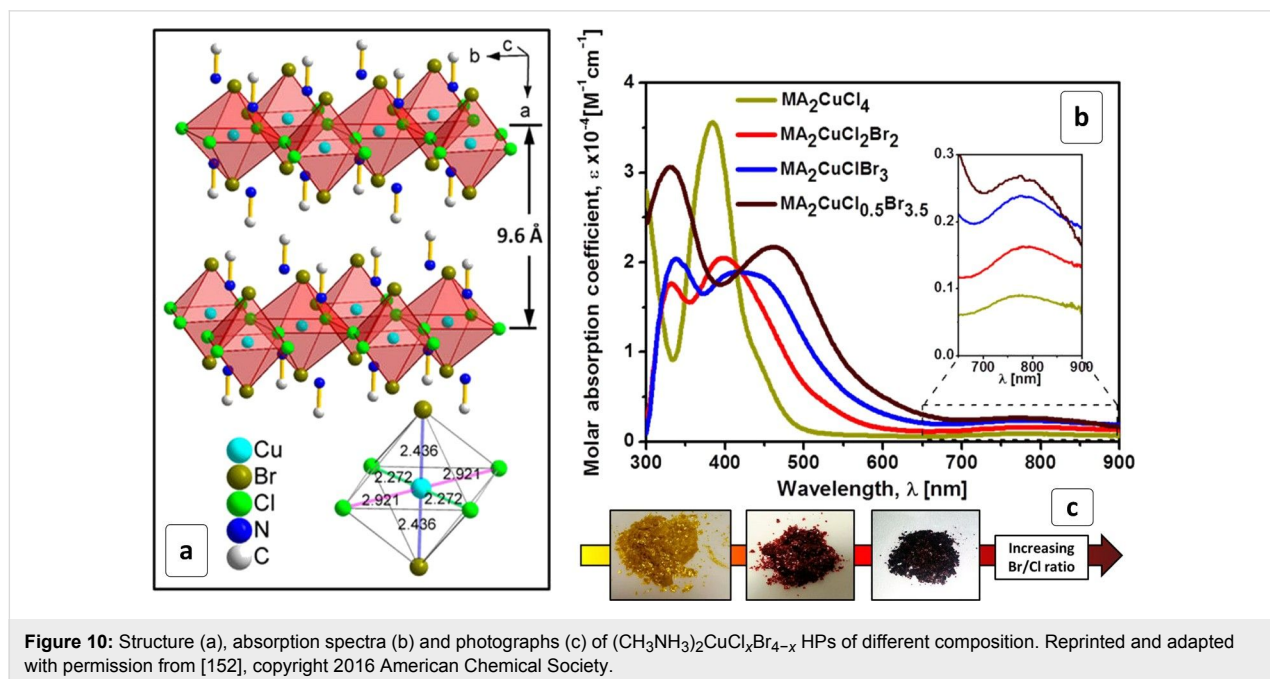
Figure 10: Structure (a), absorption spectra (b) and photographs (c) of (CH$_3$NH$_3$)$_2$CuCl$_x$Br$_{4-x}$ HPs of different composition. Reprinted and adapted with permission from [152], copyright 2016 American Chemical Society.

Table 3: Bandgap and approximate absorption band edge position (λ_e) of selected Bi- and Sb-based hybrid perovskites.

Perovskite	E_g, eV	λ_e, nm	Ref.
$MA_3Bi_2I_9$	1.99	630	[155]
	2.11	590	[85]
	2.17	570	[86]
	2.40	520	[161]
$(MA_2)KBiCl_6$	3.04	410	[166]
$MA_3Sb_2I_9$	1.80	690	[154]
	1.95	640	[90]
	2.14	580	[153]
$MA_3Sb_2I_8Cl$	1.90	650	[154]
$MA_3Sb_2I_7Cl_2$	2.00	620	[154]
$MASbSI_2$	2.03	610	[87]
$Cs_3Sb_2I_9$	2.00	620	[90]
	2.05	600	[88]
$Rb_3Sb_2I_9$	1.98	630	[91]

cent $Cs_3Bi_2X_9$ NCs [159]. A study of single-crystal and polycrystalline MABI showed that both materials have a long exciton lifetime and a high carrier mobility [161,163].
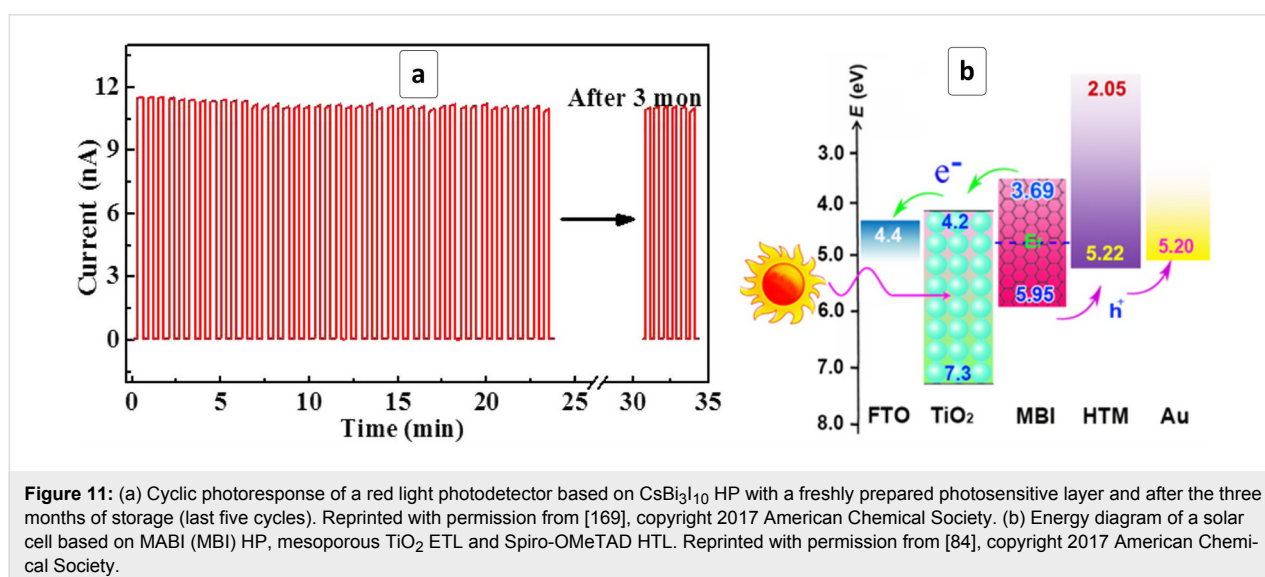
A transient absorption study of MABI crystals showed only a minor change of the exciton dynamics when the crystal size was reduced from micrometers to a few hundred nanometers [167]. A combination of MABI with a TiO_2 scaffold resulted in a depopulation of bound excitons and electron transfer to the titania. These observations indicate that, in contrast to Pb-based HPs, for MABI, a bulk-heterojunction solar cell architecture is preferable to sub-micrometer HP domains.

Typically, the MABI-based solar cells demonstrate a high resistivity to air oxidation and ambient humidity [85,155-157,160,168]. Similar high stability to the degradation under

ambient atmosphere was reported for highly luminescent $Cs_3Bi_2X_9$ (X = Cl, Br, I) crystals emitting in a broad range from ≈390 to ≈550 nm depending on the composition of the halide component [164]. It is assumed that the moisture stability of the perovskites can originate from inherent self-passivation with a surface BiOX layer [164]. The water vapors were found to passivate the surface of $Cs_3Bi_2X_9$ NCs resulting in a drastic PL enhancement [165]. The water was found to act similar to the addition of the surfactant oleic acid, confirming the assumption of the moisture-induced passivation of the surface trap states and providing the nanocrystalline $Cs_3Bi_2X_9$ luminophores with prolonged stability [165]. Along with the chemical and photochemical stability, MABI retains perfect integrity during charging/discharging events. In particular, a MABI-based electrochemical capacitor retains around 85% of its initial maximal capacitance after more than ten thousand charge/discharge cycles [158].

A cell comprised on a MABI layer sandwiched between an FTO/TiO_2 scaffold and a Spiro-MeOTAD/Au layer showed a PCE of 0.164% and very good stability of photovoltaic parameters even when stored in the open humid air [157]. The cell also showed almost no hysteresis over a broad range of scan rates (150–1500 mV/s). A hysteresis-free cell was also constructed by combining the single-crystalline MABI with a P3HT HTL [85].

A layer of $CsBi_3I_{10}$ perovskite deposited by a conventional spin-coating/drying method on top of gold electrodes demonstrated a high photoresponse in the range of λ < 700 nm [169]. The photodetector is characterized by an on/off ratio as high as ≈10^5 and a prolonged stability retaining the unvaried response after a shelf-storage for at least three months (Figure 11a).

Figure 11: (a) Cyclic photoresponse of a red light photodetector based on $CsBi_3I_{10}$ HP with a freshly prepared photosensitive layer and after the three months of storage (last five cycles). Reprinted with permission from [169], copyright 2017 American Chemical Society. (b) Energy diagram of a solar cell based on MABI (MBI) HP, mesoporous TiO_2 ETL and Spiro-OMeTAD HTL. Reprinted with permission from [84], copyright 2017 American Chemical Society.

The efficiency of solar cells based on $Cs_3Bi_2I_9$ HP nanosheets was found to depend on the composition of the HTL layer. The best PCE of 3.2% was observed for copper(I) iodide HTLs, a value claimed to be the highest achieved to date for the Bi-based HP family [170].

The morphology of MABI layers produced on titania scaffolds by a simple spin-coating of a BiI_3+MAI mixture followed by a heat treatment was found to depend on the morphology of the scaffold, varying from island-like for the compact TiO_2 layers to a more homogeneous MABI deposit on the mesoporous TiO_2 [157].

The TiO_2/MABI composites can be produced by a double-step interdiffusion method including sequential deposition of BiI_3 and CH_3NH_3I layers followed by annealing at 100 °C [162]. The last step yields a much more uniform and homogeneous MABI layer than conventional single-step spin-coating/annealing resulting in almost doubled PCE.

Highly compact and pin-hole-free MABI films can be produced by a two-step process including the high-vacuum deposition of BiI_3 followed by the conversion of bismuth triiodide into MABI [84]. The high quality of the HP layer resulted in a record PCE of 1.54% in a cell with a titania ETL and a Spiro-MeOTAD HTL (Table 1). The cell configuration allows for an efficient electron transfer from MABI to the TiO_2 scaffold while the holes are withdrawn to the Spiro-MeOTAD HTL and then – into the gold back contact (Figure 11b). The charge separation efficiency is evidenced by a relatively high FF of almost 80%, while a high V_{oc} of 0.83 V observed for such cells attests to the structural perfection of the light-absorbing HP layer [84].

A similar V_{oc} (0.895 V) was reported for a MABI-based cell produced without HTLs with a single carbon back contact [86]. In this case, a top light conversion efficiency was only 0.054% (Table 1), indicating the crucial role of the hole transfer dynamics for the total cell performance.

The efficiency of MABI-based cells with the solution-processed HP layers is also limited by a rough interface between MABI and typical ETL/HTL materials. The interface quality can be increased by controlling the rate of MABI crystallization, in particular, by introducing additions of *N*-methylpyrrolidone (NMP) to DMF which is typically used as a solvent for the spin-coating deposition of MABI layers [160]. NMP slows the HP crystallization favoring the formation of a more uniform MABI layer and providing a ≈50% enhancement of the photocurrent generation efficiency. Simultaneously, the optimized morphology shows an enhanced stability, the cells retaining their charac-

teristics after 30 days of exposure to ambient conditions (relative humidity of 50–60%) [160].

The structure and characteristics of $(MA)_2KBiCl_6$ perovskite [166] are very similar to $MAPbCl_3$, however, the high bandgap of this material (3.04 eV) is more suitable for UV photodetectors than for the photovoltaic applications.

The organo–inorganic iodobismuthates $C_5H_6NBiI_4$, $C_6H_8NBiI_4$ and $(C_6H_{13}N)_2BiI_5$ displayed bandgaps of around 2 eV and stability under the ambient conditions [171,172]. Aromatic cations were found to contribute to the conduction band of these compounds, facilitating the transport of charge carriers. As a result, mesoscopic solar cells based on such iodobismuthates showed a PCE of ≈1% even without additional HTLs [171].

Sb-based hybrid perovskites

Antimony-based $MA_3Sb_2I_9$ and $Cs_3Sb_2I_9$ perovskites displayed bandgaps of 1.95 eV and 2 eV, respectively, and CB/VB positions suitable for most of ETL/HTL combinations (Figure 2d) [90]. Amorphous $MA_3Sb_2I_9$ films were reported to have a bandgap of 2.14 eV and relatively high absorption coefficients of an order of 10^5 cm^{-1} [153]. The films also demonstrated considerable sub-bandgap absorption with a characteristic Urbach energy of ≈60 meV, indicating a substantial level of structural and energetic disorder. Due to the disorder, planar inverted solar cells based on amorphous $MA_3Sb_2I_9$ showed low photocurrent densities, however, with a relatively high open-circuit voltage (≈890 meV) and a decent fill factor (55%) [153], indicating the good potential of this light absorber for further studies and improvements. In particular, a careful control of the $MA_3Sb_2I_9$ stoichiometry and introduction of HI additives during the film formation as well as an additional fullerene ETL into the solar cell configuration allowed for a PCE beyond 2% [90].

$Cs_3Sb_2I_9$ HP has a bandgap of ≈2 eV and an intrinsic weak p-type conductivity [88,90]. The energies of lowest direct (E_g^d) and indirect (E_g^i) electron transitions differ only by ≈0.02 eV and both transitions are characterized by absorption coefficients similar to those of MAPI [88].

$Cs_3Sb_2I_9$ can exist as two polymorphs – a layered (2D) modification built by two-dimensional layers of polyanions and a "dimer" (0D) form built of isolated dioctahedral $Sb_2I_9^{3-}$ anions [89]. The HP formation can be directed to one of these forms by tailoring the temperature of annealing, the 0D and 2D modifications forming at 150 and 250 °C, respectively. The layered 2D form demonstrated higher electron and hole mobilities and a better tolerance to defects as compared to the dimer-built 0D

polymorph. The 2D-$Cs_3Sb_2I_9$ HP can be formed by annealing the original metal iodide mixture at 250 °C provided that a portion of SbI_3 lost during the heating due to a high SbI_3 vapor pressure at the annealing temperature is compensated [89]. A comparative study of inverted solar cells composed of 2D- and 0D-$Cs_3Sb_2I_9$ (produced at 150 °C), a PEDOT:PSS HTL and a $PC_{70}BM$ ETL resulted in PCEs of 1.5% and 0.89% for 2D- and 0D-form, respectively [89]. This finding, along with a higher stability of 2D-HP-based devices, suggests that the layered form of $Cs_3Sb_2I_9$ is preferable for photovoltaic applications.

The incorporation of other halide ions allows the crystal structure and optoelectronic properties of $MA_3Sb_2I_9$ HP to be altered. In particular, the introduction of chloride results in a transformation of dimer-like $MA_3Sb_2I_9$ built of bi-octahedral Sb_2I_9 units into a layered $MA_3Sb_2Cl_xI_{9-x}$ compound where

antimony iodide octahedra are bound to infinite chains via a shared I^- anion (Figure 12a) [154]. Simultaneously, the bandgap broadens from 1.8 eV ($MA_3Sb_2I_9$) to 2.0 eV for $MA_3Sb_2Cl_2I_7$. Solar cells comprising such 2D $MA_3Sb_2Cl_xI_{9-x}$ HPs displayed PCEs surpassing 2% (Table 1), while the highest PCE reported for "conventional" Sb-based halide HPs is lower than 1% [154]. Similar to the Bi-based HPs, such cells demonstrated good stability in the humid air environment and no hysteresis between *C–V* curves obtained at a direct and reverse potential scans (Figure 12b).

The Sb_2I_9 dimer-based modification of Sb-HPs is typical for the compounds with both bulky organic cations and Cs^+ and forms as a result of steric factors (Figure 13a). As this modification has a relatively low charge transport efficiency, various approaches are developed to forward the HP formation to other
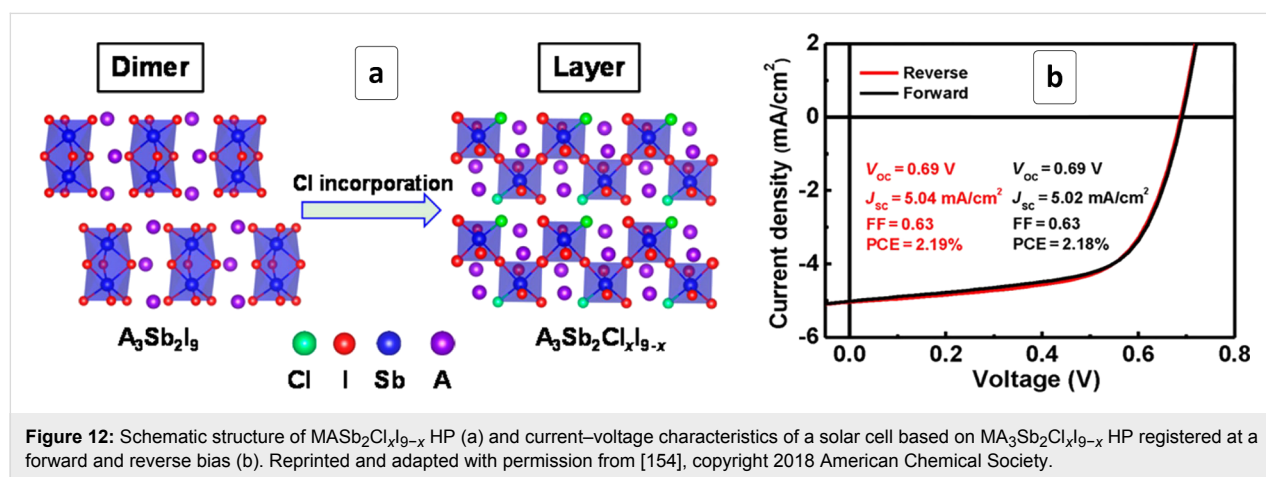
Figure 12: Schematic structure of $MASb_2Cl_xI_{9-x}$ HP (a) and current–voltage characteristics of a solar cell based on $MA_3Sb_2Cl_xI_{9-x}$ HP registered at a forward and reverse bias (b). Reprinted and adapted with permission from [154], copyright 2018 American Chemical Society.
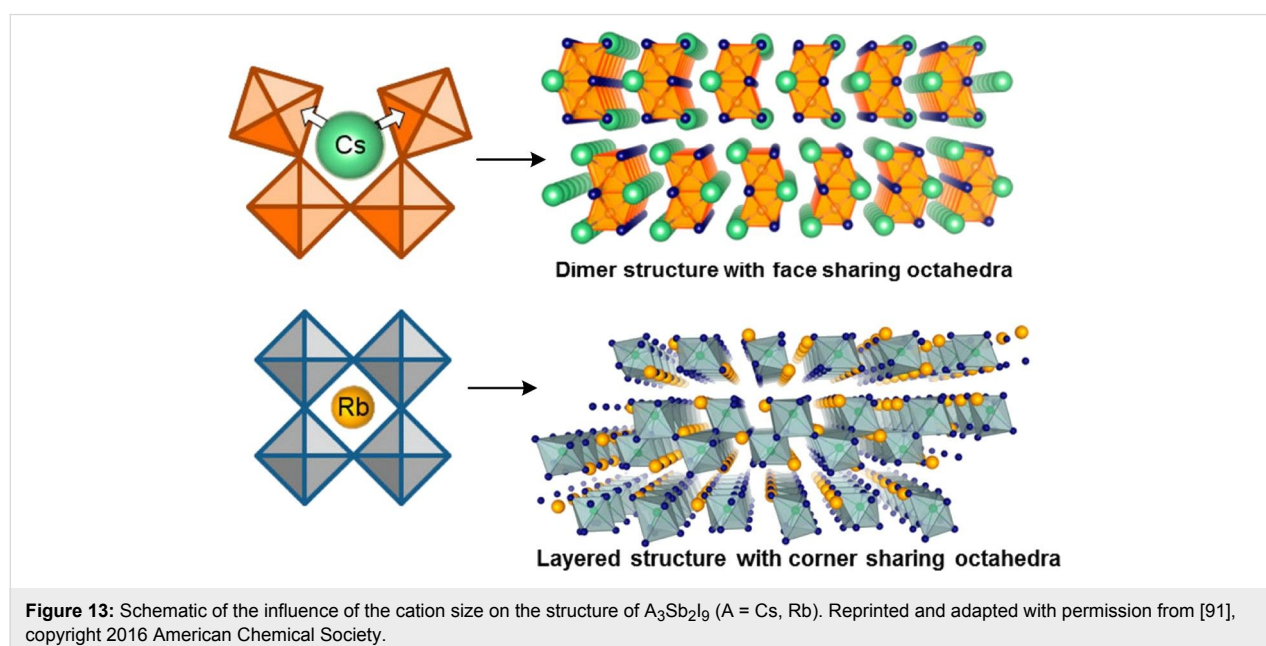
Figure 13: Schematic of the influence of the cation size on the structure of $A_3Sb_2I_9$ (A = Cs, Rb). Reprinted and adapted with permission from [91], copyright 2016 American Chemical Society.

modifications, including the above-discussed introduction of Cl^- ions as well as the replacement of bulky cations with smaller ones, for example, with Rb^+ [91]. The rubidium cations can be accommodated by the layered modification (Figure 13b) and the latter forms irrespective of the HP synthesis method [91]. The $Rb_3Sb_2I_9$ HP is characterized by a bandgap of 1.98 eV and a higher (less negative) CB position as compared to the MA^+ and Cs^+-based counterparts, which is favorable for the electron transfer to typical ETL materials (Figure 2d).

Using a combination of halide and chalcogenide anions for building an organo–inorganic pHP structure potentially allows for the introduction of central metal ions in the oxidation states of +3 and +4. This idea was realized in the case of $MASbSI_2$ HP produced by a sequential stepwise method by reacting Sb_2S_3 with SbI_3 and then with MAI on the surface of a mesoporous TiO_2 scaffold [87]. The $MASbSI_2$ HP displayed a bandgap of 1.62 eV and CB/VB positions suitable for the electron/hole transport to TiO_2 and a variety of HTL materials, respectively (Figure 14a). A $MASbSI_2$-based solar cell demonstrated a PCE of more than 3% (Table 1), in addition to a reasonable stability in a 30-day trial (Figure 14b) and no discernible hysteresis between the forward and reverse C–V scans (Figure 14c) [87].

Recently it was found that organo–inorganic bromoantimonate (N-ethylpyridinium)$_3$SbBr$_6$ forms perovskite-like 3D crystalline framework compounds that have great potential as solar cell absorbers [173]. A solar cell based on the particular (N-ethylpyridinium)$_3$SbBr$_6$ displayed an external quantum efficiency of ≈80% and a PCE of ≈4% thus coming into the same league as lead-halide HPs [173].

A series of (N-methylpyrrolidinium)$_3$Sb$_2$Cl$_{9-9x}$Br$_{9x}$ ($x = 0-1$) HPs was reported to have bandgaps tunable from 2.76 eV ($x = 1$) to 3.31 eV ($x = 0$) and to exhibit photosensitivity levels high enough for the application of such compounds in UV–vis photodetectors [174].

The search for new lead-free HPs based on M^{3+} cations continues on. It often starts from the theoretical estimation of the stability, structure and optoelectronic properties of various HPs and selection of the most promising ones, stimulating further experimental work. For example, a broad theoretical screening of various mono- and bi-metallic lead-free perovskites among more than 480 materials focused on the 10 most promising in terms of the bandgap. Among these, the smallest E_g was found for $Cs_3Ga_2I_9$ ($E_g = 1.72$ eV) [175], which is still to be synthesized and tested in photovoltaic applications.

A series of HPs based on lanthanide cations was modeled and Eu-, Dy-, Tm-, and Yb-based HPs selected as the materials with the most promising bandgaps in the range of 2.0–3.2 eV [176]. It was found that localized f-electrons of lanthanide ions have a strong contribution to the VB top, where a strong influence of the lanthanide ion on the properties of HPs is expected. A combination of a theoretical screening with a following experimental verification recently led to a series of $Cs_2TiI_xBr_{6-x}$ HPs with bandgaps varying from 1.38 eV to 1.78 eV depending on the I/Br ratio [177].

Lead-free hybrid perovskites based on A^+/A^{3+} metal compositions

Ag-Bi, Ag-Sb: A series of stable lead-free bimetallic HPs with a cation pair aliovalent to a pair of Pb^{2+} (Sn^{2+}) ions such as

Figure 14: Energy diagram (a), normalized IPCE tested for a period of 30 days (b) as well as current–voltage characteristics registered at forward and reverse bias (c) of a solar cell based on $MASbSI_2$ HP. The PCPSTBT abbreviation is explained in the notes of Table 1. Reprinted and adapted with permission from [87], copyright 2018 American Chemical Society.
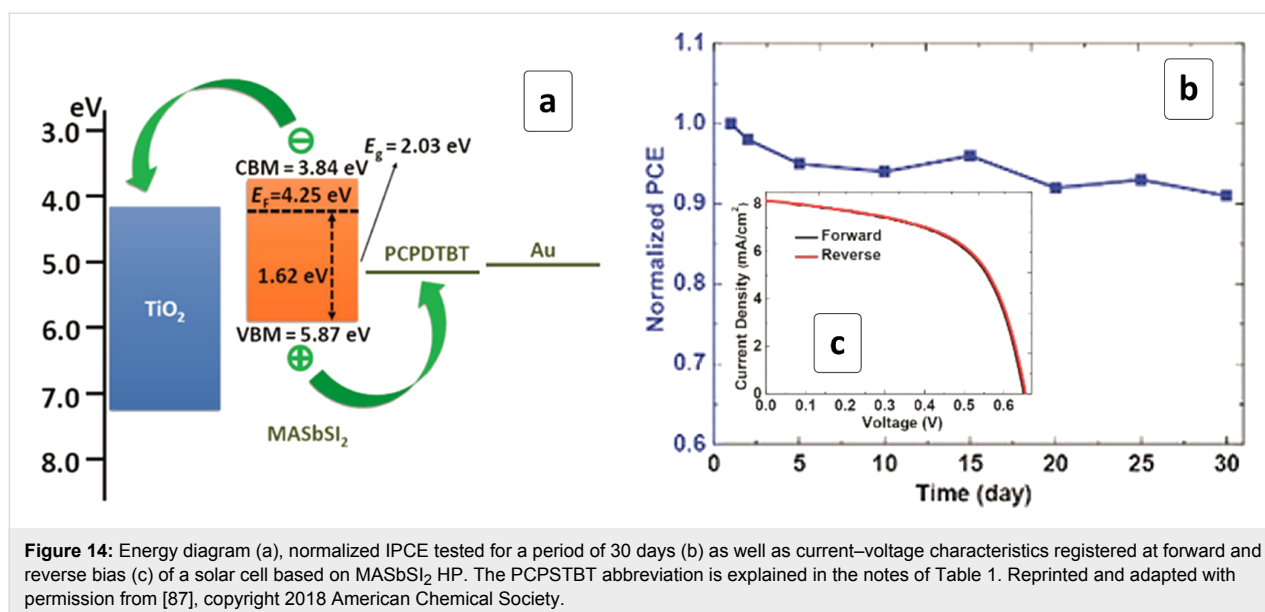
A_2AgBiX_6, A_2AgSbX_6, and A_2AgInX_6 (A = MA or Cs, X = Cl, Br) was reported. The bandgaps of selected A^+/A^{3+}-HPs are presented in Table 4.

Table 4: Bandgap and approximate absorption band edge position (λ_e) of selected A^+/A^{3+}-based HPs.

Perovskite	E_g, eV	λ_e, nm	Ref.
MA_2AgInI_6	1.93	640	[178]
$Cs_2AgInCl_6$	3.2–3.3	380–390	[179]
$Cs_2AgBiCl_6$	2.77	450	[180]
	2.20	560	[181,182]
$Cs_2AgBiBr_6$	1.90–1.95	640–650	[182-184]
	2.19–2.25	550–570	[150,185,186]
$MA_2AgBiBr_6$	2.02	610	[187]
MA_2AgBiI_6	1.96	630	[188]
$Cs_2Au_2I_6$	1.31	950	[189]

$Cs_2AgInCl_6$ HP was produced by a hydrothermal synthesis allowing the size of the final crystallites to be tailored by adjusting the hydrothermal treatment duration [179]. The perovskite crystallizes in the rock-salt structure with alternating $[AgCl_6]$ and $[InCl_6]$ octahedra (Figure 15a) and shows a direct bandgap of 3.23 eV, as well as an excellent stability to the ambient moisture, light, and heat [179].

$Cs_2AgSbCl_6$ HP (Figure 15b) [190] and $Cs_2AgBiCl_6$ HP (Figure 15c) [180,181] are isostructural to $Cs_2AgInCl_6$ and display comparable photochemical, hydrolytic and thermal stability.

Despite a more complex composition as compared with the Pb-based analog, the $Cs_2AgInCl_6$ HP can be prepared with a trap state density of ≈10^9 cm^{-3}, which is much lower than that reported for the best lead halide HPs [191]. Such close-to-ideal materials can be used as light-absorbing bodies of very sensi-

tive, stable and fast UV photodetectors. The doping of $Cs_2AgInCl_6$ HPs with Mn^{2+} imparts this HP with the property of visible-range luminescence [192].

Theoretical studies predicted $Cs_2AgInBr_6$ HP to be thermodynamically stable [193,194], showing a distinct n-type conductivity and shallow trap levels for Ag-rich and Br-poor compositions [194].

MA_2AgSbI_9 HP was found to be a stable compound both by DFT calculations and experimental evidence, showing excellent resistivity to the ambient air/humidity [178]. The material revealed a band gap of 1.93 eV and CB/VB positions (−6.28 eV/−4.35 eV) suitable for most ETL/HTL materials used in the HP solar cells.

The substitution of chloride ions with Br$^-$ in Ag-Bi-based HP results in a shrinking of the bandgap from 2.77 eV to 2.19 eV [180], both values being smaller than E_g of corresponding Pb-based HPs. The electron transitions contributing to the absorption band edge were found to be of an indirect character in accordance with DFT predictions [182,195,196] with the calculated bandgaps of 2.2 eV [181,182] and 1.9 eV [182] for the Cl-based and Br-based HPs, respectively. The calculations also showed that a partial substitution of silver(I) with copper(I) should result in a narrowing of the bandgap to 1.6–1.9 eV, which would not compromise the HP stability [197], but these conclusions are still to be verified experimentally.

A DFT modeling of TiO_2/Cs_2AgBiX_6 (X = Cl, Br) interfaces showed them to be very favorable for the photoinduced charge separation due to an appropriate band alignment and a state density gradient along the interface [198]. The calculations also showed that the bandgap of $Cs_2AgBiBr_6$ HP can be continuously tuned from 1.93 eV down to 0.44 eV by introducing a control lattice disorder the latter value characteristic of completely
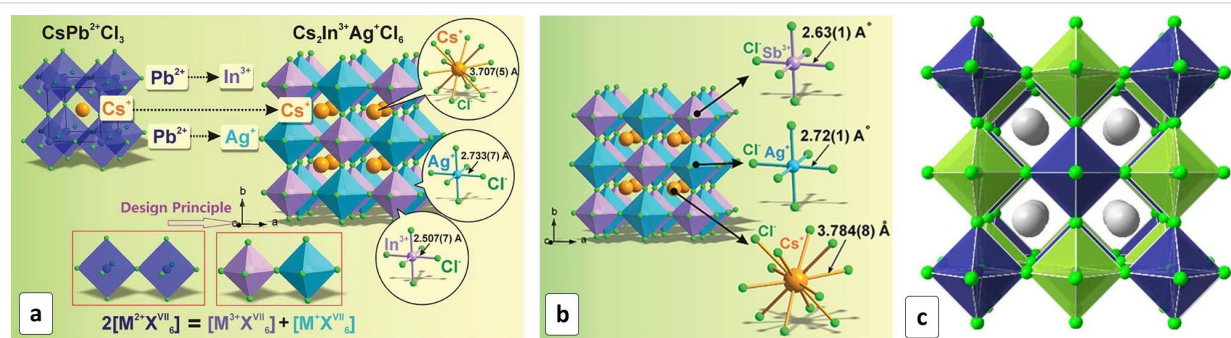
Figure 15: (a) Evolution of the crystal structure from $CsPbCl_3$ to $Cs_2AgInCl_6$ HP; (b) Crystal structure of $Cs_2AgSbCl_6$ HP; (c) Crystal structure of $Cs_2AgBiCl_6$ HP; Cs^+ ions are presented as gray spheres and Cl^- as green spheres, the Ag and Bi centered octahedra are shown as blue and green ones, respectively. (a) Reproduced with permission from [179], copyright 2017 The Royal Society of Chemistry; (b) Reproduced with permission from [190], copyright 2018 The Royal Society of Chemistry; (c) Reprinted with permissions from [180], copyright 2016 American Chemical Society.

disordered alloy [183]. As a practical means to exert such a disordering, the controlled doping of the perovskite was proposed [183]. However, such disordering will inevitably limit the charge transport efficiency and boost the electron–hole recombination and, therefore, a certain equilibrium between the light harvesting capability and the photovoltaic efficiency can be expected in such approach.

The bandgap of $Cs_2AgBiBr_6$ HP was also found to decrease upon application of a high-pressure treatment [185]. Under 15 GPa pressure, the AgBi-based perovskite displays a bandgap of ≈1.7 eV (≈22% lower than at the ambient pressure) close to the E_g of the "classical" MAPI, retaining about 8% residual E_g shrinkage after the pressure is released [185].

The results of the DFT simulations of the electron structure of more than 11,000 various compositions of lead-free HPs were assembled as a material database available for the screening of possible light harvesters of the photovoltaic solar cells [199]. A comprehensive theoretical screening of more than 480 $A_2MM'X_6$, AMX_4, and $A_3M_2X_9$ compounds put the focus on the ten most promising materials with bandgaps between 1.5–2.5 eV [175].

Time-resolved microwave conductance studies of $Cs_2AgBiBr_6$ HP in the form of thin films and crystals revealed the presence of mobile charges with lifetimes on the order of microseconds as well as a low level of trap-state-mediated recombination, which is promising for the photovoltaic applications of this material [200].

Similar to MABI, $Cs_2AgBiBr_6$ perovskite showed a remarkable tolerance to a variation of the grain size and the defect density, maintaining an unchanged PL yield both for the bulk crystal and finely powdered samples [183]. These findings show the feasibility of the design of bulk heterojunction solar cell architectures with nanometer- and micrometer-sized HP domains.

The performance of $Cs_2AgBiBr_6$ HP-based solar cells is typically limited by the low quality of the HP layer, resulting from the poor solubility of the Ag and Bi halide precursors. To address this problem, a variety of solvents and deposition modes were tested and an approach to produce very uniform $Cs_2AgBiBr_6$ films was proposed by exploiting DMSO as a "universal" solvent and a special series of thermal treatments of both the precursor solutions and spin-coated films [186]. The solar cells with the optimized films sandwiched between a TiO_2 ETL and a Spiro-MeOTAD HTL showed a PCE of 2.43% and an open-circuit voltage of almost one volt, which is the highest value currently reported for Bi-based HPs. The devices also

displayed a remarkable stability in working conditions even without additional encapsulation [186].

The superior stability of $Cs_2AgBiBr_6$ HP as compared to MAPI was rationalized by a detailed theoretical structural analysis [201] that showed the framework of the AgBi-HP to be much more rigid with considerably lower thermal expansion coefficients as a result of the presence of relatively stronger Ag–Br and Bi–Br bonds.
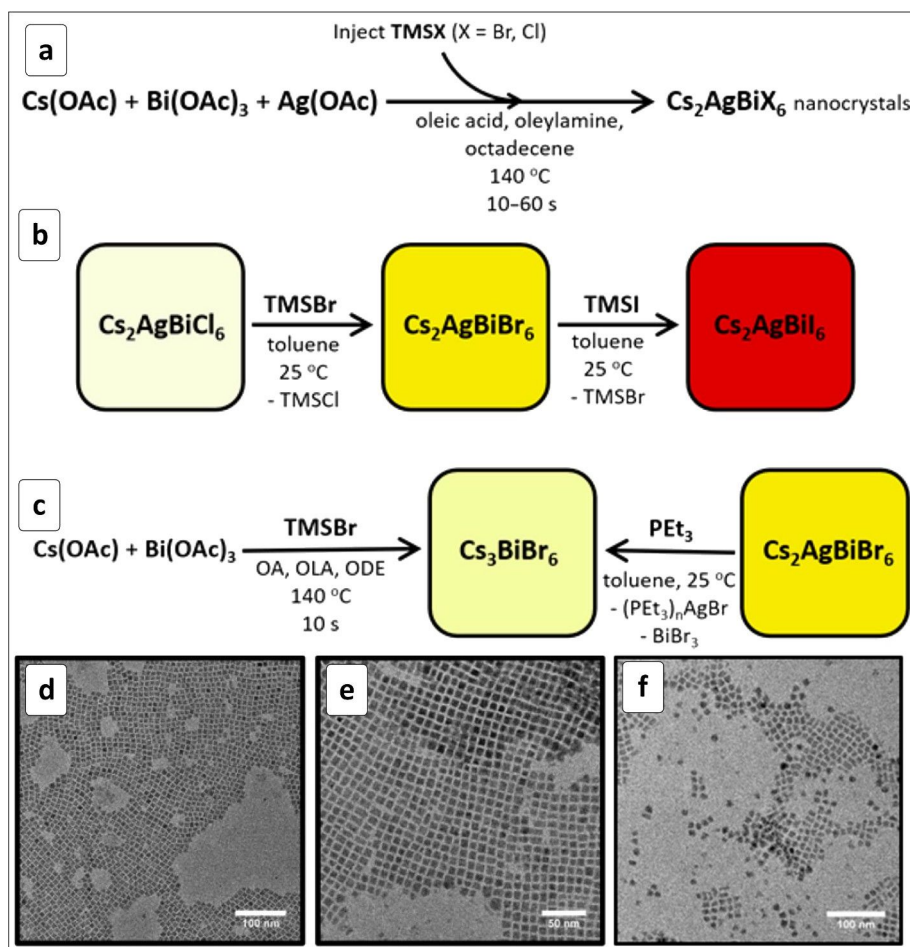
The $Cs_2AgBiCl_6$ and $Cs_2AgBiBr_6$ NCs synthesized by a hot-injection approach (Figure 16a) can be converted to the Cs_2AgBiI_6 phase either by exchanging Cl(Br) with iodide anions (Figure 16b) or by exchanging Cs^+ cations in Cs_3BiBr_6 NCs with Ag^+ (Figure 16c) [202]. The NCs preserve the average size (≈8 nm) and size distribution (Figure 16d–e) during the ion-exchange conversions, showing a good morphology control provided by this method. The indirect band gap of Cs_2AgBiX_6 NCs decreases from ≈2.8 eV for X = Cl to ≈2.2 eV for X = Br to ≈1.75 eV for X = I [202].

Stable $MA_2AgBiBr_6$ HP was produced by a hydrothermal treatment of a mixture of MABr, $BiBr_3$, AgBr, and HBr in water [187]. The formation of the bimetallic HP proceeds, most probably, via a step of the $MA_3Bi_2Br_9$ phase formation, which is present as a residual in the final $MA_2AgBiBr_6$ HP, making this approach similar to the above-discussed ion exchange method. Additionally, the authors note the unsuccessful attempts to apply the hydrothermal method for the synthesis of $(MA)_2AgBiI_6$ and $(FA)_2AgBiBr_6$, the reaction yielding only the monometallic Bi-based phases [187]. The $MA_2AgBiBr_6$ HP revealed an indirect bandgap of ≈2 eV close to the range reported for the Cs-based analog (1.95–2.19 eV) [187].

The lead-free MA_2AgBiI_6 HP was synthesized by a solid-state reaction and revealed an indirect bandgap of 1.96 eV and a high stability to air exposure [188].

A broad theoretical modeling of the structures and properties of $A_2M^+M^{3+}X_6$ HP materials focused on two prospective materials with a direct bandgap of around 1 eV – Cs_2InSbX_6 and Cs_2InBiX_6 [203]. However, experimental attempts to exchange Ag^+ to In^+ in $Cs_2AgBiBr_6$ HP were unsuccessful due to the ready oxidation of In^+ to In^{3+} [204]. At the same time, theoretical calculations [204] predicted that introduction of bulky MA or FA cations will stabilize In^+, providing the compound with the optoelectronic properties close to those of MAPI and, therefore, a further pursuit in this direction may be fruitful. DFT calculations also indicated that $MATl_{0.5}Bi_{0.5}I_3$ may be a potential candidate for a solar cell absorber with properties similar to those of MAPI [205].

Figure 16: Scheme of the synthesis of Cs_2AgBiX_6 NCs (a–c) and TEM images of $Cs_2AgBiCl_6$ (d), $Cs_2AgBiBr_6$ (e), and Cs_2AgBiI_6 NCs (f). OAc is acetate anion, Et – ethyl, OA – oleic acid, OLA – oleylamine, ODE – octadecene, TMS – trimethylsilyl. Reprinted and adapted with permission from [202], copyright 2018 American Chemical Society.

Recently, a new $Cs_2Au_2I_6$ HP was reported to have crystallized in a distorted tetragonal mix-valence Au^+/Au^{3+} perovskite structure with a "close-to-ideal" bandgap of 1.31 eV [189]. Preliminary tests showed high promise of this material for thin-film photovoltaics.

Conclusion and outlook

The present review shows that lead-free hybrid perovskites combine the many possibilities in composition with environmentally benign constituents, in addition to being relatively robust against the influence of light, air and moisture, and can be synthesized in a variety of possible morphologies (0D, 1D, 2D, etc.). The progress in this area is evident with the highest PCEs achieved to date already comparable and competitive with the efficiency of "conventional" lead-based perovskites. This progress is even more pronounced on the background of a saturation of the studies of Pb HPs and the light conversion efficiency achieved. The lead-free HP-based solar cells could soon become competitive to their Pb-based analogs in the near future because even with an inferior PCE, lead-free HPs are not acutely toxic and do not pose the severe concerns of possible environmental damage and the post-utilization recycling problems that Pb-based HPs do.

To increase the competitiveness of lead-free HP-based solar cells, several vital issues should be addressed. Among them – an inferior efficiency of charge transport, high recombination losses, and a limited spectral sensitivity range that is typical for such materials. The most promising avenues for addressing the charge separation/transport issues seem to be in an adapted morphological design of lead-free HPs, in particular, by implementing nanodimensional and layered architectures. The limitations in spectral sensitivity can be solved by designing composite light-harvesting systems with other semiconductors, such as narrow-bandgap Cd- and Pb-free binary and multinary metal chalcogenides.

In contrast to Pb-based HPs, the lead-free analogs typically display a relatively short-range free charge migration distance on the order of several tens of nanometers. In this view, a decrease of the HP crystal size to 10–100 nm should not fundamentally affect the charge transport properties but might open broad possibilities of increasing the efficiency of interfacial electron transfer and allow the construction of "ideal" bulk heterojunctions with ETL and HTL materials by intermixing nanometer-sized particles of components. In this view, the lead-free HPs can potentially be utilized in the nano-dispersed form, differing drastically from Pb-HPs where a larger HP grain size and a smaller grain boundary typically mean a higher light conversion efficiency.

The utilization of nanometer building blocks for the design of lead-free HP-based solar cells requires reliable synthetic methods allowing for a precise control over the HP morphology. In this area, conventional synthetic strategies are typically used, and the HP NCs are grown in high-boiling-point solvents in the presence of surface-passivating ligands. These approaches seem to be quite appropriate for the synthesis of highly luminescent perovskites. However, for photovoltaic applications, new methods are needed to produce NCs with a free surface or containing only small passivating ligands as well as to form various composites; in particular, HP NCs supported on mesoporous metal oxide scaffolds. In this view, of particular significance are methods based on the formation of metal NCs as precursors for development of perovskite NCs. The metal NCs can be deposited by a variety of methods, but only the evaporative deposition of Pb and Sn NCs followed by their transformation into corresponding HPs has been probed (recently by Hodes et al. [136]). The transformation of metal NCs into perovskites was found to yield light absorbers of a higher quality and allowed for better morphology control as compared to the conventional spin/cast dropping deposition. At the same time, this method excludes toxic (Pb) or unstable (Sn) precursors. This strategy may be considered as very promising because metal NCs can be deposited by a variety of methods (electrochemical/electrocatalytic deposition, photochemical/ photocatalytic deposition, thermal evaporation, "seed" growth on pre-deposited nuclei, etc.). This could allow for a precise method of control over the metal NC size that is suitable both for single metals (Sn, Sb, Bi, etc.) and for bimetallic alloys (Ag–Bi, Ag–Sb, Ag–In, etc.) that can then be converted into a plethora of hybrid perovskites. The feasibility of the exact translation of the morphology of primary metal NCs into the morphology of the final HPs still remains to be explored.

Layered 1D and 2D HP materials show great promise due to a strong anisotropy of electron properties, facilitating the charge separation and transport, as well as the unique morphological variability [57,58,64]. The latter can be achieved both by introducing various interlayer additives and by varying the thickness and composition of the layers themselves. For example, a strong effect on the light absorption, electron mobility, and internal electric field was predicted for ultra-thin $CsSnI_3$ HP with the layer number as small as 1–3 [206]. The thickness dependence seems to resemble that of layered metal dichalcogenides, MoS_2 and WS_2, where single and few-layer materials differ drastically from corresponding bulk semiconductors. We may expect similar effects arising for layered lead-free HPs, potentially contributing to new designs of solar cells and enhanced light conversion efficiencies [14,207].

Simultaneously, the formation of interlayer voids or intermediate layers of other semiconductors/dielectrics may result in a regular quantum-well structure that is strongly beneficial for the photoinduced charge separation between the separated HP sheets [207,208]. Finally, a combination of single layers of two and more different lead-free HPs into a composite material may offer unprecedented variability of optical properties and band design. The feasibility of such an approach was probed by DFT calculations for $Cs_{3+n}M_nSb_2X_{9+3n}$ (M = Sn, Ge) compounds formed by inserting variable $[SnI_6]$ or $[GeI_6]$ octahedral layers into the $[Sb_2I_9]$ bilayers. It was found, in particular, that adjusting the thickness of the inserted octahedral layers is an effective approach to tune the bandgap and effective mass of the charge carriers over a broad range [209].

Except for Sn-based HPs, the lead-free perovskites typically have larger bandgaps than "conventional" Pb-based compounds and, therefore, a limited spectral sensitivity range. This limitation can be avoided by designing tandem solar cells, for example with silicon or kesterite $Cu_2ZnSn(S,Se)_4$ absorbers. The feasibility of such an approach was demonstrated in 2014 by Todorov et al. who reported a relatively simple tandem solar cell based on a planar heterojunction between microcrystalline layers of kesterite and MAPI that displayed an unprecedented high V_{oc} of 1350 mV and a PCE exceeding 20% [210].

Alternatively, the lead-free HPs can be directly coupled with broadband-absorbing inorganic NCs to give a double benefit of extended spectral sensitivity range and a possibility of the photoinduced electron/hole separation between HP and inorganic NCs. Such systems have recently emerged as a new research hotspot, the attention focused mainly on combinations of PbS or PbSe NCs with Pb-based perovskites. In particular, PbS NCs introduced into MAPI-based solar cells were found to act simultaneously as a co-absorber and an HTL, rendering the use of additional organic hole transporting materials superfluous [211,212]. A shell of MAPI on the surface of PbS NCs was found to act as an efficient electron acceptor and a passivating

agent, minimizing the recombinational losses in lead sulfide NCs [213,214].

To date, no reports can be found on analogous systems comprising lead-free HPs and cadmium- and lead-free semiconductors, such as CuInS(Se)$_2$ or Cu$_2$ZnSnS(Se)$_4$, where both an "ideal" spectral sensitivity range and an efficient charge carrier separation between n-conducting HPs and p-conducting metal chalcogenides can be simultaneously achieved. This venue seems to be especially promising in view of recent developments in the synthetic approaches to both multinary metal chalcogenide NCs and lead-free HP NCs with highly controlled composition and morphology. We may expect that the combination of nanometer building blocks of inorganic semiconductors and hybrid perovskites will allow for the construction of "green" and efficient bulk-heterojunction configurations with a panchromatic spectral response and competitive light conversion efficiencies.

Acknowledgements

ORCID® iDs

Oleksandr Stroyuk - https://orcid.org/0000-0001-5054-2746

References

1. Green, M. A.; Hishikawa, Y.; Warta, W.; Dunlop, E. D.; Levi, D. H.; Hohl-Ebinger, J.; Ho-Baillie, A. W. H. *Prog. Photovoltaics* **2017,** *25,* 668–676. doi:10.1002/pip.2909

2. Hagfeldt, A.; Boschloo, G.; Sun, L.; Kloo, L.; Pettersson, H. *Chem. Rev.* **2010,** *110,* 6595–6663. doi:10.1021/cr900356p

3. Sandroni, M.; Wegner, K. D.; Aldakov, D.; Reiss, P. *ACS Energy Lett.* **2017,** *2,* 1076–1088. doi:10.1021/acsenergylett.7b00003

4. Reiss, P.; Carrière, M.; Lincheneau, C.; Vaure, L.; Tamang, S. *Chem. Rev.* **2016,** *116,* 10731–10819. doi:10.1021/acs.chemrev.6b00116

5. Wang, W.; Feng, W.; Du, J.; Xue, W.; Zhang, L.; Zhao, L.; Li, Y.; Zhong, X. *Adv. Mater.* **2018,** *30,* 1705746. doi:10.1002/adma.201705746

6. Kazim, S.; Nazeeruddin, M. K.; Grätzel, M.; Ahmad, S. *Angew. Chem., Int. Ed.* **2014,** *53,* 2812–2824. doi:10.1002/anie.201308719

7. Wang, B.; Xiao, X.; Chen, T. *Nanoscale* **2014,** *6,* 12287–12297. doi:10.1039/c4nr04144e

8. Gamliel, S.; Etgar, L. *RSC Adv.* **2014,** *4,* 29012–29021. doi:10.1039/c4ra03981e

9. Giorgi, G.; Yamashita, K. *J. Mater. Chem. A* **2015,** *3,* 8981–8991. doi:10.1039/c4ta05046k

10. Jung, H. S.; Park, N.-G. *Small* **2015,** *11,* 10–25. doi:10.1002/smll.201402767

11. Liu, X.; Zhao, W.; Cui, H.; Xie, Y.; Wang, Y.; Xu, T.; Huang, F. *Inorg. Chem. Front.* **2015,** *2,* 315–335. doi:10.1039/c4qi00163j

12. Luo, S.; Daoud, W. A. *J. Mater. Chem. A* **2015,** *3,* 8992–9010. doi:10.1039/c4ta04953e

13. Zuo, C.; Bolink, H. J.; Han, H.; Huang, J.; Cahen, D.; Ding, L. *Adv. Sci.* **2016,** *3,* 1500324. doi:10.1002/advs.201500324

14. Pedesseau, L.; Sapori, D.; Traore, B.; Robles, R.; Fang, H.-H.; Loi, M. A.; Tsai, H.; Nie, W.; Blancon, J.-C.; Neukirch, A.; Tretiak, S.; Mohite, A. D.; Katan, C.; Even, J.; Kepenekian, M. *ACS Nano* **2016,** *10,* 9776–9786. doi:10.1021/acsnano.6b05944

15. bin Mohd Yusoff, A. R.; Nazeeruddin, M. K. *J. Phys. Chem. Lett.* **2016,** *7,* 851–866. doi:10.1021/acs.jpclett.5b02893

16. Saparov, B.; Mitzi, D. B. *Chem. Rev.* **2016,** *116,* 4558–4596. doi:10.1021/acs.chemrev.5b00715

17. Polman, A.; Knight, M.; Garnett, E. C.; Ehrler, B.; Sinke, W. C. *Science* **2016,** *352,* aad4424. doi:10.1126/science.aad4424

18. Correa-Baena, J.-P.; Abate, A.; Saliba, M.; Tress, W.; Jesper Jacobsson, T.; Grätzel, M.; Hagfeldt, A. *Energy Environ. Sci.* **2017,** *10,* 710–727. doi:10.1039/c6ee03397k

19. Bhatt, M. D.; Lee, J. S. *New J. Chem.* **2017,** *41,* 10508–10527. doi:10.1039/c7nj02691a

20. Niu, G.; Guo, X.; Wang, L. *J. Mater. Chem. A* **2015,** *3,* 8970–8980. doi:10.1039/C4TA04994B

21. Ono, L. K.; Juarez-Perez, E. J.; Qi, Y. *ACS Appl. Mater. Interfaces* **2017,** *9,* 30197–30246. doi:10.1021/acsami.7b06001

22. Calvo, M. E. *J. Mater. Chem. A* **2017,** *5,* 20561–20578. doi:10.1039/c7ta05666d

23. Yang, S.; Fu, W.; Zhang, Z.; Chen, H.; Li, C.-Z. *J. Mater. Chem. A* **2017,** *5,* 11462–11482. doi:10.1039/c7ta00366h

24. Dou, L. *J. Mater. Chem. C* **2017,** *5,* 11165–11173. doi:10.1039/c7tc02863f

25. Matthews, P. D.; Lewis, D. J.; O'Brien, P. *J. Mater. Chem. A* **2017,** *5,* 17135–17150. doi:10.1039/c7ta04544a

26. Assadi, M. K.; Bakhoda, S.; Saidur, R.; Hanaei, H. *Renewable Sustainable Energy Rev.* **2018,** *81,* 2812–2822. doi:10.1016/j.rser.2017.06.088

27. Dubey, A.; Adhikari, N.; Mabrouk, S.; Wu, F.; Chen, K.; Yang, S.; Qiao, Q. *J. Mater. Chem. A* **2018,** *6,* 2406–2431. doi:10.1039/c7ta08277k

28. Kostopoulou, A.; Kymakis, E.; Stratakis, E. *J. Mater. Chem. A* **2018,** *6,* 9765–9798. doi:10.1039/c8ta01964a

29. Ansari, M. I. H.; Qurashi, A.; Nazeeruddin, M. K. *J. Photochem. Photobiol., C* **2018,** *35,* 1–24. doi:10.1016/j.jphotochemrev.2017.11.002

30. Nakazaki, J.; Segawa, H. *J. Photochem. Photobiol., C* **2018,** *35,* 74–107. doi:10.1016/j.jphotochemrev.2018.02.002

31. Kim, B. J.; Lee, S.; Jung, H. S. *J. Mater. Chem. A* **2018,** *6,* 12215–12236. doi:10.1039/C8TA02159G

32. Sum, T. C.; Mathews, N. *Energy Environ. Sci.* **2014,** *7,* 2518–2534. doi:10.1039/c4ee00673a

33. Hsiao, Y.-C.; Wu, T.; Li, M.; Liu, Q.; Qin, W.; Hu, B. *J. Mater. Chem. A* **2015,** *3,* 15372–15385. doi:10.1039/c5ta01376c

34. Shi, J.; Xu, X.; Li, D.; Meng, Q. *Small* **2015,** *11,* 2472–2486. doi:10.1002/smll.201403534

35. Zhao, Y.; Zhu, K. *Chem. Soc. Rev.* **2016,** *45,* 655–689. doi:10.1039/c4cs00458b

36. Berhe, T. A.; Su, W.-N.; Chen, C.-H.; Pan, C.-J.; Cheng, J.-H.; Chen, H.-M.; Tsai, M.-C.; Chen, L.-Y.; Dubale, A. A.; Hwang, B.-J. *Energy Environ. Sci.* **2016,** *9,* 323–356. doi:10.1039/c5ee02733k

37. Saba, M.; Quochi, F.; Mura, A.; Bongiovanni, G. *Acc. Chem. Res.* **2016,** *49,* 166–173. doi:10.1021/acs.accounts.5b00445

38. Johnston, M. B.; Herz, L. M. *Acc. Chem. Res.* **2016,** *49,* 146–154. doi:10.1021/acs.accounts.5b00411

39. Mehmood, U.; Al-Ahmed, A.; Afzaal, M.; Al-Sulaiman, F. A.; Daud, M. *Renewable Sustainable Energy Rev.* **2017,** *78,* 1–14. doi:10.1016/j.rser.2017.04.105

40. Kadro, J. M.; Hagfeldt, A. *Joule* **2017,** *1,* 29–46. doi:10.1016/j.joule.2017.07.013

41. Peng, J.; Chen, Y.; Zheng, K.; Pullerits, T.; Liang, Z. *Chem. Soc. Rev.* **2017,** *46,* 5714–5729. doi:10.1039/c6cs00942e

42. Abate, A. *Joule* **2017,** *1,* 659–664. doi:10.1016/j.joule.2017.09.007

43. Ahmadi, M.; Wu, T.; Hu, B. *Adv. Mater.* **2017,** *29,* 1605242. doi:10.1002/adma.201605242

44. Chakraborty, S.; Xie, W.; Mathews, N.; Sherburne, M.; Ahuja, R.; Asta, M.; Mhaisalkar, S. G. *ACS Energy Lett.* **2017,** *2,* 837–845. doi:10.1021/acsenergylett.7b00035

45. Green, M. A.; Ho-Baillie, A. *ACS Energy Lett.* **2017,** *2,* 822–830. doi:10.1021/acsenergylett.7b00137

46. Ono, L. K.; Qi, Y. *J. Phys. D: Appl. Phys.* **2018,** *51,* 093001. doi:10.1088/1361-6463/aaa727

47. Chen, P.; Bai, Y.; Lyu, M.; Yun, J.-H.; Hao, M.; Wang, L. *Sol. RRL* **2018,** *2,* 1700186. doi:10.1002/solr.201700186

48. Saliba, M.; Correa-Baena, J.-P.; Grätzel, M.; Hagfeldt, A.; Abate, A. *Angew. Chem., Int. Ed.* **2018,** *57,* 2554–2569. doi:10.1002/anie.201703226

49. Chen, H.; Xiang, S.; Li, W.; Liu, H.; Zhu, L.; Yang, S. *Sol. RRL* **2018,** *2,* 1700188. doi:10.1002/solr.201700188

50. Zhang, Q.; Yin, Y. *ACS Cent. Sci.* **2018,** *4,* 668–679. doi:10.1021/acscentsci.8b00201

51. Konstantakou, M.; Stergiopoulos, T. *J. Mater. Chem. A* **2017,** *5,* 11518–11549. doi:10.1039/c7ta00929a

52. Dong, Y.; Zou, Y.; Song, J.; Song, X.; Zeng, H. *J. Mater. Chem. C* **2017,** *5,* 11369–11394. doi:10.1039/c7tc03612d

53. Swarnkar, A.; Ravi, V. K.; Nag, A. *ACS Energy Lett.* **2017,** *2,* 1089–1098. doi:10.1021/acsenergylett.7b00191

54. Sun, J.; Yang, J.; Lee, J. I.; Cho, J. H.; Kang, M. S. *J. Phys. Chem. Lett.* **2018,** *9,* 1573–1583. doi:10.1021/acs.jpclett.8b00301

55. Yang, G.-L.; Zhong, H.-Z. *Chin. Chem. Lett.* **2016,** *27,* 1124–1130. doi:10.1016/j.cclet.2016.06.047

56. Bai, S.; Yuan, Z.; Gao, F. *J. Mater. Chem. C* **2016,** *4,* 3898–3904. doi:10.1039/c5tc04116c

57. Chatterjee, S.; Pal, A. J. *J. Mater. Chem. A* **2018,** *6,* 3793–3823. doi:10.1039/c7ta09943f

58. Yan, J.; Qiu, W.; Wu, G.; Heremans, P.; Chen, H. *J. Mater. Chem. A* **2018,** *6,* 11063–11077. doi:10.1039/c8ta02288g

59. Hu, H.; Dong, B.; Zhang, W. *J. Mater. Chem. A* **2017,** *5,* 11436–11449. doi:10.1039/c7ta00269f

60. Giustino, F.; Snaith, H. J. *ACS Energy Lett.* **2016,** *1,* 1233–1240. doi:10.1021/acsenergylett.6b00499

61. Zhang, M.; Lyu, M.; Chen, P.; Hao, M.; Yun, J.-H.; Wang, L. *Asia-Pac. J. Chem. Eng.* **2016,** *11,* 392–398. doi:10.1002/apj.1998

62. Ganose, A. M.; Savory, C. N.; Scanlon, D. O. *Chem. Commun.* **2017,** *53,* 20–44. doi:10.1039/c6cc06475b

63. Liu, C.; Li, W.; Fan, J.; Mai, Y. *J. Energy Chem.* **2018,** *27,* 1054–1066. doi:10.1016/j.jechem.2017.10.028

64. Liang, L.; Gao, P. *Adv. Sci.* **2018,** *5,* 1700331. doi:10.1002/advs.201700331

65. Pazoki, M.; Edvinsson, T. *Sustainable Energy Fuels* **2018,** *2,* 1430–1445. doi:10.1039/C8SE00143J

66. Boix, P. P.; Agarwala, S.; Koh, T. M.; Mathews, N.; Mhaisalkar, S. G. *J. Phys. Chem. Lett.* **2015,** *6,* 898–907. doi:10.1021/jz502547f

67. Kojima, A.; Teshima, K.; Shirai, Y.; Miyasaka, T. *J. Am. Chem. Soc.* **2009,** *131,* 6050–6051. doi:10.1021/ja809598r

68. Ogomi, Y.; Morita, A.; Tsukamoto, S.; Saitho, T.; Fujikawa, N.; Shen, Q.; Toyoda, T.; Yoshino, K.; Pandey, S. S.; Ma, T.; Hayase, S. *J. Phys. Chem. Lett.* **2014,** *5,* 1004–1011. doi:10.1021/jz5002117

69. Liang, J.; Zhao, P.; Wang, C.; Wang, Y.; Hu, Y.; Zhu, G.; Ma, L.; Liu, J.; Jin, Z. *J. Am. Chem. Soc.* **2017,** *139,* 14009–14012. doi:10.1021/jacs.7b07949

70. Yang, Z.; Rajagopal, A.; Jen, A. K.-Y. *Adv. Mater.* **2017,** *29,* 1704418. doi:10.1002/adma.201704418

71. Ke, W.; Stoumpos, C. C.; Spanopoulos, I.; Mao, L.; Chen, M.; Wasielewski, M. R.; Kanatzidis, M. G. *J. Am. Chem. Soc.* **2017,** *139,* 14800–14806. doi:10.1021/jacs.7b09018

72. Chen, L.-J.; Lee, C.-R.; Chuang, Y.-J.; Wu, Z.-H.; Chen, C. *J. Phys. Chem. Lett.* **2016,** *7,* 5028–5035. doi:10.1021/acs.jpclett.6b02344

73. Tsai, C.-M.; Mohanta, N.; Wang, C.-Y.; Lin, Y.-P.; Yang, Y.-W.; Wang, C.-L.; Hung, C.-H.; Diau, E. W.-G. *Angew. Chem., Int. Ed.* **2017,** *56,* 13819–13823. doi:10.1002/anie.201707037

74. Hao, F.; Stoumpos, C. C.; Cao, D. H.; Chang, R. P. H.; Kanatzidis, M. G. *Nat. Photonics* **2014,** *8,* 489–494. doi:10.1038/NPHOTON.2014.82

75. Cao, D. H.; Stoumpos, C. C.; Yokoyama, T.; Logsdon, J. L.; Song, T.-B.; Farha, O. K.; Wasielewski, M. R.; Hupp, J. T.; Kanatzidis, M. G. *ACS Energy Lett.* **2017,** *2,* 982–990. doi:10.1021/acsenergylett.7b00202

76. Shao, S.; Liu, J.; Portale, G.; Fang, H.-H.; Blake, G. R.; ten Brink, G. H.; Koster, L. J. A.; Loi, M. A. *Adv. Energy Mater.* **2018,** *8,* 1702019. doi:10.1002/aenm.201702019

77. Zhu, Z.; Chueh, C.-C.; Li, N.; Mao, C.; Jen, A. K.-Y. *Adv. Mater.* **2018,** *30,* 1703800. doi:10.1002/adma.201703800

78. Jung, M.-C.; Raga, S. R.; Qi, Y. *RSC Adv.* **2016,** *6,* 2819–2825. doi:10.1039/c5ra21291j

79. Bernal, C.; Yang, K. *J. Phys. Chem. C* **2014,** *118,* 24383–24388. doi:10.1021/jp509358f

80. Song, T.-B.; Yokoyama, T.; Aramaki, S.; Kanatzidis, M. G. *ACS Energy Lett.* **2017,** *2,* 897–903. doi:10.1021/acsenergylett.7b00171

81. Yu, Y.; Zhao, D.; Grice, C. R.; Meng, W.; Wang, C.; Liao, W.; Cimaroli, A. J.; Zhang, H.; Zhu, K.; Yan, Y. *RSC Adv.* **2016,** *6,* 90248–90254. doi:10.1039/c6ra19476a

82. Koh, T. M.; Krishnamoorthy, T.; Yantara, N.; Shi, C.; Leong, W. L.; Boix, P. P.; Grimsdale, A. C.; Mhaisalkar, S. G.; Mathews, N. *J. Mater. Chem. A* **2015,** *3,* 14996–15000. doi:10.1039/c5ta00190k

83. Jiang, Y.; Zhang, H.; Qiu, X.; Cao, B. *Mater. Lett.* **2017,** *199,* 50–52. doi:10.1016/j.matlet.2017.04.046

84. Zhang, Z.; Li, X.; Xia, X.; Wang, Z.; Huang, Z.; Lei, B.; Gao, Y. *J. Phys. Chem. Lett.* **2017,** *8,* 4300–4307. doi:10.1021/acs.jpclett.7b01952

85. Lyu, M.; Yun, J.-H.; Cai, M.; Jiao, Y.; Bernhardt, P. V.; Zhang, M.; Wang, Q.; Du, A.; Wang, H.; Liu, G.; Wang, L. *Nano Res.* **2016,** *9,* 692–702. doi:10.1007/s12274-015-0948-y

86. Kong, M.; Hu, H.; Wan, L.; Chen, M.; Gan, Y.; Wang, J.; Chen, F.; Dong, B.; Eder, D.; Wang, S. *RSC Adv.* **2017,** *7,* 35549–35557. doi:10.1039/c7ra04924b

87. Nie, R.; Mehta, A.; Park, B.-w.; Kwon, H.-W.; Im, J.; Seok, S. I. *J. Am. Chem. Soc.* **2018,** *140,* 872–875. doi:10.1021/jacs.7b11332

88. Saparov, B.; Hong, F.; Sun, J.-P.; Duan, H.-S.; Meng, W.; Cameron, S.; Hill, I. G.; Yan, Y.; Mitzi, D. B. *Chem. Mater.* **2015,** *27,* 5622–5632. doi:10.1021/acs.chemmater.5b01989

89. Singh, A.; Boopathi, K. M.; Mohapatra, A.; Chen, Y. F.; Li, G.; Chu, C. W. *ACS Appl. Mater. Interfaces* **2018,** *10,* 2566–2573. doi:10.1021/acsami.7b16349

90. Boopathi, K. M.; Karuppuswamy, P.; Singh, A.; Hanmandlu, C.; Lin, L.; Abbas, S. A.; Chang, C. C.; Wang, P. C.; Li, G.; Chu, C. W. *J. Mater. Chem. A* **2017,** *5,* 20843–20850. doi:10.1039/c7ta06679a

91. Harikesh, P. C.; Mulmudi, H. K.; Ghosh, B.; Goh, T. W.; Teng, Y. T.; Thirumal, K.; Lockrey, M.; Weber, K.; Koh, T. M.; Li, S.; Mhaisalkar, S.; Mathews, N. *Chem. Mater.* **2016,** *28,* 7496–7504. doi:10.1021/acs.chemmater.6b03310

92. Stoumpos, C. C.; Malliakas, C. D.; Kanatzidis, M. G. *Inorg. Chem.* **2013,** *52,* 9019–9038. doi:10.1021/ic401215x

93. Zong, Y.; Wang, N.; Zhang, L.; Ju, M.-G.; Zeng, X. C.; Sun, X. W.; Zhou, Y.; Padture, N. P. *Angew. Chem., Int. Ed.* **2017,** *56,* 12658–12662. doi:10.1002/anie.201705965

94. Tsai, C.-M.; Wu, H.-P.; Chang, S.-T.; Huang, C.-F.; Wang, C.-H.; Narra, S.; Yang, Y.-W.; Wang, C.-L.; Hung, C.-H.; Diau, E. W.-G. *ACS Energy Lett.* **2016,** *1,* 1086–1093. doi:10.1021/acsenergylett.6b00514

95. Liu, F.; Ding, C.; Zhang, Y.; Ripolles, T. S.; Kamisaka, T.; Toyoda, T.; Hayase, S.; Minemoto, T.; Yoshino, K.; Dai, S.; Yanagida, M.; Noguchi, H.; Shen, Q. *J. Am. Chem. Soc.* **2017,** *139,* 16708–16719. doi:10.1021/jacs.7b08628

96. Leijtens, T.; Prasanna, R.; Gold-Parker, A.; Toney, M. F.; McGehee, M. D. *ACS Energy Lett.* **2017,** *2,* 2159–2165. doi:10.1021/acsenergylett.7b00636

97. Eperon, G. E.; Ginger, D. S. *ACS Energy Lett.* **2017,** *2,* 1190–1196. doi:10.1021/acsenergylett.7b00290

98. Liu, C.; Li, W.; Li, H.; Zhang, C.; Fan, J.; Mai, Y. *Nanoscale* **2017,** *9,* 13967–13975. doi:10.1039/c7nr03507a

99. Arunkumar, P.; Gil, K. H.; Won, S.; Unithrattil, S.; Kim, Y. H.; Kim, H. J.; Im, W. B. *J. Phys. Chem. Lett.* **2017,** *8,* 4161–4166. doi:10.1021/acs.jpclett.7b01440

100. Liu, H.; Wu, Z.; Shao, J.; Yao, D.; Gao, H.; Liu, Y.; Yu, W.; Zhang, H.; Yang, B. *ACS Nano* **2017,** *11,* 2239–2247. doi:10.1021/acsnano.6b08747

101. Singh, P.; Rana, P. J. S.; Dhingra, P.; Kar, P. *J. Mater. Chem. C* **2016,** *4,* 3101–3105. doi:10.1039/c6tc00650g

102. Lau, C. F. J.; Zhang, M.; Deng, X.; Zheng, J.; Bing, J.; Ma, Q.; Kim, J.; Hu, L.; Green, M. A.; Huang, S.; Ho-Baillie, A. *ACS Energy Lett.* **2017,** *2,* 2319–2325. doi:10.1021/acsenergylett.7b00751

103. Lau, C. F. J.; Deng, X.; Zheng, J.; Kim, J.; Zhang, Z.; Zhang, M.; Bing, J.; Wilkinson, B.; Hu, L.; Patterson, R.; Huang, S.; Ho-Baillie, A. *J. Mater. Chem. A* **2018,** *6,* 5580–5586. doi:10.1039/c7ta11154a

104. Wang, Z.-K.; Li, M.; Yang, Y.-G.; Hu, Y.; Ma, H.; Gao, X.-Y.; Liao, L.-S. *Adv. Mater.* **2016,** *28,* 6695–6703. doi:10.1002/adma.201600626

105. Zhu, F.; Gentry, N. E.; Men, L.; White, M. A.; Vela, J. *J. Phys. Chem. C* **2018,** *122,* 14082–14090. doi:10.1021/acs.jpcc.8b01191

106. Wang, L.-Z.; Zhao, Y.-Q.; Liu, B.; Wu, L.-J.; Cai, M.-Q. *Phys. Chem. Chem. Phys.* **2016,** *18,* 22188–22195. doi:10.1039/c6cp03605h

107. Yao, Z.; Yang, Z.; Liu, Y.; Zhao, W.; Zhang, X.; Liu, B.; Wu, H.; Liu, S. (Frank). *RSC Adv.* **2017,** *7,* 38155–38159. doi:10.1039/c7ra07101a

108. Zhang, M.; Lyu, M.; Yun, J.-H.; Noori, M.; Zhou, X.; Cooling, N. A.; Wang, Q.; Yu, H.; Dastoor, P. C.; Wang, L. *Nano Res.* **2016,** *9,* 1570–1577. doi:10.1007/s12274-016-1051-8

109. Rahul; Singh, P. K.; Singh, R.; Singh, V.; Bhattacharya, B.; Khan, Z. H. *Mater. Res. Bull.* **2018,** *97,* 572–577. doi:10.1016/j.materresbull.2017.09.054

110. Moghe, D.; Wang, L.; Traverse, C. J.; Redoute, A.; Sponseller, M.; Brown, P. R.; Bulović, V.; Lunt, R. R. *Nano Energy* **2016,** *28,* 469–474. doi:10.1016/j.nanoen.2016.09.009

111. Noel, N. K.; Stranks, S. D.; Abate, A.; Wehrenfennig, C.; Guarnera, S.; Haghighirad, A.-A.; Sadhanala, A.; Eperon, G. E.; Pathak, S. K.; Johnston, M. B.; Petrozza, A.; Herz, L. M.; Snaith, H. J. *Energy Environ. Sci.* **2014,** *7,* 3061–3068. doi:10.1039/c4ee01076k

112. Qiu, X.; Cao, B.; Yuan, S.; Chen, X.; Qiu, Z.; Jiang, Y.; Ye, Q.; Wang, H.; Zeng, H.; Liu, J.; Kanatzidis, M. G. *Sol. Energy Mater. Sol. Cells* **2017,** *159,* 227–234. doi:10.1016/j.solmat.2016.09.022

113. Fujihara, T.; Terakawa, S.; Matsushima, T.; Qin, C.; Yahiro, M.; Adachi, C. *J. Mater. Chem. C* **2017,** *5,* 1121–1127. doi:10.1039/c6tc05069g

114. Hao, F.; Stoumpos, C. C.; Guo, P.; Zhou, N.; Marks, T. J.; Chang, R. P. H.; Kanatzidis, M. G. *J. Am. Chem. Soc.* **2015,** *137,* 11445–11452. doi:10.1021/jacs.5b06658

115. Yokoyama, T.; Cao, D. H.; Stoumpos, C. C.; Song, T.-B.; Sato, Y.; Aramaki, S.; Kanatzidis, M. G. *J. Phys. Chem. Lett.* **2016,** *7,* 776–782. doi:10.1021/acs.jpclett.6b00118

116. Lee, Y. M.; Park, J.; Yu, B. D.; Hong, S.; Jung, M.-C.; Nakamura, M. *J. Phys. Chem. Lett.* **2018,** *9,* 2293–2297. doi:10.1021/acs.jpclett.8b00494

117. Jung, Y.-K.; Lee, J.-H.; Walsh, A.; Soon, A. *Chem. Mater.* **2017,** *29,* 3181–3188. doi:10.1021/acs.chemmater.7b00260

118. Handa, T.; Yamada, T.; Kubota, H.; Ise, S.; Miyamoto, Y.; Kanemitsu, Y. *J. Phys. Chem. C* **2017,** *121,* 16158–16165. doi:10.1021/acs.jpcc.7b06199

119. Song, T.-B.; Yokoyama, T.; Stoumpos, C. C.; Logsdon, J.; Cao, D. H.; Wasielewski, M. R.; Aramaki, S.; Kanatzidis, M. G. *J. Am. Chem. Soc.* **2017,** *139,* 836–842. doi:10.1021/jacs.6b10734

120. Lee, S. J.; Shin, S. S.; Im, J.; Ahn, T. K.; Noh, J. H.; Jeon, N. J.; Seok, S. I.; Seo, J. *ACS Energy Lett.* **2018,** *3,* 46–53. doi:10.1021/acsenergylett.7b00976

121. Li, W.; Li, J.; Li, J.; Fan, J.; Mai, Y.; Wang, L. *J. Mater. Chem. A* **2016,** *4,* 17104–17110. doi:10.1039/c6ta08332c

122. Waleed, A.; Tavakoli, M. M.; Gu, L.; Wang, Z.; Zhang, D.; Manikandan, A.; Zhang, Q.; Zhang, R.; Chueh, Y.-L.; Fan, Z. *Nano Lett.* **2017,** *17,* 523–530. doi:10.1021/acs.nanolett.6b04587

123. Nishikubo, R.; Ishida, N.; Katsuki, Y.; Wakamiya, A.; Saeki, A. *J. Phys. Chem. C* **2017,** *121,* 19650–19656. doi:10.1021/acs.jpcc.7b06294

124. Gupta, S.; Cahen, D.; Hodes, G. *J. Phys. Chem. C* **2018,** *122,* 13926–13936. doi:10.1021/acs.jpcc.8b01045

125. Ma, L.; Hao, F.; Stoumpos, C. C.; Phelan, B. T.; Wasielewski, M. R.; Kanatzidis, M. G. *J. Am. Chem. Soc.* **2016,** *138,* 14750–14755. doi:10.1021/jacs.6b09257

126. Peedikakkandy, L.; Bhargava, P. *RSC Adv.* **2016,** *6,* 19857–19860. doi:10.1039/c5ra22317b

127. Sabba, D.; Mulmudi, H. K.; Prabhakar, R. R.; Krishnamoorthy, T.; Baikie, T.; Boix, P. P.; Mhaisalkar, S.; Mathews, N. *J. Phys. Chem. C* **2015,** *119,* 1763–1767. doi:10.1021/jp5126624

128. Zhu, W.; Xin, G.; Wang, Y.; Min, X.; Yao, T.; Xu, W.; Fang, M.; Shi, S.; Shi, J.; Lian, J. *J. Mater. Chem. A* **2018,** *6,* 2577–2584. doi:10.1039/c7ta10040j

129. Lee, B.; Krenselewski, A.; Baik, S. I.; Seidman, D. N.; Chang, R. P. H. *Sustainable Energy Fuels* **2017,** *1,* 710–724. doi:10.1039/c7se00100b

130. Dolzhnikov, D. S.; Wang, C.; Xu, Y.; Kanatzidis, M. G.; Weiss, E. A. *Chem. Mater.* **2017,** *29,* 7901–7907. doi:10.1021/acs.chemmater.7b02803

131. Jellicoe, T. C.; Richter, J. M.; Glass, H. F. J.; Tabachnyk, M.; Brady, R.; Dutton, S. E.; Rao, A.; Friend, R. H.; Credgington, D.; Greenham, N. C.; Böhm, M. L. *J. Am. Chem. Soc.* **2016,** *138,* 2941–2944. doi:10.1021/jacs.5b13470

132. Wong, A. B.; Bekenstein, Y.; Kang, J.; Kley, C. S.; Kim, D.; Gibson, N. A.; Zhang, D.; Yu, Y.; Leone, S. R.; Wang, L.-W.; Alivisatos, A. P.; Yang, P. *Nano Lett.* **2018,** *18,* 2060–2066. doi:10.1021/acs.nanolett.8b00077

133. Wang, A.; Yan, X.; Zhang, M.; Sun, S.; Yang, M.; Shen, W.; Pan, X.; Wang, P.; Deng, Z. *Chem. Mater.* **2016,** *28,* 8132–8140. doi:10.1021/acs.chemmater.6b01329

134. Rajendra Kumar, G.; Kim, H.-J.; Karuppannan, S.; Prabakar, K. *J. Phys. Chem. C* **2017,** *121,* 16447–16453. doi:10.1021/acs.jpcc.7b06278

135. Wang, A.; Guo, Y.; Muhammad, F.; Deng, Z. *Chem. Mater.* **2017,** *29,* 6493–6501. doi:10.1021/acs.chemmater.7b02089

136. Rakita, Y.; Gupta, S.; Cahen, D.; Hodes, G. *Chem. Mater.* **2017,** *29,* 8620–8629. doi:10.1021/acs.chemmater.7b02314

137. Hsu, H.-Y.; Ji, L.; Du, M.; Zhao, J.; Yu, E. T.; Bard, A. J. *Electrochim. Acta* **2016,** *220,* 205–210. doi:10.1016/j.electacta.2016.10.049

138. Ma, S.; Shang, M.; Yu, L.; Dong, L. *J. Mater. Chem. A* **2015,** *3,* 1222–1229. doi:10.1039/c4ta04593a

139. Sun, P.-P.; Li, Q.-S.; Yang, L.-N.; Li, Z.-S. *Nanoscale* **2016,** *8,* 1503–1512. doi:10.1039/c5nr05337d

140. Krishnamoorthy, T.; Ding, H.; Yan, C.; Leong, W. L.; Baikie, T.; Zhang, Z.; Sherburne, M.; Li, S.; Asta, M.; Mathews, N.; Mhaisalkar, S. G. *J. Mater. Chem. A* **2015,** *3,* 23829–23832. doi:10.1039/c5ta05741h

141. Ming, W.; Shi, H.; Du, M.-H. *J. Mater. Chem. A* **2016,** *4,* 13852–13858. doi:10.1039/c6ta04685a

142. Zhao, Y.-Q.; Liu, B.; Yu, Z.-L.; Cao, D.; Cai, M.-Q. *Electrochim. Acta* **2017,** *247,* 891–898. doi:10.1016/j.electacta.2017.06.154

143. Cheng, P.; Wu, T.; Zhang, J.; Li, Y.; Liu, J.; Jiang, L.; Mao, X.; Lu, R.-F.; Deng, W.-Q.; Han, K. *J. Phys. Chem. Lett.* **2017,** *8,* 4402–4406. doi:10.1021/acs.jpclett.7b01985

144. Kopacic, I.; Friesenbichler, B.; Hoefler, S. F.; Kunert, B.; Plank, H.; Rath, T.; Trimmel, G. *ACS Appl. Energy Mater.* **2018,** *1,* 343–347. doi:10.1021/acsaem.8b00007

145. Sun, P.-P.; Chi, W.-J.; Li, Z.-S. *Phys. Chem. Chem. Phys.* **2016,** *18,* 24526–24536. doi:10.1039/c6cp04344e

146. Nagane, S.; Ghosh, D.; Hoye, R. L. Z.; Zhao, B.; Ahmad, S.; Walker, A. B.; Islam, M. S.; Ogale, S.; Sadhanala, A. *J. Phys. Chem. C* **2018,** *122,* 5940–5947. doi:10.1021/acs.jpcc.8b00480

147. Zhang, X.; Yin, J.; Nie, Z.; Zhang, Q.; Sui, N.; Chen, B.; Zhang, Y.; Qu, K.; Zhao, J.; Zhou, H. *RSC Adv.* **2017,** *7,* 37419–37425. doi:10.1039/c7ra04235c

148. Nie, Z.; Yin, J.; Zhou, H.; Chai, N.; Chen, B.; Zhang, Y.; Qu, K.; Shen, G.; Ma, H.; Li, Y.; Zhao, J.; Zhang, X. *ACS Appl. Mater. Interfaces* **2016,** *8,* 28187–28193. doi:10.1021/acsami.6b08962

149. Xiao, Z.-L.; Chen, H.-Z.; Shi, M.-M.; Wu, G.; Zhou, R.-J.; Yang, Z.-S.; Wang, M.; Tang, B.-Z. *Mater. Sci. Eng., B* **2005,** *117,* 313–316. doi:10.1016/j.mseb.2004.12.052

150. Li, X.; Zhong, X.; Hu, Y.; Li, B.; Sheng, Y.; Zhang, Y.; Weng, C.; Feng, M.; Han, H.; Wang, J. *J. Phys. Chem. Lett.* **2017,** *8,* 1804–1809. doi:10.1021/acs.jpclett.7b00086

151. Li, X.; Li, B.; Chang, J.; Ding, B.; Zheng, S.; Wu, Y.; Yang, J.; Yang, G.; Zhong, X.; Wang, J. *ACS Appl. Energy Mater.* **2018,** *1,* 2709–2716. doi:10.1021/acsaem.8b00372

152. Cortecchia, D.; Dewi, H. A.; Yin, J.; Bruno, A.; Chen, S.; Baikie, T.; Boix, P. P.; Grätzel, M.; Mhaisalkar, S.; Soci, C.; Mathews, N. *Inorg. Chem.* **2016,** *55,* 1044–1052. doi:10.1021/acs.inorgchem.5b01896

153. Hebig, J.-C.; Kühn, I.; Flohre, J.; Kirchartz, T. *ACS Energy Lett.* **2016,** *1,* 309–314. doi:10.1021/acsenergylett.6b00170

154. Jiang, F.; Yang, D.; Jiang, Y.; Liu, T.; Zhao, X.; Ming, Y.; Luo, B.; Qin, F.; Fan, J.; Han, H.; Zhang, L.; Zhou, Y. *J. Am. Chem. Soc.* **2018,** *140,* 1019–1027. doi:10.1021/jacs.7b10739

155. McDonald, C.; Ni, C.; Švrček, V.; Lozac'h, M.; Connor, P. A.; Maguire, P.; Irvine, J. T. S.; Mariotti, D. *Nanoscale* **2017,** *9,* 18759–18771. doi:10.1039/c7nr05764d

156. Eckhardt, K.; Bon, V.; Getzschmann, J.; Grothe, J.; Wisser, F. M.; Kaskel, S. *Chem. Commun.* **2016,** *52,* 3058–3060. doi:10.1039/c5cc10455f

157. Singh, T.; Kulkarni, A.; Ikegami, M.; Miyasaka, T. *ACS Appl. Mater. Interfaces* **2016,** *8,* 14542–14547. doi:10.1021/acsami.6b02843

158. Pious, J. K.; Lekshmi, M. L.; Muthu, C.; Rakhi, R. B.; Nair, V. C. *ACS Omega* **2017,** *2,* 5798–5802. doi:10.1021/acsomega.7b00973

159. Zhang, Y.; Yin, J.; Parida, M. R.; Ahmed, G. H.; Pan, J.; Bakr, O. M.; Brédas, J.-L.; Mohammed, O. F. *J. Phys. Chem. Lett.* **2017,** *8,* 3173–3177. doi:10.1021/acs.jpclett.7b01381

160. Kulkarni, A.; Singh, T.; Ikegami, M.; Miyasaka, T. *RSC Adv.* **2017,** *7,* 9456–9460. doi:10.1039/c6ra28190g

161. Abulikemu, M.; Ould-Chikh, S.; Miao, X.; Alarousu, E.; Murali, B.; Ngongang Ndjawa, G. O.; Barbé, J.; El Labban, A.; Amassian, A.; Del Gobbo, S. *J. Mater. Chem. A* **2016,** *4,* 12504–12515. doi:10.1039/c6ta04657f

162. Wang, H.; Tian, J.; Jiang, K.; Zhang, Y.; Fan, H.; Huang, J.; Yang, L.-m.; Guan, B.; Song, Y. *RSC Adv.* **2017,** *7,* 43826–43830. doi:10.1039/c7ra07123j

163. Ni, C.; Hedley, G.; Payne, J.; Svrcek, V.; McDonald, C.; Jagadamma, L. K.; Edwards, P.; Martin, R.; Jain, G.; Carolan, D.; Mariotti, D.; Maguire, P.; Samuel, I.; Irvine, J. *Nat. Commun.* **2017,** *8,* 170. doi:10.1038/s41467-017-00261-9

164. Leng, M.; Yang, Y.; Zeng, K.; Chen, Z.; Tan, Z.; Li, S.; Li, J.; Xu, B.; Li, D.; Hautzinger, M. P.; Fu, Y.; Zhai, T.; Xu, L.; Niu, G.; Jin, S.; Tang, J. *Adv. Funct. Mater.* **2018,** *28,* 1704446. doi:10.1002/adfm.201704446

165. Yang, B.; Chen, J.; Hong, F.; Mao, X.; Zheng, K.; Yang, S.; Li, Y.; Pullerits, T.; Deng, W.; Han, K. *Angew. Chem., Int. Ed.* **2017,** *56,* 12471–12475. doi:10.1002/anie.201704739

166. Wei, F.; Deng, Z.; Sun, S.; Xie, F.; Kieslich, G.; Evans, D. M.; Carpenter, M. A.; Bristowe, P. D.; Cheetham, A. K. *Mater. Horiz.* **2016,** *3,* 328–332. doi:10.1039/c6mh00053c

167. Scholz, M.; Flender, O.; Oum, K.; Lenzer, T. *J. Phys. Chem. C* **2017,** *121,* 12110–12116. doi:10.1021/acs.jpcc.7b04543

168. Khoram, P.; Brittman, S.; Dzik, W. I.; Reek, J. N. H.; Garnett, E. C. *J. Phys. Chem. C* **2016,** *120,* 6475–6481. doi:10.1021/acs.jpcc.6b02011

169. Tong, X.-W.; Kong, W.-Y.; Wang, Y.-Y.; Zhu, J.-M.; Luo, L.-B.; Wang, Z.-H. *ACS Appl. Mater. Interfaces* **2017,** *9,* 18977–18985. doi:10.1021/acsami.7b04616

170. Bai, F.; Hu, Y.; Hu, Y.; Qiu, T.; Miao, X.; Zhang, S. *Sol. Energy Mater. Sol. Cells* **2018,** *184,* 15–21. doi:10.1016/j.solmat.2018.04.032

171. Li, T.; Hu, Y.; Morrison, C. A.; Wu, W.; Han, H.; Robertson, N. *Sustainable Energy Fuels* **2017,** *1,* 308–316. doi:10.1039/c6se00061d

172. Zhang, W.; Tao, K.; Ji, C.; Sun, Z.; Han, S.; Zhang, J.; Wu, Z.; Luo, J. *Inorg. Chem.* **2018,** *57,* 4239–4243. doi:10.1021/acs.inorgchem.8b00152

173. Adonin, S. A.; Frolova, L. A.; Sokolov, M. N.; Shilov, G. V.; Korchagin, D. V.; Fedin, V. P.; Aldoshin, S. M.; Stevenson, K. J.; Troshin, P. A. *Adv. Energy Mater.* **2018,** *8,* 1701140. doi:10.1002/aenm.201701140

174. Ji, C.; Sun, Z.; Zeb, A.; Liu, S.; Zhang, J.; Hong, M.; Luo, J. *J. Phys. Chem. Lett.* **2017,** *8,* 2012–2018. doi:10.1021/acs.jpclett.7b00673

175. Jain, A.; Voznyy, O.; Sargent, E. H. *J. Phys. Chem. C* **2017,** *121,* 7183–7187. doi:10.1021/acs.jpcc.7b02221

176. Pazoki, M.; Röckert, A.; Wolf, M. J.; Imani, R.; Edvinsson, T.; Kullgren, J. *J. Mater. Chem. A* **2017,** *5,* 23131–23138. doi:10.1039/c7ta07716e

177. Ju, M.-G.; Chen, M.; Zhou, Y.; Garces, H. F.; Dai, J.; Ma, L.; Padture, N. P.; Zeng, X. C. *ACS Energy Lett.* **2018,** *3,* 297–304. doi:10.1021/acsenergylett.7b01167

178. Li, Y.-J.; Wu, T.; Sun, L.; Yang, R.-X.; Jiang, L.; Cheng, P.-F.; Hao, Q.-Q.; Wang, T.-J.; Lu, R.-F.; Deng, W.-Q. *RSC Adv.* **2017,** *7,* 35175–35180. doi:10.1039/c7ra06130g

179. Zhou, J.; Xia, Z.; Molokeev, M. S.; Zhang, X.; Peng, D.; Liu, Q. *J. Mater. Chem. A* **2017,** *5,* 15031–15037. doi:10.1039/c7ta04690a

180. McClure, E. T.; Ball, M. R.; Windl, W.; Woodward, P. M. *Chem. Mater.* **2016,** *28,* 1348–1354. doi:10.1021/acs.chemmater.5b04231

181. Volonakis, G.; Filip, M. R.; Haghighirad, A. A.; Sakai, N.; Wenger, B.; Snaith, H. J.; Giustino, F. *J. Phys. Chem. Lett.* **2016,** *7,* 1254–1259. doi:10.1021/acs.jpclett.6b00376

182. Filip, M. R.; Hillman, S.; Haghighirad, A. A.; Snaith, H. J.; Giustino, F. *J. Phys. Chem. Lett.* **2016,** *7,* 2579–2585. doi:10.1021/acs.jpclett.6b01041

183. Yang, J.; Zhang, P.; Wei, S.-H. *J. Phys. Chem. Lett.* **2018,** *9,* 31–35. doi:10.1021/acs.jpclett.7b02992

184. Slavney, A. H.; Hu, T.; Lindenberg, A. M.; Karunadasa, H. I. *J. Am. Chem. Soc.* **2016,** *138,* 2138–2141. doi:10.1021/jacs.5b13294

185. Li, Q.; Wang, Y.; Pan, W.; Yang, W.; Zou, B.; Tang, J.; Quan, Z. *Angew. Chem., Int. Ed.* **2017,** *56,* 15969–15973. doi:10.1002/anie.201708684

186. Greul, E.; Petrus, M. L.; Binek, A.; Docampo, P.; Bein, T. *J. Mater. Chem. A* **2017,** *5,* 19972–19981. doi:10.1039/c7ta06816f

187. Wei, F.; Deng, Z.; Sun, S.; Zhang, F.; Evans, D. M.; Kieslich, G.; Tominaka, S.; Carpenter, M. A.; Zhang, J.; Bristowe, P. D.; Cheetham, A. K. *Chem. Mater.* **2017,** *29,* 1089–1094. doi:10.1021/acs.chemmater.6b03944

188. Cheng, P.; Wu, T.; Li, Y.; Jiang, L.; Deng, W.; Han, K. *New J. Chem.* **2017,** *41,* 9598–9601. doi:10.1039/c7nj02365k

189. Debbichi, L.; Lee, S.; Cho, H.; Rappe, A. M.; Hong, K.-H.; Jang, M. S.; Kim, H. *Adv. Mater.* **2018,** *30,* 1707001. doi:10.1002/adma.201707001

190. Zhou, J.; Rong, X.; Molokeev, M. S.; Zhang, X.; Xia, Z. *J. Mater. Chem. A* **2018,** *6,* 2346–2352. doi:10.1039/c7ta10062k

191. Luo, J.; Li, S.; Wu, H.; Zhou, Y.; Li, Y.; Liu, J.; Li, J.; Li, K.; Yi, F.; Niu, G.; Tang, J. *ACS Photonics* **2018,** *5,* 398–405. doi:10.1021/acsphotonics.7b00837

192. Nila Nandha, K.; Nag, A. *Chem. Commun.* **2018,** *54,* 5205–5208. doi:10.1039/c8cc01982g

193. Dai, J.; Ma, L.; Ju, M.; Huang, J.; Zeng, X. C. *Phys. Chem. Chem. Phys.* **2017,** *19,* 21691–21695. doi:10.1039/c7cp03448b

194. Xu, J.; Liu, J.-B.; Liu, B.-X.; Huang, B. *J. Phys. Chem. Lett.* **2017,** *8,* 4391–4396. doi:10.1021/acs.jpclett.7b02008

195. Lozhkina, O. A.; Murashkina, A. A.; Elizarov, M. S.; Shilovskikh, V. V.; Zolotarev, A. A.; Kapitonov, Y. V.; Kevorkyants, R.; Emeline, A. V.; Miyasaka, T. *Chem. Phys. Lett.* **2018,** *694,* 18–22. doi:10.1016/j.cplett.2018.01.031

196. Savory, C. N.; Walsh, A.; Scanlon, D. O. *ACS Energy Lett.* **2016,** *1,* 949–955. doi:10.1021/acsenergylett.6b00471

197. Filip, M. R.; Liu, X.; Miglio, A.; Hautier, G.; Giustino, F. *J. Phys. Chem. C* **2018,** *122,* 158–170. doi:10.1021/acs.jpcc.7b10370

198. Feng, H.-J.; Deng, W.; Yang, K.; Huang, J.; Zeng, X. C. *J. Phys. Chem. C* **2017,** *121,* 4471–4480. doi:10.1021/acs.jpcc.7b00138

199. Nakajima, T.; Sawada, K. *J. Phys. Chem. Lett.* **2017,** *8,* 4826–4831. doi:10.1021/acs.jpclett.7b02203

200. Bartesaghi, D.; Slavney, A. H.; Gélvez-Rueda, M. C.; Connor, B. A.; Grozema, F. C.; Karunadasa, H. I.; Savenije, T. J. *J. Phys. Chem. C* **2018,** *122,* 4809–4816. doi:10.1021/acs.jpcc.8b00572

201. Dong, L.; Sun, S.; Deng, Z.; Li, W.; Wei, F.; Qi, Y.; Li, Y.; Li, X.; Lu, P.; Ramamurty, U. *Comput. Mater. Sci.* **2018,** *141,* 49–58. doi:10.1016/j.commatsci.2017.09.014

202. Creutz, S. E.; Crites, E. N.; De Siena, M. C.; Gamelin, D. R. *Nano Lett.* **2018,** *18,* 1118–1123. doi:10.1021/acs.nanolett.7b04659

203. Zhao, X.-G.; Yang, J.-H.; Fu, Y.; Yang, D.; Xu, Q.; Yu, L.; Wei, S.-H.; Zhang, L. *J. Am. Chem. Soc.* **2017,** *139,* 2630–2638. doi:10.1021/jacs.6b09645

204. Volonakis, G.; Haghighirad, A. A.; Snaith, H. J.; Giustino, F. *J. Phys. Chem. Lett.* **2017,** *8,* 3917–3924. doi:10.1021/acs.jpclett.7b01584

205. Giorgi, G.; Yamashita, K. *Chem. Lett.* **2015,** *44,* 826–828. doi:10.1246/cl.150143

206. Liu, B.; Long, M.; Cai, M.-Q.; Yang, J. *J. Phys. D: Appl. Phys.* **2018,** *51,* 105101. doi:10.1088/1361-6463/aaa7ca

207. Etgar, L. *Energy Environ. Sci.* **2018,** *11,* 234–242. doi:10.1039/c7ee03397d

208. Straus, D. B.; Kagan, C. R. *J. Phys. Chem. Lett.* **2018,** *9,* 1434–1447. doi:10.1021/acs.jpclett.8b00201

209. Tang, G.; Xiao, Z.; Hosono, H.; Kamiya, T.; Fang, D.; Hong, J. *J. Phys. Chem. Lett.* **2018,** *9,* 43–48. doi:10.1021/acs.jpclett.7b02829

210. Todorov, T.; Gershon, T.; Gunawan, O.; Sturdevant, C.; Guha, S. *Appl. Phys. Lett.* **2014,** *105,* 173902. doi:10.1063/1.4899275

211. Etgar, L.; Gao, P.; Qin, P.; Graetzel, M.; Nazeeruddin, M. K. *J. Mater. Chem. A* **2014,** *2,* 11586–11590. doi:10.1039/c4ta02711f

212. Li, Y.; Zhu, J.; Huang, Y.; Wei, J.; Liu, F.; Shao, Z.; Hu, L.; Chen, S.; Yang, S.; Tang, J.; Yao, J.; Dai, S. *Nanoscale* **2015,** *7,* 9902–9907. doi:10.1039/c5nr00420a

213. Hu, L.; Yang, Z.; Mandelis, A.; Melnikov, A.; Lan, X.; Walters, G.; Hoogland, S.; Sargent, E. H. *J. Phys. Chem. C* **2016,** *120,* 14416–14427. doi:10.1021/acs.jpcc.6b04468

214. Yang, Z.; Janmohamed, A.; Lan, X.; García de Arquer, F. P.;
Voznyy, O.; Yassitepe, E.; Kim, G.-H.; Ning, Z.; Gong, X.; Comin, R.;
Sargent, E. H. *Nano Lett.* **2015,** *15,* 7539–7543.
doi:10.1021/acs.nanolett.5b03271

License and Terms

Performance analysis of rigorous coupled-wave analysis and its integration in a coupled modeling approach for optical simulation of complete heterojunction silicon solar cells

Ziga Lokar[*], Benjamin Lipovsek, Marko Topic and Janez Krc

Abstract

A variety of light management structures have been introduced in solar cells to improve light harvesting and further boost their conversion efficiency. Reliable and accurate simulation tools are required to design and optimize the individual structures and complete devices. In the first part of this paper, we analyze the performance of rigorous coupled-wave analysis (RCWA) for accurate three-dimensional optical simulation of solar cells, in particular heterojunction silicon (HJ Si) solar cells. The structure of HJ Si solar cells consists of thin and thick layers, and additionally, micro- and nano-textures are also introduced to further exploit the potential of light trapping. The RCWA was tested on the front substructure of the solar cell, including the texture, thin passivation and contact layers. Inverted pyramidal textures of different sizes were included in the simulations. The simulations rapidly converge as long as the textures are small (in the (sub)micrometer range), while for larger microscale textures (feature sizes of a few micrometers), this is not the case. Small textures were optimized to decrease the reflectance, and consequently, increase the absorption in the active layers of the solar cell. Decreasing the flat parts of the texture was shown to improve performance. For simulations of structures with microtextures, and for simulations of complete HJ Si cells, we propose a coupled modeling approach (CMA), where the RCWA is coupled with raytracing and the transfer matrix method. By means of CMA and nanotexture optimization, we show the possible benefits of nanotextures at the front interface of HJ Si solar cells, demonstrating a 13.4% improvement in the short-circuit current density with respect to the flat cell and 1.4% with respect to the cell with double-sided random micropyramids. We additionally demonstrate the ability to simulate a combination of nano- and microtextures at a single interface, although the considered structure did not show an improvement over the pyramidal textures.

Introduction

Light management techniques can be applied to increase the short-circuit current density and consequently the conversion efficiency of solar cells. Such techniques aim to improve the coupling of light into the structure (e.g., antireflective coatings and nanostructures at the front side of solar cells) and the light trapping ability of the structure (e.g., nano- and micrometer size textures for light scattering and refraction). The latter is especially important in solar cells where indirect semiconductors such as silicon (Si) are used as an absorber layer, where the absorption coefficient at the photon energy approaching the value of energy bandgap is small. Furthermore, efficient light management is important in wafer-based Si photovoltaic technologies as the wafers are being thinned down to 150 μm and below. Nowadays different photonic structures (and among them, mostly surface textures of different shapes and sizes) are being tested in solar cells in order to exploit their potential to couple and trap light into solar cells [1-5]. The use of different techniques for the wet and dry etching of Si wafers [6] in combination with thermal or UV nanoimprint lithography [6,7] has opened new potential for design of (nano)textures with superior antireflection, light scattering and trapping properties. Besides the optical properties, proper passivation techniques of textured interfaces are crucial to keep surface recombination velocities as low as possible and thus to maintain the good electrical properties of the device [8,9].

To design and optimize textures applied to the front and/or rear side of solar cells, reliable and accurate optical models implemented in numerical simulation tools are of great importance [10]. The models that enable simulations of thick incoherent and thin coherent layers, including textures of nano-, micro- and several micro-(macro) meter size, are required. Different modeling techniques have been used in simulations of solar cells [11-14], and among them, rigorous coupled-wave analysis (RCWA) has been employed for the optical simulation of thin film or wafer-based solar cells with various textures [2,3,15-17]. However, its applicability, limitations and accuracy in simulation of structures with textures of different types and sizes used in silicon solar cells have not been investigated systematically.

In this paper, we report on three-dimensional optical modeling and simulations applied to a representative of Si-wafer-based technology aiming at low cost production and high conversion efficiency, namely, heterojunction silicon (HJ Si) solar cells [18]. First, we present our optical models and approaches: RCWA and the so-called coupled modeling approach (CMA). The general idea of CMA as a combination of simulators was presented in [19], while its realization by coupling RCWA,

raytracing (RT) and the transfer-matrix method (TMM) and its application is presented in this work.

We proceed with the results of the analysis of the applicability and accuracy of the RCWA method for simulation of different textures in nano- and micrometer size, as applied to the front side of a solar cell structure. We quantify the simulation errors with a $|\Delta J_{SC}|$ measure for the various number of sublayers and modes considered in the simulations. The analysis shows that RCWA is an efficient simulation tool for small textures, which is a further verification of the results obtained previously [20]. However, we also show that the method can suffer in terms of accuracy for large (5 μm) textures for what is considered reasonable simulation time (about one day for the complete wavelength range of interest on a typical desktop PC). Additionally, RCWA may have convergence difficulties if systems of equations are large and the layers in the structure have low absorption.
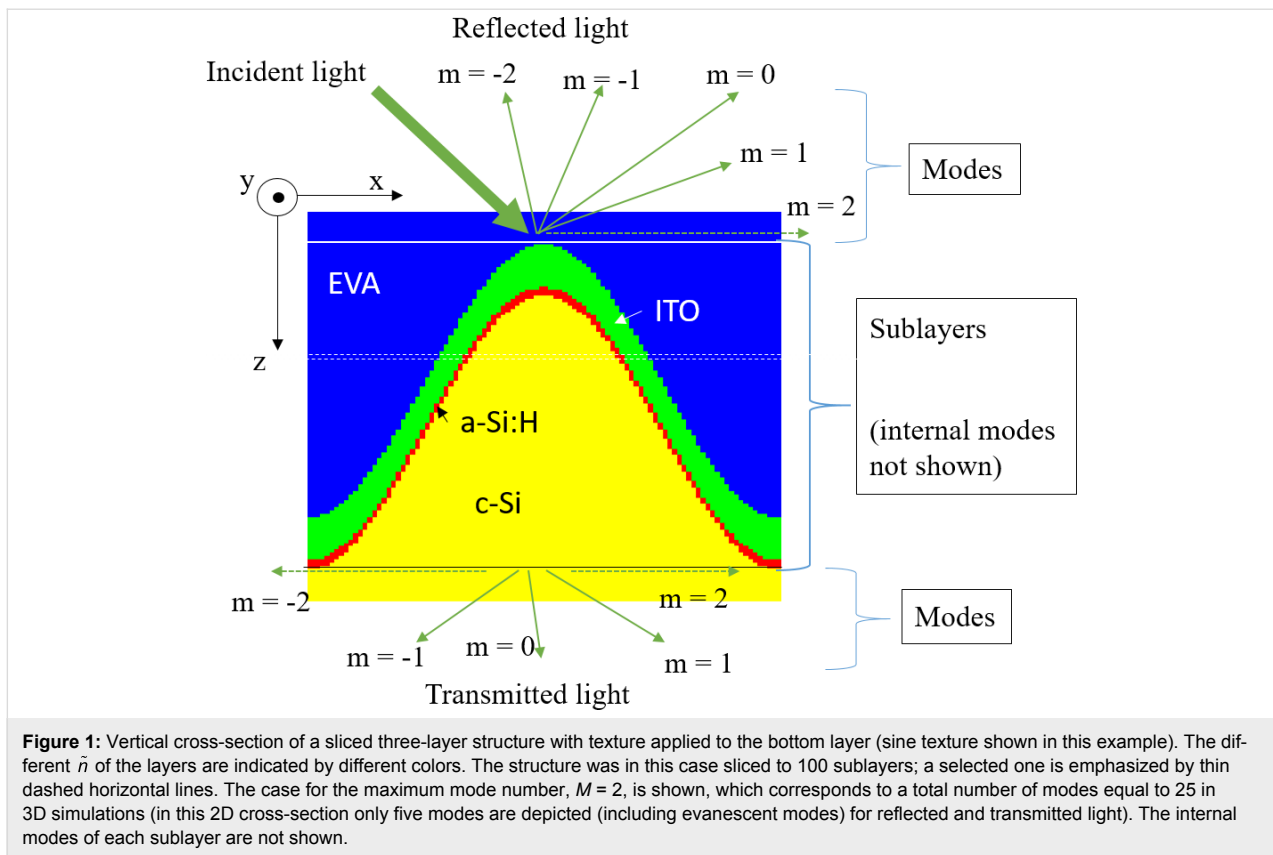
After the applicability and accuracy of RCWA have been successfully tested and analyzed, we apply the RCWA method to optimize inverted-pyramid nanotextures on the front side of the HJ Si solar cell to minimize the reflectivity losses. The CMA approach, where we couple RCWA for nanotextures with RT for thick layers and large textures and the TMM for thin coherent layers, is applied to optimize the complete HJ Si solar cell, which is too complex for any individual simulator due to its size. We show the results of the simulations and discuss the potential and suggestions for improvements in external quantum efficiency (EQE) and short-circuit current density, J_{SC}, of the HJ Si solar cell by applying different textures (nano, micro and combined nano + micro) to the solar cell structure. As an extension of our previous work presented in [20] and to other coupling approaches such as the OPTOS matrix formulation [21], our CMA was used for the simulation of the solar cell structure including a double (nano + micro) texture.

Modeling
Rigorous coupled-wave analysis method
RCWA, also called the Fourier modal method (FMM), has been widely used in simulations of photovoltaic devices [2,3,15-17], including the structures similar to the ones explored in this paper [3]. It assumes lateral periodicity of the simulated structure.

In the RCWA, an analyzed (multilayer) structure is sliced into thin sublayers [22] (see Figure 1) as an example of a multilayer structure with applied texture. Inside a sublayer, materials with different complex refractive indices $\tilde{n}$ are involved in lateral directions (x, y). No vertical dependence (z) of $\tilde{n}$ is assumed

Figure 1: Vertical cross-section of a sliced three-layer structure with texture applied to the bottom layer (sine texture shown in this example). The different $\tilde{n}$ of the layers are indicated by different colors. The structure was in this case sliced to 100 sublayers; a selected one is emphasized by thin dashed horizontal lines. The case for the maximum mode number, *M* = 2, is shown, which corresponds to a total number of modes equal to 25 in 3D simulations (in this 2D cross-section only five modes are depicted (including evanescent modes) for reflected and transmitted light). The internal modes of each sublayer are not shown.

inside a sublayer, while lateral changes of $\tilde{n}$ are considered to be abrupt. This results in a staircase approximation of $\tilde{n}$. While lateral periodicity of the simulated structure is assumed in RCWA, random textures can be simulated by including a sufficient segment of the structure to form a pseudo-periodic simulation domain, where the statistical parameters of the random roughness are still well represented [3]. Spatial 2D discrete Fourier transform of $\tilde{n}$ staircase distributions is applied to all (*N*) sublayers, obtaining a discrete power spectrum of $\tilde{n}$ distribution for each sublayer. These Fourier components are then combined with wavevectors in a matrix describing the propagation of light inside each sublayer separately. The matrix size depends on the number of modes considered. Based on this matrix, complex vectors of the electric and magnetic field, *E* and *H*, inside each sublayer can be defined at the end of the calculation. Eigenvectors of the matrix define lateral dependence of *E* and *H*, while eigenvalues describe their vertical dependence. Finally, boundary conditions at the interfaces of sublayers are defined considering that tangential components of *E* and *H* need to be conserved for conservation of momentum. When solving the system, an S-matrix algorithm is typically used in the RCWA method to couple equations between different sublayers [23-25]. For the purpose of further integration and adaptation, we developed and verified our own RCWA simulation tool in MATLAB, following the physics described above.

To carry out reliable and accurate simulations of solar cell structures with RCWA, it is of prime importance to study the role of input settings first. In our analysis, we focus on the role of the number of sublayers and the number of modes used in simulations. A higher number of sublayers improves the geometrical description of the structure. The maximum mode number, *M*, defines where the discrete Fourier spectrum of $\tilde{n}$ is cut and at the same time how many diffraction modes (directions) of light we consider in our calculation (some might also be evanescent). A higher number of modes leads to both a better description of the actual light propagation and diffraction, as well as improved structure accuracy ($\tilde{n}$ distribution) by taking more Fourier components. However, it also leads to an increase of the size of the system of equations, so it is desirable to use as low number of modes as possible, while maintaining suitable accuracy of simulations. The results of the analysis are shown in the section "RCWA accuracy analysis of partial cell structure" for selected realistic nano- and microtextures for the case of a HJ Si solar cell.

## Integration of RCWA into the coupled modeling approach (CMA)

The next simulation approach that we will use in our simulation study enables simulations of a complete HJ Si solar cell structure, including either nano-, micro-, or combined

(nano + micro) textures in the same structure. Furthermore, thin coherent and thick incoherent layers are included. The realization of high efficiency solar cells requires the capability of modeling such optical structures [26]. We successfully coupled 3D RCWA with 3D raytracing and transfer matrix formalism (TMM) and call the approach the coupled modeling approach (CMA) [27]. The experimental validation of the RCWA and CMA has been performed. Besides comparing simulation results to the results obtained with other simulators (such as FEM as presented), experimental verification of the RCWA and CMA has been performed. The results will be published elsewhere, whereby the focus of this paper is firstly a detailed analysis of RCWA simulation applicability and accuracy, and secondly to use RCWA for optimization of the inverted-pyramid nanotexture, and thirdly, integration in CMA and applicability of CMA for simulation of a fully encapsulated silicon heterojunction solar cell. For the combination of RT and TMM we employed the previously developed optical simulator CROWM [13,28,29], which was previously tested and experimentally verified on different solar cell structures, including thick macrotextured layers (RT simulation) and thin-film layers (TMM simulation). Whereas RCWA is used for detailed description of optical situation in thin nanometer-textured stacks, raytracing and TMM are utilized to define the optical situation in the region of micro- or macrotextured thick or thin layers. The incoherent nature of light in thick layers is assured by the RT algorithm, while coherent RCWA requires wavelength averaging to eliminate interference fringes. The principle of the presented CMA is schematically shown in Figure 2.

Both plane waves of RCWA and TMM as well as geometric rays of the RT method have well defined wavelength, angles of propagation (θ and ϕ correspond to polar and azimuth angle, respectively) and intensities. The intensities are divided into transversal electric (TE) and transversal magnetic (TM) polarization components. The RCWA waves can be simply transformed into rays and back, as the phase is not needed when propagating in incoherent parts of the cell. This makes the combination of the methods very suitable to couple, as there is no need for additional transformations, unlike the combinations of raytracing with other methods. However, the phase can also be considered in the presented CMA if, e.g., only thin coherent layers would be coupled. One should note that in general, the polarization of a wave with respect to the normal of the interface can change from TE to TM or vice versa. This is unlike in (locally) flat interfaces considered with ray optics or TMM, where local TE and TM polarization persist after reflection or refraction. This difference in 3D wave simulations is caused by the diffracted waves, which may not propagate in the same plane as the incident wave. Significant errors are produced if polarization changes are not considered properly.

In CMA simulation, RCWA results for the assigned sub-structure are calculated in advance for various predefined discrete incident angles. For discretized directions and wavelengths, a scattering matrix of outgoing waves (modes) is generated – an individual scattering matrix is generated per each discretized direction. Then this matrix is considered in iterative coupling of RCWA part with RT&TMM. In case of presented simulations, the matrices were calculated for each 5° polar incident angle θ and 15° azimuth incident angle ϕ, for both TE and TM polarization, for each discrete wavelength λ in the range from 350 nm to 1200 nm in steps of 10 nm. Random selection of waves was used, as given by the intensity of light in a particular direction in the scattering matrix, since the number of applied and reflected/transmitted waves was sufficiently large for this type of approach. In comparison of the presented CMA to the OPTOS simulation tool [29] which generates scattering matrices for all layers and stacks them together, we are able to trace rays throughout the structure at their exact angles and positions, which gives us greater versatility in structure we are able to consider. For example, we are able to simulate the previously
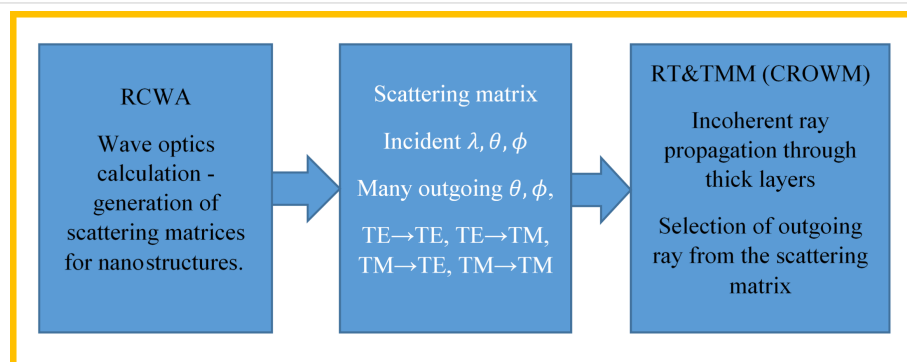
Figure 2: Principle of the coupled modeling approach (CMA). RCWA is applied to the parts of the structure where nanotextures are present to produce scattering matrices. These matrices are an input for the RT and TMM part of the simulator. By applying iterative coupling, the optical situation in the region of nanostructures, microstructures, thin and thick layers can be simulated in an effective and accurate way.

mentioned nanotexture + microtexture on the same interface (see section Simulations of an encapsulated solar cell with textures). Additionally, similar to the approach of Rothemund et al. [30], we are also able to perform RCWA calculation of each individual ray at exact angle and polarization if even greater accuracy is desired; however, at the expense of longer simulation times. The CMA enables simulation of single and multijunction solar cells and photovoltaic modules, such as perovskite-crystalline silicon tandem solar cells [31] including nano, micro and combined textures. In this paper, we focus only on heterojuction silicon solar cells.

CMA simulations were performed for different discretization steps in the polar and azimuth angle to determine the proper input settings for the simulations. The simulation results of the considered structures indicated that for a 5° discretization step of the polar angle and 15° step for of the azimuth angle, only small differences in the results were observed as compared to 1° discretization steps for selected wavelengths. Increasing the discretization step to 10° for the polar angle or 90° for the azimuth angle leads to noticeable simulation errors. Applying the mentioned discretization of 5° and 15° leads to 75 times less simulations than simulating with 1° discretization and was thus used to speed up simulations for the complete wavelength range of interest. Even these parameters lead to approximately 25,000 RCWA simulations for the complete wavelength range of interest, resulting in a total of approximately three days for a simulation of the complete wavelength spectrum on a desktop PC. The same set of RCWA-generated scattering matrices with given nanotexture was then used for all presented CMA simulations of the given structure, leading to significant timesaving.

Analyzed structure and textures

We simulated a realistic structure of an n-type HJ Si solar cell, including front glass and ethylene-vinyl acetate (EVA) encapsulation (Figure 3).
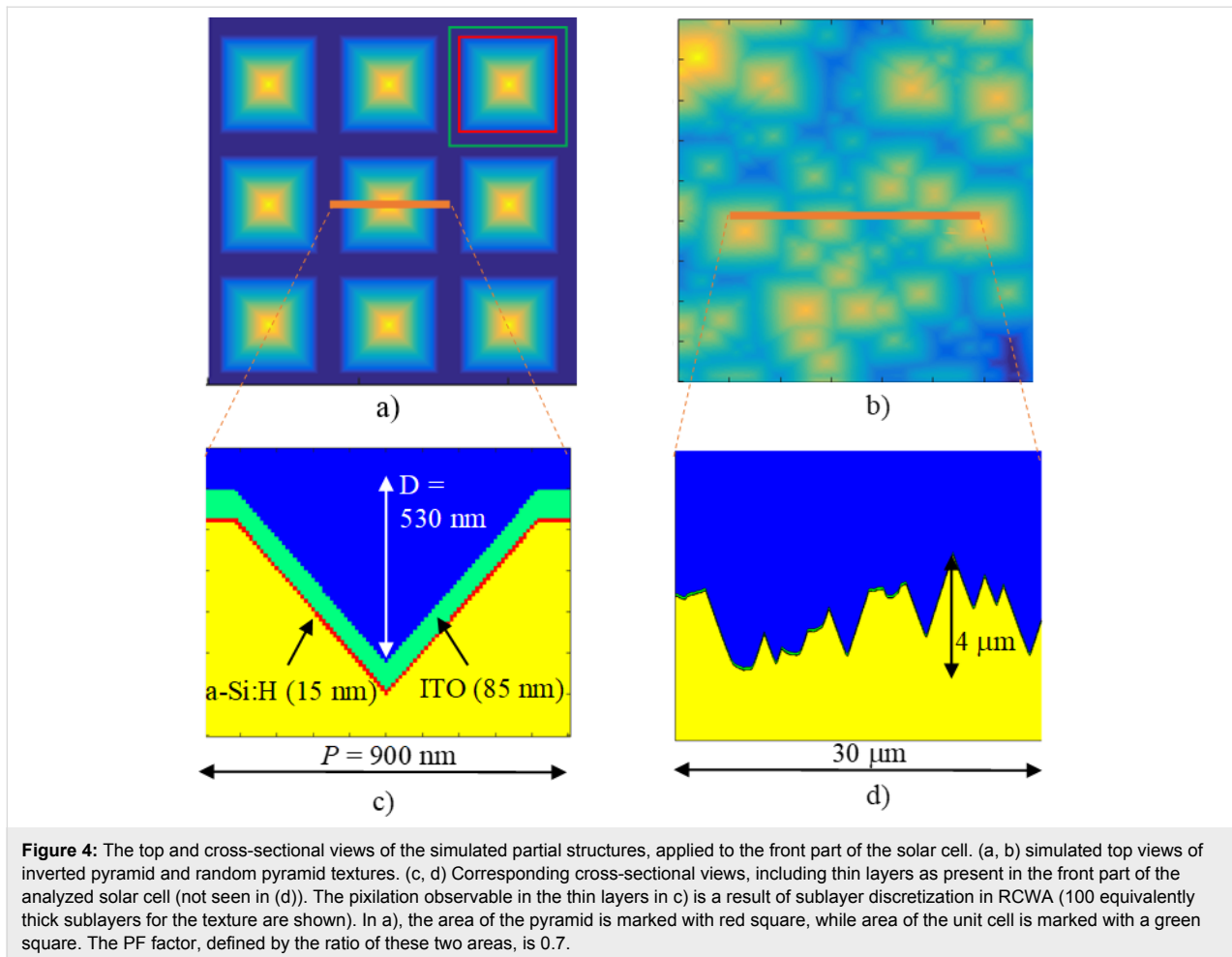
The front of the basic solar cell structure consists of transparent conductive oxide (e.g., indium tin oxide (ITO)), a thin p-doped and intrinsic amorphous silicon (a-Si:H) layer for electrical passivation, a slightly n-doped crystalline Si (c-Si) wafer (absorber), and an intrinsic and n-doped a-Si:H stack; the rear consists of an ITO/Al contact. The textures can be applied to the front and/or rear part of the wafer. In our model, thin layers follow the applied wafer textures. The complex refractive indices of the layers used as input for optical simulations were taken from the PV Lighthouse database [32] and correspond to measurements of realistic layers [18,33-35].

In our analysis, two types of textures were included and applied to either the front or rear interfaces: periodic inverted pyramids or random pyramids. We intentionally focus on the two textures that are commonly applied in HJ Si solar cells. The first one can be experimentally realized on the nanometer scale by UV nanoimprint lithography (NIL) in combination with dry and wet etching of the wafer [6]. The second, the random pyramid texture, is typically used as a microtexture in c-Si solar cells and can be obtained by wet etching with KOH [36].

In Figure 4 simulated top views and cross-sectional profiles of the two textures are presented, in this case applied to the front part of the analyzed solar cell. The corresponding front thin layers are indicated by different colors. In Figure 4a,c the periodic inverted nanopyramid texture is shown for the case of a
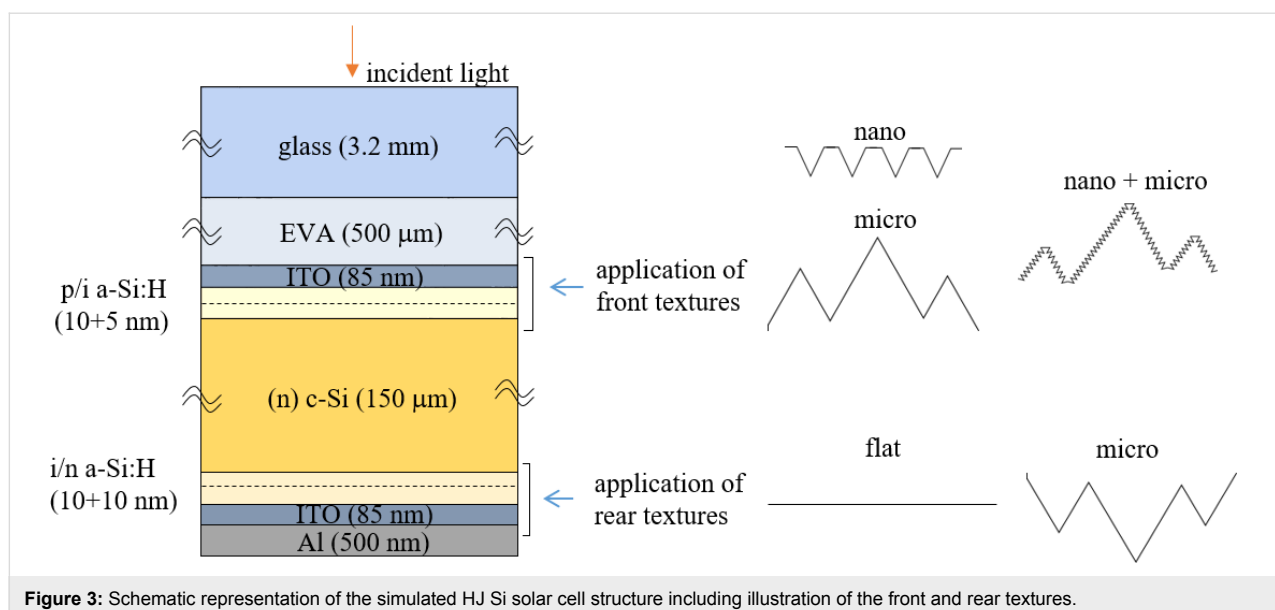
Figure 3: Schematic representation of the simulated HJ Si solar cell structure including illustration of the front and rear textures.

Figure 4: The top and cross-sectional views of the simulated partial structures, applied to the front part of the solar cell. (a, b) simulated top views of inverted pyramid and random pyramid textures. (c, d) Corresponding cross-sectional views, including thin layers as present in the front part of the analyzed solar cell (not seen in (d)). The pixilation observable in the thin layers in c) is a result of sublayer discretization in RCWA (100 equivalently thick sublayers for the texture are shown). In a), the area of the pyramid is marked with red square, while area of the unit cell is marked with a green square. The PF factor, defined by the ratio of these two areas, is 0.7.

period P = 900 nm and depth D = 530 nm, giving an aspect ratio D/P of 0.59. Besides these parameters, the pyramid fraction (PF) is defined as the ratio between the area of the inverted pyramid (red square) and the area of the unit cell (green square) and is 0.7. The depth is dependent on the PF as the pyramid facets are defined by the slow-etching crystallographic plane 111 [6]. In Figure 4b,d the top view of the random microtexture is shown for lateral range of 40×40 μm^2, and a 30 μm long cross-section is shown. In simulations, a random texture from an AFM scan was mirrored across the x and y axis, resulting in an 80×80 μm^2 so-called pseudo-periodic texture used in simulations. A similar approach was also taken in [3]. The micropyramid faces are also defined by the slow-etching 111 crystallographic plane, leading to the same 54.7° angle. The vertical span of the random micropyramids is 9.5 μm, while the correlation length is 3.1 μm.

Figure 4 shows the textures at the front part of the solar cell, although in the analysis of the complete solar cell (see the section "Simulations of an encapsulated solar cell with textures") the random microtexture will also be applied to the rear side of the

solar cell. Moreover, the combination of both textures (nano + micro) will be applied to the front interfaces. The combination assumes a nanotexture (including thin layers) superimposed on the random micropyramid texture in the direction normal to the random micropyramids. The top view corresponds to the top view of random micropyramids in Figure 4b. In the RCWA analysis, only the inverted pyramid texture is investigated, while the pseudo-random microtexture will be simulated using CROWM. The CMA will be used for all the simulations that contain nanotexture on the solar cell level. The simulated structure combinations are summarized in Table 1.

The partial structures were analyzed in the sections "Nanoscale inverted pyramids" (texture 1), "Microscale inverted pyramids" (textures 2) and "Optimization of the nanopyramids with RCWA" (textures 3) with RCWA (also FEM and RT/TMM in comparison). Smaller inverted pyramids (textures 1 and 3) were analyzed at an angle of incidence of 0° and 45°, while larger inverted pyramids (texture 2) were analyzed only for normal incident light. Full cell simulations were performed in the section "Simulations of an encapsulated solar cell with textures"

Table 1: Analyzed structures.

	layers (Figure 3)	textures (Figure 4)
partial structure (front part)	EVA (incident medium)/ITO/a-Si:H/c-Si (outgoing medium)	1. inverted pyramids, *P* = 900 nm, *D* = 530 nm, PF 0.7 2. inverted pyramids, *P* = 1800 and 5000 nm, *D* = 1060 nm and 2940 nm, PF 0.7 3. inverted pyramids, P = 900 nm, *D* = 530–570 nm, PF 0.7–1
full cell	air (incident medium)/EVA/ITO/a-Si:H/c-Si/ a-Si:H/ITO/Ag/air (outgoing medium)	front (EVA→c-Si): 1. inverted pyramids (*P* = 900 nm, *D* = 730 nm, PF 1) 2. microtexture (median height 5 μm, 6 x 10^4 pyramids/mm) 3. microtexture + inverted pyramids superimposed (1+2) rear (c-Si→Ag): 1. flat 2. microtexture

using RCWA for generation of scattering matrices for nanotextures, while RT/TMM was used for the simulation of microtextures and propagation through thick (incoherent) layers. All full cell simulations were performed at 0° light incidence.

Results and Discussion
RCWA accuracy analysis of partial cell structure

The applicability and accuracy of RCWA for solar cell simulations was tested first on a simpler structure – the front part of the analyzed solar cell (EVA/ITO/p/i a-si:H/c-Si) with the inverted pyramid texture (as shown in Figure 4). With this we avoid inclusion of the rear texture at the same time and the incoherent c-Si layer (a c-Si wafer was considered in these simulations only as infinite medium in transmission; the same holds for EVA in reflection direction). In the analysis, we include the inverted pyramid nano- and microscale textures and check the accuracy of simulations. In particular, the effect of the number of sublayers and number of modes used in RCWA simulations was analyzed for two different angles of incidence (0° and 45°). This is an important step before applying the RCWA simulation in the optimization of the texture (see the section "Optimization of the nanopyramids with RCWA"). Normal incident light analysis is a common case in measurements and an important case in outdoor conditions; therefore, we consider it as an important case for verification and optimizations [37]. The incident angle of 45° has been chosen as a representative of oblique illumination. According to the results of additional simulations, the inclusion of other angles would lead to similar conclusions.

Increasing the number of sublayers requires solving more systems of equations and thus the computational time grows linearly. Increasing number of modes greatly increases the size of the system of equations and is especially demanding for both memory and computational time, with approximate time dependence on the order of M^5 [38]. Thus, simulations of structures requiring many modes or sublayers may quickly become unfea-

sible for efficient simulation and optimization of solar cell structures. On the other hand, smaller number of sublayers and modes may lead to inaccuracies of results.

In next subsections we present simulation results on total reflectance, *R*, in the EVA medium of the analyzed partial structure. Besides comparison of wavelength-dependent *R* for different numbers of sublayers and modes used in simulations, we introduce another quantitative measure that highlights the deviations of the different simulations. As the J_{SC} of the solar cell is the most important quantity related to optical confinement in solar cells, we calculated an absolute difference (error) in J_{SC} reflectance loss, $|\Delta J_{SC}|$, from deviations in *R*, as given in Equation 1 as

$$|\Delta J_{\mathrm{sc}}| = \int_{350\,\mathrm{nm}}^{1200\,\mathrm{nm}} |R_1(\lambda) - R_2(\lambda)| S(\lambda) \frac{\lambda q}{\hbar c} d\lambda, \qquad (1)$$

where *q* is the elementary charge, $\hbar$ is the reduced Planck constant and *c* is the speed of light. This parameter is defined as the absolute value of the reflectance difference, which is weighted by the AM1.5g solar spectrum $S(\lambda)$. The $R_2(\lambda)$ is defined as the most accurate simulation obtained, which was ten modes and 300 sublayers for all the cases presented. We validated these parameters with a 20 mode, 1000 sublayer simulation at the reflectance peak, but full analysis at such accuracy is time prohibitive. $R_1(\lambda)$ is defined as the reflectance of the tested simulation.

In this study, the validation of RCWA is performed by comparison to simulation results obtained by applying different simulation techniques (finite element method (FEM) for nanotextures and RT/TMM for microtextures). In this way, measurement uncertainties of samples are avoided and internal quantities, such as the internal reflectance in EVA, can be determined and compared. The FEM and RT simulators used here for reference have been experimentally validated [37], whereas detailed experimental validation of RCWA will be published elsewhere.

Nanoscale inverted pyramids

The period and height, as well as the resulting aspect ratio and pyramid fraction of the analyzed nanoscale inverted pyramids were chosen to be $P = 900$ nm and $D = 530$ nm in this nanoscale section. They had an aspect ratio of $D/P = 0.59$ and PF = 0.7 (the same as depicted in Figure 4). Textures with P and D in this range were previously identified for this particular type of solar cell as one of the most efficient light management structures [6]. The analyzed structures also contain thin layers – 85 nm thick ITO and 15 nm thick a-Si:H. The total height of the simulated structure is $H = 630$ nm.

The plots on the left side of Figure 5 show the effects of the variation in the number of sublayers. The plots on the right side demonstrate the effects of the variation of the number of modes. The top two graphs of Figure 5 (a) and (b) correspond to the reflectance of the substructure with inverted pyramid textures and vertical light incidence, the middle two graphs (c) and (d) present the reflectance of the same substructure at 45° light incidence, whereas the bottom two graphs (e) and (f) are the corresponding $|\Delta J_{SC}|$ values for RCWA simulations with different numbers of sublayers and modes compared to the reference simulation.

A general observation from the reflectance curves (Figure 5) is that the vertical light incidence (0°) leads to somewhat lower reflectance than other angles of incidence (shown for 45°). For validation of the reflectance behavior, simulations obtained by FEM [39] are added for the case of the inverted pyramid texture for normal incidence light. 45° light incidence prevents the use of all symmetries. This angle leads to larger simulation volumes and large simulation errors in FEM simulations. It must be mentioned that this simulation was not taken as a reference for the accuracy study. Its purpose is to additionally validate the wavelength dependence of the reflectance obtained by RCWA.

Furthermore, we analyze the effects of the number of sublayers used in the RCWA simulation. The results in Figure 5a,c suggest that for good convergence towards a steady solution, 30 sublayers are sufficient for both angles of incidence, at least for wavelengths above 450 nm. The errors in J_{SC} as a function of the number of sublayers (Figure 5e) indicate a lower $|\Delta J_{SC}|$ for the case of normal incident light. 300 sublayers were used as the reference (most accurate) simulation. For 30 or more sublayers, the simulated $|\Delta J_{SC}|$ drops below the chosen threshold line of 0.1 mA/cm^2 for 0° light incidence, while 50 sublayers are required for 45° incidence. This threshold corresponds to 0.27% of the total J_{SC} reflectance loss (36.87 mA/cm^2) of the structure with inverted pyramidal nanotexture on the front side and flat rear side.

We proceed with the analysis of the number of modes used in RCWA simulations (Figure 5b,d). The first observation is that even three modes are sufficient for predicting the correct reflectance trends for both the vertical and non-vertical light incidence. The convergence of non-vertical incidence is again a bit worse than for the vertical incidence, although the differences are small from 500 nm onwards. The errors in J_{SC} as a function of the number of sublayers show that the $|J_{SC}|$ error corresponding to case of normal incident light drops below the threshold of 0.1 mA/cm^2 with three modes (ten modes were used as the reference), while in case of non-normal incident light, at least six modes are required to meet this threshold.

When comparing the $|\Delta J_{SC}|$ plots corresponding to the variation in the number of sublayers (Figure 5e) and number of modes (Figure 5f), we generally observe a smaller effect for the changing number of modes (note the different scales). 50 sublayers and six modes were found to be sufficient for both normal incident light as well as at 45° incidence, considering the chosen 0.1 mA/cm^2 threshold. These settings were considered as the minimal required values in our further simulations of structures with nanotexture. In application of RCWA to optimize the inverted pyramid nanotextures (see section "Optimization of the nanopyramids with RCWA"), we used 300 sublayers and ten modes. In CMA simulations (see section "Simulations of an encapsulated solar cell with textures"), we used 100 sublayers and 5 modes in the RCWA part as the initial angle of incidence of light is perpendicular to the surface (0°), and we tested the parameters to be sufficient for good accuracy.

Microscale inverted pyramids

The lateral and vertical dimensions of the inverted pyramid texture were extended here by the same factor compared to textures analyzed in the previous section, while maintaining a constant thin-layer thickness. The same convergence analysis was carried out for the textures with $P = 1800$ nm and 5000 nm to detect possible limitations of the RCWA method with respect to feature size. The same number of modes and sublayers were used to make the comparison at equal simulation times (approximately one day for the most accurate case of ten modes and 300 sublayers on a typical desktop PC). The first period was selected as the double of the $P = 900$ nm nanotexture, while the second value was selected to approach the size of an individual micropyramid of the given random texture. The aspect ratio D/P was kept constant at 0.59 with respect to the nanotextures, resulting in $D = 1060$ nm ($P = 1800$ nm) and 2940 nm ($P = 5000$ nm). Likewise, the PF was also kept constant at 0.7, as was the thickness of ITO (85 nm) and a-Si:H (15 nm). For validation we added in this case simulations with RT/TMM (using the simulator CROWM) for the texture with
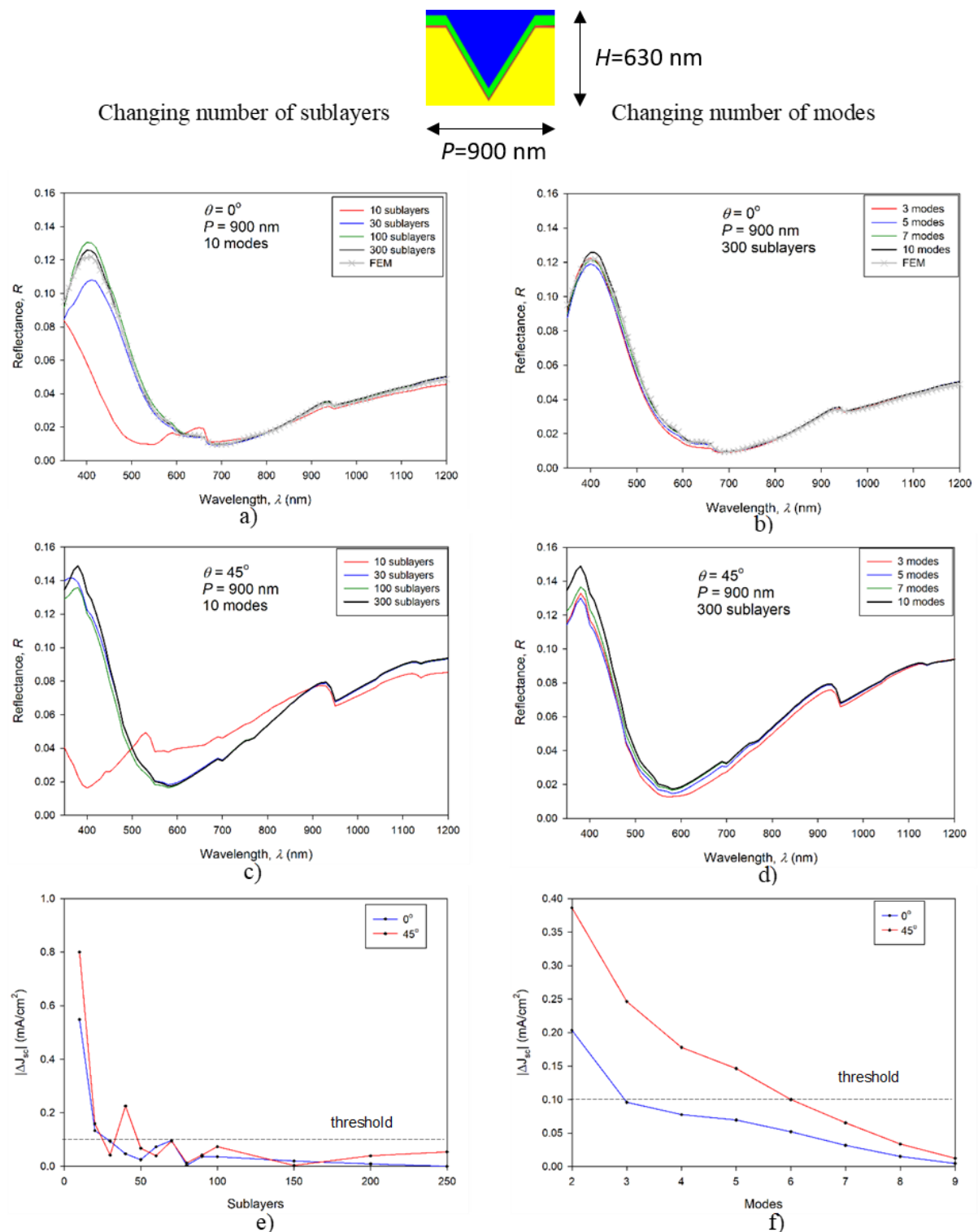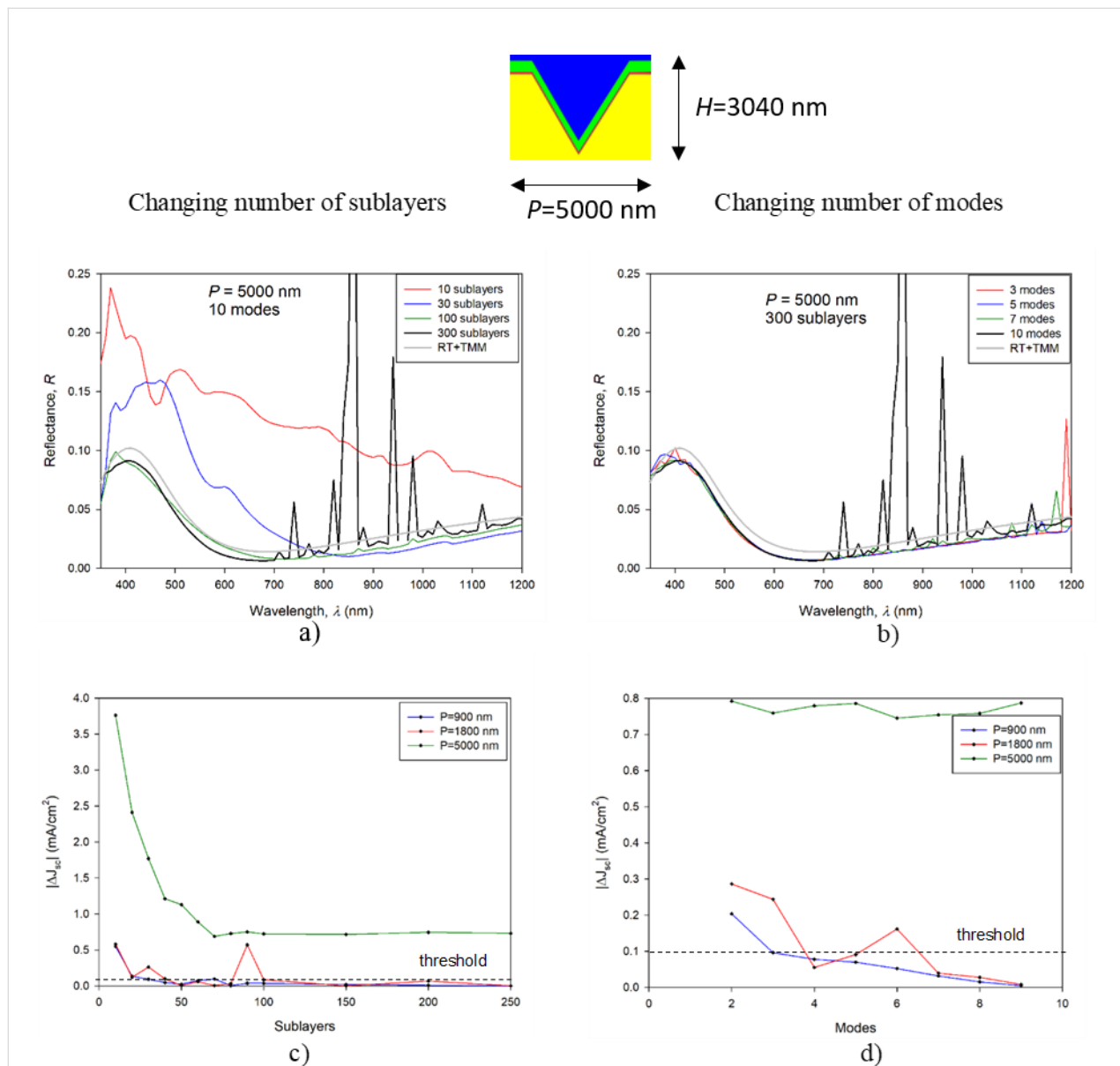
Figure 5: Analysis of the RCWA convergence for the nanoscale textures. All graphs on the left hand side correspond to the results of the variation in the number of sublayers with a fixed number of modes (ten modes) whereas the right hand side graphs represent the results of the variation in the number of mode with a fixed number of sublayers (300 sublayers). The top two graphs (a, b) correspond to an incident angle of 0° whereas the middle two (c, d) are for the incident angle of 45°. The bottom two graphs (e, f) quantify deviations between RCWA results using the |ΔJ_{SC}| measure.

P = 5000 nm. Such large features can be tackled with geometrical optics and are too large for FEM simulation, which was used for simulation of the nanotextures. The results corresponding to normal incident light are presented here.

The reflectance curves in Figure 6a,b correspond only to the largest texture (*P* = 5000 nm, *H* = 2950 nm), whereas the $|\Delta J_{SC}|$ results in Figure 6c,d are presented for the textures with *P* = 900 nm (from the previous analysis), 1800 nm and 5000 nm.

The results for the texture with *P* = 5000 nm indicate a much larger effect of the number of sublayers on the reflectance curves (Figure 6a), compared to the texture with *P* = 900 nm (Figure 5a). Smaller deviations are observed with respect to the number of modes (Figure 6b). Many artefacts occur for ten modes and 300 sublayers with some present for lower numbers of modes as well. We assign these artefacts to numerical errors in the RCWA simulations. In particular, with an increasing number of sublayers and modes, the system of equations becomes rank deficient either due to numerical difficulties or

Figure 6: Analysis of RCWA convergence for micrometer-sized textures. Left hand side graphs correspond to the results of variation of the number of sublayers with a fixed number of modes, while the right hand side graphs correspond to the results of variation of the number of modes with a fixed number of sublayers. The top two graphs (a, b) show visual pyramidal texture convergence with number of sublayers and modes. Graphs (c) and (d) quantify the difference between the RCWA results using the $|\Delta J_{SC}|$ measure.

due to particular match between period and wavelength [22]. Rank deficiency leads to inaccurate results, as can be seen with the artefacts, or even results in no solution. The additional simulations of structures with macrotextures showed that the system becomes more stable if materials with higher absorption are used, as the numerical artefacts cannot propagate throughout the layers.

Furthermore, the results do not converge to the final solution even if the number of sublayers is increased to 300, as they did in the case of the substructure with $P = 900$ nm. The general trend of the results shows a gradual approach towards the shape of the curve obtained by RT/TMM results, while the offset remains even at 300 sublayers. This offset is not assigned to any systematic error in RCWA or RT/TMM simulations. A single wavelength simulation of the structure sliced to 1000 sublayers was performed at $\lambda = 400$ nm, obtaining 1% error in R ($\lambda = 400$ nm) compared to RT/TMM, whereas in the simulation with 300 sublayers, this error was 10%. A further increase in the number of sublayers was not attempted for the entire wavelength range due to calculation time constraints. On the level of $|\Delta J_{SC}|$ (Figure 6c), we can observe an increasing error with respect to increasing period for the same number of sublayers and modes. By doubling the texture period (e.g., from $P = 900$ nm to 1800 nm) we need to increase the number of sublayers by more than a factor of two to achieve comparable accuracy. On the other hand, there is no significant increase in the error with respect to the number of required modes. This trend suggests that the $P = 5000$ nm result would require at least roughly 500 sublayers with ten modes for suitable accuracy (excluding artefacts), and above 1000 sublayers and 15 modes for high-accuracy simulation of such structures.

The presented analysis shows that the RCWA method can be efficiently applied for the simulation of structures with textures up to 2–3 μm periods (on a typical current desktop computer with four cores, eight threads at 4 GHz, 32 GB RAM, though presented simulations required only about 8 GB) for wide-wavelength-range simulations (350–1200 nm at a step of 10 nm). We also have to keep in mind that we simulated only a partial structure of the solar cell. Larger textures and structures of complete devices (including rear textures) would need a large number of sublayers and modes. Faster computers or clusters would enable simulation of structures larger than those presented, but still, it needs to be emphasized that doubling of both the total modes and sublayers requires a computer approximately ten times faster to solve the problem in the same time [38], ultimately limiting the size of the texture that can be considered. Larger structures such as the (pseudo-)random micropyramids introduced in Figure 4 cannot reasonably be

attempted, even on current and upcoming supercomputers, and thus require additional simulation approaches that can accurately deal with large sizes.
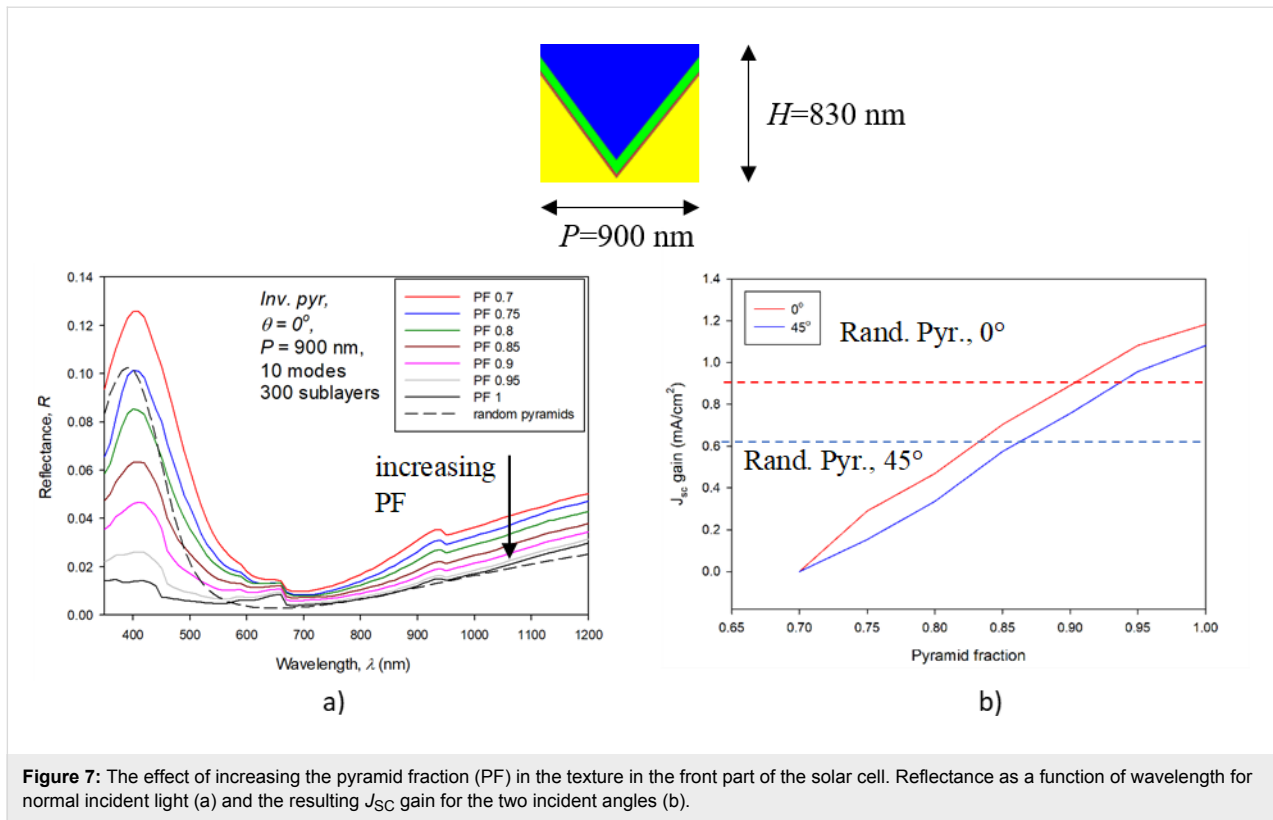
Application of the simulation tools
Optimization of the nanopyramids with RCWA
We performed optimization of the inverted nanopyramids by means of RCWA simulations. In particular, the PF was varied from the starting value of 0.7 (as depicted in Figure 4) to 1. The PF was found to be an important parameter for optimization of the antireflection effect. In this optimization, the period of the unit cell was held at 900 nm. The depth of the pyramid was changed accordingly with the PF, maintaining the same angle of the pyramid facets (linked to anisotropic etching), while the thickness of ITO and a-Si:H was kept constant.

In Figure 7 the effects of PF variation on reflectance and on the corresponding J_{SC} gain are shown. The front part of the solar cell was simulated by RCWA as in previous sections. In these simulations, ten modes and 300 sublayers were used. We optimized the PF with respect to decreased reflectance of the front part of the cell, giving the possibility to additionally increase J_{SC}. The presented J_{SC} gain shows the full potential of the improved antireflection effect, where all additionally in-coupled light would be absorbed and transferred into photocurrent. Thus, these are the maximal potential gains related to the given PF variation. As a reference (zero gain) the structure with PF 0.7 was taken. In Figure 7a the reflectance curves are shown for the case of normal incident light. As a reference, the reflectance curve corresponding to the random micropyramid texture is added to the graph (calculated by RT/TMM). The results indicated that by increasing the PF of the inverted nanopyramids, the antireflection effect is improved (reflectance curves decrease monotonically). In the short-wavelength region ($\lambda < 600$ nm) the textures with an increased pyramid fraction (PF > 0.75) exhibit smaller reflection than the typically used random microtextures. However, at longer wavelengths, only the curve corresponding to the highest pyramid fraction (PF 1) approaches the results of the random pyramid case.

In Figure 7b the corresponding J_{SC} gains are shown for the case of normal (0°) and non-normal (45°) incident light. In both cases, the J_{SC} gain increases monotonically while increasing the PF. The zero-gain case is set to the structure with PF 0.7. The reference lines corresponding to the random microtexture are added for the two incident angles. The results of the optimization show the potential for a J_{SC} gain of 1.18 mA/cm^2 and 1.08 mA/cm^2 for normal incident light and 45° incident illumination, respectively. Additional simulations were performed to investigate the effect of the period of the inverted pyramid

Figure 7: The effect of increasing the pyramid fraction (PF) in the texture in the front part of the solar cell. Reflectance as a function of wavelength for normal incident light (a) and the resulting J_{SC} gain for the two incident angles (b).

texture and showed that increasing the P from 900 nm to 1800 nm with PF 0.7 leads to further (minor) improvement; however, the difference is just 0.1 mA/cm^2.
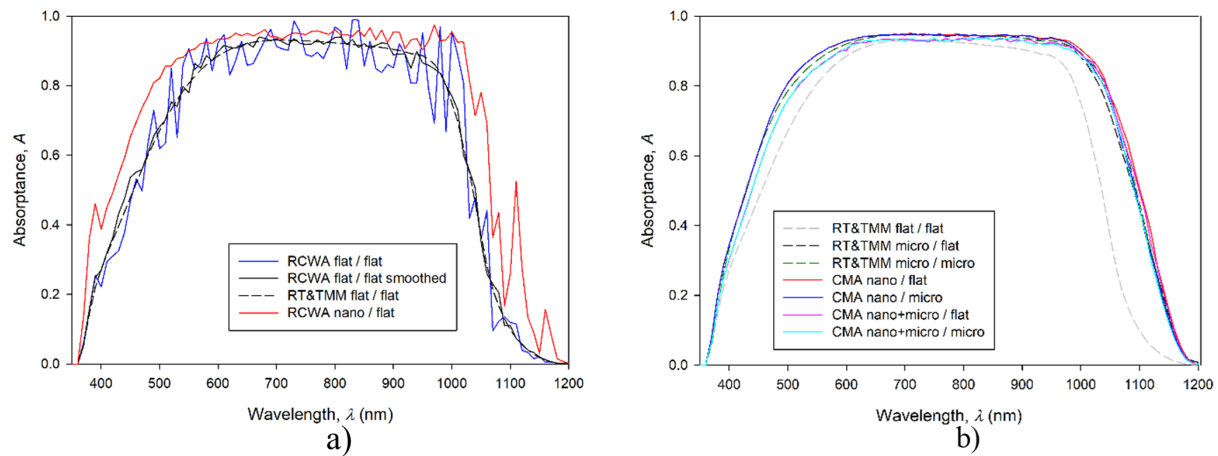
Simulations of an encapsulated solar cell with textures

In the following, we present simulation results of complete HJ Si solar cell (structure from Figure 3) with different textures (as indicated in Figure 4) applied to the front and to the rear side of the solar cell. We are using the optimized nanotexture from the preceding section (P = 900 nm, D = 730 nm, PF = 1) in all graphs presented in Figure 8. Incident light is at 0°. Simulation parameters are summarized in Table 1.

In Figure 8 simulated absorptance curves (A) in the c-Si wafer of the encapsulated HJ Si solar cell are presented for various textures applied to the front and/or rear part of the solar cell. Different simulation approaches were applied. We assumed an ideal extraction of light-generated charge carriers from the c-Si wafer and neglected contributions of carriers from thin amorphous layers (replicating state-of-the-art devices). Under this realistic assumption, the A can be assumed to be equal to the external quantum efficiency, EQE, of the device [18]. In this case, the potential J_{SC} of the solar cells can be calculated directly from A by applying the AM1.5g solar spectrum (S) with the following equation (see J_{SC} values in Table 2):

$$J_{sc} = \int_{350\,\text{nm}}^{1200\,\text{nm}} A(\lambda)S(\lambda)\frac{\lambda q}{\hbar c}d\lambda. \tag{2}$$

We additionally assume that, due to the same thickness of the ITO and a-Si:H layers, the electrical performance should be similar for all simulated structures.

In Figure 8a we show the results of the RCWA and RT/TMM simulations applied to a complete HJ Si solar cell structure with (i) flat front and flat rear interfaces (denoted by flat/flat) and (ii) nanotextured front (inverted nanopyramids) and flat rear interfaces (nano/flat). In RCWA simulations of the complete device, interference fringes are observed. They originate from the fully coherent treatment of the thick c-Si wafer in RCWA and are not present in experimental spectral measurements of solar cells (not shown here). The interferences can be smoothed out by averaging the simulation results, especially if simulated at 1 nm wavelength accuracy. The smoother result shown in the figure was achieved by averaging the absorption at 11 wavelengths simulated on 1 nm and presented on 10 nm, as with all other simulations. The convolution of the absorption with a Gaussian function produces similar results to this averaging (not shown). This averaged curve is in good agreement with the result of the same (flat/flat) structure simulated by the RT/TMM tool, although the RT/TMM simulation results are still smoother.

Figure 8: Simulated absorptances in the c-Si layer of the HJ Si solar cell using RCWA, RT/TMM (CROWM simulator) and CMA. Comparison between RCWA and RT/TMM is shown in (a). (b) RT/TMM and CMA simulations of the solar cell with a nanotexture with PF 1. Corresponding J_{SC} values calculated from the absorptance curves are listed in Table 2.

Table 2: Simulated J_{SC} of the encapsulated solar cells with different textures.

simulation method	front texture/rear texture	J_{SC} (mA/cm^2)	relative J_{SC} gain (%)
RT/TMM	flat/flat	32.96	0
CMA	nano+micro/micro	36.24	10.0
CMA	nano+micro/flat	36.43	10.5
RT/TMM	micro/flat	36.69	11.3
RT/TMM	micro/micro	36.88	11.9
CMA	nano/micro	37.11	12.6
CMA	nano/flat	37.39	13.4

The simulation of the structure in nano/flat configuration simulated by RCWA is shown only for the non-averaged case. Even this non-smoothed curve indicates the improvement trend in *A* when a nanotexture is introduced at the front. The improvements are observed in short- and long-wavelength regions of *A*. The short-wavelength range improvement is a consequence of better antireflection (AR) properties at the front interfaces, compared to the flat structure in this case. For wavelengths in the range 500–800 nm, the optimized front thin film stack serves as an efficient AR coating already in the flat device, so the addition of nanotexture does not improve the results much further in this wavelength region. The differences in the long-wavelength region of *A* are a consequence of light scattering on the front nanotexture, enhancing the light trapping effect in the structure. With the results shown in Figure 8a, we exploit the potential of efficient simulation of the cell with RCWA and proceed with the CMA, which opens possibilities for a broad range of textures and their combinations.

Figure 8b presents the results of CMA simulations for various combinations of front and rear textures. To indicate the improvements in *A* related to different textures and their combinations, a reference curve corresponding to the RT/TMM simulation of the flat/flat cell is shown also in this figure (grey curve). In all simulations shown in Figure 8b no interference fringes are observed since in the RT/TMM and CMA methods, thick layers are treated incoherently. Whereas the RT/TMM method itself is applied to the structures (including flat interfaces and microtextures), the CMA is used for all structures, including nanotextures. Next, we focus on the improvements in solar cell performance related to the different textures and their combinations. The first observation is that in the wavelength region 650–750 nm, all *A* curves are relatively close together as the selected thicknesses of the front thin layers assure good AR properties (already in the flat/flat case). However, significant improvements related to the textures are observed in short- and especially in long-wavelength region. According to the optimi-

zation results obtained in the section "Optimization of the nanopyramids with RCWA" for the front part of the structure, the cells with a nanotextured front interfaces (nano/flat, nano/micro) exhibit the highest gain in A in the short-wavelength part (λ < 600 nm). In this wavelength region, the rear part of the cell does not influence A as the light is absorbed before reaching there. In the long-wavelength region, the simulation showed that the total increase in the optical path due to light scattering or refraction of long-wavelength light is mainly caused by increased back reflections at the front interfaces of the devices. By internal redirection of light propagation, total reflection of light waves can occur at front interfaces if the incident angles meet the condition of total reflection. The nano/flat combination of textures performed the best, while the second-best nano/microtexture had comparable light trapping ability, but higher parasitic absorption in the textured rear layers.

Among the combinations tested, special attention should be paid to the combined nano + micro front texture. From the simulation results, it can be observed that such a combined texture surprisingly does not outperform the solar cells with (single) nano- or microtextures on the front. Its main drawback was poor AR performance in the short-wavelength region. However, it is known that, in general, combined textures have potential to outperform the corresponding individual textures [4], but as indicated from the results, they must be carefully optimized for the particular solar cell structure. Here simulations can play an important role.

The improvements in A shown in Figure 8b were also transferred to the J_{SC} values of the complete solar cells. The absolute J_{SC} values and their relative improvement to the flat/flat case are summarized in Table 2. The simulated results are listed from lowest to highest J_{SC}.

Table 2 shows simulated J_{SC} values in ascending order. All textures significantly improved the J_{SC} of the solar cell by at least 10% compared to the flat case. The nano/flat texture performs the best, in accordance with the observed A trends in Figure 8b, reaching J_{SC} = 37.39 mA/cm^2. In addition to the J_{SC} being 4.43 mA/cm^2 (13.4%) higher than that of the untextured solar cell, it also outperforms the microtextured solar cell by 0.51 mA/cm^2 (1.4%). This is significantly higher than the accuracy of the CMA, estimated at 0.1 mA/cm^2. At the solar cell level, further improvement in J_{SC} might be achieved for example by optimizing the thin-layer thickness for the particular texture. Furthermore, the optimization of the solar cell or photovoltaic module structure might include additional antireflective and light management coatings.

Conclusion

In the paper, we have analyzed the RCWA performance in terms of reliability and accuracy of the optical simulation of solar cell structures, in particular for HJ Si solar cells with textures for light management. For efficient simulation of whole HJ Si solar cells, including nano- and microtextures, a coupled modeling approach (CMA) was introduced where RCWA is coupled with RT/TMM. We tested the applicability and accuracy of RCWA by changing the number of sublayers and modes in RCWA simulations. The analysis showed that RCWA is an efficient simulation method for structures with textures in the nanometer size range. RCWA was applied to optimize inverted nanopyramid textures at the front side of a HJ Si solar cell by changing the pyramid fraction (PF). The optimized nanotexture had a PF of 1, i.e., full pyramid coverage.

We applied the CMA to simulate the complete HJ Si solar cell structure, including the front encapsulation and glass, including nano- and microtextures at the interfaces of the cell. The simulation results showed that optimized nanotextures can outperform currently used microtextures, resulting in a J_{SC} increase of 0.51 mA/cm2 (1.4%). A combined nano/microtexture was shown to require further individual optimization as the simulations currently indicate it does not outperform the front nano- or microtexture individually.

ORCID® iDs

Ziga Lokar - https://orcid.org/0000-0002-4957-5900
Benjamin Lipovsek - https://orcid.org/0000-0002-7978-3671
Marko Topic - https://orcid.org/0000-0001-8089-2974

References

1. Nam, W. I.; Yoo, Y. J.; Song, Y. M. *Opt. Express* **2016,** *24,* A1033–A1044. doi:10.1364/OE.24.0A1033
2. Bett, A. J.; Eisenlohr, J.; Höhn, O.; Repo, P.; Savin, H.; Bläsi, B.; Goldschmidt, J. C. *Opt. Express* **2016,** *24,* A434–A445. doi:10.1364/OE.24.00A434
3. Muller, J.; Herman, A.; Mayer, A.; Deparis, O. *Opt. Express* **2015,** *23,* A657–A670. doi:10.1364/OE.23.00A657
4. Ingenito, A.; Isabella, O.; Zeman, M. *Prog. Photovoltaics* **2015,** *23,* 1649–1659. doi:10.1002/pip.2606
5. Wangyang, P.; Wang, Q.; Hu, K.; Wan, X.; Huang, K. *Opt. Commun.* **2013,** *294,* 395–400. doi:10.1016/j.optcom.2012.12.024
6. Trompoukis, C.; Abdo, I.; Cariou, R.; Cosme, I.; Chen, W.; Deparis, O.; Dmitriev, A.; Drouard, E.; Foldyna, M.; Garcia-Caurel, E.; Gordon, I.; Heidari, B.; Herman, A.; Lalouat, L.; Lee, K.-D.; Liu, J.; Lodewijks, K.; Mandorlo, F.; Massiot, I.; Mayer, A.; Mijkovic, V.; Muller, J.; Orobtchouk, R.; Poulain, G.; Prod'Homme, P.; Roca i Cabarrocas, P.; Seassal, C.; Poortmans, J.; Mertens, R.; El Daif, O.; Depauw, V. *Phys. Status Solidi A* **2015,** *212,* 140–155. doi:10.1002/pssa.201431180
7. Khaleque, T.; Svavarsson, H. G.; Magnusson, R. *Opt. Express* **2013,** *21,* A631–A641. doi:10.1364/OE.21.00A631

8. Trompoukis, C.; El Daif, O.; Pratim Sharma, P.; Sivaramakrishnan Radhakrishnan, H.; Debucquoy, M.; Depauw, V.; Van Nieuwenhuysen, K.; Gordon, I.; Mertens, R.; Poortmans, J. *Prog. Photovoltaics* **2015**, *23,* 734–742. doi:10.1002/pip.2489

9. Karakasoglu, I.; Wang, K. X.; Fan, S. *ACS Photonics* **2015**, *2,* 883–889. doi:10.1021/acsphotonics.5b00081

10. Krc, J.; Topic, M. *Optical Modeling and Simulation of Thin-Film Photovoltaic Devices;* CRC Press: New York, 2013. doi:10.1201/b14551

11. Wang, C.; Yu, S.; Chen, W.; Sun, C. *Sci. Rep.* **2013**, *3,* No. 1025. doi:10.1038/srep01025

12. Sever, M.; Krč, J.; Čampa, A.; Topič, M. *Opt. Express* **2015**, *23,* A1549–A1563. doi:10.1364/OE.23.0A1549

13. Lipovšek, B.; Čampa, A.; Guo, F.; Brabec, C. J.; Forberich, K.; Krč, J.; Topič, M. *Opt. Express* **2017**, *25,* A176–A190. doi:10.1364/OE.25.00A176

14. Shokeen, P.; Jain, A.; Kapoor, A. *J. Nanophotonics* **2016**, *10,* 036013. doi:10.1117/1.JNP.10.036013

15. Onwudinanti, C.; Vismara, R.; Isabella, O.; Grenet, L.; Emieux, F.; Zeman, M. *Opt. Express* **2016**, *24,* A693–A707. doi:10.1364/OE.24.00A693

16. Civiletti, B. J.; Anderson, T. H.; Ahmad, F.; Monk, P. B.; Lakhtakia, A. *Opt. Eng. (Bellingham, WA, U. S.)* **2018**, *57,* 057101. doi:10.1117/1.OE.57.5.057101

17. Ahmad, F.; Anderson, T. H.; Civiletti, B. J.; Monk, P. B.; Lakhtakia, A. *J. Nanophotonics* **2018**, *12,* 016017. doi:10.1117/1.JNP.12.016017

18. Holman, Z. C.; Descoeudres, A.; Barraud, L.; Fernandez, F. Z.; Seif, J. P.; De Wolf, S.; Ballif, C. *IEEE J. Photovoltaics* **2012**, *2,* 7–15. doi:10.1109/JPHOTOV.2011.2174967

19. Topič, M.; Sever, M.; Lipovšek, B.; Čampa, A.; Krč, J. *Sol. Energy Mater. Sol. Cells* **2015**, *135,* 57–66. doi:10.1016/j.solmat.2014.09.026

20. Lokar, Ž.; Krč, J.; Topič, M. Analysis of RCWA Validity for Optical Simulations of Si Solar Cells with Various Textures. *Light, Energy and the Environment;* OSA Technical Digest (online); Optical Society of America, 2016; PTh2A.7. doi:10.1364/PV.2016.PTh2A.7

21. Tucher, N.; Eisenlohr, J.; Kiefel, P.; Höhn, O.; Hauser, H.; Peters, M.; Müller, C.; Goldschmidt, J. C.; Bläsi, B. *Opt. Express* **2015**, *23,* A1720–A1734. doi:10.1364/OE.23.0A1720

22. Moharam, M. G.; Grann, E. B.; Pommet, D. A.; Gaylord, T. K. *J. Opt. Soc. Am. A* **1995**, *12,* 1068–1076. doi:10.1364/JOSAA.12.001068

23. Moharam, M. G.; Pommet, D. A.; Grann, E. B.; Gaylord, T. K. *J. Opt. Soc. Am. A* **1995**, *12,* 1077–1086. doi:10.1364/JOSAA.12.001077

24. Li, L. *J. Opt. Soc. Am. A* **1997**, *14,* 2758–2767. doi:10.1364/JOSAA.14.002758

25. Rumpf, R. C. *Prog. Electromagn. Res.* **2011**, *B 35,* 241–261. doi:10.2528/PIERB11083107

26. Yoshikawa, K.; Kawasaki, H.; Yoshida, W.; Irie, T.; Konishi, K.; Nakano, K.; Uto, T.; Adachi, D.; Kanematsu, M.; Uzu, H.; Yamamoto, K. *Nat. Energy* **2017**, *2,* No. 17032. doi:10.1038/nenergy.2017.32

27. Topic, M.; Jost, M.; Sever, M.; Filipic, M.; Lokar, Z.; Lipovsek, B.; Campa, A.; Krc, J. Design Challenges for Light Harvesting in Photovoltaic Devices. In *Proceedings Volume 9898,* Photonics for Solar Energy Systems VI; 2016. doi:10.1117/12.2231756

28. Lipovšek, B.; Krč, J.; Topič, M. *Informacije MIDEM* **2011**, *41,* 264–271.

29. LPVO:CROWM. http://lpvo.fe.uni-lj.si/en/software/crowm/ (accessed Aug 4, 2017).

30. Rothemund, R.; Umundum, T.; Meinhardt, G.; Hingerl, K.; Fromherz, T.; Jantsch, W. *Solid State Phenom.* **2011**, *178–179,* 446–450. doi:10.4028/www.scientific.net/SSP.178-179.446

31. Raja, W.; Schmid, M.; Toma, A.; Wang, H.; Alabastri, A.; Proietti Zaccaria, R. *ACS Photonics* **2017**, *4,* 2025–2035. doi:10.1021/acsphotonics.7b00406

32. Refractive index library. https://www2.pvlighthouse.com.au/resources/photovoltaic%20materials/refractive%20index/refractive%20index.aspx (accessed June 8, 2017).

33. Vogt, M. R.; Holst, H.; Schulte-Huxel, H.; Blankemeyer, S.; Witteck, R.; Hinken, D.; Winter, M.; Min, B.; Schinke, C.; Ahrens, I.; Köntges, M.; Bothe, K.; Brendel, R. *Energy Procedia* **2016**, *92,* 523–530. doi:10.1016/j.egypro.2016.07.136

34. Holman, Z. C.; Filipič, M.; Descoeudres, A.; De Wolf, S.; Smole, F.; Topič, M.; Ballif, C. *J. Appl. Phys.* **2013**, *113,* No. 013107. doi:10.1063/1.4772975

35. Green, M. A. *Sol. Energy Mater. Sol. Cells* **2008**, *92,* 1305–1310. doi:10.1016/j.solmat.2008.06.009

36. Muñoz, D.; Carreras, P.; Escarré, J.; Ibarz, D.; De Nicolás, S. M.; Voz, C.; Asensi, J. M.; Bertomeu, J. *Thin Solid Films* **2009**, *517,* 3578–3580. doi:10.1016/j.tsf.2009.01.024

37. Lipovšek, B.; Krč, J.; Topič, M. *IEEE J. Photovoltaics* **2014**, *4,* 639–646. doi:10.1109/JPHOTOV.2013.2293875

38. Lokar, Z.; Krč, J.; Topič, M. Optical Model Based on RCWA for Efficient Simulations of Solar Cells. In *MIDEM 2015 conference proceedings*; pp 34–39.

39. Multiphysics Simulation Software - Platform for Physics-Based Modeling. https://www.comsol.com/comsol-multiphysics#overview (accessed Aug 12, 2016).

Hydrothermal-derived carbon as a stabilizing matrix for improved cycling performance of silicon-based anodes for lithium-ion full cells

Mirco Ruttert[1], Florian Holtstiege[1], Jessica Hüsker[1], Markus Börner[1], Martin Winter[*1,2,§] and Tobias Placke[*1,¶]

Abstract

In this work, silicon/carbon composites are synthesized by forming an amorphous carbon matrix around silicon nanoparticles (Si-NPs) in a hydrothermal process. The intention of this material design is to combine the beneficial properties of carbon and Si, i.e., an improved specific/volumetric capacity and capacity retention compared to the single materials when applied as a negative electrode in lithium-ion batteries (LIBs). This work focuses on the influence of the Si content (up to 20 wt %) on the electrochemical performance, on the morphology and structure of the composite materials, as well as the resilience of the hydrothermal carbon against the volumetric changes of Si, in order to examine the opportunities and limitations of the applied matrix approach. Compared to a physical mixture of Si-NPs and the pure carbon matrix, the synthesized composites show a strong improvement in long-term cycling performance (capacity retention after 103 cycles: ≈55% (20 wt % Si composite) and ≈75% (10 wt % Si composite)), indicating that a homogeneous embedding of Si into the amorphous carbon matrix has a highly beneficial effect. The most promising Si/C composite is also studied in a LIB full cell vs a NMC-111 cathode; such a configuration is very seldom reported in the literature. More specifically, the influence of electrochemical prelithiation on the cycling performance in this full cell set-up is studied and compared to non-prelithiated full cells. While prelithiation is able to remarkably enhance the initial capacity of the full cell by ≈18 mAh g^{-1}, this effect diminishes with continued cycling and only a slightly enhanced capacity of ≈5 mAh g^{-1} is maintained after 150 cycles.

Introduction

Since their market launch in 1991, the energy density of lithium-ion batteries (LIBs) has increased steadily. However, further improvements in terms of power density and energy density are essential to meet the rising requirements for automotive applications, e.g., extended driving range and fast charging ability. Such improvements can either be achieved by the optimized engineering of cell components or the development of new cell chemistries with advanced active materials [1-6].

In this context, it is remarkable that the LIB cell chemistry concerning the negative electrode (anode) of commercial cells is still quite similar to that of the very first LIBs, based on carbonaceous anode materials. There are several good reasons why carbonaceous anode materials, especially graphite, are still state of the art. For example, they maintain a high specific capacity (372 mAh g^{-1}) compared to cathode materials, high electrochemical stability in suitable electrolytes, a low operation potential (0.2 V vs Li/Li$^+$), low voltage hysteresis, low cost, and are environmentally friendly [7,8]. Nonetheless, alternative anode materials, such as silicon (Si) and tin (Sn), have aroused great interest in the last decade with the aim to replace graphite, as these materials offer considerably higher theoretical, specific capacities of 3,579 mAh g^{-1} and 990 mAh g^{-1}, respectively, compared to that of graphite [9-12]. The high capacity of Si results from a different lithium-ion storage mechanism compared to graphite: while graphite intercalates Li-ions into its host structure, Si "alloys" with Li (or more precisely, forms various intermetallic phases) at a maximum stoichiometry of Li$_{15}$Si$_4$ at ≈50 mV vs Li/Li$^+$ [13]. Si is considered as the most promising candidate to replace graphite because, aside from the high gravimetric and volumetric capacity, this material can be obtained from inexpensive and highly available precursors (e.g., silicon dioxide) and still offers a relatively low operating potential (≈0.4 vs Li/Li$^+$). Therefore, high cell voltages can be achieved using appropriate cathode materials [10,12,14].

Based on energy density calculations, it was reported that the total specific capacity can significantly be increased on the cell level by the application of high capacity anode materials. Considering the specific capacities of cathode materials that are available today (≤200 mAh g^{-1}), these calculations show that it is reasonable to aim for anode materials with specific target capacities of ≈1000–1200 mAh g^{-1}, as a further increase to even higher capacities would yield only a small additional energy gain [1,15]. In some commercial cells, Si is already added in small amounts (≤5 wt %) to the graphite anode [5].

Yet, there are several major drawbacks that have to be overcome for a successful application of Si-based anodes, i.e., the low electronic conductivity, as well as the huge volume changes of ≈300–400% during the lithiation/delithiation process [15-17]. The latter issue leads to severe mechanical stress and causes rupturing of the electrode, electronic contact loss between active material and current collector/conductive carbon network and pulverization. Furthermore, the drastic volume changes during cycling hinder the formation of a dimensionally stable solid electrolyte interphase (SEI), as it is known for carbonaceous anodes, formed on the negative electrode surface from electrolyte decomposition products in the first charge/discharge cycles [18-20]. In the case of Si anodes, the SEI formation is an ongoing process because of the recurring breakage of the already formed SEI and exposure of fresh Si to the electrolyte. Consequently, a very thick SEI may form after several cycles, affecting the reaction kinetics detrimentally. All these aforementioned factors contribute to a decreasing capacity with each cycle, either due to consumption of active Li, trapping of Li in disconnected Si or a growing resistivity [17,21-25].

With the aim to tackle these problems and to obtain Si anodes with a stable cycling performance at high capacity, several promising approaches have been reported in the recent years. Some of the concepts that led to enormous improvements include the adaption of well-know concepts from Sn-based materials [11,26], such as reduction of the Si particle size to the nanoscale [15,27-29], the improvement of binders for composite electrodes [30-33], the search for effective SEI-forming electrolyte additives [34,35], as well as the embedding of Si into different matrix materials [36-41]. The general idea behind the latter concept is the combination of Si with a second phase, which can be either active or inactive towards lithiation itself. This phase should be able to provide high mechanical stability and accommodate the volumetric changes of Si, alleviating the aforementioned detrimental effects. Thus, these matrices should exhibit no (or less) volume changes compared to Si, and ideally, offer high electronic conductivity. Besides carbon-based matrices, intermetallic, silicide phases consisting of Si and different metals, such as Mg [42,43], Fe [40], Cr [44] or Ni [39,45] are the most prominent representatives of this approach. There is a vast amount of publications focusing on carbon/silicon composites (Si/C), dealing with the incorporation of Si into a variety of different carbon materials, such as graphite, graphene sheets [46,47], porous carbon structures [37,38,48] or the coating of Si using different precursors as carbon sources [49-51]. One simple method to form amorphous carbon structures, depicts the hydrothermal synthesis of carbohydrates [52]. Due to the fact, that this synthesis can be carried out at mild reaction conditions (<200 °C), using water as a solvent and carbohydrates as a carbon source, this process is environmentally friendly and quite inexpensive. Cakan et al. [41] showed that Si nanoparticles (Si-NPs) can be embedded in spherical hydro-

thermal carbon via a simple one-step hydrothermal process and Hu et al. [53] used hydrothermal carbonization to form a thin carbon and SiO_x layer around Si-NPs and reported a great improvement in cycling stability compared to pure Si-NPs. Shen et al. [37] also used a hydrothermal method to synthesize a pomegranate-inspired Si/C composite with Si-NPs distributed within a porous carbon structure and reported a capacity of 581 mAh g^{-1} after 100 cycles with a capacity retention of ≈77%. These previously mentioned publications clearly point out the potential of hydrothermal-derived carbons as promising matrix material, however, they do not investigate the influence of different Si contents on the resilience of the carbon matrix and possible limitations of this approach. Furthermore, the electrochemical characterizations in these publications do not include the application in a real LIB full cell set-up, but only investigations vs Li-metal counter electrodes ("half-cell" set-up).

In general, it should be stated that even though some impressive cycling results of Si-based anode materials with stable cycling performances at high capacities have been reported in the recent years, most of these results are obtained vs Li-metal electrodes. This means that the amount of Li in this cell set-up is unlimited and capacity fading related to active lithium loss cannot be detected. In a LIB full cell set-up, however, the amount of active Li is limited by the cathode material [25]. The restricted Li content is a very critical aspect regarding the application of Si in a full cell set-up, considering the lower Coulombic efficiencies (CEs) of Si-based anodes, especially in the first cycle. A powerful method to counterbalance the active Li loss in the first cycle and thus improve the energy density of the cell, is prelithiation, meaning that additional active Li is added to the system before the operation of the cell [54,55]. In this context, Chevrier et al. [56] developed an idealized model, correlating prelithiation with variations in energy density. Depending on the amount of added Li, prelithiation can compensate the irreversible capacity loss of the negative electrode in the first cycle and, therefore, improve the energy density. Alternatively, when further Li is added, prelithiation can also be used to create a Li reservoir in order to compensate for active lithium loss with ongoing cycling and increase the cycle life of a cell. Further, Marinaro et al. [57] reported an approach to add Li to Si anodes by depositing a suspension of stabilized Li-metal powder (SLMP) in toluene onto an electrode via airbrushing, leading to significantly improved first cycle CEs and enhanced cycle life of the prelithiated electrodes in comparison to the non-prelithiated electrodes.

In this work, we use a simple hydrothermal process, followed by a carbonization step to synthesize Si/C composites, in which Si-NPs are homogeneously dispersed within an amorphous carbon matrix. The aim of the applied synthesis route is to combine the beneficial properties of Si and carbon in a Si/C composite material with high specific capacity, good rate performance and long-term cycling stability. Thereby this contribution lays focus on the influence of the Si to C ratio to identify the chances and limitations of the applied hydrothermal carbon matrix approach. The synthesized materials are characterized regarding their composition, structure and morphology. The Si/C composites are also investigated in terms of their electrochemical performance, i.e., by rate performance and long-term cycling experiments. The most promising composite material is also characterized in a LIB full cell set-up to verify the applicability in a real cell system. Further, the influence of prelithiation on the LIB full cell long-term capacity retention is studied.

Experimental
Synthesis of silicon/carbon composites and of the pure hydrothermal carbon matrix

Silicon/carbon (Si/C) composites and the pure carbon matrix were synthesized in a hydrothermal process using a solution of anhydrous D-glucose (Fisher Scientific) in water (0.75 mol L^{-1}) as the carbon source in the presence or absence of commercially available Si-NPs (100 nm, NANO Si, Creavis) with D-glucose:Si weight ratios of 77.5:1 and 45.5:1, respectively. Therefore, D-glucose was dissolved in deionized (DI) water by stirring for 15 min. At the same time, in the case of Si-containing samples, Si-NPs were dispersed in a small amount of DI water and added to the D-glucose solution. A specific volume was set to obtain a glucose concentration of 0.75 mol L^{-1}. The (combined) solution was treated in an ultrasonic bath for 45 min in order to break agglomerates and obtain a homogeneous suspension. For the hydrothermal treatment, the solution was transferred into a pressure reactor (Parr Instrument Company), equipped with a 600 mL polytetrafluoroethylene (PTFE) liner and two six-blade impellers, one near the bottom and one near the surface of the solution. The hydrothermal treatment consisted of a 150 min heating-up phase to 180 °C, followed by a holding phase of 330 min at a nitrogen prepressure of 4.8 bar and a stirring rate of 200 rotations per minute (rpm). The product of the hydrothermal process was collected by filtration using a membrane with 0.2 μm pores (Merck Millipore) and washed with DI water, ethanol and acetone and dried at 60 °C in ambient atmosphere.

Afterwards, the dried products were carbonized at a temperature of 900 °C for six hours in an argon atmosphere, applying a heating ramp of 300 °C h^{-1}, in order to remove heteroatoms and increase the electronic conductivity of the materials.

Electrode preparation

Composite electrodes with a composition of 90 wt % active material (Si/C composite, pure carbon matrix or mixture of pure

carbon matrix and Si-NPs), 5 wt % sodium carboxymethyl cellulose (Na-CMC) as binder (Walocel CRT 2000 PPA 12; Dow Wolff Cellulosics) and 5 wt % conductive agent (C-nergy Super C65; Imerys Graphite & Carbon) were prepared by coating a dispersion of the aforementioned materials and water onto a dendritic copper foil (Carl Schlenk AG). At first, the Na-CMC was dissolved in DI water, followed by the addition of the conductive agent and of the active material. After dispersing the electrode paste for one hour at 10,000 rpm (VMA-GETZMANN GmbH), it was cast onto a previously purified (ethanol) dendritic copper foil with a speed of 50 mm s^{-1} using a doctor blade technique (Zehntner GmbH) in combination with an automatic film applicator (Sheen Instruments). A wet coating thickness of 100 μm was applied, leading to an average mass loading of ≈2.0 mg cm^{-2}. After drying for one hour at 50 °C, circular electrodes with a diameter of 12 mm were punched out and dried under reduced pressure (<0.05 mbar) at 170 °C for at least 24 h and stored in a glove box with argon atmosphere.

Cell assembly and electrochemical investigations

Electrochemical investigations were carried out in a three electrode configuration using Swagelok-type T-cells that were assembled in a glove box (UNIlab, MBraun) with argon atmosphere and H_2O and O_2-values below 0.1 ppm. The composite electrodes containing the synthesized materials were used as working electrodes (WE), while lithium metal (Li; Albemarle Corporation) was used as counter and reference (RE) electrodes. In the full cell set-up, the Si/C composite electrodes were cycled vs lithium nickel manganese cobalt oxide ($LiNi_{1/3}Mn_{1/3}Co_{1/3}O_2$, NMC-111; Umicore; D90: 17.0 μm; mass loading ≈6.5 mg cm^{-2}) electrodes with an active material: polyvinylidene difluoride (PVDF) binder: Super C65 composition of 93:4:3 wt % and Li-metal was used as reference electrode. A six-layered polyolefin separator (Freudenberg 2190; diameter: 13 mm) soaked with 140 μL of electrolyte was placed between negative and positive electrode. The reference electrode was spaced apart from the other electrodes by a three-layered separator (diameter: 8 mm) containing 60 μL of electrolyte. The used electrolyte was a mixture of ethylene carbonate (EC) and dimethyl carbonate (DMC) in a ratio of 1:1 by weight, 1 M $LiPF_6$ (LP30, BASF) plus 5 vol % of fluoroethylene carbonate (FEC, BASF).

A Maccor Series 4000 automated test system (Maccor) was used to carry out constant current charge (=lithiation)/discharge (=delithiation) experiments. The cut-off potentials during the long-term cycling experiments were set as 0.01 V vs Li/Li$^+$ and 1.50 V vs Li/Li$^+$. During the rate performance experiments, cut-off potentials of 0.02 V vs Li/Li$^+$ and 1.50 V vs Li/Li$^+$ were chosen in order to avoid Li-metal plating at high charging rates.

In the rate performance studies, specific charge/discharge currents between 40 mA g^{-1} and 1,000 mA g^{-1} were applied. Long-term cycling experiments were carried out at a specific charge/discharge current of 400 mA g^{-1} after three formation cycles with a specific current of 80 mA g^{-1}.

In the full cell set-up an anode/cathode capacity balancing (Q_A/Q_C) of 1:1 was used and the cells were cycled at a cell voltage of 3.0 V and 4.3 V. In addition, the reference electrode was used to monitor the anode potential. After three formation cycles with 10 mA g^{-1}, a specific current of 100 mA g^{-1} was applied for cycling.

The currents refer to the active material mass of the working electrode in Li-metal cells or to the active material mass of the NMC-111 cathode in the full cell set-up, respectively.

Electrochemical prelithiation was carried out by performing one formation cycle in a Si/C vs Li-metal cell at a charge/discharge current of 50 mA g^{-1}, followed by disassembling the cell in a glove box and assembling of a full cell using the prelithiated Si/C electrode as the negative electrode.

Characterization methods

A Bruker Senterra Raman microscope (Bruker Optics Inc.) was used to record the Raman spectra using a green laser with a wavelength of 532 nm and a laser power of 5.00 mW.

X-ray diffraction (XRD) patterns in a 2θ range of 20° to 80° were recorded with the help of a Bruker D8 Advance X-ray diffractometer (Bruker AXS GmbH) with a Cu Kα-wavelength of λ = 0.154 nm and a step size of 0.039°.

Thermogravimetric analysis (TGA) was carried out in a temperature range between 25 °C and 800 °C on a TGA Q500 (TA Instruments) in an oxygen/nitrogen atmosphere (nitrogen flow: 10 mL min^{-1}, oxygen flow: 25 mL min^{-1}) in order to determine the Si content. A heating ramp of 20 °C min^{-1} was applied.

Scanning electron microscopy (SEM) with a field emission gun (Schottky-type) was used to investigate the morphology of the synthesized composite materials. Cycled electrodes were analyzed after washing with DMC and drying in an argon filled glovebox. Multiple areas per sample were analyzed using an Auriga CrossBeam workstation from Zeiss at an acceleration voltage of 3 kV. Energy-dispersive X-ray spectroscopy (EDX) measurements were used to investigate the elemental composition of the composite materials using an acceleration voltage of 20 kV. The EDX signal was detected by an X-Max 80 mm^2 detector and evaluated with the INCA software, both from

Oxford Instruments. Cross-sections were prepared by a focused ion beam (FIB) milling process using gallium ions extracted from a high brightness liquid metal ion source.

Nitrogen adsorption experiments were performed on a 3Flex Physisorption device (Micromeritics GmbH) at the temperature of liquid nitrogen (−196 °C). Before the measurements, the samples were degassed at 200 °C for two days. The surface areas were calculated in accordance to the BET (Brunauer–Emmett–Teller) theory.

Tap densities were measured using an AUTOTAP tapped density analyzer (Quantachrome Instruments). Therefore, the samples were accurately weighed, filled in a measuring cylinder and tapped for 5000 times before the volume was determined.

Results and Discussion
Morphology and internal structure of the synthesized Si/C materials

The stoichiometry of silicon nanoparticles (Si-NPs) during the hydrothermal process was calculated with the goal to obtain Si/C composites containing 0 wt % (pure carbon matrix), 10 wt % (C:Si 90:10) and 20 wt % (C:Si 80:20) of Si, homogeneously embedded in a carbonaceous matrix. The morphology of the synthesized samples was investigated by means of SEM
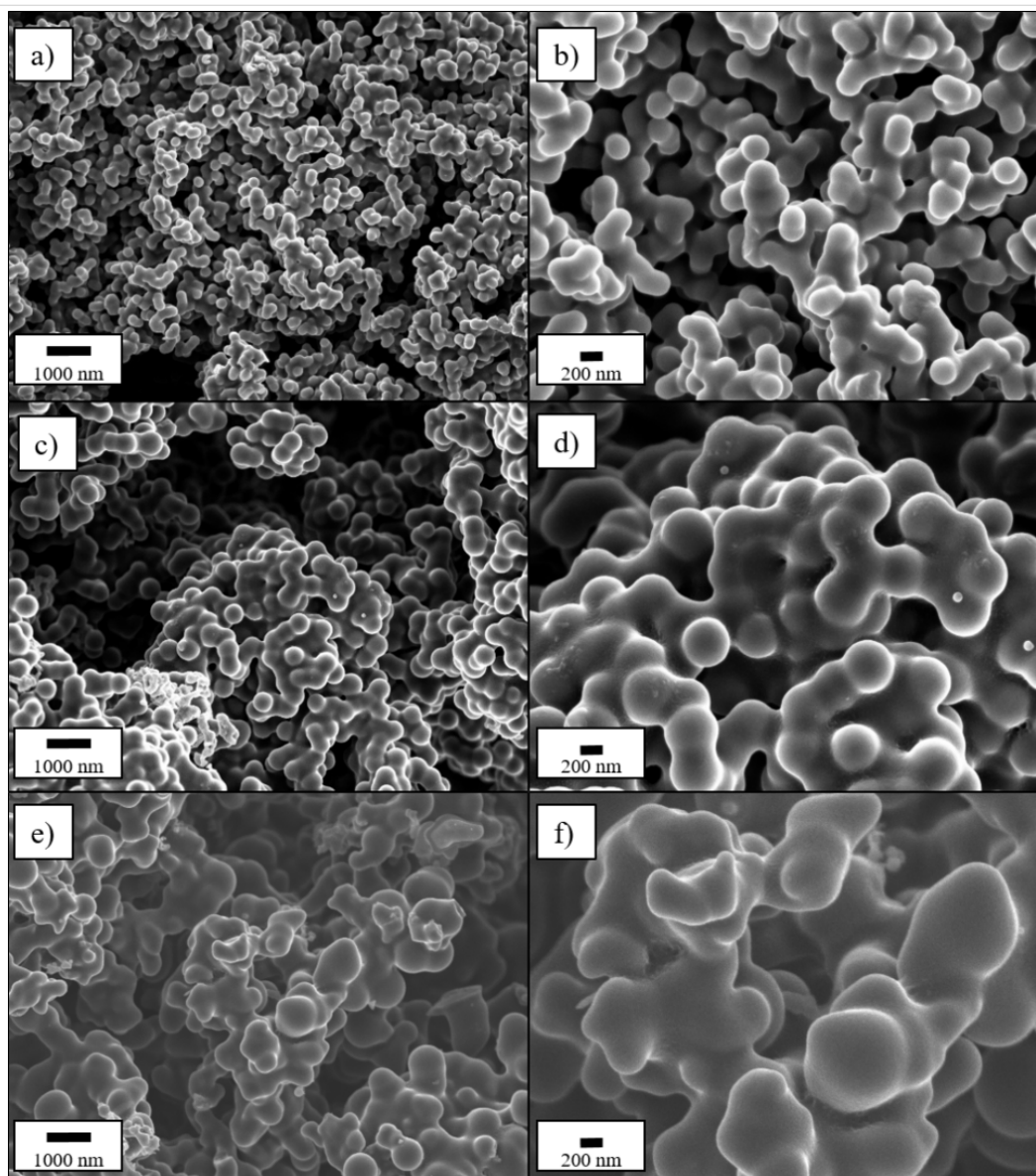
Figure 1: SEM micrographs of the different synthesized Si/C composite materials with a carbon to silicon ratio of 100:0 (a, b), 90:10 (c, d) and 80:20 (e, f) in a magnification of 10k× (a, c, e) and 25k× (b, d, f).
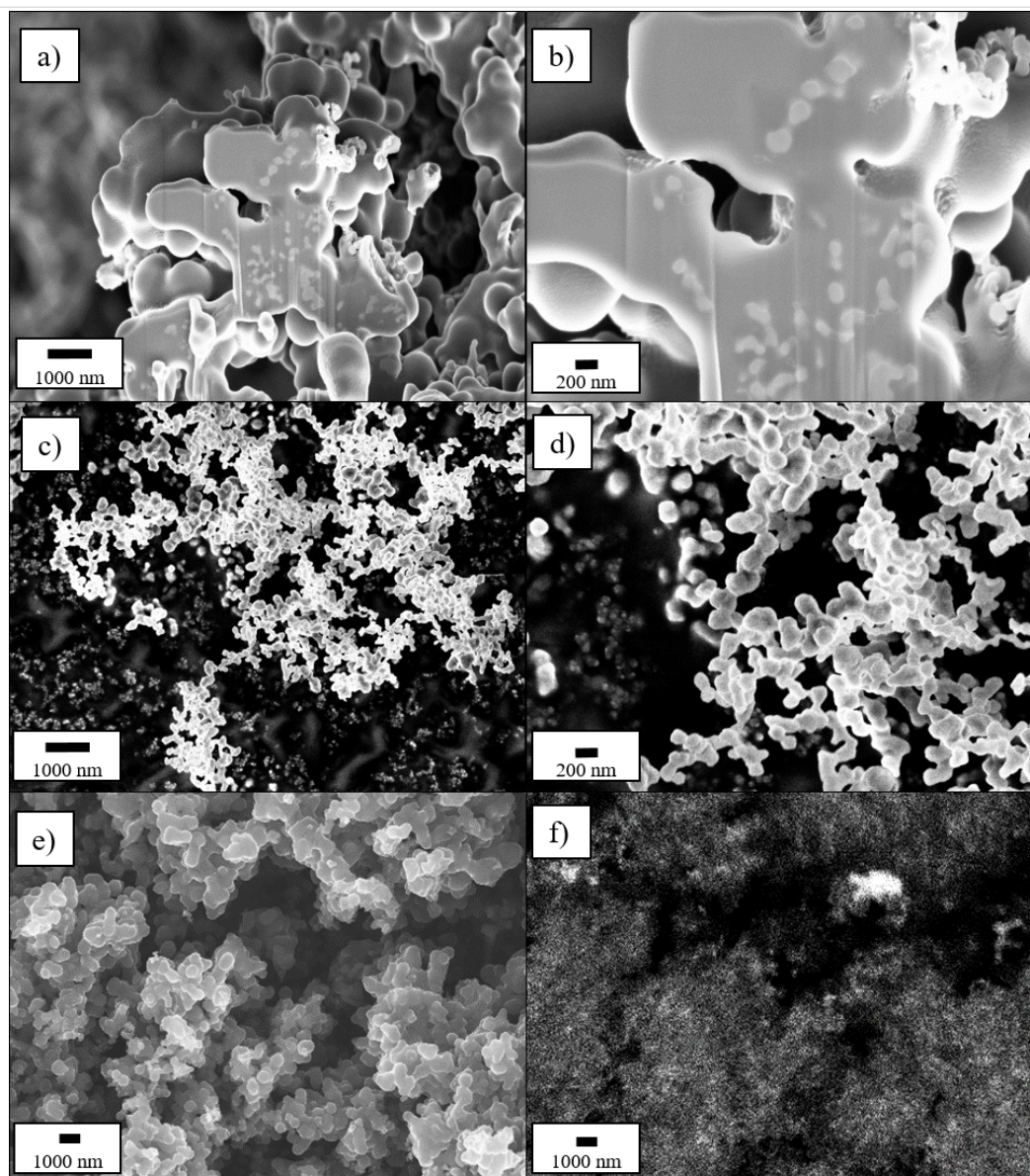
Figure 2: FIB-SEM cross section of the C:Si 80:20 composite (a, b) and SEM micrographs of the pure Si-NPs (c, d) and an EDX mapping of the C:Si 80:20 composite, showing the Si distribution (=white areas) within the matrix (f) and the corresponding SEM micrograph (e).

as presented in Figure 1. From Figure 1a and Figure 2b it can be seen that the chosen reaction conditions lead to spherical carbon particles with a diameter of ≈200 nm that are quite strongly fused together and, therefore, form large agglomerates. Chain-like aggregates of spherical carbon particles, were also found by Tien et al. [58], when they synthesized carbon spheres by thermal decomposition. Jin et al. [59] and Kristianto et al. [60] also reported the presence of conglomerated carbon spheres rather than single spherical particles, which might be caused by extended reaction times or the cooling phase after the synthesis [61]. A continuous, interconnected network of nanospheres was also reported by Xia et al. [62] during the synthesis of carbon spheres containing electrocatalysts for oxygen reduction reac-

tions. Heckmann et al. [63] investigated the use of high-temperature-treated hydrothermal carbon spheres as cathode materials for dual-ion cells and found spherical particles up to a heat treatment temperature of 2100 °C, while at temperature of 2400 °C, they observed the additional formation of rod-shaped particles.

The addition of Si-NPs results in a visible increase in primary particle size, which is especially stressed for the sample with the higher Si content of 20 wt % (Figure 1e and 1f). The spherical shape of the single particles is still recognizable for the C:Si 90:10 sample, despite the strong particle fusion (Figure 1c and 1d), whereas the morphology of the C:Si 80:20 sample is more

irregular-shaped and not as uniform and round-shaped as for the C:Si 90:10 sample.

The SEM micrographs also show that nearly no Si-NPs are located outside of the matrix, indicating a successful embedding of Si into carbon. To further verify this assumption, the internal structure of the C:Si 80:20 sample was investigated with the help of FIB-SEM and EDX to obtain a cross-section of the material and identify the Si distribution inside the composite (Figure 2). The cross section in Figure 2a and 2b shows several lighter spots located inside the matrix material. In comparison with Figure 2c and 2d which show the pure Si-NPs that were added during the synthesis, the similarities in shape and size to the Si particles (=white spots) in Figure 2a and 2b can be seen. The EDX mapping results in Figure 2e and 2f also supports the results from the FIB-SEM investigations that Si is homogeneously distributed within the carbon matrix. For comparison reasons, SEM micrographs of a physical mixture of the pure carbon matrix and the pure Si-NPs in a weight ratio of 80:20, where the Si-NPs are not embedded in the carbon matrix, are presented in Figure S1 (Supporting Information File 1).

Determination of the silicon content and structural characteristics

To identify the actual Si content of the Si/C composites, TGA was carried out in an oxidative atmosphere, as presented in Figure 3a. While the pure carbon matrix burns off completely and the remaining weight at a temperature of 630 °C is ≈0%, the Si-containing samples exhibit a small plateau at a temperature of ≈630 °C where the remaining weight is constant. Due to the fact that the pure Si-NPs show only an insignificant weight gain up to 650 °C of ≈1%, caused by the beginning oxidation of Si and the formation of silicon dioxide, the remaining weight of the plateau for the Si/C composites can be considered as the Si content of these materials [39]. The Si contents determined in this way amount to 11 wt % for the C:Si 90:10 composite and 21 wt % for the C:Si 80:20 composite, which is close to the desired values and means that the C:Si ratio can be controlled accurately by the Si to glucose ratio during the first step of the synthesis.

The XRD patterns of the Si/C composites, the pure carbon matrix and the pure Si-NPs are depicted in Figure 3b. Both Si/C composites exhibit sharp reflections that are characteristic for the diamond structure of crystalline silicon (ICDD-PDF 04-002-0118, space group $Fd\bar{3}m$ (no. 227)) at 2θ values of 28.4°, 47.3°, 56,1°, 69,1° and 76.3°, as can be seen in comparison to the pattern of the pure Si-NPs [39]. In contrast to the Si-containing materials, the pure carbon matrix exhibits no sharp reflections but two broad humps at 2θ values of ≈22° and ≈43° that are also observable for both Si/C composites. This indicates an amor-
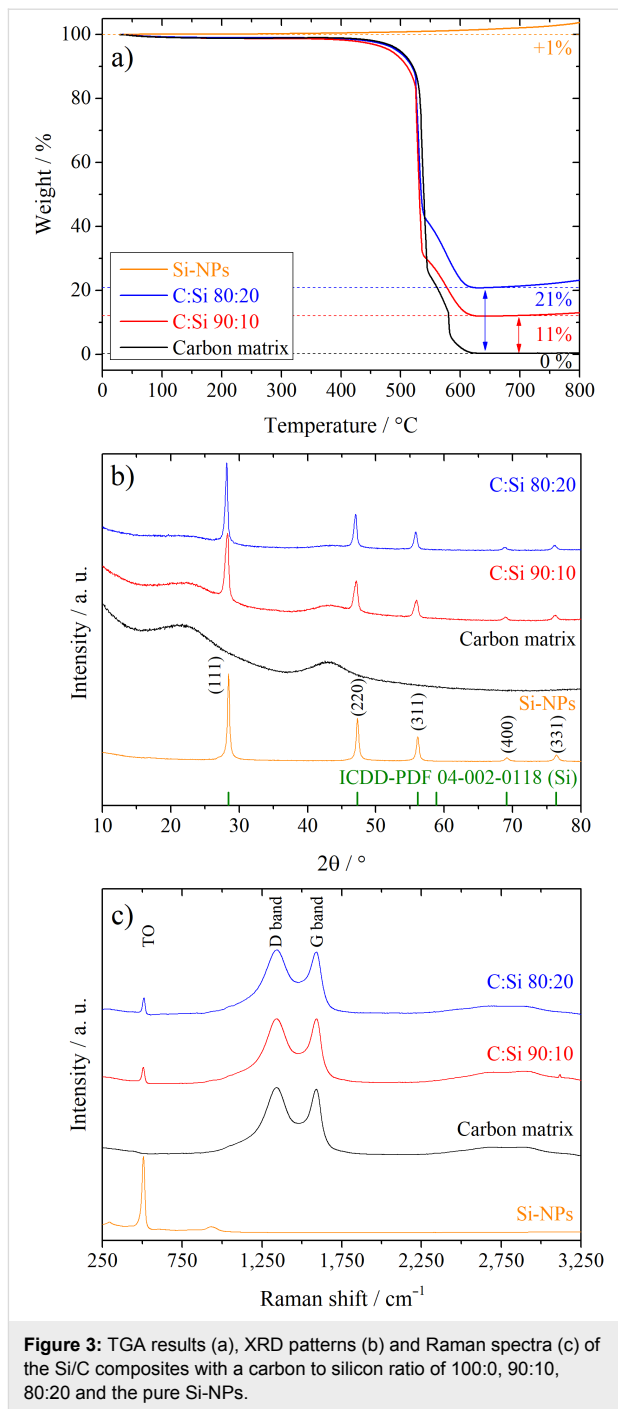
Figure 3: TGA results (a), XRD patterns (b) and Raman spectra (c) of the Si/C composites with a carbon to silicon ratio of 100:0, 90:10, 80:20 and the pure Si-NPs.

phous structure of the carbon and can be explained with the carbonization temperature of 900 °C that is way below the temperature needed to grow large crystalline, graphitic domains [64,65]. This carbonization temperature was chosen with the aim to synthesize a material with a porous, amorphous structure that is able to accommodate the volumetric changes of the Si during the lithiation/delithiation process. The formation of silicon carbide (SiC) or any other crystalline SiO_x phases in detectable amounts is also avoided at this temperature as can be

reasoned from the absence of any further sharp reflections, other than that of the crystalline Si.

The amorphous nature of the carbon matrix was also confirmed with the help of Raman spectroscopy, as depicted in Figure 3c. Both Si/C composites, as well as the pure carbon matrix exhibit two bands at 1,345 cm^{-1} and 1,593 cm^{-1} that show a similar intensity and strong overlap. These bands can be attributed to the *D*- and *G*-band and are characteristic for amorphous or disordered carbons [41,64]. The band at ≈510 cm^{-1} originates from a transverse optical mode of Si [27,53].

In order to determine the achievable energy density of the synthesized Si/C composite materials, the tap density of these materials was determined and summarized in Table S1 (Supporting Information File 1). In general, nanometer-sized materials suffer from a low tap density, which is detrimental in terms of energy density (Wh L^{-1}). In comparison to the pure Si-NPs (tap density of 0.13 g cm^{-3}), the tap densities of the Si/C composites are considerably higher, however, they are still quite low compared to state-of-the-art micrometer-sized graphite anode materials (typically ≥1 g cm^{-3}). Thus, further improvements are mandatory to achieve higher tap densities and, therefore, practical energy densities for mobile applications. While the pure carbon matrix exhibits a tap density of ≈0.16 g cm^{-3}, the tap densities of the C:Si 90:10 and C:Si 80:20 sample increase to ≈0.19 g cm^{-3} and ≈0.24 g cm^{-3}. For a meaningful statement in terms of energy density of the Si/C composites, it is important to consider their volume in the lithiated state [10,66]. This is important as Si expands severely when it alloys with lithium. In this regard, we assume that the synthesized Si/C composites benefit from the fact that the Si is incorporated in carbon and, thus, these composites are expected to show quite small volumetric changes compared to composites where the Si is not embedded in the carbon.

Electrochemical investigations of Si/C vs lithium metal

The Li-ion storage capabilities of the different materials were investigated in symmetrical rate performance experiments (Figure 4a) with specific charge (=lithiation)/discharge (=delithiation) currents between 40 mA g^{-1} and 1,000 mA g^{-1} and in constant current long-term cycling investigations (Figure 4b). 100 charge/discharge cycles at a specific current of 400 mA g^{-1} were performed after three formations cycles with a formation current of 80 mA g^{-1}. In Figure 4a, the excellent rate performance of the pure amorphous carbon matrix can be seen with only a low capacity decrease at high charge/discharge rates. At a current of 100 mA g^{-1}, a capacity of ≈215 mAh g^{-1} is reached that is only slightly reduced to ≈172 mAh g^{-1} at the highest charge/discharge rate of
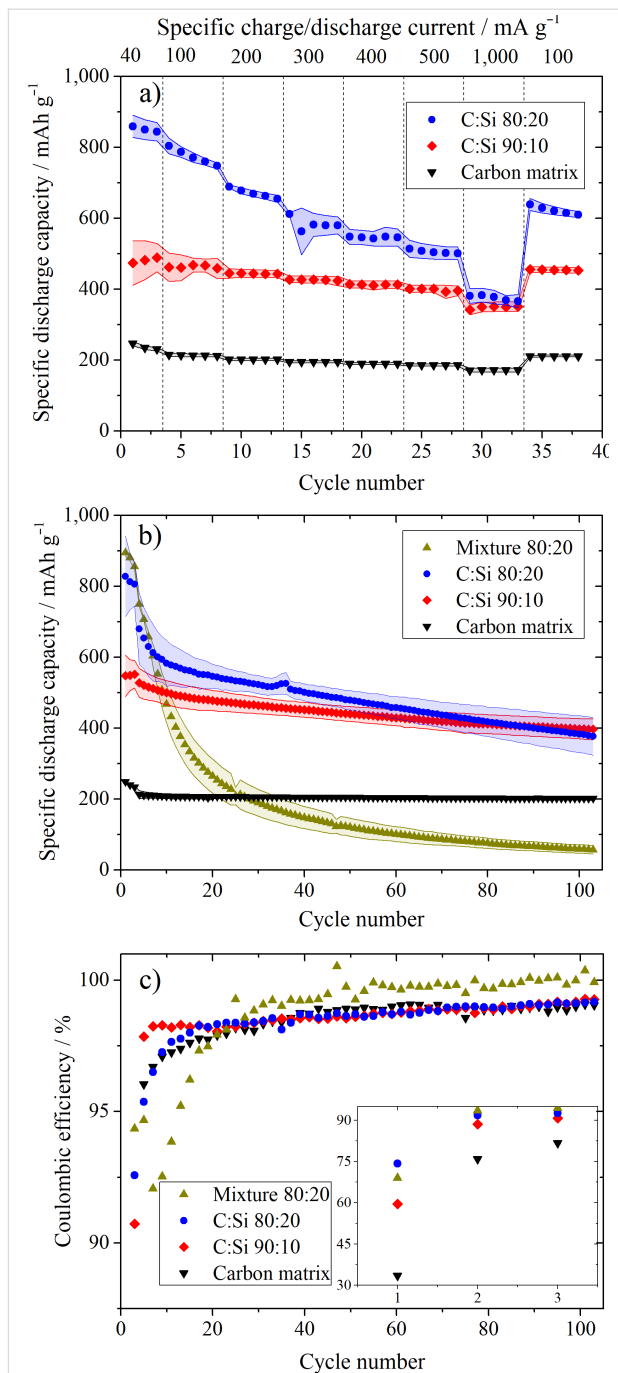
Figure 4: Constant current rate performance investigations at different charge/discharge currents (a) of the Si/C composites with a carbon to silicon ratio of 100:0, 90:10, 80:20 and constant current long-term cycling experiments (b) at a specific charge/discharge current of 400 mA g^{-1} after three formation cycles at 80 mA g^{-1} and the corresponding Coulombic efficiencies (c). In addition to the synthesized materials, a physical mixture of the pure carbon matrix and the Si-NPs is shown in b and c. CE and RE: metallic lithium; potential range 0.02 V and 1.5 V vs Li/Li$^+$ (a) and 0.01 V and 1.5 V vs Li/Li$^+$ (b, c).

1,000 mA g^{-1}, which corresponds to a C-rate of 4.65C considering a practical capacity of 215 mAh g^{-1}. Through the addition of Si, a significant increase in capacity is achieved with

capacities of ≈470 mAh g^{-1} and ≈770 mAh g^{-1} at a specific current of 100 mA g^{-1} for the C:Si 90:10 and C:Si 80:20 composite, respectively. These capacities are in a comparable range to the specific capacities achieved by Cakan et al. of ≈160 mAh g^{-1} for a pure hydrothermal carbon and 460 mAh g^{-1} for a Si/C composite with a Si content of ≈15 wt % at a specific current of 300 mA g^{-1} for 20 cycles [41].

The capacity decrease of the Si/C composites with increasing current rate is stronger compared to the pure carbon matrix, especially for the C:Si 80:20 composite, and therefore, can be directly related to the Si content of the samples. The CEs, voltage efficiencies (VEs) and energy efficiencies (EEs) of the pure carbon matrix, the C:Si 90:10, and C:Si 80:20 composite in the rate performance experiments are summarized in Figure S2 (Supporting Information File 1). The EEs and VEs were calculated as described by Meister et al. [8], using a virtual lithium iron phosphate (LFP) cathode with a potential of 3.4 V vs Li/Li$^+$ as the positive electrode. From Figure S2, it can be seen that the pure carbon matrix (Figure S2a) exhibits the highest VE at each specific charge/discharge current, while the VE slightly decreases with the Si content, meaning that the C:Si 80:20 (Figure S2c) composite shows the lowest VE at all specific currents. At the highest specific charge/discharge rate of 1,000 mA g^{-1} all materials show the lowest VE with ≈96% for the pure carbon matrix (Figure S2a), ≈92% for the C:Si 90:10 (Figure S2b) and ≈90% for the C:Si 80:20 composite (Figure S2c). A similar trend can be observed regarding the correlation between the Si content and the CE, with the pure carbon matrix showing the highest CE and the C:Si 80:20 composite showing the lowest CEs at different specific charge/discharge currents, except for the formation cycles. Because of the higher VE and CE, the pure carbon matrix also shows the highest EE at different specific charge/discharge currents after the formation cycles.

In Figure 4b, the pure carbon matrix reveals a stable capacity of ≈200 mA g^{-1} with only minor capacity decay during the long-term cycling at a charge/discharge current of 400 mA g^{-1} and a capacity retention of ≈95% after the 103rd cycle referred to the 4th cycle (first cycle after formation). The Si/C composites,

however, suffer from a stronger capacity decay that is again more pronounced with higher Si content, leading to a capacity retention of ≈75% and ≈55% for the C:Si 90:10 and C:Si 80:20 composite. A slightly higher capacity retention of ≈77% after 100 cycles was reported by Shen et al. [37] at a specific current of 200 mA g^{-1} for a pomegranate-inspired Si/C composite with a porous hydrothermal carbon matrix and a Si content of ≈10 wt %, retaining a capacity of 581 mAh g^{-1}. For a reasonable comparison regarding the capacity retention of different materials, it should be considered though that in our experiments higher currents of 400 mA g^{-1} were applied during the long-term cycling experiments and electrodes with higher active material content of 90 wt % were used.

The slightly higher capacities of the different materials in the long-term performance investigations compared to the rate performance experiments can be explained with a different lower cut-off potential of 0.01 V vs Li/Li$^+$ compared to 0.02 V vs Li/Li$^+$ in the rate performance studies, which was chosen to avoid Li-metal plating at high charging rates. In order to verify if the incorporation of the Si into the carbon has a beneficial effect, a physical mixture of the pure carbon matrix and the pure Si-NPs was prepared in a ratio of 80:20, where the Si-NPs did not take part in the hydrothermal process. This mixture shows the highest capacity of all investigated materials with ≈750 mAh g^{-1} in the fourth cycle, but suffers at the same time from by far the strongest capacity decay (see Table 1). After 12 cycles the capacity already drops below the capacity of the C:Si 90:10 composite and after 35 cycles the capacity is even lower than that of the pure carbon matrix. The capacity retention after the 103rd cycle amounts to only ≈8% referring to the capacity in the 4th cycle. These results point out the highly beneficial effect of embedding Si into a carbon matrix. It has to be noted that the physical mixture as a "non-optimized system" might not be the optimum "reference system", however, it clearly shows the improvement of embedding Si into the carbon matrix. Overall, many different factors (specific surface area, particle size, porosity, Si content, mass loading, etc.) of the reference system should be comparable to the prepared materials for a fair comparison, thus, it is rather difficult to find any suitable reference material.

Table 1: Overview of the specific discharge (=delithiation) capacities, capacity retention and first cycle Coulombic efficiencies of the different samples during the long-term cycling investigations.

Active material	Specific discharge capacity / mAh g^{-1}			Capacity retention / %	Coulombic efficiency / %
	1st cycle	4th cycle	103rd cycle	4th to 103rd cycle	1st cycle
carbon matrix	249 ± 1	213 ± 9	202 ± 5	95 ± 2	34 ± 3
C:Si 90:10	548 ± 47	528 ± 33	397 ± 24	75 ± 2	60 ± 6
C:Si 80:20	829 ± 90	680 ± 80	377 ± 43	55 ± 13	74 ± 4
mixture C + Si 80:20	895 ± 8	750 ± 5	57 ± 10	8 ± 1	69 ± 1

The CEs determined during the long-term cycling tests are summarized in Figure 4c. The first cycle CE is ≈34% for the pure carbon matrix, whereas it amounts to ≈60% and ≈74% for the C:Si 90:10 and C:Si 80:20 composites. Even lower initial CEs of ≈52% and ≈40% for comparable hydrothermal carbon based Si/C composites were reported by Shen et al. [37] and Cakan et al. [41] for composites with a Si-content of 10 wt % and 15 wt %, respectively. The low CEs values can be explained with the high surface areas of the materials due to the small particle sizes and the presence of functional groups that can irreversibly consume Li-ions [25]. The higher CEs with higher Si content can be correlated to the BET surface areas of 367 ± 7 m^2 g^{-1} for the C:Si 80:20 sample and 402 ± 7 m^2 g^{-1} for the pure carbon matrix and are also in agreement with the SEM images (Figure 1), indicating that the surface area decreases with the Si content, due to morphological changes of the carbon matrix.

Morphological changes during lithiation/ delithiation

With the aim to understand the reason for the strong capacity decay with increasing Si content, cycled electrodes were examined by means of SEM after 13 charge/discharge cycles (including three formation cycles), as presented in Figure 5. In Figure 5c and 5d, the electrode of the C:Si 80:20 composite exhibits several cracks (marked by red arrows in Figure 5c) that cannot be found on the surface of the electrode in Figure 5a and 5b, showing the C:Si 90:10 composite. It can be concluded that the mechanical stress caused by the volume expansion of the Si during the lithiation/delithiation process cannot be completely buffered by the amorphous carbon matrix and results in the formation of cracks when the Si content is too high, which is the case when the Si content is ≈20%. The crack formation during the lithiation/delithiation process is accompanied by severe consequences such as mechanical and electronic contact loss and pulverization of the active material, the trapping of Li inside detached Si, exposure of fresh Si to the electrolyte and breaking and reformation of the solid electrolyte interphase (SEI) layer [16,21,22,24]. All these factors contribute to an ongoing capacity loss with each cycle, leading to poor capacity retention. With higher Si content, the factors increase accordingly and explain the stronger fading of the C:Si 80:20 composite.

## Si/C vs NMC-111 full cell investigations

The anode and cathode in a LIB full cell mutually affect each other [67]. LIB full cell investigations were carried out using positive electrodes containing NMC-111 as active material in
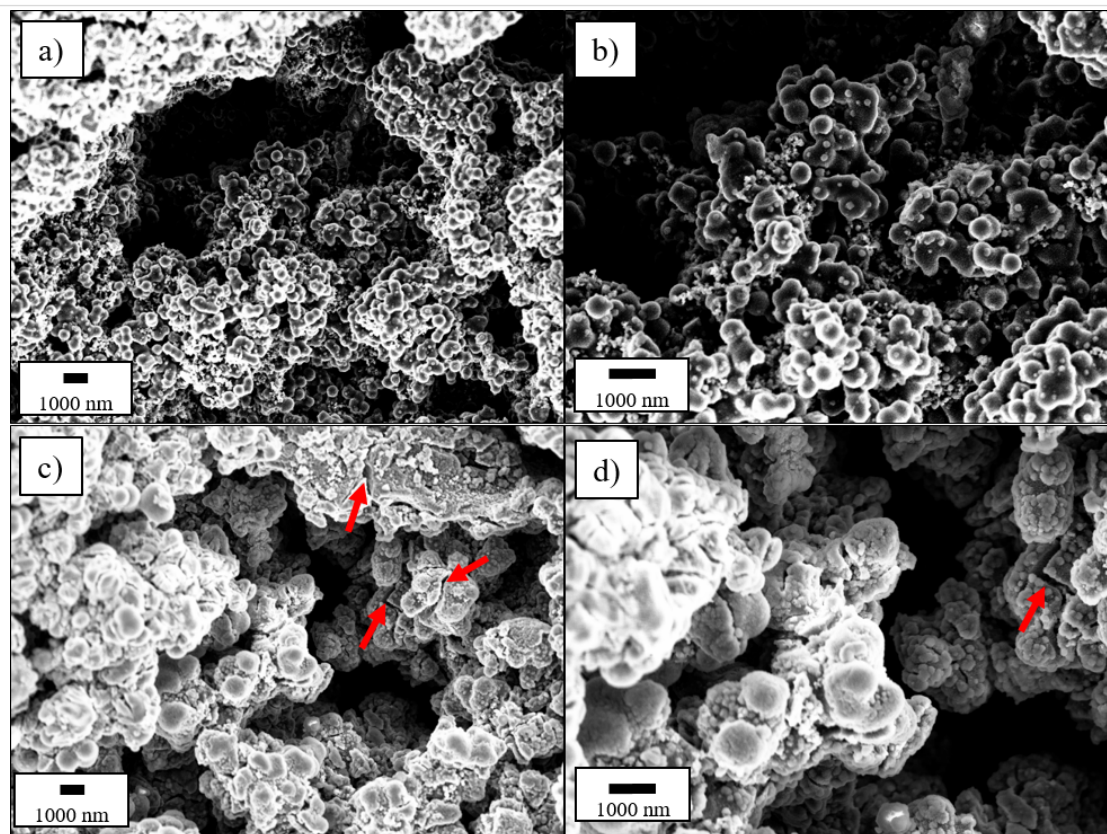
Figure 5: SEM micrographs of cycled electrodes after 13 cycles (including 3 formation cycles) of the C:Si 90:10 (a, b) and C:Si 80:20 composite (c,d).

combination with the C:Si 90:10 composite as the negative electrode. The C:Si 90:10 composite was chosen over the C:Si 80:20 composite due to the improved capacity retention in the previously shown investigations. In general, the anode/cathode capacity balancing of LIB full cells needs to be tailored in order to achieve the maximum energy density, but should avoid safety issues such as lithium-metal plating at the anode [68]. In our experiments, the negative electrode was not overbalanced in regard to the capacity of the positive electrode, since the first cycle CE of the C:Si 90:10 composite is quite low with ≈60%, as is known from the electrochemical investigations vs Li-metal (see Figure 4c). This leads to a relatively high consumption of active lithium from the cathode during the formation process [25] and, hence, a low risk of lithium metal plating at the anode. Additionally, the influence of electrochemical prelithiation on the cycling performance was investigated, as shown in Figure 6. Electrochemical prelithiation was, therefore, carried out via charging/discharging the C:Si 90:10 electrode vs Li-metal for one formation cycle, followed by the assembling of the full cell. In Figure 6a, the cycling performance of the prelithiated and non-prelithiated LIB full cells is compared, while Figure 6b and 6c summarize the corresponding CEs, VEs and EEs for the prelithiated (Figure 6b) and non-prelithiated (Figure 6c) full cells. In general, it can be stated that the discharge capacity of the prelithiated full cell is shifted to higher values. Despite the fact that the discharge capacity difference between prelithiated and non-prelithiated full cells diminishes with ongoing cycling, the discharge capacity of the prelithiated full cells is still higher than that of the non-prelithiated full cell even after 150 cycles. A similar trend of diminishing capacity differences between prelithiated and non-prelithiated full cells with ongoing cycling, can also be found in a publication by Kim et al., using a carbon-coated silicon monoxide anode vs a Li[Ni$_{0.8}$Co$_{0.15}$Al$_{0.05}$]O$_2$ cathode [69]. Even though prelithiation of Si-based anodes has become a huge research field in the recent years, there is still a lack of publications dealing with the effect of prelithiation on the long-term performance of LIB full cells using Si-based anodes. Thus, further investigations are necessary to identify the reasons for the stronger fading of the prelithiated full cells. In the context of optimizing the cycling performance of LIB full cells with Si-containing anode materials, it is important to take into consideration that prelithiation can not only be used to compensate the irreversible capacity loss in the first cycle, but also to generate a Li reservoir which can have a significant influence on the long-term performance of the cell [56].

In the first cycle, a discharge capacity of 101 mAh g^{-1} is achieved for the non-prelithiated full cell with a first cycle CE of 57%, while the prelithiated full cell delivers a discharge capacity of 119 mAh g^{-1} with a first cycle CE of 67%. The EE, VE and CE were determined in accordance to the procedure de-
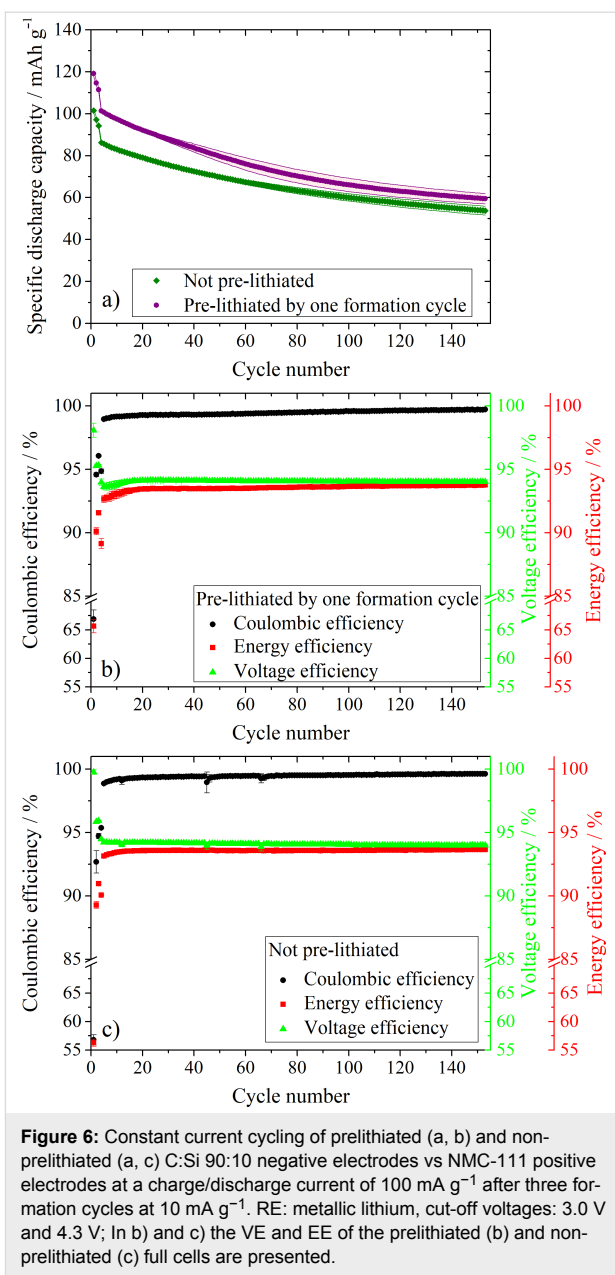
Figure 6: Constant current cycling of prelithiated (a, b) and non-prelithiated (a, c) C:Si 90:10 negative electrodes vs NMC-111 positive electrodes at a charge/discharge current of 100 mA g^{-1} after three formation cycles at 10 mA g^{-1}. RE: metallic lithium, cut-off voltages: 3.0 V and 4.3 V; In b) and c) the VE and EE of the prelithiated (b) and non-prelithiated (c) full cells are presented.

scribed by Meister et al. [8]. There it was shown that the EE can be calculated as the product of the CE and VE. The main differences between the prelithiated and non-prelithiated cell can be again found in the first cycle. The prelithiated full cells obtain an EE of ≈66%, while the EE of the non-prelithiated cells is just ≈56% in the first cycle, which is strongly influenced by differences of the CE. However, in general it can be stated that the development of the EE, VE and CE in dependence of the cycle number, are very similar for the prelithiated and non-prelithiated full cells. In the first cycle the VE reaches the highest value, higher than 98%, and then slightly decreases to ≈95% for the next two formation cycles. After the formation cycles, the VE is lower than before and stabilizes at ≈94% in both cases.

The decrease compared to the formation cycles is most likely due to stronger polarization effects of the electrodes at higher currents [8,70]. A high VE indicates a small voltage hysteresis between charge and discharge of the cell. After the formation, the EE and VE are very similar to each other, with the VE being slightly higher in each cycle. The EEs and VEs obtained in this work are in a very similar range to those reported by Meister et al. for hard carbon and graphite anodes, where a virtual lithium iron phosphate cathode was used as the positive electrode for calculation [8].

Figure 7 presents the cell voltage, as well as the anode potential of the prelithiated (Figure 7a and 7b) and non-prelithiated (Figure 7c and 7d) LIB full cells as a function of the specific capacity during the first charge/discharge process. The main difference between the prelithiated and non-prelithiated full cells is the presence of a sloping plateau at ≈1 V vs Li/Li⁺ in the anode potential profile of the non-prelithiated full cell (Figure 7d). This can be attributed to the formation of the SEI by electrolyte decomposition. The absence of this plateau in Figure 7b is due to the fact that a major part the SEI is already formed during the prelithiation step before the first electrochemical charge. The presence/absence of the same plateau is also reflected in the cell voltage vs the specific capacity plot in Figure 7a and 7c at ≈2.7 V. The prolonged discharge plateau at ≈0.45 V vs Li/Li⁺ in the anode potential profile for the prelithiated full cell that originates from the delithiation of lithiated silicon (transition from crystalline to amorphous Si) depicts another difference between the prelithiated and non-prelithiated full cell.

Figure 8 presents the development of the anode and cathode potentials of the prelithiated (a) and non-prelithiated (b) full cells vs time during cycling. With ongoing cycling, a shift of the end of charge (EOC) potential to higher potentials occurs in both cases. For the prelithiated full cell, the EOC anode potential in the first cycle is 0.004 ± 0.002 V vs Li/Li⁺, while the anode potential in the non-prelithiated full cell reaches a EOC potential of just 0.033 ± 0.002 V vs Li/Li⁺. This is a direct consequence of the lower amount of available active lithium in the non-prelithiated system, as more of the active Li is consumed during the SEI formation (lower first cycle CE) and, therefore, cannot be stored in the anode [25]. After 153 cycles, the EOC anode potential is considerably higher than that in the first cycle and reaches potentials of 0.138 ± 0.004 V vs Li/Li⁺ and 0.169 ± 0.004 V vs Li/Li⁺ for the prelithiated and non-prelithiated system, respectively. This results in a very comparable potential increase of 0.134 V and 0.136 V with respect to the first cycle for the prelithiated and non-prelithiated system. The EOC potential shift towards higher values most likely arises from a continuous loss of active lithium with the conse-
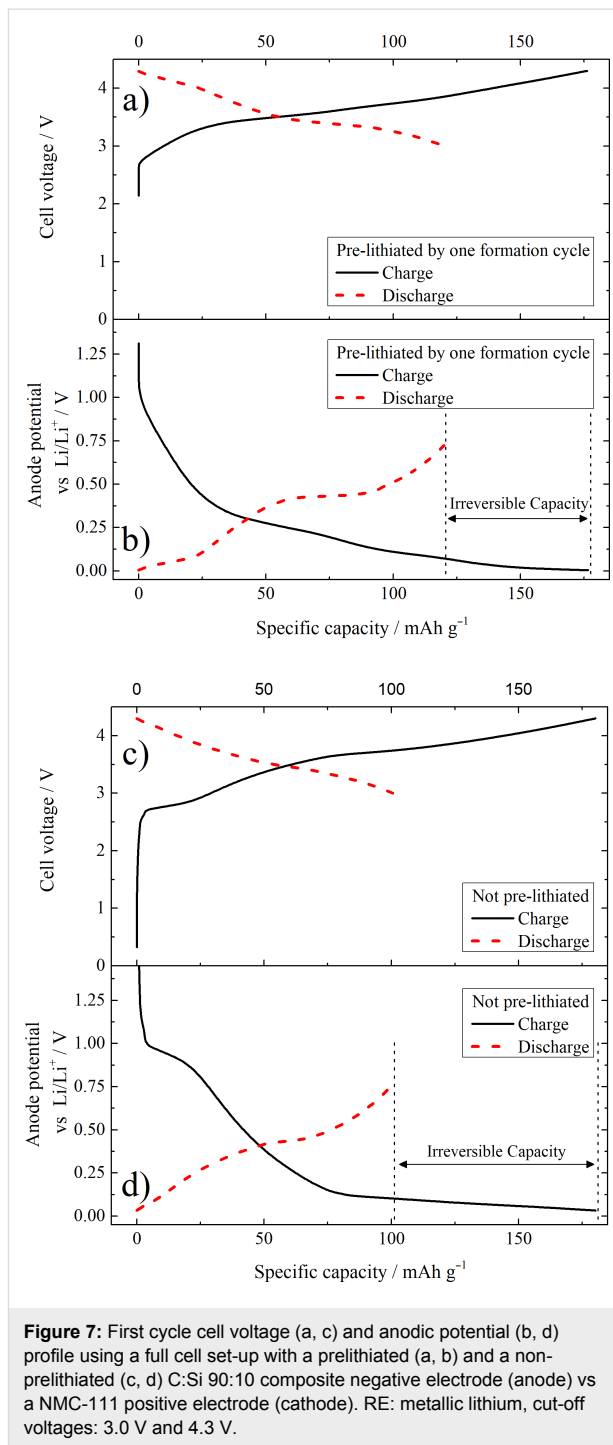
Figure 7: First cycle cell voltage (a, c) and anodic potential (b, d) profile using a full cell set-up with a prelithiated (a, b) and a non-prelithiated (c, d) C:Si 90:10 composite negative electrode (anode) vs a NMC-111 positive electrode (cathode). RE: metallic lithium, cut-off voltages: 3.0 V and 4.3 V.

quence that the anode gets less and less lithiated with ongoing cycle number. Therefore, the lithiation already stops at a higher potential than in the cycle before. As a consequence of the anode potential shift, the cathode potential is likewise shifted to higher potentials because of the constant cell voltage range of 3.0 V and 4.3 V during cycling. The detrimental consequences of such a voltage shift has been described in detail by Krüger et al. [67] and later by Beattie et al. [71].

Figure 8: Development of the anode (negative electrode) and cathode (positive electrode) potential vs Li/Li$^+$ in dependence of the time during cycling using a LIB full cell set-up with a prelithiated (a) and a non-prelithiated (b) C:Si 90:10 composite anode vs a NMC-111 cathode. RE: metallic lithium, cut-off voltages: 3.0 V and 4.3 V.
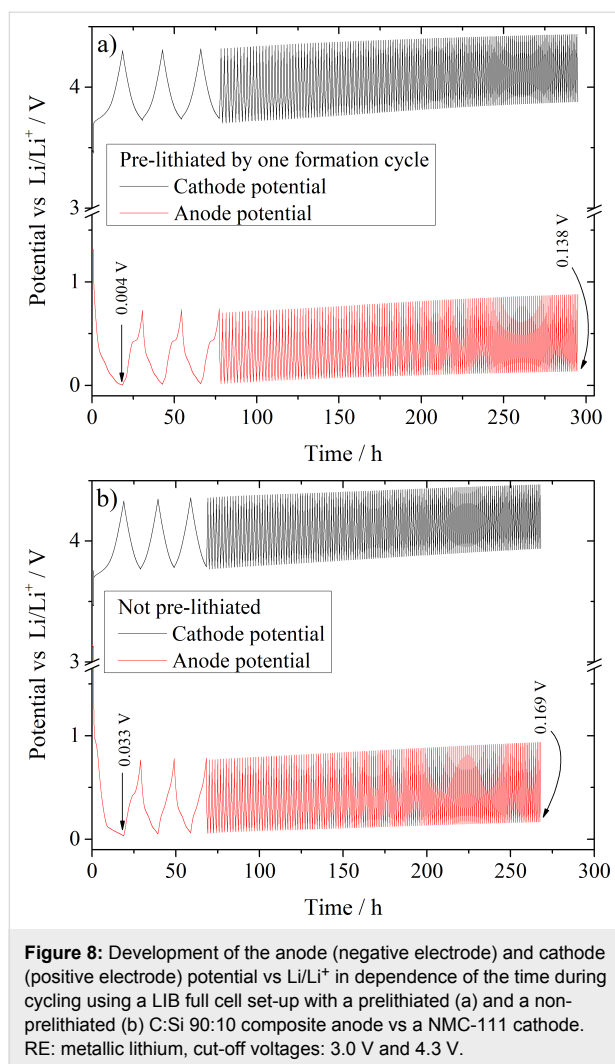
Even though the first cycle CE is still quite low at ≈67% after the prelithiation, and thus requires further optimization, the high importance of this method regarding the application of Si-based anode materials with low initial CE is clearly discernable.

Conclusion

In this study, we investigated a facile synthesis approach where Si-NPs are embedded into an amorphous carbon matrix via a hydrothermal process. The aim of the applied synthesis route was to obtain Si/C composite materials that combine the advantageous properties of Si and C. In summary, it can be stated that a strong improvement in capacity retention could be achieved compared to a mixture of Si and carbon in which Si-NPs were not incorporated into the matrix. At the same time though, the capacity fading was still observed with ongoing cycling. Especially the sample with the highest Si content of ≈20 wt % suffered from quite strong capacity decay due to the inability of the carbon matrix to buffer the volume changes of the Si-NPs sufficiently. This resulted in mechanical stress and the forma-

tion of cracks within the electrodes, as well as continuous SEI formation. Despite the fact that the initial Coulombic efficiency of the synthesized materials was quite low, we could show that these materials are applicable as anode material in a LIB full cell set-up vs NMC-111 cathodes with limited lithium content. Further, the performance could be improved by prelithiation of the anode. Even though the reported results indicated that the presented approach is limited to the use of small amounts of Si (less than 20 wt %), one should consider that there are many potential modifications of the synthesis process that could affect the mechanical properties of the carbon matrix. By changing the temperature, holding time, heating rate or stirring rate, the morphology and particle size of the formed carbon can be adjusted, which might lead to a more flexible, porous and stable matrix. However, further systematic investigations are necessary to identify the influence of different reaction parameters on the structure and morphology of the formed carbon matrix in order to optimize the electrochemical performance of hydrothermal-derived Si/C composites.

Supporting Information

Additional figure, showing SEM micrographs of the physical mixture of Si and C in different magnifications, and a table, summarizing the tap densities of the C:Si composites. Additional figure showing the CEs, EEs and VEs in the charge/discharge current experiments for the Si/C composites with a carbon to silicon ratio of 100:0 (a), 90:10 (b) and 80:20 (c).

Supporting Information File 1
Supporting information.
[https://www.beilstein-journals.org/bjnano/content/supplementary/2190-4286-9-223-S1.pdf]

ORCID® iDs
Martin Winter - https://orcid.org/0000-0003-4176-5811
Tobias Placke - https://orcid.org/0000-0002-2097-5193

References
1. Placke, T.; Kloepsch, R.; Dühnen, S.; Winter, M.
   J. Solid State Electrochem. **2017,** *21,* 1939–1964.
   doi:10.1007/s10008-017-3610-7

2. Nitta, N.; Wu, F.; Lee, J. T.; Yushin, G. *Mater. Today* **2015,** *18,* 252–264. doi:10.1016/j.mattod.2014.10.040

3. Blomgren, G. E. *J. Electrochem. Soc.* **2017,** *164,* A5019–A5025. doi:10.1149/2.0251701jes

4. Goodenough, J. B.; Park, K.-S. *J. Am. Chem. Soc.* **2013,** *135,* 1167–1176. doi:10.1021/ja3091438

5. Schmuch, R.; Wagner, R.; Hörpel, G.; Placke, T.; Winter, M. *Nat. Energy* **2018,** *3,* 267–278. doi:10.1038/s41560-018-0107-2

6. Chao, D.; Xia, X.; Liu, J.; Fan, Z.; Ng, C. F.; Lin, J.; Zhang, H.; Shen, Z. X.; Fan, H. J. *Adv. Mater.* **2014,** *26,* 5794–5800. doi:10.1002/adma.201400719

7. Winter, M.; Besenhard, J. O. Lithiated Carbons. In *Handbook of Battery Materials,* 2nd ed.; Daniel, C.; Besenhard, J. O., Eds.; Wiley-VCH Verlag GmbH & Co. KGaA: Weinheim, Germany, 2011; pp 433–478. doi:10.1002/9783527637188.ch15

8. Meister, P.; Jia, H.; Li, J.; Kloepsch, R.; Winter, M.; Placke, T. *Chem. Mater.* **2016,** *28,* 7203–7217. doi:10.1021/acs.chemmater.6b02895

9. Winter, M.; Besenhard, J. O.; Albering, J. H.; Yang, J.; Wachtler, M. *Prog. Batteries Battery Mater.* **1998,** *17,* 208–213.

10. Obrovac, M. N.; Chevrier, V. L. *Chem. Rev.* **2014,** *114,* 11444–11502. doi:10.1021/cr500207g

11. Besenhard, J. O.; Yang, J.; Winter, M. *J. Power Sources* **1997,** *68,* 87–90. doi:10.1016/s0378-7753(96)02547-5

12. Nitta, N.; Yushin, G. *Part. Part. Syst. Charact.* **2014,** *31,* 317–336. doi:10.1002/ppsc.201300231

13. Obrovac, M. N.; Christensen, L. *Electrochem. Solid-State Lett.* **2004,** *7,* A93–A96. doi:10.1149/1.1652421

14. Obrovac, M. N.; Krause, L. J. *J. Electrochem. Soc.* **2007,** *154,* A103–A108. doi:10.1149/1.2402112

15. Kasavajjula, U.; Wang, C.; Appleby, A. J. *J. Power Sources* **2007,** *163,* 1003–1039. doi:10.1016/j.jpowsour.2006.09.084

16. Zuo, X.; Zhu, J.; Müller-Buschbaum, P.; Cheng, Y.-J. *Nano Energy* **2017,** *31,* 113–143. doi:10.1016/j.nanoen.2016.11.013

17. Zhang, W.-J. *J. Power Sources* **2011,** *196,* 13–24. doi:10.1016/j.jpowsour.2010.07.020

18. Peled, E.; Menkin, S. *J. Electrochem. Soc.* **2017,** *164,* A1703–A1719. doi:10.1149/2.1441707jes

19. Winter, M. *Z. Phys. Chem.* **2009,** *223,* 1395–1406. doi:10.1524/zpch.2009.6086

20. Schmitz, R. W.; Murmann, P.; Schmitz, R.; Müller, R.; Krämer, L.; Kasnatscheew, J.; Isken, P.; Niehoff, P.; Nowak, S.; Röschenthaler, G.-V.; Ignatiev, N.; Sartori, P.; Passerini, S.; Kunze, M.; Lex-Balducci, A.; Schreiner, C.; Cekic-Laskovic, I.; Winter, M. *Prog. Solid State Chem.* **2014,** *42,* 65–84. doi:10.1016/j.progsolidstchem.2014.04.003

21. Winter, M.; Appel, W. K.; Evers, B.; Hodal, T.; Möller, K.-C.; Schneider, I.; Wachtler, M.; Wagner, M. R.; Wrodnigg, G. H.; Besenhard, J. O. *Monatsh. Chem.* **2001,** *132,* 473–486. doi:10.1007/s007060170110

22. Wachtler, M.; Besenhard, J. O.; Winter, M. *J. Power Sources* **2001,** *94,* 189–193. doi:10.1016/S0378-7753(00)00585-1

23. Vogl, U. S.; Lux, S. F.; Das, P.; Weber, A.; Placke, T.; Kostecki, R.; Winter, M. *J. Electrochem. Soc.* **2015,** *162,* A2281–A2288. doi:10.1149/2.0361512jes

24. Wu, H.; Cui, Y. *Nano Today* **2012,** *7,* 414–429. doi:10.1016/j.nantod.2012.08.004

25. Holtstiege, F.; Wilken, A.; Winter, M.; Placke, T. *Phys. Chem. Chem. Phys.* **2017,** *19,* 25905–25918. doi:10.1039/C7CP05405J

26. Wachtler, M.; Wagner, M. R.; Schmied, M.; Winter, M.; Besenhard, J. O. *J. Electroanal. Chem.* **2001,** *510,* 12–19. doi:10.1016/S0022-0728(01)00532-0

27. Reyes Jiménez, A.; Klöpsch, R.; Wagner, R.; Rodehorst, U. C.; Kolek, M.; Nölle, R.; Winter, M.; Placke, T. *ACS Nano* **2017,** *11,* 4731–4744. doi:10.1021/acsnano.7b00922

28. Liu, X. H.; Zhong, L.; Huang, S.; Mao, S. X.; Zhu, T.; Huang, J. Y. *ACS Nano* **2012,** *6,* 1522–1531. doi:10.1021/nn204476h

29. Szczech, J. R.; Jin, S. *Energy Environ. Sci.* **2011,** *4,* 56–72. doi:10.1039/C0EE00281J

30. Hochgatterer, N. S.; Schweiger, M. R.; Koller, S.; Raimann, P. R.; Wöhrle, T.; Wurm, C.; Winter, M. *Electrochem. Solid-State Lett.* **2008,** *11,* A76–A80. doi:10.1149/1.2888173

31. Kwon, T.-w.; Choi, J. W.; Coskun, A. *Chem. Soc. Rev.* **2018,** *47,* 2145–2164. doi:10.1039/c7cs00858a

32. Han, Z.-J.; Yabuuchi, N.; Shimomura, K.; Murase, M.; Yui, H.; Komaba, S. *Energy Environ. Sci.* **2012,** *5,* 9014–9020. doi:10.1039/c2ee22292b

33. Vogl, U. S.; Das, P. K.; Weber, A. Z.; Winter, M.; Kostecki, R.; Lux, S. F. *Langmuir* **2014,** *30,* 10299–10307. doi:10.1021/la501791q

34. Nguyen, C. C.; Lucht, B. L. *J. Electrochem. Soc.* **2014,** *161,* A1933–A1938. doi:10.1149/2.0731412jes

35. Etacheri, V.; Haik, O.; Goffer, Y.; Roberts, G. A.; Stefan, I. C.; Fasching, R.; Aurbach, D. *Langmuir* **2012,** *28,* 965–976. doi:10.1021/la203712s

36. Liu, W.-R.; Yen, Y.-C.; Wu, H.-C.; Winter, M.; Wu, N.-L. *J. Appl. Electrochem.* **2009,** *39,* 1643–1649. doi:10.1007/s10800-009-9854-x

37. Shen, T.; Xia, X.-h.; Xie, D.; Yao, Z.-j.; Zhong, Y.; Zhan, J.-y.; Wang, D.-h.; Wu, J.-b.; Wang, X.-l.; Tu, J.-p. *J. Mater. Chem. A* **2017,** *5,* 11197–11203. doi:10.1039/C7TA03294C

38. Liu, N.; Wu, H.; McDowell, M. T.; Yao, Y.; Wang, C.; Cui, Y. *Nano Lett.* **2012,** *12,* 3315–3321. doi:10.1021/nl3014814

39. Jia, H.; Stock, C.; Kloepsch, R.; He, X.; Badillo, J. P.; Fromm, O.; Vortmann, B.; Winter, M.; Placke, T. *ACS Appl. Mater. Interfaces* **2015,** *7,* 1508–1515. doi:10.1021/am506486w

40. Chen, Y.; Qian, J.; Cao, Y.; Yang, H.; Ai, X. *ACS Appl. Mater. Interfaces* **2012,** *4,* 3753–3758. doi:10.1021/am300952b

41. Demir Cakan, R.; Titirici, M.-M.; Antonietti, M.; Cui, G.; Maier, J.; Hu, Y.-S. *Chem. Commun.* **2008,** 3759–3761. doi:10.1039/b805671b

42. Schmuelling, G.; Winter, M.; Placke, T. *ACS Appl. Mater. Interfaces* **2015,** *7,* 20124–20133. doi:10.1021/acsami.5b05382

43. Moriga, T.; Watanabe, K.; Tsuji, D.; Massaki, S.; Nakabayashi, I. *J. Solid State Chem.* **2000,** *153,* 386–390. doi:10.1006/jssc.2000.8787

44. Courtel, F. M.; Duguay, D.; Abu-Lebdeh, Y.; Davidson, I. J. *J. Power Sources* **2012,** *202,* 269–275. doi:10.1016/j.jpowsour.2011.11.047

45. Liu, W.-R.; Wu, N.-L.; Shieh, D.-T.; Wu, H.-C.; Yang, M.-H.; Korepp, C.; Besenhard, J. O.; Winter, M. *J. Electrochem. Soc.* **2007,** *154,* A97–A102. doi:10.1149/1.2402106

46. Huang, Y.-H.; Bao, Q.; Duh, J.-G.; Chang, C.-T. *J. Mater. Chem. A* **2016,** *4,* 9986–9997. doi:10.1039/C6TA03260E

47. Chou, S.-L.; Wang, J.-Z.; Choucair, M.; Liu, H.-K.; Stride, J. A.; Dou, S.-X. *Electrochem. Commun.* **2010,** *12,* 303–306. doi:10.1016/j.elecom.2009.12.024

48. Xing, Y.; Shen, T.; Guo, T.; Wang, X.; Xia, X.; Gu, C.; Tu, J. *J. Power Sources* **2018,** *384,* 207–213. doi:10.1016/j.jpowsour.2018.02.051

49. Liu, Y.; Wen, Z. Y.; Wang, X. Y.; Yang, X. L.; Hirano, A.; Imanishi, N.; Takeda, Y. *J. Power Sources* **2009**, *189,* 480–484. doi:10.1016/j.jpowsour.2008.12.045

50. Dimov, N.; Kugino, S.; Yoshio, M. *Electrochim. Acta* **2003**, *48,* 1579–1587. doi:10.1016/S0013-4686(03)00030-6

51. Lee, H.-Y.; Lee, S.-M. *Electrochem. Commun.* **2004**, *6,* 465–469. doi:10.1016/j.elecom.2004.03.005

52. Wang, Q.; Li, H.; Chen, L.; Huang, X. *Carbon* **2001**, *39,* 2211–2214. doi:10.1016/S0008-6223(01)00040-9

53. Hu, Y.-S.; Demir-Cakan, R.; Titirici, M.-M.; Müller, J.-O.; Schlögl, R.; Antonietti, M.; Maier, J. *Angew. Chem., Int. Ed.* **2008**, *47,* 1645–1649. doi:10.1002/anie.200704287

54. Forney, M. W.; Ganter, M. J.; Staub, J. W.; Ridgley, R. D.; Landi, B. J. *Nano Lett.* **2013**, *13,* 4158–4163. doi:10.1021/nl401776d

55. Holtstiege, F.; Bärmann, P.; Nölle, R.; Winter, M.; Placke, T. *Batteries (Basel, Switz.)* **2018**, *4,* 4–42. doi:10.3390/batteries4010004

56. Chevrier, V. L.; Liu, L.; Wohl, R.; Chandrasoma, A.; Vega, J. A.; Eberman, K. W.; Stegmaier, P.; Figgemeier, E. *J. Electrochem. Soc.* **2018**, *165,* A1129–A1136. doi:10.1149/2.1161805jes

57. Marinaro, M.; Weinberger, M.; Wohlfahrt-Mehrens, M. *Electrochim. Acta* **2016**, *206,* 99–107. doi:10.1016/j.electacta.2016.03.139

58. Tien, B.; Xu, M.; Liu, J. *Mater. Lett.* **2010**, *64,* 1465–1467. doi:10.1016/j.matlet.2010.03.061

59. Jin, Y. Z.; Gao, C.; Hsu, W. K.; Zhu, Y.; Huczko, A.; Bystrzejewski, M.; Roe, M.; Lee, C. Y.; Acquah, S.; Kroto, H.; Walton, D. R. *Carbon* **2005**, *43,* 1944–1953. doi:10.1016/j.carbon.2005.03.002

60. Kristianto, H.; Putra, C. D.; Arie, A. A.; Halim, M.; Lee, J. K. *Procedia Chem.* **2015**, *16,* 328–333. doi:10.1016/j.proche.2015.12.060

61. Nieto-Márquez, A.; Romero, R.; Romero, A.; Valverde, J. L. *J. Mater. Chem.* **2011**, *21,* 1664–1672. doi:10.1039/C0JM01350A

62. Xia, X.; Wang, Y.; Wang, D.; Zhang, Y.; Fan, Z.; Tu, J.; Zhang, H.; Fan, H. J. *Nano Energy* **2016**, *20,* 244–253. doi:10.1016/j.nanoen.2015.12.015

63. Heckmann, A.; Meister, P.; Meyer, H. W.; Rohrbach, A.; Winter, M.; Placke, T. *ECS Trans.* **2015**, *66,* 1–12. doi:10.1149/06611.0001ecst

64. Fromm, O.; Heckmann, A.; Rodehorst, U. C.; Frerichs, J.; Becker, D.; Winter, M.; Placke, T. *Carbon* **2018**, *128,* 147–163. doi:10.1016/j.carbon.2017.11.065

65. Heckmann, A.; Fromm, O.; Rodehorst, U.; Münster, P.; Winter, M.; Placke, T. *Carbon* **2018**, *131,* 201–212. doi:10.1016/j.carbon.2018.01.099

66. Freunberger, S. A. *Nat. Energy* **2017**, *2,* 17091. doi:10.1038/nenergy.2017.91

67. Krueger, S.; Kloepsch, R.; Li, J.; Nowak, S.; Passerini, S.; Winter, M. *J. Electrochem. Soc.* **2013**, *160,* A542–A548. doi:10.1149/2.022304jes

68. Kasnatscheew, J.; Placke, T.; Streipert, B.; Rothermel, S.; Wagner, R.; Meister, P.; Laskovic, I. C.; Winter, M. *J. Electrochem. Soc.* **2017**, *164,* A2479–A2486. doi:10.1149/2.0961712jes

69. Kim, H. J.; Choi, S.; Lee, S. J.; Seo, M. W.; Lee, J. G.; Deniz, E.; Lee, Y. J.; Kim, E. K.; Choi, J. W. *Nano Lett.* **2016**, *16,* 282–288. doi:10.1021/acs.nanolett.5b03776

70. Dreyer, W.; Jamnik, J.; Guhlke, C.; Huth, R.; Moškon, J.; Gaberšček, M. *Nat. Mater.* **2010**, *9,* 448–453. doi:10.1038/nmat2730

71. Beattie, S. D.; Loveridge, M. J.; Lain, M. J.; Ferrari, S.; Polzin, B. J.; Bhagat, R.; Dashwood, R. *J. Power Sources* **2016**, *302,* 426–430. doi:10.1016/j.jpowsour.2015.10.066

Thickness-dependent photoelectrochemical properties of a semitransparent Co_3O_4 photocathode

Malkeshkumar Patel[1,2] and Joondong Kim[*1,2]

Full Research Paper

Address:
[1]Department of Electrical Engineering, Incheon National University, 119 Academy Rd. Yeonsu, Incheon, 22012, Republic of Korea and [2]Photoelectric and Energy Device Application Lab (PEDAL), Multidisciplinary Core Institute for Future Energies (MCIFE), Incheon National University, 119 Academy Rd. Yeonsu, Incheon, 22012, Republic of Korea

Email:
Joondong Kim[*] - joonkim@incheon.ac.kr

* Corresponding author

Abstract

Co_3O_4 has been widely studied as a catalyst when coupled with a photoactive material during hydrogen production using water splitting. Here, we demonstrate a photoactive spinel Co_3O_4 electrode grown by the Kirkendall diffusion thermal oxidation of Co nanoparticles. The thickness-dependent structural, physical, optical, and electrical properties of Co_3O_4 samples are comprehensively studied. Our analysis shows that two bandgaps of 1.5 eV and 2.1 eV coexist with p-type conductivity in porous and semitransparent Co_3O_4 samples, which exhibit light-induced photocurrent in photoelectrochemical cells (PEC) containing the alkaline electrolyte. The thickness-dependent properties of Co_3O_4 related to its use as a working electrode in PEC cells are extensively studied and show potential for the application in water oxidation and reduction processes. To demonstrate the stability, an alkaline cell was composed for the water splitting system by using two Co_3O_4 photoelectrodes. The oxygen gas generation rate was obtained to be 7.17 mL·h^{-1} cm^{-1}. Meanwhile, hydrogen gas generation rate was almost twice of 14.35 mL·h^{-1}·cm^{-1} indicating the stoichiometric ratio of 1:2. We propose that a semitransparent Co_3O_4 photoactive electrode is a prospective candidate for use in PEC cells via heterojunctions for hydrogen generation.

Introduction

Hydrogen production using water splitting in photoelectrochemical (PEC) cells may help to overcome challenges in the conversion and storage of solar energy. Most of the metal oxides are earth-abundant, non-toxic, stable and easy to synthesise, and hence attractive regarding low-cost and reliable PEC cells [1-8].

For a widespread application of PEC cells, the photoelectrodes need to fulfill the criteria of (i) a low band gap (1.7–2.2 eV), (ii) low resistivity, (iii) low cost, (iv) corrosion stability and (v) a correct alignment of band edges with respect to the water redox potential [3,9,10]. The spinel Co_3O_4 is interesting

because of its dual bandgap (1.5 and 2.2 eV), high absorption coefficient, intrinsic p-type doping and chemical stability. It has found application as a light-absorbing entity in all-metal-oxide photovoltaic cells [11-17]. Dual-bandgap Co_3O_4 films provide distinct band states in the energy–momentum diagram, which is advantageous to reduce the thermalisation-related losses in the sunlight-driven hydrogen generation. Dual bandgaps in Co_3O_4 originate from the crystal-field split Co 3d states at the octahedral (Co^{3+}) and tetrahedral (Co^{2+}) cobalt sites, where Co vacancies are the dominant sources of the p-type conductivity of Co_3O_4 under oxygen-rich conditions [9,13]. Despite these interesting properties of Co_3O_4 its application in photocathodes has been rarely studied [18-23]. Existing studies have measured a photocurrent of 33.6 $\mu A \cdot cm^{-2}$ in 0.5 M Na_2S on a mesoporous Co_3O_4 nanosheet grown through in situ transformation from hexagonal $Co(OH)_2$ to spinel Co_3O_4 [18]. Hong et al. demonstrated a photocurrent of 0.4 $mA \cdot cm^{-2}$ from Co_3O_4 nanowire photocathodes, which could be enhanced to 4.5 $mA \cdot cm^{-2}$ with Ag nanowires [24]. Interestingly, a high photocurrent density of 29 $mA \cdot cm^{-2}$ can be achieved from Co_3O_4 under one-sun illumination (AM1.5G) suggesting a high (solar-to-hydrogen) efficiency of 35.8% [3].

Studies using Co_3O_4 as a catalyst have explored the oxygen evolution reaction (OER) [25,26] and the hydrogen evolution reaction (HER) [20,27] to prove its outstanding stability [28] for the use in water-splitting applications. It therefore may be applied as a protective heterojunction layer to overcome the typical overpotential in photoactive materials. Examples of materials used in such applications include Cu_xO [19,29], CdS [30], TiO_2 [31], Fe_2O_3 [32], and $BiVO_4$ [33,34]. To absorb light with Co_3O_4, an adequately thick film is required. However, the low mobility of photogenerated charge carriers in Co_3O_4 can result in a low carrier lifetime, which is detrimental for efficient charge collection in photoactive applications [9,13,20]. In this context, relatively thin Co_3O_4 samples can overcome charge collection problems due to its semitransparency, which has been investigated in this study. To fabricate Co_3O_4 samples, Kirkendall diffusion is effective to induce the thermal oxidation of Co under atmospheric conditions, which provides an enhanced surface area due to porous features [19,32-38].

Our previous study on porous Co_3O_4 films grown by Kirkendall diffusion exhibited efficient photoelectrocatalystical seawater splitting due to its favourable HER properties [20]. We also developed compact Co_3O_4 films by a reactive sputtering method, in which sputtered Co particles were converted into a compact Co_3O_4 film by controlling the flowing O_2 gas, to offer a self-powered ultraviolet photodetector [17] and semitransparent photovoltaics [39]. It is noteworthy to mention that Co_3O_4 films grown by Kirkendall diffusion have the advantages of a porous structure, a higher growth rate, and easy fabrication.

Here, we report thickness-controlled Co_3O_4 photoactive electrodes in PEC cells that include the water oxidation and the reduction potentials. We thermally oxidize Co nanoparticles in air that form a porous semitransparent Co_3O_4 layer through Kirkendall diffusion. The structural, physical, optical, electrical and photoelectrochemical properties of Co_3O_4 samples are presented as functions of the thickness. The alkaline cell was composed for water splitting by using two Co_3O_4 photoelectrodes. We propose a promising route for photoactive, semitransparent Co_3O_4 embedded in PEC cells for the light-driven hydrogen generation through water splitting.
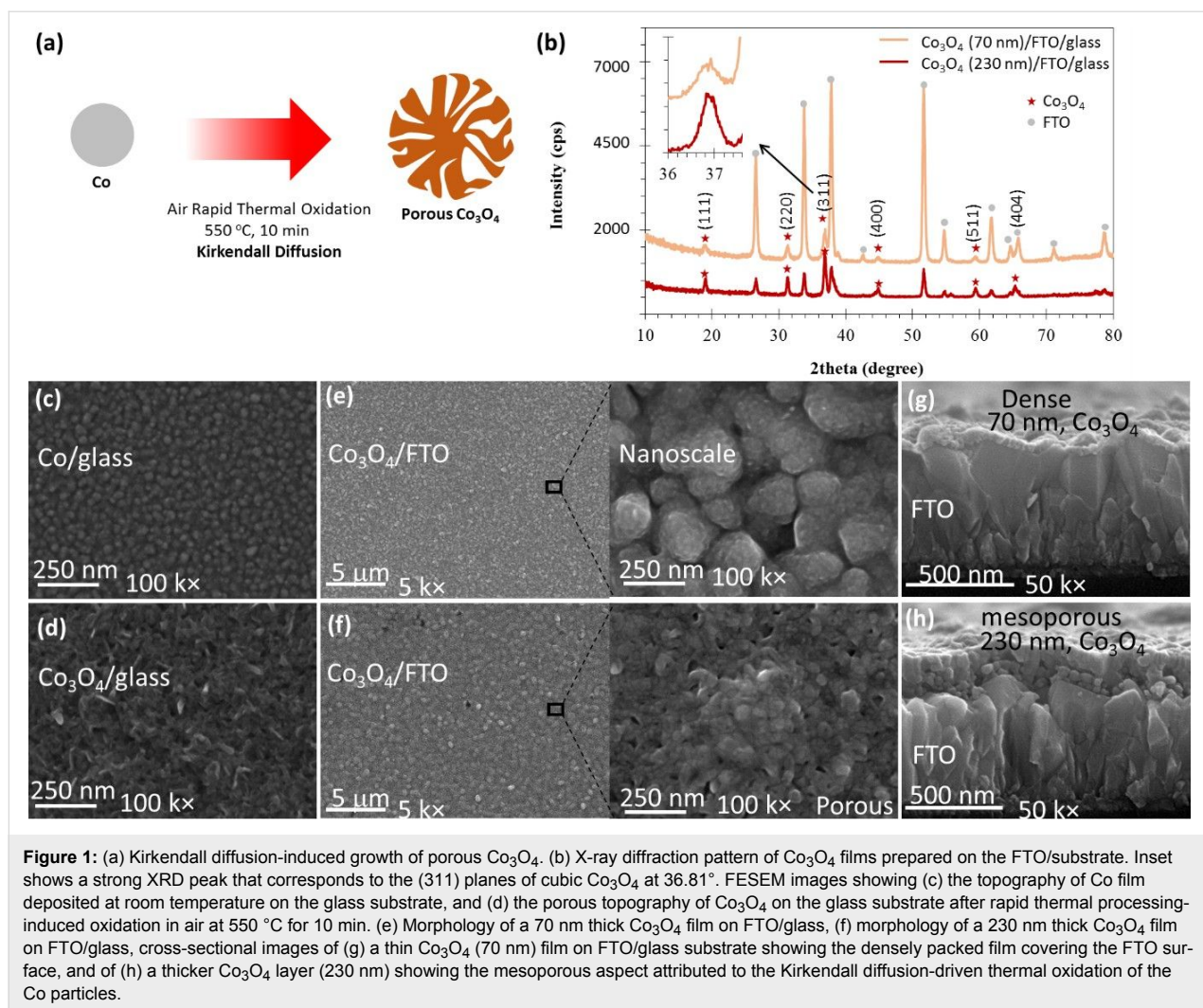
Results and Discussion

The oxidation of Co nanoparticles formed a porous Co_3O_4 structure due to the nanoscale Kirkendall effect as shown in Figure 1a, which arises from the difference in diffusion rates between the anions and cations [35,40]. We applied rapid thermal oxidation to sputtered Co nanoparticles in air at 500 °C for 10 min to convert them into Co_3O_4 [20]. Co films of varying thickness were deposited using large-area (4 inch diameter) sputtering on glass and FTO/glass substrates. Identical rapid thermal processing (RTP) oxidation was applied to these Co films to allow the formation of Co_3O_4 films of varying thickness and porosity.

Figure 1b shows the XRD pattern of two prepared Co_3O_4 samples, 70 nm and 230 nm thick, grown on the FTO/glass substrate. XRD confirmed the formation of a crystalline Co_3O_4 phase due to the air-induced diffusion-driven oxidation of Co. XRD peaks corresponding to Co_3O_4 and $F:SnO_2$ (substrate) were identified and marked. A stronger XRD peak at $2\theta = 36.81°$ corresponds to the (311) planes of cubic Co_3O_4 with a d-spacing of 2.411 Å, in agreement with the crystallographic open database file COD-9005888. According to this XRD pattern, the Co_3O_4 material has a lattice parameter of $a = 8.09$ Å (cubic, $a = b = c$). The XRD peaks at 18.90°, 31.20°, 44.73°, 59.30°, and 65.12° correspond to the (111), (220), (400), (511), and (404) crystal planes, respectively [20,41].

When compared to the $F:SnO_2$ substrate material, the XRD peaks corresponding to the 230 nm thick Co_3O_4 sample are more intense. The absence of XRD peaks of pure Co indicates that the applied RTP fully oxidized the Co film into a Co_3O_4 film with controlled thickness and porosity, which is further validated below.

Figure 1c,d shows the surface morphology of both the deposited Co and the RTP-grown Co_3O_4 film on the glass substrate, re-

**Figure 1:** (a) Kirkendall diffusion-induced growth of porous Co_3O_4. (b) X-ray diffraction pattern of Co_3O_4 films prepared on the FTO/substrate. Inset shows a strong XRD peak that corresponds to the (311) planes of cubic Co_3O_4 at 36.81°. FESEM images showing (c) the topography of Co film deposited at room temperature on the glass substrate, and (d) the porous topography of Co_3O_4 on the glass substrate after rapid thermal processing-induced oxidation in air at 550 °C for 10 min. (e) Morphology of a 70 nm thick Co_3O_4 film on FTO/glass, (f) morphology of a 230 nm thick Co_3O_4 film on FTO/glass, cross-sectional images of (g) a thin Co_3O_4 (70 nm) film on FTO/glass substrate showing the densely packed film covering the FTO surface, and of (h) a thicker Co_3O_4 layer (230 nm) showing the mesoporous aspect attributed to the Kirkendall diffusion-driven thermal oxidation of the Co particles.

spectively. FESEM results confirm that the deposited film contains spherical Co particles, and conversion into porous Co_3O_4 is attributed to Kirkendall-diffusion-induced thermal oxidation.

The planar morphology is shown in Figure 1e and Figure 1f, and corresponds to 70 nm and 230 nm thick Co_3O_4 films grown on the FTO substrate, respectively. The as-grown Co_3O_4 films are uniform and interconnected. A cross-sectional FESEM image of the 70 nm thick Co_3O_4 film, shown in Figure 1g, reveals compact and dense features, while the 230 nm thick Co_3O_4 film, seen in Figure 1h, reveals porous features uniformly distributed across the FTO surface. This subtle morphology change in the crystalline Co_3O_4 can be applied to grade its porosity by simply varying the Co thicknesses prior to thermal oxidation. Therefore, we prepared Co_3O_4 samples with varying thicknesses from 70 to 230 nm, which were extensively studied with regard to their optical, electrical, interfacial, and photoelectrochemical cell properties.

Figure 2a shows the thickness-dependent transmittance (T) and absorbance (A) spectra of the Co_3O_4 samples. Interestingly, all the Co_3O_4 samples exhibited fair absorbance with semitransparent optical properties. Absorbance dominates the shorter wavelengths ($\lambda = 300$–500 nm) with transmittance dominating at longer wavelengths from 600 nm to the infrared (IR). Two distinct transitions in both the T and A spectra of all Co_3O_4 samples are attributed to two bandgaps coexisting in the Co_3O_4 material. A 70 nm thick Co_3O_4 sample exhibited a higher T in the IR region than the other Co_3O_4 samples, which is attributed to its dense and compact film, which causes lower absorption of free carriers than the porous surface.

The absorption coefficient (α), which determines the absorption length of the Co_3O_4 samples was estimated using the relation

$$\alpha(\lambda) = \frac{1}{d} \ln\left(\frac{(1 - R(\lambda))^2}{T(\lambda)}\right),$$
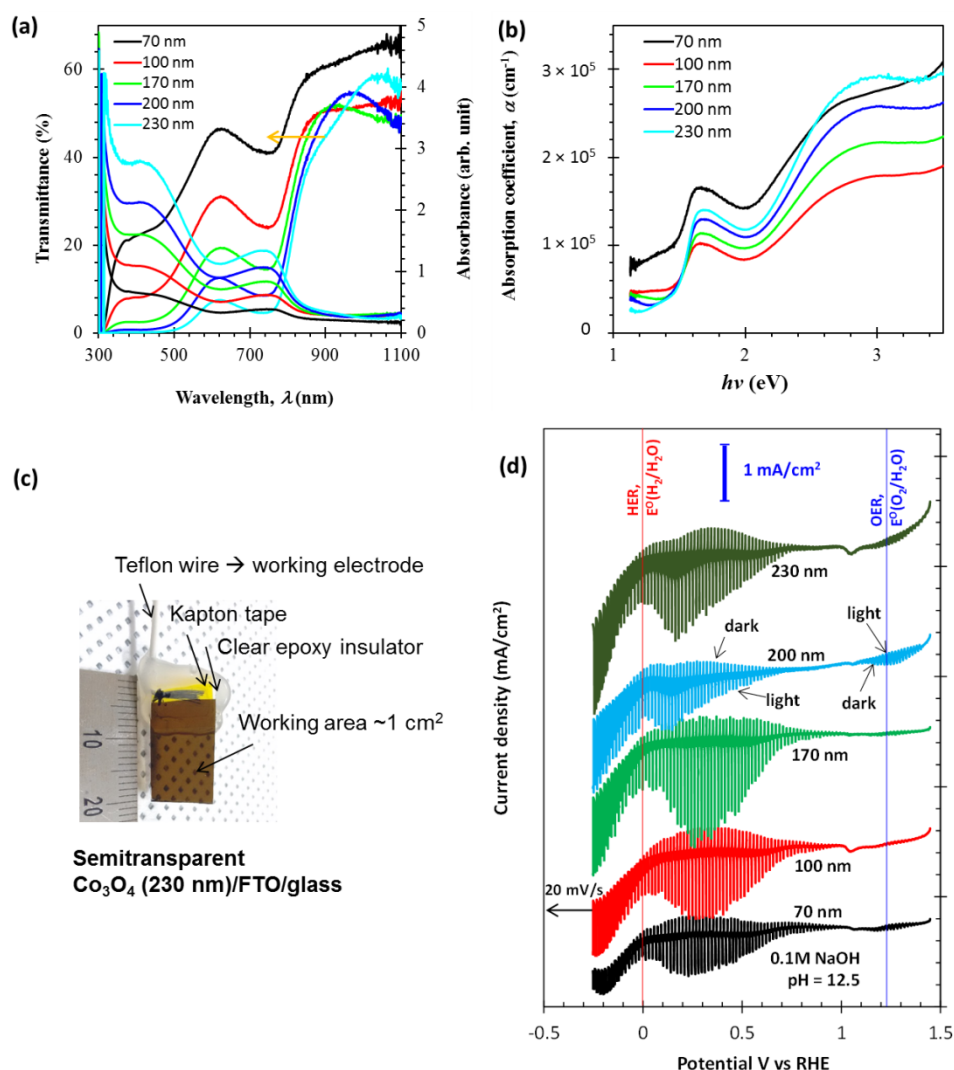
Figure 2: (a) Optical characteristics including the transmittance and absorbance spectra of Co_3O_4 films. (b) Absorption coefficient (α) as a function of the photon energy (*hv*). (c) Photograph of a Co_3O_4 electrode for photoelectrochemical cell studies. (d) Linear sweep voltammogram (from 1.45 to −0.28 V vs RHE) of Co_3O_4 electrodes under pulsed light (100 mW·cm^{-2}).

where *d* and *R* are the thickness of the Co_3O_4 layer and the reflectance, respectively. Figure 2b shows α estimated as a function of photon energy (*hv*). The influence of the Co_3O_4 morphology on α is interesting. Except for the 70 nm film, α increases with thickness, suggesting an increase in porosity as well. A higher porosity led to higher α values, which are prominent in the 440–350 nm region. This feature is useful for a porous Co_3O_4 material as a semitransparent electrode in water-splitting PEC cells. Moreover, two distinct transitions (positive slope) around 1.5 and 2.4 eV in Figure 2b have different α values, providing optical selectivity that can be controlled by film thickness.

Having identified this useful semitransparency of Co_3O_4, we prepared working electrodes to study the thickness-dependent

performance of the photoelectrochemical cell. Figure 2c shows a semitransparent Co_3O_4 working electrode with an active area of 1 cm^2. Clear epoxy resin was applied to the rest of the surface to prevent an electrical connection to the working terminal of the potentiostat/galvanostat. Co_3O_4 has evolved as a chemically resistive and stable material for electrolysis reactions [20,25-27], and therefore the potential of the Co_3O_4 working electrode was swept from 1.5 to −0.3 V vs RHE in a 0.1 M NaOH electrolyte (pH 12.5). The thickness-dependent linear sweep voltammogram (LSV) of the PEC cell under chopped light illumination is shown in Figure 2d. These results provide an overview of the photoinduced OER at 1.23 V vs RHE, the HER at 0 V vs RHE, and the operation of the photocathode. The value of the onset potential (V_{on}), which is the condition attributed to a minimum charge transfer of the cell, was found to be

just below that of the OER potential. All of the Co_3O_4 samples exhibited a photoresponse, suggesting photoabsorption and the utilization of photogenerated charges in the PEC cells. A strong thickness dependence on the photoresponse was found and showed that thicknesses of 100–170 nm are adequate to gain significant photocurrents. More interestingly, the 170 nm Co_3O_4 sample exhibited maximum photocurrent values in the applied potential region of 0.2–0.4 V vs RHE as described below in detail. It is fundamental to optimise the thickness of the Co_3O_4 film. In order to improve light absorption, a thicker film is better. However, the Co_3O_4 film has a short carrier diffusion length due to the slow electron extraction kinetics, resulting in a degraded conversion efficiency [14]. This is the reason for the current decrease for the relatively thick Co_3O_4 films from 170 to 230 nm.

The thickness-dependent LSV for the potentials applied to the Co_3O_4 photoelectrode includes the water oxidation and reduction potentials as shown in Figure 3a–c. The photoresponse of the Co_3O_4 samples in the potential range from −0.25 to 0.2 V vs RHE corresponds to the hydrogen evaluation reaction as shown in Figure 3a. The Co_3O_4 samples with thicknesses from 100 to 230 nm showed identical photocurrent values of ca. 1 mA·cm^{-2}. An increased dark-current level, indicating catalytic properties of the Co_3O_4 material, may have an advantage as the photoinduced current is of great interest in achieving photoinduced water reduction reactions in PEC cells.

When the PEC cell containing the Co_3O_4 working electrode went to the depletion region from a flat band condition, the photoresponse was prominent, as shown in Figure 3b. The low

dark current (J_d), which is consistent throughout the potential from 0.8 to 0.1 V vs RHE, confirms the chemical stability of the Co_3O_4 material. Meanwhile, these results also characterized the photoactive properties of the depletion region and its modulation in the Co_3O_4 electrode. The height of the spikes seems to be related to the bias voltage.

Figure 3c shows the LSV photoresponse near the onset potential of 1.05 V vs RHE, the V_{on} region, for all the samples confirming that the variation in thickness and porosity do not affect V_{on}. However, thicker samples exhibited a higher photocurrent density in the anodic region, which can be interesting for studying the possibilities of light-induced water oxidation reactions. In this context, specifically, the Co_3O_4 film with a thickness of 200 nm showed a photocurrent density (J_{photo}) up to 120 μA·cm^{-2} at 1.23 V vs RHE.

For precise observation, we provided the morphologies of the 170 nm thick Co_3O_4 film in Figure 4. The FESEM images clearly showed the pores (diameter 14–20 nm) and the nanocrystals (diameter 24–42 nm). Through the pores the surface area of Co_3O_4 film can be enhanced. Meanwhile, the nanocrystals work as the efficient routes for charge collection.

Next, the current–time characteristics of the 170 nm thick semitransparent Co_3O_4 photocathode were studied in transient light as shown in Figure S1 (Supporting Information File 1). Chronoamperometry studies at 0 V vs RHE for the Co_3O_4 photocathode show an initial $J_{photo} = 0.7$ mA·cm^{-2} that stabilized to 0.55 mA·cm^{-2} after 30 min of operation, demonstrating a stable PEC cell operation. This also indicates that porous
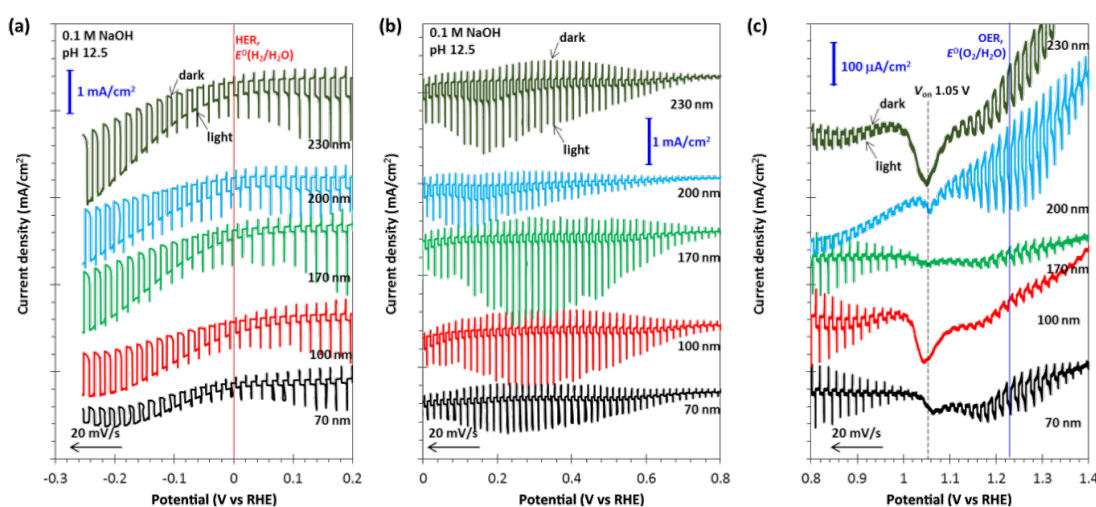
Figure 3: Thickness-dependent linear sweep voltammetry of a Co_3O_4 working electrode under pulsed light. (a) 0.2 to −0.3 V vs RHE (inversion to deep inversion condition as well as HER); (b) 0.8 to 0 V vs RHE (Co_3O_4 undergoing flat band to depletion condition); (c) 1.4 to 0.8 V vs RHE (covering the onset potential, which is close to the flat band potential as well as OER).
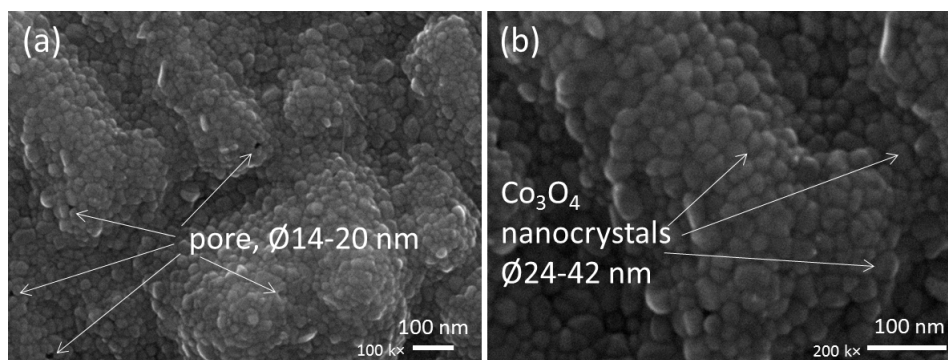
Figure 4: Surface morphology of the 170 nm thick Co_3O_4 film on FTO/glass showing (a) the pores with diameters of 14–20 nm and (b) Co_3O_4 nanocrystals with diameters of 24–42 nm.

Co_3O_4 can be a candidate for a semitransparent photocathode as a chemically stable and optically active material.

In order to better understand the photoactivity and semitransparency of the Co_3O_4 photocathode, transmission electron microscopy was performed on the 170 nm thick Co_3O_4 sample as shown in Figure 5a–c. The cross-sectional TEM image of the Co_3O_4 photocathode seen in Figure 5a shows the flawless Co_3O_4/FTO interface, which is desirable for efficient transport of photogenerated charges. Moreover, the TEM image shows the nanocrystalline nature of the porous Co_3O_4 due to the Kirkendall diffusion that drove the thermal oxidation of Co nanoparticles on the FTO layer. The bright-field distribution observed from the TEM image further illuminates the porous features of the Co_3O_4 nanocrystals and the enhanced photocurrent in the PEC cell performance.
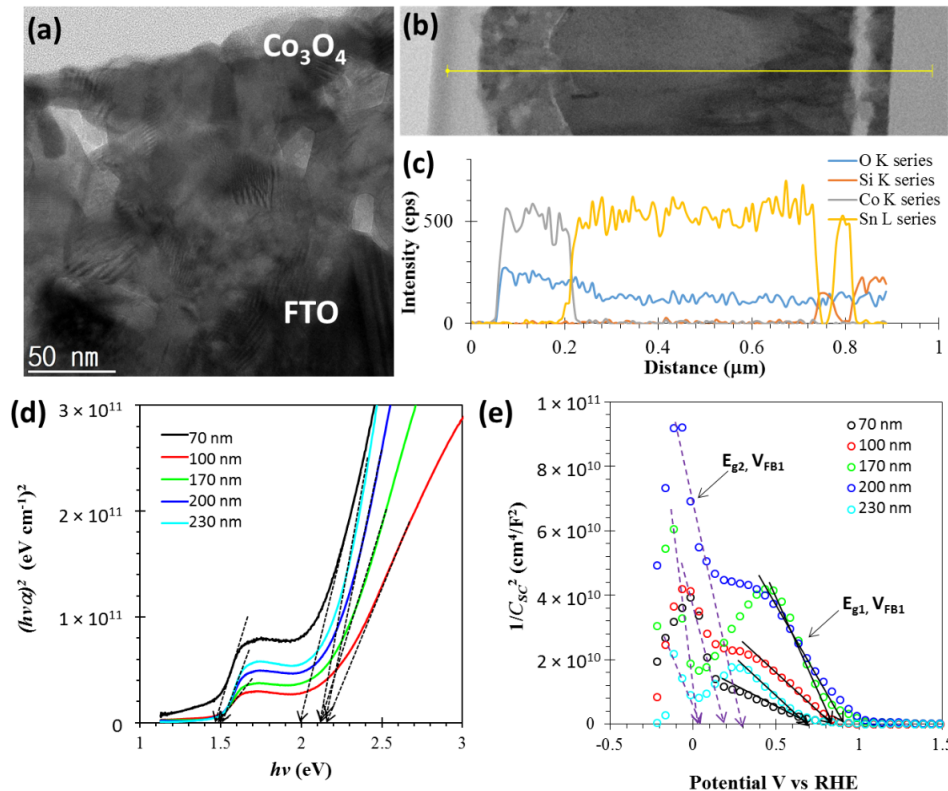
Figure 5: (a) Transmittance electron micrograph featuring nanocrystalline features of a Co_3O_4 electrode prepared on FTO/glass. (b) Cross-sectional image and (c) elemental line profile of Co_3O_4/FTO/glass electrode. (d) Tauc's relation showing the values of two direct bandgaps in Co_3O_4 and their dependence on the thickness of the film. (e) Thickness-dependent Mott–Schottky characteristics of Co_3O_4/FTO electrodes.

A complete cross-sectional image of the Co_3O_4/FTO/glass using the TEM is shown in Figure 5b. This confirms a void-free interface, which is typically difficult to obtain in samples grown using Kirkendall diffusion oxidation, as it generally leads to a core–shell structures. However, here it yielded a porous Co_3O_4 film that can be applied in water-splitting devices. An elemental line profile garnered from energy dispersive spectroscopy as shown in Figure 5c supports the claim of porosity in the grown Co_3O_4 film and the void-free interface between Co_3O_4/FTO.

Further, we estimated the thickness-dependent band-gap energies (E_g) of the Co_3O_4 samples using Tauc's relation as shown in Figure 5d. The coexistence of bandgaps two distinct band gaps with direct E_g values of around 1.5 and 2.1 eV is confirmed. Due to the porous and nanocrystalline nature of the Co_3O_4 samples, a blueshift in the E_g values is seen, compared to the dense 70 nm thick Co_3O_4 sample. Table 1 shows the summarized thickness-dependent optical and electrical properties of the Co_3O_4 samples.

Mott–Schottky (MS) characteristics allow us to describe the type of conductivity, free carrier concentration, and flat-band potential (V_{FB}) of the samples. Figure 5e shows the thickness-dependent MS characteristics ($1/C^2$ as a function of V vs RHE) of the Co_3O_4 samples, obtained at an applied frequency of 5 kHz and under dark conditions. The negative slope in the MS characteristics indicates a p-type material, and the two distinct slopes correspond to two E_g values. The intersect of the $1/C^2$ values on the potential axis indicates the flat-band potential, for which band edges are flat and PEC cells under this condition exhibit the minimum charge transfer. Additional details on the identification of band edges and V_{FB} in the Co_3O_4 samples can be found elsewhere [20]. Figure S2 and Figure S3 (Supporting Information File 1) provide analysis of the MS characteristics including the values of N_{A1}, N_{A2}, V_{FB1}, and V_{FB2}, which are also summarized in Table 1, where N_A is the acceptor carrier concentration. Thickness-dependent parameters including the T, E_g, and N_A values of the Co_3O_4 samples suggest that the enhanced photocurrent performance of the PEC cell containing a 170 nm thick Co_3O_4 film are primarily due to

its enhanced porosity and optical absorption. We also studied the thickness dependent optical and electrical properties of Co_3O_4 film grown by reactive sputtering [17]. In fact, we can see the systematic variation of Mott–Schottky characteristics, and so of the V_{FB} and N_A values of the samples grown by Kirkendall diffusion. This variation is attributed to the varying porosity that does not occur shown in the compact Co_3O_4 film [20].

In order to investigate the long-term stability, the PEC cell was tested for 24 h as shown in Figure 6a. The PEC cell has dual Co_3O_4 electrodes with a potential of 1.65 V vs a Co_3O_4 electrode in 400 mL of an alkaline bath (1 M KOH). The measured current value is presented in Figure 6b for a current density of 25 mA·cm^{-2} that is stable over a period of 24 h. In order to see the morphological changes after 24 h, the Co_3O_4 electrodes were observed by using FESEM as shown in Figure 6c. The OER side of the Co_3O_4 film seems to be similar to a pristine film. The HER side of the Co_3O_4 electrode is also in good shape. As a reference, the FTO image is also presented.

Further, varying bias values (1.4, 1.7 and 2 V) were applied to monitor the water-splitting reaction. Figure 6d shows bias-dependent current profiles. At 1.4 V a current density of 5.25 mA·cm^{-2} with a photocurrent density of 0.75 mA·cm^{-2} under illumination was observed. With an enhanced bias of 2 V, a significantly enhanced photocurrent density (6.5 mA·cm^{-2}) was obtained. This result clearly shows the potential of the Co_3O_4 electrode to achieve high photocurrents at a realtively low potential value. The obtained photocurrent density value for overall water splitting from dual Co_3O_4 electrodes in alkaline bath is more efficient in terms of the required overpotential than the seawater splitting (Co_3O_4‖Pt electrodes) in our previous report [20].

In order to verify the PEC performance, a PEC cell with dual Co_3O_4 electrodes was set up for volumetric measurements. The Co_3O_4 electrodes were loaded into two seperated vials (15 mL, Figure 7) and placed into the 1 M KOH electrolyte bath as shown in Figure 8a. A potential of 1.75 V was supplied

Table 1: Summarized properties of the Co_3O_4/FTO samples. Here t, T, λ, E_g, V_{FB} and N_A are the thickness of the Co_3O_4 layer, transmittance, photon wavelength, band gap, flat-band potential, and acceptor carrier concentration, respectively.

t (nm)	T (%)		E_{g1} (eV)	E_{g2} (eV)	V_{FB1} (V vs RHE)	V_{FB2} (V vs RHE)	N_{A1} (cm^{-3})	N_{A2} (cm^{-3})
	λ = 820 nm	λ = 560 nm						
70	53	39	1.45	2	0.7	0.18	4.9 × 10^{20}	6.1 × 10^{19}
100	41	24	1.47	2.16	0.84	0.32	2.5 × 10^{20}	9.7 × 10^{19}
170	35	15	1.49	2.14	0.82	0.06	8.8 × 10^{19}	5.0 × 10^{19}
200	29	8	1.5	2.13	0.93	0.3	1.4 × 10^{20}	5.3 × 10^{19}
230	25	4	1.51	2.12	0.7	0.08	2.5 × 10^{20}	1.1 × 10^{20}
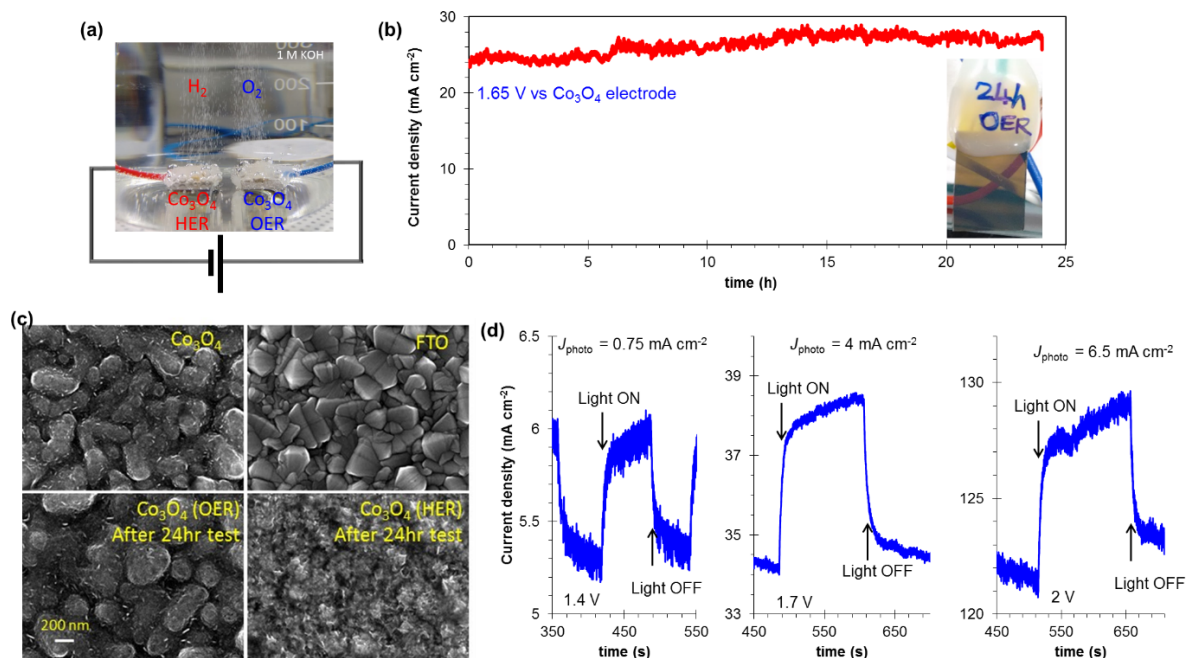
Figure 6: (a) PEC cell setup by using dual Co_3O_4 electrodes to show O_2 gas generation in OER side and H_2 gas generation in HER side. (b) Current stability test for 24 h at a bias of 1.65 V vs Co_3O_4 electrode (inset is the photograph of the Co_3O_4 electrode after 24 h test). (c) FESEM images after test. (d) Current–time plots (at bias values of 1.4, 1.7, and 2 V vs Co_3O_4 electrode) under pulsed light illumination.
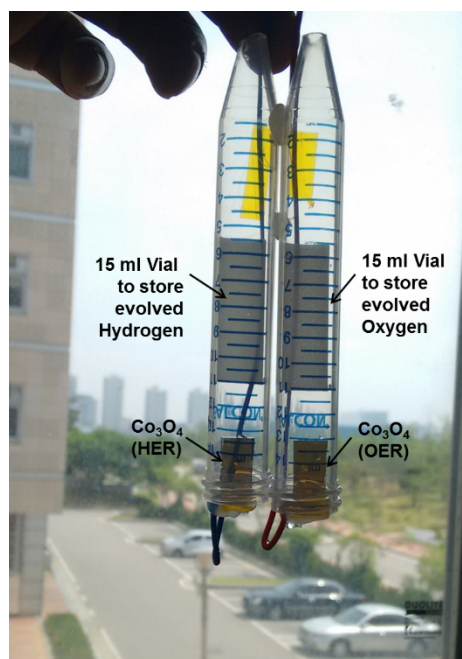
Figure 7: PEC cell setup with dual Co_3O_4 electrodes for volumetric measurements.

Evolution of the gases was clearly monitored in the two vials as presented in Figure 8b. After 23 min, 5.5 mL of hydrogen and 2.75 mL of were accumulated, corresponding to the ratio of 2:1 of water splitting. The hydrogen and oxygen gas evolution as a function of the time is presented in Figure 8c. The results show a hydrogen gas generation rate of 14.35 mL·h^{-1}·cm^{-1} and an oxygen generation rate of 7.17 mL·h^{-1}·cm^{-1} at a bias of 1.75 V vs Co_3O_4 electrode.

Our results demonstrate a stable photoinduced PEC cell performance with a semitransparent Co_3O_4 material made through an easy fabrication process. This could be of great interest for improving the water-splitting performance of emerging, earth-abundant light-absorber materials such as metal sulfides and metal oxides via heterojunction. The photocurrent can be further improved by three approaches: The first one is to improve the optoelectronic processes in the Co_3O_4 film [39], the second is to improve the composition of the heterojunction, i.e. Co_3O_4/Ga_2O_3 [42,43], and the third is the combination with a catalyst such as NiMo and transition-metal dichalcogenide 2D materials [43,44].

Conclusion

We fabricated porous, semitransparent Co_3O_4 working electrodes of varying thickness using Kirkendall diffusion thermal oxidation in air. The thickness-dependent structural, physical, optical and electrical properties of the porous Co_3O_4 samples

to the Co_3O_4 electrode. The Co_3O_4 electrodes exhibited stoichiometric water splitting with an average current density of 39.5 mA·cm^{-2}.
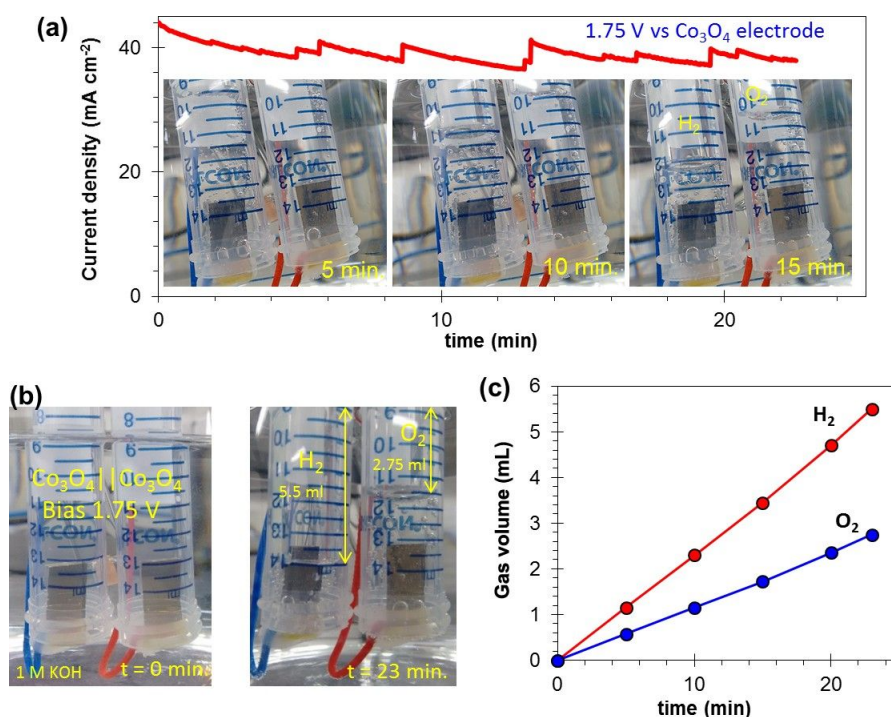
Figure 8: (a) Current density as a function of the time. The Co_3O_4 electrode was biased at 1.75 V in 1 M KOH electrolyte. Inset shows the photograph of gas evolution by time. (b) Photographs of the gas evolution at $t = 0$ and $t = 23$ min. (c) The hydrogen and oxygen gas evolution as a function of the time.

were studied. The application of a thickness-controlled Co_3O_4 film in a water-splitting PEC cell showed a light-induced photocurrent that included water oxidation and reduction processes. In particular, a photocurrent value of 1.5 mA·cm^{-2} corresponded to the reduction of the water when using a 170 nm thick Co_3O_4 sample. This sample provided enhanced photocurrent performance in the PEC cell, due to its enhanced porosity and absorbance. By using dual Co_3O_4 photoelectrodes, a hydrogen gas generation rate of 14.35 mL·h^{-1}·cm^{-1} and an oxygen generation rate of 7.17 mL·h^{-1}·cm^{-1} were obtained at a bias of 1.75 V vs Co_3O_4 electrode. The demonstration of a large-area, easy fabrication process to grow semitransparent Co_3O_4 samples would be pivotal for further application of light-driven water-splitting cells with heterojunctions.

Experimental

Sample fabrication: The photocathode was composed of Co_3O_4/fluorine-doped tin oxide (FTO)/glass. The general synthesis of Kirkendall diffusion grown Co_3O_4 film was analogue to our previous study [20]. In brief, a commercial fluorine-doped tin oxide (FTO)-coated glass (735167, Sigma-Aldrich, sheet resistance of 7 Ω/sq) and a glass microscope slide were used as substrates. These were cleaned using a sequence of isopropyl alcohol, acetone and distilled water using ultrasonication. Then, various thicknesses of Co films were

deposited using a dc magnetron sputtering system (dc power ca. 10 W·cm^{-2}) was applied to a 4″ Co target (purity 99.99%). At a base pressure of 5×10^{-5} Torr sputtering gas (Ar) at a flow rate of 50 sccm was injected. To form the Co_3O_4 film, an atmospheric rapid thermal processing was applied at 550 °C for 10 min. The processing temperature was achieved in two stages. Ramp 1 increased the room temperature of 25 to 300 °C in 5 min. Ramp 2 then increased the temperature from 300 to 550 °C in 5 min. Natural cooling followed the RTP and at 100 °C samples were removed from the RTP chamber for characterization and electrochemical studies.

The Co_3O_4 working electrode was made of Teflon-coated wire that was applied to the FTO film with Kapton tape. Then, a clear insulating epoxy was applied to the Kapton tape and glass edges to provide a working area of 1 cm^2.

Materials characterization: In order to examine the crystalline structure of Co_3O_4, an X-ray diffraction microscope (XRD, Rigaku, SmartLab) (Cu Kα radiation, λ = 1.540598 Å, in grazing mode with a glancing angle of 0.5°, step size of 0.05°, and a 2θ range of 10–80°) as well as a field-emission transmission electron microscope (FETEM, JEOL, JEM-2100F) were used. Cross-sectional TEM samples were prepared using a focused ion beam system (FIB, FEI, Quanta 3D FEG). The

elemental compositions in the cross sections of the Co_3O_4 layers in the working electrode were determined as line profiles by an energy dispersive spectroscopy (EDS) attachment to the FETEM. Thickness and average surface roughness of the deposited films were characterized using a surface profiler (Vecco, Dektak XT-E). The planar and cross-sectional morphologies were analysed using a field-emission scanning electron microscope (FESEM, JEOL, JSM_7800F) with 5 kV of field voltage, using an SE2 secondary detector. Optical characterization was carried out using a UV–visible spectrophotometer (Shimadzu, UV-2600) by recording the transmittance, absorbance, and reflection of the Co_3O_4 films in the range of 300–1100 nm.

Photoelectrochemical cell measurements: Photoelectrochemical measurements were performed in a three-electrode cell with a potentiostat/galvanostat (PG-stat) (WonA Tech, ZIVE SP1). Co_3O_4/FTO/glass, Ag/AgCl (KCl, 3 M), and platinum gauze were connected to the working, reference, and counter electrodes of the PG-stat, respectively. All PEC cell measurements were carried out in 0.1 M NaOH aqueous electrolyte pH 12.5 at room temperature. A white light source (5800 K, Bridgelux, ES Star Array, BXRA-56C0700-A) with a light intensity of 100 mW·cm^{-2} was calibrated with a power meter (KUSAM-MECO, KM-SPM-11). Scan rates of 20 mV·s^{-1} with a 0.1 mV step were set to record the linear sweep voltammetry (LSV), with the scan direction from positive to negative potentials in all cases. The measured potential vs Ag/AgCl were converted to the reversible hydrogen electrode (RHE) scale according to the Nernst relation, $E_{RHE} = E_{Ag/AgCl} + 0.059$ pH $+ E^0_{Ag/AgCl}$, where E_{RHE} is the converted potential vs RHE, $E_{Ag/AgCl}$ is the experimentally measured potential against the Ag/AgCl reference, and $E^0_{Ag/AgCl} = 0.210$ V at 25 °C. A chronoamperometry (current–time characteristic) technique was applied at 0 V vs RHE to study the stability of the Co_3O_4 working electrode under pulsed light. In all of the photoinduced experiments, the Co_3O_4 surface was exposed to illumination. A Mott–Schottky ($1/C_{SC}^2$ as a function of V) analysis of the photoelectrodes was performed at an ac amplitude of 10 mV and in a frequency range from 5 kHz to 500 Hz. The dc potential was scanned from 1.4 to −0.4 V vs RHE with a sampling interval of 25 mV. All the PEC measurements were performed in an Ar purging environment at room temperature with 40 mL of electrolyte.

Supporting Information

Supporting Information File 1
Additional experimental data.
[https://www.beilstein-journals.org/bjnano/content/supplementary/2190-4286-9-228-S1.pdf]

ORCID® iDs
Malkeshkumar Patel - https://orcid.org/0000-0002-8590-0985
Joondong Kim - https://orcid.org/0000-0002-9159-0733

References

1. Lewis, N. S. *Science* **2016,** *351,* aad1920.
   doi:10.1126/science.aad1920
2. Niishiro, R.; Takano, Y.; Jia, Q.; Yamaguchi, M.; Iwase, A.; Kuang, Y.; Minegishi, T.; Yamada, T.; Domen, K.; Kudo, A. *Chem. Commun.* **2017,** *53,* 629–632. doi:10.1039/C6CC08262A
3. Chen, Z.; Dinh, H. N.; Miller, E. *Photoelectrochemical Water Splitting;* SpringerBriefs in Energy; Springer New York: New York, NY, U.S.A., 2013. doi:10.1007/978-1-4614-8298-7
4. Reece, S. Y.; Hamel, J. A.; Sung, K.; Jarvi, T. D.; Esswein, A. J.; Pijpers, J. J. H.; Nocera, D. G. *Science* **2011,** *334,* 645–648. doi:10.1126/science.1209816
5. Kim, M.-w.; Yoon, H.; Ohm, T. Y.; Mali, M. G.; Choi, S. K.; Park, H.; Al-Deyab, S. S.; Lim, D. C.; Ahn, S.; Yoon, S. S. *J. Alloys Compd.* **2017,** *692,* 294–300. doi:10.1016/j.jallcom.2016.08.313
6. Kim, S.; Piao, G.; Han, D. S.; Shon, H. K.; Park, H. *Energy Environ. Sci.* **2018,** *11,* 344–353. doi:10.1039/C7EE02640D
7. Patel, M.; Kumar, M.; Kim, J.; Kim, Y. K. *J. Phys. Chem. Lett.* **2017,** *8,* 6099–6105. doi:10.1021/acs.jpclett.7b02998
8. Rühle, S.; Anderson, A. Y.; Barad, H.-N.; Kupfer, B.; Bouhadana, Y.; Rosh-Hodesh, E.; Zaban, A. *J. Phys. Chem. Lett.* **2012,** *3,* 3755–3764. doi:10.1021/jz3017039
9. Walsh, A.; Ahn, K.-S.; Shet, S.; Huda, M. N.; Deutsch, T. G.; Wang, H.; Turner, J. A.; Wei, S.-H.; Yan, Y.; Al-Jassim, M. M. *Energy Environ. Sci.* **2009,** *2,* 774–782. doi:10.1039/b822903a
10. Lewerenz, H.-J.; Peter, L., Eds. *Photoelectrochemical Water Splitting;* Energy and Environment Series; Royal Society of Chemistry: Cambridge, United Kingdom, 2013. doi:10.1039/9781849737739
11. Kupfer, B.; Majhi, K.; Keller, D. A.; Bouhadana, Y.; Rühle, S.; Barad, H. N.; Anderson, A. Y.; Zaban, A. *Adv. Energy Mater.* **2015,** *5,* 1401007. doi:10.1002/aenm.201401007
12. Patel, M.; Kim, H.-S.; Kim, J.; Yun, J.-H.; Kim, S. J.; Choi, E. H.; Park, H.-H. *Sol. Energy Mater. Sol. Cells* **2017,** *170,* 246–253. doi:10.1016/j.solmat.2017.06.006
13. Lohaus, C.; Morasch, J.; Brötz, J.; Klein, A.; Jaegermann, W. *J. Phys. D: Appl. Phys.* **2016,** *49,* 155306. doi:10.1088/0022-3727/49/15/155306
14. Majhi, K.; Bertoluzzi, L.; Rietwyk, K. J.; Ginsburg, A.; Keller, D. A.; Lopez-Varo, P.; Anderson, A. Y.; Bisquert, J.; Zaban, A. *Adv. Mater. Interfaces* **2016,** *3,* 1500405. doi:10.1002/admi.201500405
15. Majhi, K.; Bertoluzzi, L.; Keller, D. A.; Barad, H.-N.; Ginsburg, A.; Anderson, A. Y.; Vidal, R.; Lopez-Varo, P.; Mora-Sero, I.; Bisquert, J.; Zaban, A. *J. Phys. Chem. C* **2016,** *120,* 9053–9060. doi:10.1021/acs.jpcc.6b01164
16. Wang, B.; Cai, Y.; Dong, W.; Xia, C.; Zhang, W.; Liu, Y.; Afzal, M.; Wang, H.; Zhu, B. *Sol. Energy Mater. Sol. Cells* **2016,** *157,* 126–133. doi:10.1016/j.solmat.2016.05.036

17. Patel, M.; Kumar, M.; Kim, H.-S.; Park, W.-H.; Choi, E. H.; Kim, J. *Mater. Sci. Semicond. Process.* **2018,** *74,* 74–79. doi:10.1016/j.mssp.2017.09.018

18. Mao, Y.; Li, W.; Liu, P.; Chen, J.; Liang, E. *Mater. Lett.* **2014,** *134,* 276–280. doi:10.1016/j.matlet.2014.07.078

19. Ebadi, M.; Mat-Teridi, M. A.; Sulaiman, M. Y.; Basirun, W. J.; Asim, N.; Ludin, N. A.; Ibrahim, M. A.; Sopian, K. *RSC Adv.* **2015,** *5,* 36820–36827. doi:10.1039/c5ra04008f

20. Patel, M.; Park, W.-H.; Ray, A.; Kim, J.; Lee, J.-H. *Sol. Energy Mater. Sol. Cells* **2017,** *171,* 267–274. doi:10.1016/j.solmat.2017.06.058

21. Zhang, D. E.; Ren, L. Z.; Hao, X. Y.; Pan, B. B.; Wang, M. Y.; Ma, J. J.; Li, F.; Li, S. A.; Tong, Z. W. *Appl. Surf. Sci.* **2015,** *355,* 547–552. doi:10.1016/j.apsusc.2015.04.018

22. Yu, C.; Zhang, W.; Gao, Y.; Chen, Y.; Ma, K.; Ye, J.; Shen, R.; Yang, Y. *Mater. Res. Bull.* **2018,** *97,* 483–489. doi:10.1016/j.materresbull.2017.09.049

23. Huang, Z.; Zhao, Y.; Xu, H.; Zhao, J. *Mater. Res. Bull.* **2018,** *100,* 83–90. doi:10.1016/j.materresbull.2017.12.008

24. Hong, T.; Liu, Z.; Zheng, X.; Zhang, J.; Yan, L. *Appl. Catal., B: Environ.* **2017,** *202,* 454–459. doi:10.1016/j.apcatb.2016.09.053

25. Chen, H.; Sun, Z.; Liu, X.; Han, A.; Du, P. *J. Phys. Chem. C* **2015,** *119,* 8998–9004. doi:10.1021/jp511584z

26. Jeon, H. S.; Jee, M. S.; Kim, H.; Ahn, S. J.; Hwang, Y. J.; Min, B. K. *ACS Appl. Mater. Interfaces* **2015,** *7,* 24550–24555. doi:10.1021/acsami.5b06189

27. Yan, X.; Tian, L.; He, M.; Chen, X. *Nano Lett.* **2015,** *15,* 6015–6021. doi:10.1021/acs.nanolett.5b02205

28. Boubault, A.; Ho, C. K.; Hall, A.; Lambert, T. N.; Ambrosini, A. *Sol. Energy Mater. Sol. Cells* **2017,** *166,* 176–184. doi:10.1016/j.solmat.2017.03.010

29. Li, X.; Guan, G.; Du, X.; Cao, J.; Hao, X.; Ma, X.; Jagadale, A. D.; Abudula, A. *Chem. Commun.* **2015,** *51,* 15012–15014. doi:10.1039/c5cc04936a

30. Yehezkeli, O.; de Oliveira, D. R. B.; Cha, J. N. *Small* **2015,** *11,* 668–674. doi:10.1002/smll.201401490

31. Huang, B.; Yang, W.; Wen, Y.; Shan, B.; Chen, R. *ACS Appl. Mater. Interfaces* **2015,** *7,* 422–431. doi:10.1021/am506392y

32. Tüysüz, H.; Hwang, Y. J.; Khan, S. B.; Asiri, A. M.; Yang, P. *J. Phys. Chem. C* **2013,** *116,* 13884–13889.

33. Chang, X.; Wang, T.; Zhang, P.; Zhang, J.; Li, A.; Gong, J. *J. Am. Chem. Soc.* **2015,** *137,* 8356–8359. doi:10.1021/jacs.5b04186

34. Zhao, X.; Chen, Z. *Beilstein J. Nanotechnol.* **2017,** *8,* 2640–2647. doi:10.3762/bjnano.8.264

35. Ha, D.-H.; Moreau, L. M.; Honrao, S.; Hennig, R. G.; Robinson, R. D. *J. Phys. Chem. C* **2013,** *117,* 14303–14312. doi:10.1021/jp402939e

36. Kim, G. M.; Park, J. H.; Lee, J. W. *ChemistrySelect* **2016,** *1,* 560–566. doi:10.1002/slct.201600112

37. Patel, M.; Kim, H.-S.; Park, H.-H.; Kim, J. *Sci. Rep.* **2016,** *6,* 25461. doi:10.1038/srep25461

38. Hu, L.; Yan, N.; Chen, Q.; Zhang, P.; Zhong, H.; Zheng, X.; Li, Y.; Hu, X. *Chem. – Eur. J.* **2012,** *18,* 8971–8977. doi:10.1002/chem.201200770

39. Patel, M.; Park, S.-H.; Kim, J. *Phys. Status Solidi A* **2018,** 1800216. doi:10.1002/pssa.201800216

40. Won, J. M.; Cho, J. S.; Chan Kang, Y. *J. Alloys Compd.* **2016,** *680,* 366–372. doi:10.1016/j.jallcom.2016.04.104

41. Liu, X.; Prewitt, C. T. *Phys. Chem. Miner.* **1990,** *17,* 168–172. doi:10.1007/bf00199669

42. Pan, L.; Kim, J. H.; Mayer, M. T.; Son, M.-K.; Ummadisingu, A.; Lee, J. S.; Hagfeldt, A.; Luo, J.; Grätzel, M. *Nat. Catal.* **2018,** *1,* 412–420. doi:10.1038/s41929-018-0077-6

43. Sivula, K.; van de Krol, R. *Nat. Rev. Mater.* **2016,** *1,* 15010. doi:10.1038/natrevmats.2015.10

44. Roger, I.; Shipman, M. A.; Symes, M. D. *Nat. Rev. Chem.* **2017,** *1,* 0003. doi:10.1038/s41570-016-0003

Femtosecond laser-assisted fabrication of chalcopyrite micro-concentrator photovoltaics

Franziska Ringleb[1], Stefan Andree[2], Berit Heidmann[3,4], Jörn Bonse[2], Katharina Eylers[1], Owen Ernst[1], Torsten Boeck[1], Martina Schmid[3,4] and Jörg Krüger[*2]

Review

`Open Access`

Address:
[1]Leibniz-Institut für Kristallzüchtung, Max-Born-Str. 2, D-12489 Berlin, Germany, [2]Bundesanstalt für Materialforschung und -prüfung (BAM), Unter den Eichen 87, D-12205 Berlin, Germany, [3]Helmholtz-Zentrum Berlin für Materialien und Energie, Hahn-Meitner-Platz 1, D-14109 Berlin, Germany and [4]Fakultät für Physik und CENIDE, Universität Duisburg-Essen, Lotharstr. 1, D-47057 Duisburg, Germany

Email:
Jörg Krüger[*] - joerg.krueger@bam.de

* Corresponding author

Keywords:
chalcopyrite; femtosecond laser patterning; laser-induced forward transfer; micro-concentrator solar cell; photovoltaics

Abstract

Micro-concentrator solar cells offer an attractive way to further enhance the efficiency of planar-cell technologies while saving absorber material. Here, two laser-based bottom-up processes for the fabrication of regular arrays of $CuInSe_2$ and $Cu(In,Ga)Se_2$ microabsorber islands are presented, namely one approach based on nucleation and one based on laser-induced forward transfer. Additionally, a procedure for processing these microabsorbers to functioning micro solar cells connected in parallel is demonstrated. The resulting cells show up to 2.9% efficiency and a significant efficiency enhancement under concentrated illumination.

Review
Introduction

In the field of renewable energies, the largest growth by far on a global scale in 2015/2016 took place in photovoltaics. However, the share of renewables in total energy consumption has recently increased only moderately, despite an enormous growth in the area of renewable energies. A major reason for this is the persistently strong increase in total energy demand [1]. This underlines the importance of the improvement of

existing solar cell concepts and technologies in order to meet the high demand for low-cost solar power.

In the present review, we provide an overview about research carried out on micro-concentrator solar cells – a new cell concept that has been emerging in recent years – using $Cu(In,Ga)Se_2$ (CIGSe) as absorber material. The review focuses

on two different laser-based fabrication methods for microabsorbers. In thin-film photovoltaics, Cu(In,Ga)Se$_2$ (CIGSe) solar cells with an efficiency record of 22.9% for planar cells [2] and 19.2% for sub-modules [3] are among the leading technologies. Figure 1 shows the structure of a planar CIGSe solar cell representing the current state of the art.

The electric back contact (molybdenum) covered with the highly-efficient light-absorber (CIGSe) on top is deposited on a carrier material (glass). A buffer layer (CdS), a window layer consisting of an intrinsic ZnO layer (ZnO) and an aluminum-doped ZnO layer (Al:ZnO) as transparent front contact are located above the solar absorber. Since the CIGSe absorber is produced from highly demanded raw materials such as indium, which is also used for the production of light emitting diodes and flat screens, strong efforts are taken to improve cell efficiency and to develop material-saving fabrication processes and cell concepts. Among other things, current research aims to use light more efficiently through photonically active nanostructures, such that the layer thickness of the approximately 2 μm thick, planar absorber can be reduced (advanced light management) [4,5]. Another approach for saving raw material whilst enhancing the cell efficiency is the concept of CIGSe micro-concentrator solar cells. Instead of planar absorbers, the cells comprise only small absorber structures such as lines or dot-shaped islands, onto which the incident light is focused by microlenses. In Figure 2, this principle is illustrated for the case of dot-shaped solar cells.

Concentrator photovoltaics (CPV) require significantly less absorber material and, at the same time, the concentration of

Figure 2: Scheme of the micro-concentrator solar cell concept.
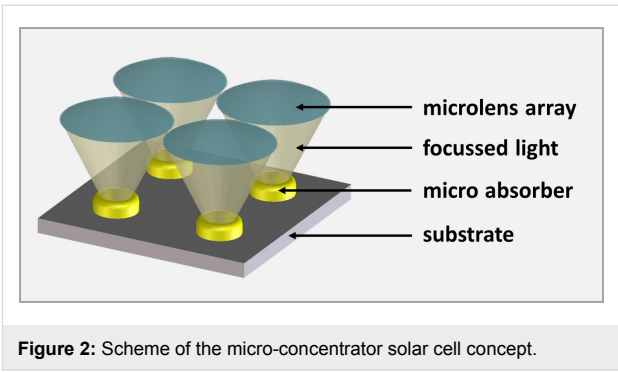
light allows for a more efficient energy conversion. The material saving potential for a squared array of microabsorbers can be estimated from the ratio of the area of one absorber island and the squared distance between the islands. For typical geometries, i.e., absorber island diameters between 40 and 100 μm and a distance of 500 μm, more than 97% of the material can be saved.

Since thickness and weight of concentrator cells both scale with the cell size, flat-plate-like weight and form factors can be realized by downsizing classical CPV to the microscale. Since the amount of heat, which is concentrated on each cell, is lower than for macroscopic concentrators, the system has a better heat dissipation, which has a positive effect on efficiency and lifetime [6-9]. In addition, the small dimensions allow for exploring unconventional architectures and for revisiting optical concepts that have been discarded in the past because of high material cost and optical absorption limits. Meanwhile, fully automated planar micro-tracking systems with less than 2 cm

Figure 1: Design of a planar CIGSe solar cell.
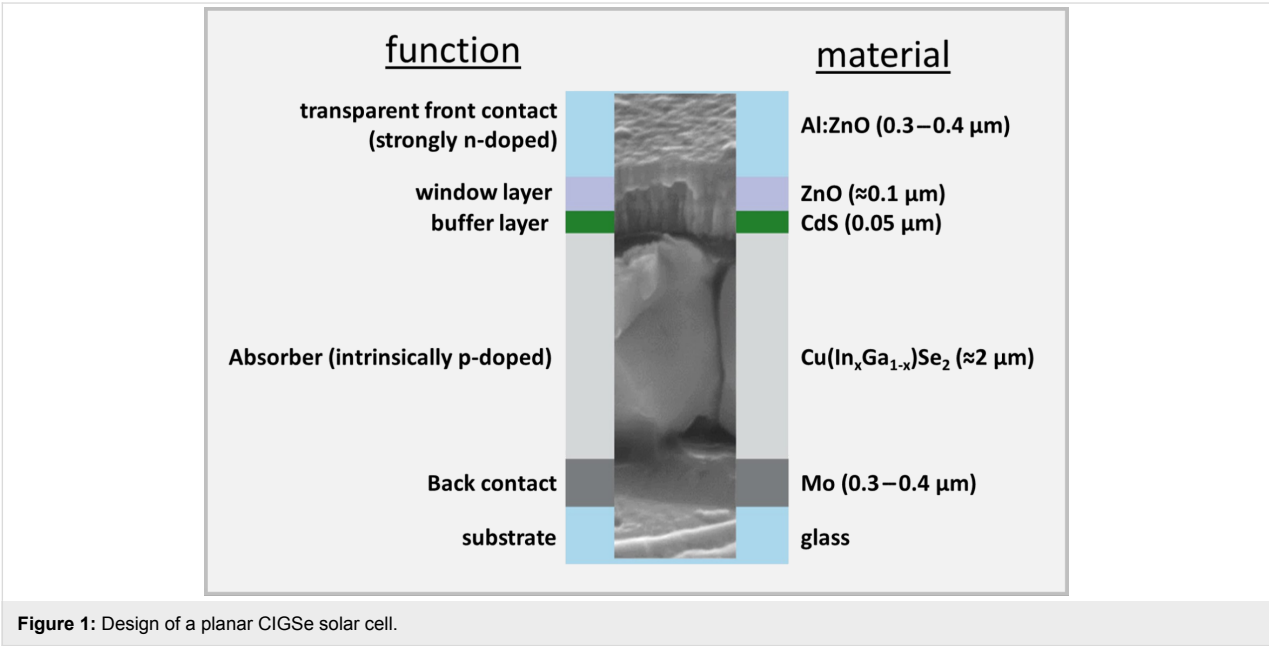
thickness have been developed, which may open up an avenue towards planar rooftop CPV [10]. Taken together, these aspects make micro-scale CPV an attractive approach for next-generation solar cells, which has been explored for several years [11]. These benefits of micro-CVP have to be traded off against the cost of additional components (e.g., lens arrays) and new production technologies for the assembly of microabsorber arrays.

Also for CIGSe, the concept of micro-concentrator solar cells has received increasing attention in recent years. On the one hand, studies were published in which CIGSe micro solar cells have been produced by top-down approaches such as etching or shading of flat absorbers. Paire et al. achieved an absolute increase in efficiency of 5% with 475 suns [12] and Reinhold et al. up to 4.8% for point-shaped cells [13]. They demonstrated that the increase in cell efficiency and the optimum light concentration varied with the size of the cells. Lotter et al. achieved a CIGSe micro cell efficiency as high as 22.5% under 77 suns by selective etching of the front contact layers [14]. While these studies show the efficiency potential of the micro-concentrator concept for CIGSe solar cells, the aspect of material saving was not considered in the chosen top-down approaches. Recently, bottom-up approaches were developed to locally deposit metallic precursors for CIGSe microabsorbers. By means of electrodeposition, the groups of Paire [15] and Sadewasser [16] successfully deposited linear and dot-shaped precursors and processed them to solar cells.

Here, we focus on reviewing two different femtosecond laser-based, material-saving approaches to produce CuInSe$_2$ (CISe) and CIGSe microabsorbers. Several studies ranging from the fabrication of metallic precursors for absorber fabrication, their transformation to microabsorbers, processing to functioning solar cells up to their characterization both under standard conditions and concentrated illumination are summarized here comprehensively and illustrate the challenges and opportunities of the novel approaches to realize this cell concept.

The first approach for microabsorber fabrication summarized here is based on the growth of metallic precursors (indium islands) on laser-structured substrates (molybdenum on glass) by means of physical vapor deposition (nucleation approach). The second method presented is based on laser-induced forward transfer (LIFT). In this method, laser radiation is used to transfer parts of a donor film (copper, indium, gallium) from a transparent carrier medium (glass) to an acceptor substrate (molybdenum on glass) in a spatially controlled manner.
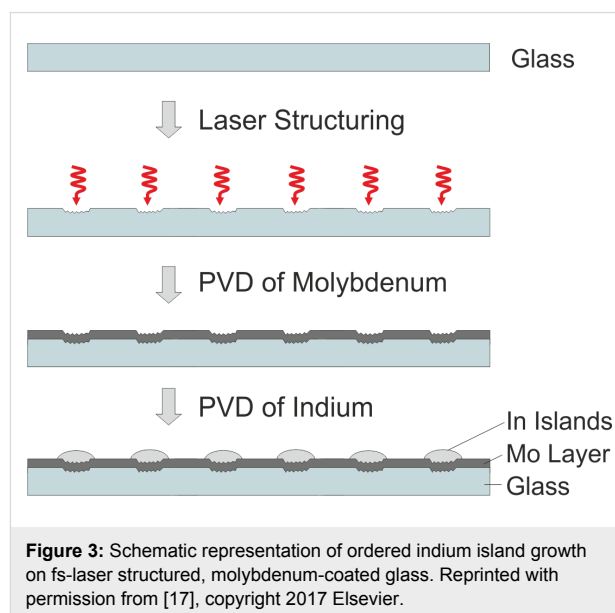
In the first part of this review regarding the fabrication of metallic precursors both approaches are discussed separately. The resulting challenges to process the precursors to microab-

sorbers and to produce functioning solar cells from these, however, were solved in an analogous manner and are thus summed up in a following joint part, which deals with the characterization of the resulting cells under different lighting conditions.

Fabrication of metallic precursors
Nucleation approach
The nucleation approach is based on the arrangement of metallic precursors by island growth on laser-structured substrates. Indium has a strong tendency towards island growth during physical vapor deposition (PVD) on molybdenum substrates. On smooth molybdenum surfaces, indium islands nucleate with random spatial distribution. Indium prefers to accumulate on rough areas. Hence, preferential island nucleation can be induced by local surface roughening. Existing indium islands then act as a material sink for further indium adatoms, such that they accumulate material and keep growing as long as further indium is deposited. At the same time, further island nucleation is suppressed in the vicinity of an existing island due to the constant depletion of freely diffusing indium. The radius around each island within which further nucleation is suppressed extends up to several hundred micrometers, depending on the experimental conditions [17]. The schematic process of indium island growth on molybdenum-covered glass substrates that were structured by a femtosecond (fs-)laser to induce nucleation at predefined locations is depicted in Figure 3. Here, the process is initiated by the laser structuring of the glass, followed by PVD of molybdenum and subsequently indium.

Figure 3: Schematic representation of ordered indium island growth on fs-laser structured, molybdenum-coated glass. Reprinted with permission from [17], copyright 2017 Elsevier.

In other experiments, the glass substrates were PVD-coated with a molybdenum layer prior to the fs-laser treatment and the

PVD of indium [18]. In both cases (fs-laser structuring of either glass substrate or molybdenum film), the resulting substrate surfaces were roughened or, upon harsher laser treatment, even exhibited crater-like depressions at well-defined spots. Figure 4 shows an optical micrograph (OM) of an array of laser-generated material modifications on glass, whereby pulse number and peak fluence of the laser (30-fs laser pulses at 800 nm center wavelength and 1 kHz repetition rate) were varied along rows and columns of the array.

The series of spots at the surface illustrates, that a stronger surface modification or even the formation of a crater can be achieved by increasing the number of laser pulses per spot as well as by increasing the laser fluence (energy density).

Selected scanning electron microscopy (SEM) images of laser modifications on glass, which were recorded at tilting angles of 0 and 52° with respect to the surface normal, are depicted in Figure 5.

Figure 5a shows a laser spot with slight surface roughening that increases towards the center. Using a somewhat higher laser fluence, pronounced laser-induced periodic surface structures (LIPSS [19]) and round melting features form on the glass surface (Figure 5b). The LIPSS with periods in the sub-micrometer range are generated via intra-pulse scattering and interference of the fs-laser radiation at the roughened glass surface, leading to the spatially modulated deposition of energy in a shallow near-surface layer and, finally, to periodic material
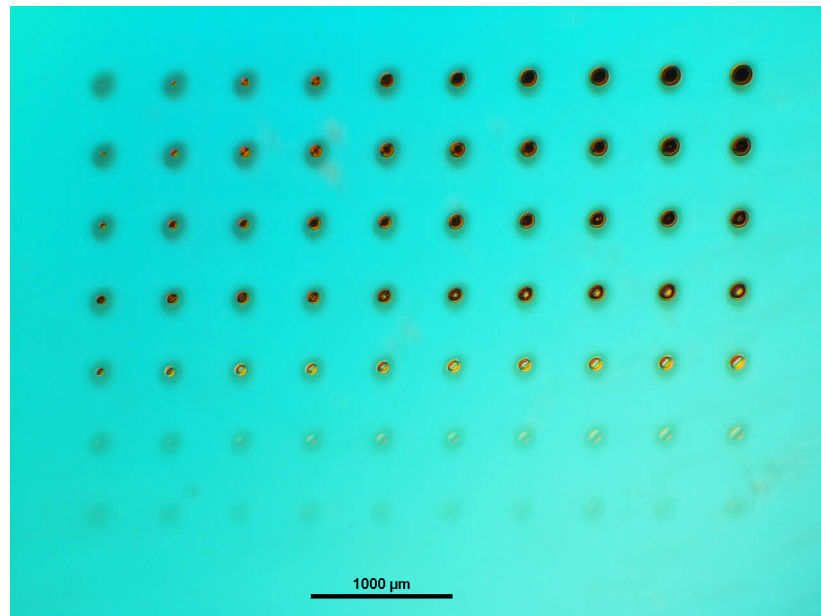
Figure 4: Optical micrographs of fs-laser-treated glass. For each line, the number of pulses per spot, *N*, is constant. From top to bottom, *N* amounts to 1000, 300, 100, 30, 10, 3 and 1. The peak laser fluence *F* varies from 1.24 J/cm^2 (left) to 3.03 J/cm^2 (right).
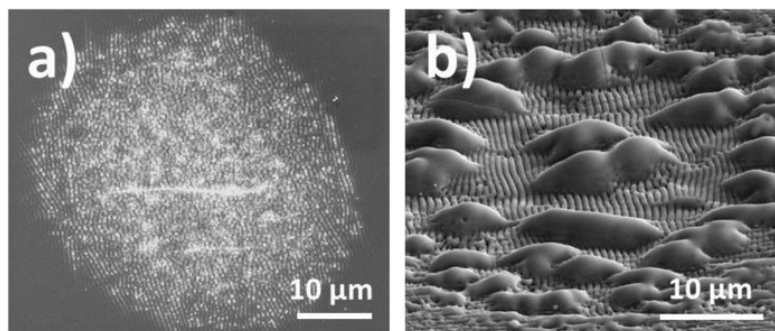
Figure 5: Scanning electron micrographs of laser-induced modifications on glass. Laser parameters: *F* = 1.63 J/cm^2, *N* = 100 (a); 1.83 J/cm^2, *N* = 30 (b). SEM tilting angle 0° (a), 52° (b).

removal [20]. The micrometer-sized melting features supposedly arise from heterogeneities of the glass composition affecting the local optical and thermo-physical properties during the multi-pulse irradiation.

Figure 6 shows SEM images of individual laser spots on glass (top row) and their corresponding profilometric cross sections (bottom row). In the middle row, the spots are depicted after subsequent deposition of molybdenum and indium. The spots were created by applying different pulse numbers N and laser fluences F (from left to right: $F = 1.63$ J/cm^2, $N = 100$; $F = 1.83$ J/cm^2, $N = 30$; $F = 1.83$ J/cm^2, $N = 100$; $F = 2.04$ J/cm^2, $N = 100$).

For all depicted laser spots, the laser-generated surface structures constitute a diffusion trap for evaporated indium during the PVD process. The fact that the strongest indium accumulation occurs at the spot centers, which exhibit the highest roughness, indicates that the island growth is driven by the condensation of indium in the capillary-like structures. For the desired growth of flat and homogeneous indium islands, the data shows that a moderate roughening of the glass/molybdenum substrate

surface, such as depicted in Figure 6, left column, provides the best results. Here, an indium island with a height of 2.6 μm and a diameter of 45 μm has grown on the glass/molybdenum substrate (Figure 6, left column, middle) on a laser-induced ablation spot in glass (Figure 6, left column, top) with a depth of about 300 nm in the center and a roughness R_a of about 25 nm averaged over the whole area (Figure 6, left column, bottom).

In general, the diameter of indium islands, the geometrical aspect ratio and the nucleation density of indium islands all depend on the deposition rate and substrate temperature of the indium PVD process. In order to grow indium islands of well-defined size and aspect ratios and also for realizing arrays of specific spacings without undesired interstitial island formation, the island density and morphology had to be optimized through systematic examination of varying growth conditions. For the PVD process, the variation of temperature and deposition rate provided the insight that island distance and size increase with increasing substrate temperature. This can be intuitively understood by the higher mobility of the indium atoms diffusing on the substrate. At the same substrate temperature, a higher island density was observed by increasing the indium deposition rate.
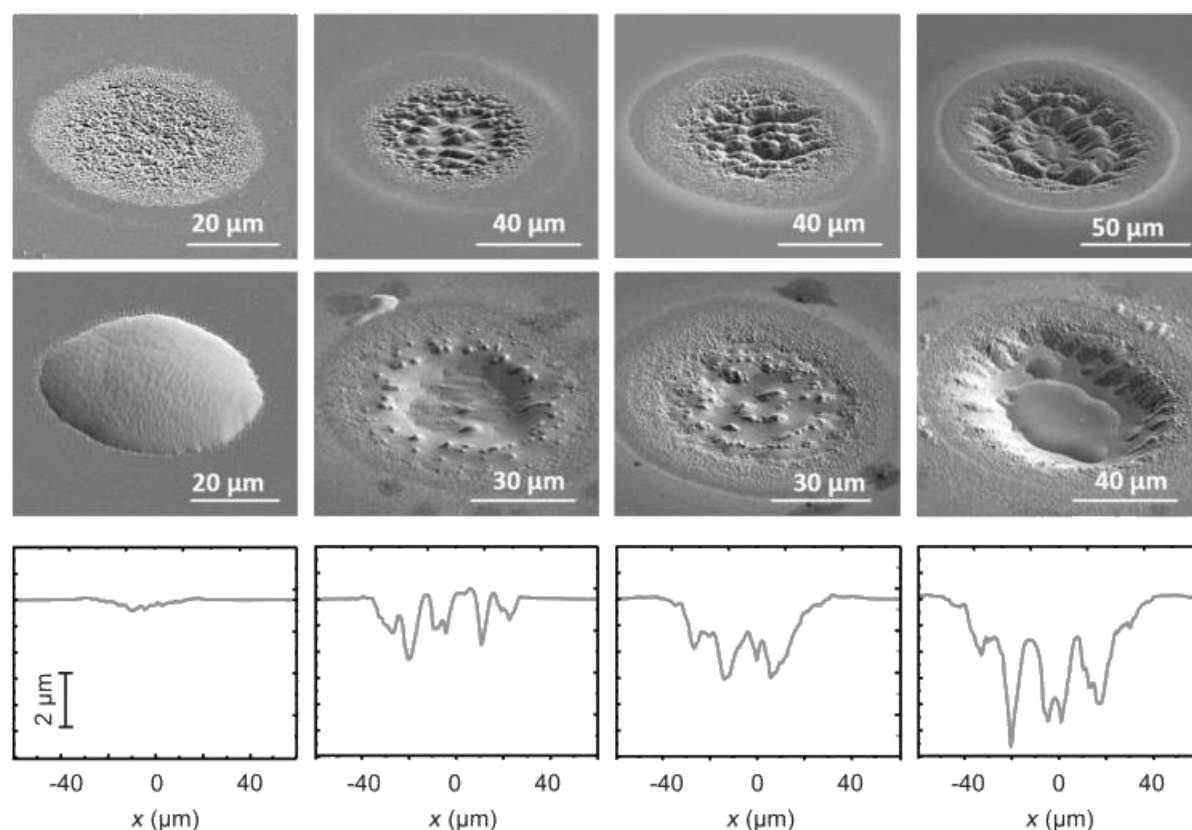
Figure 6: Scanning electron micrographs of individual laser-generated ablation spots on glass (top row) and corresponding profilometric cross sections (bottom row). Spots after deposition of molybdenum and indium (middle row). Laser parameters from left to right: $F = 1.63$ J/cm^2, $N = 100$; $F = 1.83$ J/cm^2, $N = 30$; $F = 1.83$ J/cm^2, $N = 100$; $F = 2.04$ J/cm^2, $N = 100$.

This is in line with the classical nucleation theory according to which the formation of stable nuclei depends on a critical (material specific) nucleus size. The shape of indium islands and the associated contact angle were significantly influenced by the temperature during PVD. At higher temperatures the islands became flatter, probably due to the decrease in surface tension of the liquid indium. The deposition rate of indium, however, had little influence on the contact angle of the islands. By optimizing the growth conditions, it was possible to determine parameters (ca. 500 °C substrate temperature and 0.3 Å/s deposition rate) at which suitable indium island (precursor) dimensions were achieved [17]. Figure 7 displays the result of the optimization process for an array of 500 μm spacing.

The optical micrograph on the left shows an array of laser spots on glass. The PVD of a 400 nm thick Mo back contact layer followed by indium island growth (at 500 °C substrate temperature and 0.3 Å/s indium deposition rate) led to an array of indium islands at the predefined positions (Figure 7, right). Obviously, no indium islands can be found at positions other than at the fs-laser irradiated spots, i.e., interstitial island formation was suppressed.

In contrast to indium, gallium showed a lower tendency for island growth and wetted the entire surface under all applied deposition conditions, such that a significant wetting layer formed in addition to gallium islands. Due to the different temperature dependence of surface mobility and adsorption–desorption equilibria, a sequential PVD process turned out necessary for the growth of (In,Ga) islands, whereby indium islands were grown first, onto which gallium was subsequently deposited. Optimum gallium deposition conditions were found to be a substrate temperature of ca. 400 °C and a deposition rate of 0.15 Å/s. Despite preferential aggregation of gallium at the existing indium islands, an additional gallium wetting layer was always observed. In order to avoid the undesired formation of a thin $CuGaSe_2$ layer connecting the separate CIGSe islands after

processing, this gallium wetting layer was removed by a mild reactive ion etching step in Ar^+ plasma.
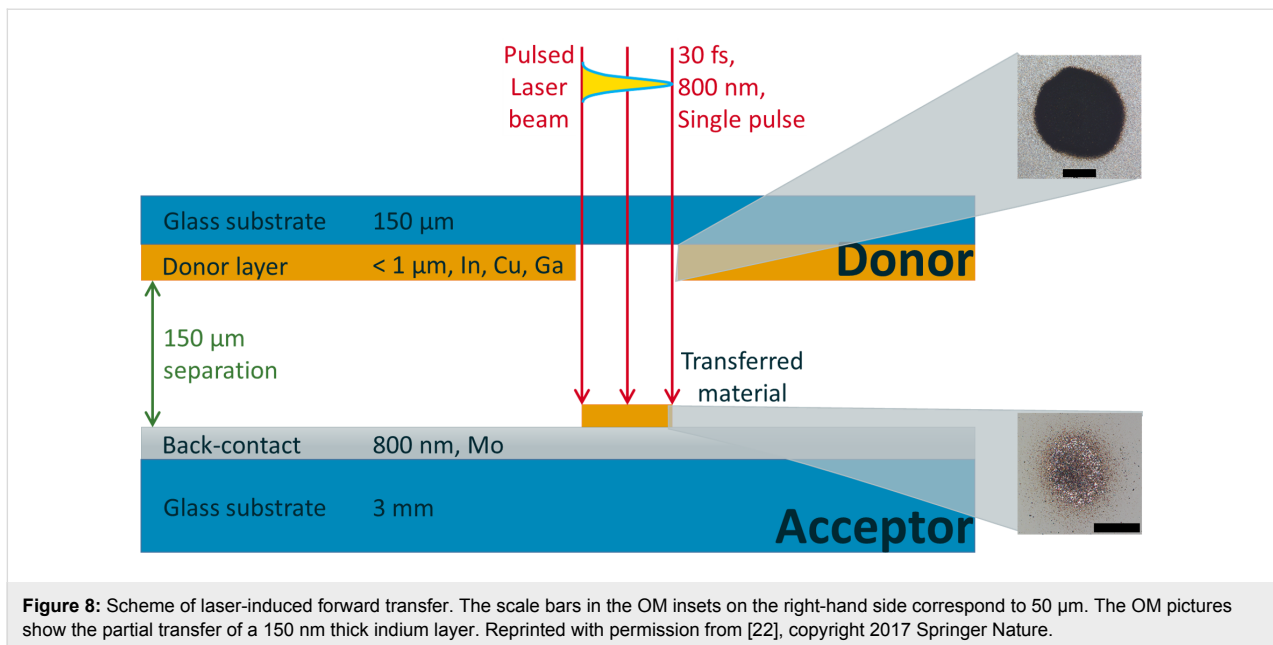
LIFT approach

The second approach presented here for the production of precursor structures for CIGSe microabsorbers is the so-called laser-induced forward transfer (LIFT). In this method, a single laser pulse is used to transfer a part of a donor film located on a transparent substrate onto an acceptor substrate in a spatially structured manner. Prior to the laser treatment, the donor material is deposited on a donor substrate (glass) by means of PVD. The LIFT process was first introduced in 1986 for the transfer of copper onto a silicon substrate using excimer-laser radiation [21]. The experimental setup for the LIFT investigations is schematically shown in Figure 8.

The laser was operated at 30 fs pulse duration and 800 nm center wavelength. Single laser pulses were focused on the glass–metal interface to transfer material from the donor substrate onto the molybdenum back contact of the future solar cell. The distance between donor and acceptor was set to 150 μm. Single layers of copper (10–100 nm thickness) or indium (150–1000 nm thickness) as well as combined copper–indium layer stacks (210–1010 nm) were used as donor materials. Copper was first applied by PVD in all layer stacks because it has a significantly higher melting point than indium [22].

In a first set of experiments, LIFT of pure copper with varying layer thickness (10–100 nm) was investigated. The donor layers were irradiated by single pulses with fluences in the range of 0.8–7.8 J/cm^2. The threshold for the LIFT decreases with decreasing copper layer thickness. In the case of the thinnest copper layers (10 nm, 20 nm), the laser energy is absorbed over the entire layer, resulting in a spray-like transfer of material. No transfer was achieved for a 100 nm thick copper layer. In the layer thickness range of 30–60 nm, a transfer was obtained, which was fragmented to varying degrees, depending on the
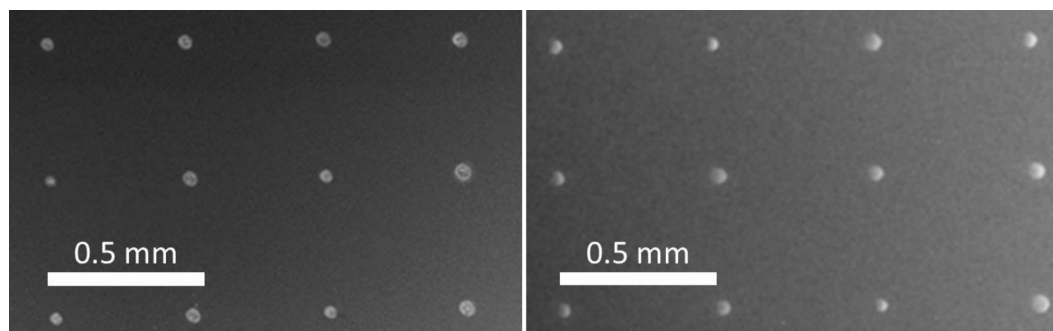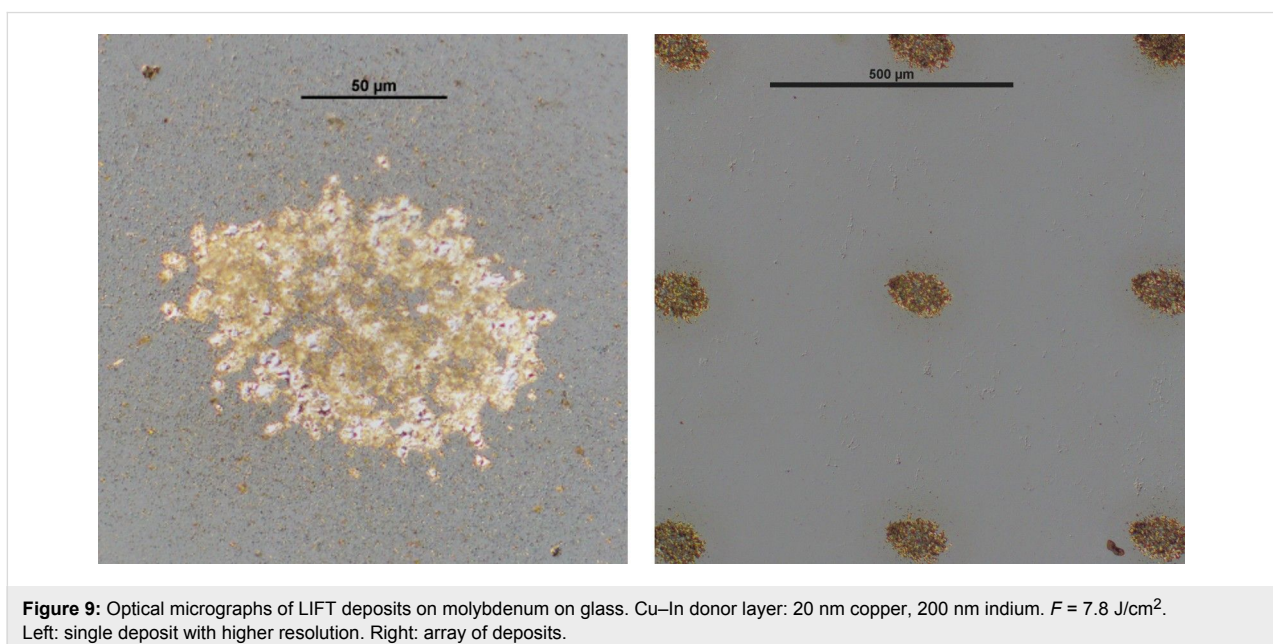
Figure 7: Optical micrographs of a laser-generated spot array on glass (left) and a corresponding array after PVD indium island growth (right).

Figure 8: Scheme of laser-induced forward transfer. The scale bars in the OM insets on the right-hand side correspond to 50 µm. The OM pictures show the partial transfer of a 150 nm thick indium layer. Reprinted with permission from [22], copyright 2017 Springer Nature.

laser fluence. In contrast to copper donor layers, indium can also be transferred from thicker donor layers. This is presumably due to different layer homogeneity (closed copper layers vs granular indium layers) and different thermo-physical properties of the materials. The quality of the transfer is generally comparable to that of copper [22]. On the right side of Figure 8, optical micrographs of LIFT results of an indium film are shown. While the upper image depicts the hole in the indium donor layer of 150 nm thickness after a single laser pulse irradiation at a peak laser fluence of $F = 7.8$ J/cm^2, the lower image displays the spray-like deposit on the acceptor side.

Figure 9 provides the result of a LIFT process of a combined copper–indium donor layer consisting of a 20 nm thick copper layer and a 200 nm thick indium layer. In contrast to pure copper or indium films [22], more homogeneous and compact deposits are formed on the acceptor using the combined copper–indium donor layer (Figure 9, left). Figure 9, right, shows the possibility of arranging compact copper–indium deposits in a freely selected array geometry by LIFT. Here, a square pattern of deposits with a distance of 500 µm was chosen, which is compatible with a potential geometry for micro-concentrator solar cells.

Figure 9: Optical micrographs of LIFT deposits on molybdenum on glass. Cu–In donor layer: 20 nm copper, 200 nm indium. $F = 7.8$ J/cm^2. Left: single deposit with higher resolution. Right: array of deposits.

The LIFT deposits were characterized with respect to morphological and chemical homogeneity by using SEM and energy dispersive X-ray spectroscopy (EDX). It was investigated whether oxygen and carbon accumulations were formed within the transferred material, since these could have a negative effect on the resulting microabsorbers. Neither carbon enrichment nor indications for increased oxidation were detected. The thickness of the deposits was measured by optical microscopy with focus variation. The (average) thickness of a typical copper–indium LIFT deposit (Figure 9, right) is below 1 µm, which is in line with the targeted value for a whole CIGSe absorber of 1–2 µm (see Figure 1) [22].
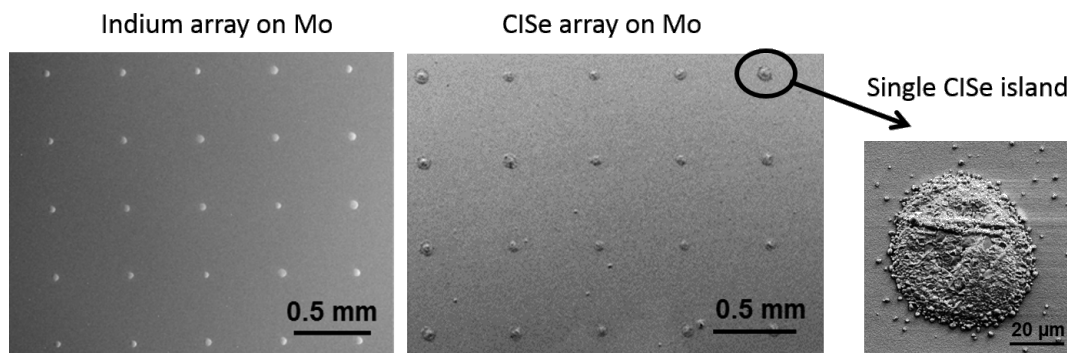
Processing to microabsorbers

In order to process In or In–Ga islands grown by the nucleation approach to CISe or CIGSe microabsorbers, the steps depicted in Figure 10 were applied. Since copper always formed flat layers regardless of the substrate temperatures investigated (from room temperature up to 500 °C), a copper layer of 500 nm thickness was routinely deposited onto In/In–Ga islands

at room temperature (Figure 10b). As a consequence, covering copper selenides formed during the subsequent selenization step in-between and also partially on top of the absorber islands (Figure 10c). These compounds were removed by selective etching in 10% aqueous KCN solution for 3 min (Figure 10d). This etching step is also a standard procedure for the removal of copper selenides in conventional CIGSe production. Figure 11 shows an indium island array prepared by the nucleation approach before (left) and the corresponding CISe array after (right) the processing steps described above. More details for the absorber formation from In islands, in particular on the influence of the Cu layer thickness, can be found in [23].

In the LIFT approach, all metal precursors were transferred from the donor layer to the acceptor substrate in a single transfer step. Therefore, no additional metal deposition step was required. However, selenization and removal of potentially formed copper selenides by etching in KCN was carried out analogous to the processes for the precursors from the nucleation approach.
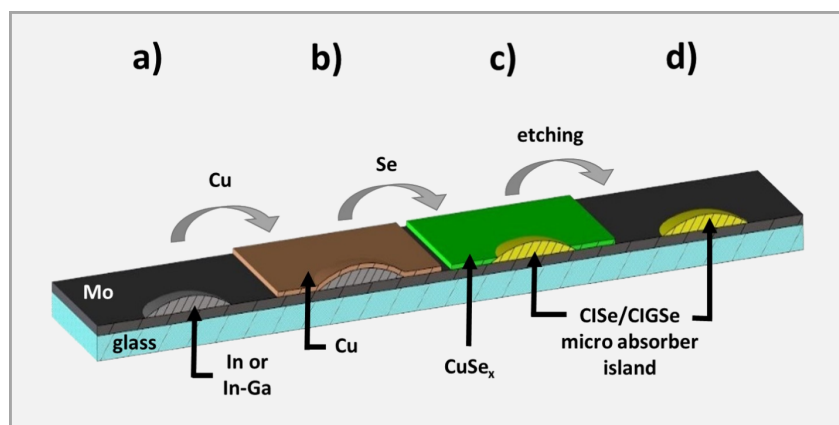
Figure 10: Scheme of the bottom-up process for the preparation of CISe or CIGSe microabsorbers via the nucleation approach. a) Bare In/In–Ga island on a molybdenum-coated substrate, b) In/In–Ga island coated with a flat copper layer, c) sample after selenization process, d) CISe/CIGSe absorber after etch removal of CuSe$_x$.

Figure 11: Processing of In precursor islands prepared by the nucleation approach (left) to CISe micro absorbers (middle and right).

Selenization was realized by rapid thermal processing either in a graphite box at near ambient pressure for CISe samples from the nucleation approach and all samples from the LIFT approach, or in an ultrahigh-vacuum chamber with a directed selenium beam for CIGSe samples from the nucleation approach. In both cases, the temperature protocol comprised an annealing step at around 200–250 °C followed by a high-temperature plateau in the range of 500–560 °C (see [24] for details). It turned out that the homogeneity of the absorbers, in particular in the case of CIGSe samples, was sensitive to the selenization parameters. This effect was particularly significant for CIGSe samples from the nucleation approach the homogeneity of which was clearly enhanced when the high-temperature plateau was increased from 500 to 560 °C.

Processing to solar cells

From microabsorbers that are regularly arranged on a common substrate, a monolithic system of microcells, which are connected in parallel, can be fabricated. A process to realize such a system is illustrated in Figure 12.

Before buffer layers (CdS, ZnO) and front contact (Al:ZnO) can be deposited, the electric insulation between back and front contact in-between the microabsorbers must be ensured. Due to its high (thermal) stability, ease of use and low electrical and high thermal conductivity, the photoresist SU8 was used for this purpose. In order to apply the photoresist, a precursor solution was distributed evenly on the sample via spin coating (Figure 12b). Subsequently, this solution was photochemically converted into SU8 and cured by means of thermal treatment. This procedure comprised a pre-bake (3 min at 95 °C), an UHV treatment (exposure for 10 min to UHV light of 385 nm wavelength), a post-bake (1 min at 65 °C followed by 2 min at 95 °C) and finally a hard bake (3 min at 200 °C). To guarantee

electric connection between the front contact and the CIGSe islands, it is necessary to remove the uppermost part of the SU8 layer, such that the top of the islands is exposed. Upon choosing an appropriate initial viscosity, the SU8 layer is significantly thicker on the substrate than on top of the islands. Therefore, a mild treatment by reactive ion etching (22 min at 250 W in Ar atmosphere), for example, is sufficient to uncover the islands while keeping the molybdenum substrate isolated (Figure 12c). Finally, the buffer layers (CdS, ZnO) and the front contact (Al:ZnO) were deposited (Figure 12d). CdS was applied by a wet-chemical bath deposition. Subsequently, ZnO and finally Al:ZnO layers were created in a sputtering process. Details for CdS and ZnO/Al:ZnO deposition can be found in [25]. Figure 13 shows an SEM image of the edge of a CISe micro island, which has been processed according to this procedure, i.e., in a state corresponding to Figure 12d.

The advantage of the spin-coating approach is that the insulating layer not only covers the molybdenum substrate, but also fills cavities or holes that might form sporadically within the islands and that would lead to power leakage in a lithography-based isolation approach.

Characterization of solar cells

The solar cells were characterized under AM (air mass) 1.5 standard test conditions and at elevated light concentration factors up to 100 suns. For the latter purpose, a concentrator sun simulator was used that also fulfilled AAA conditions (highest spatial uniformity, temporal stability and spectral match with the AM 1.5 sun spectrum). In order to achieve measurably high currents and to facilitate electric wiring, approximately 25 to 100 micro solar cells were simultaneously measured in a parallel interconnection scheme. For efficiency calculation, the active absorber areas were estimated by either calculation from
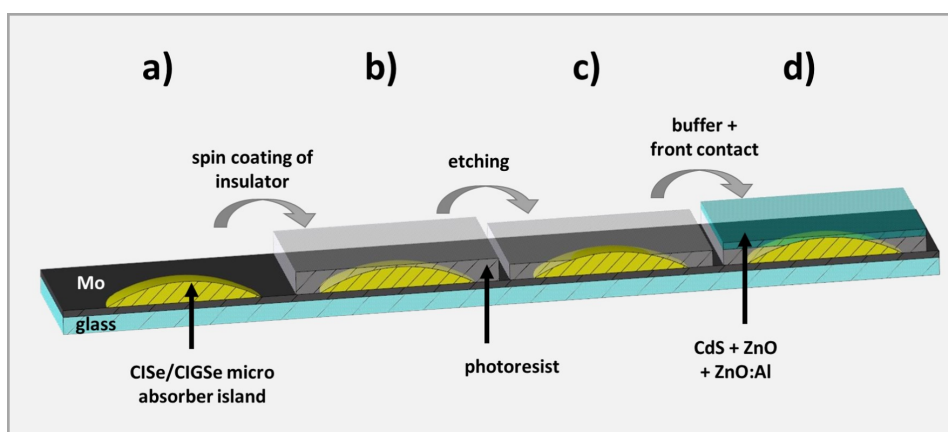
Figure 12: Scheme of the process for manufacturing solar cells from microabsorbers. a) CISe absorber, b) spin coating of photoresist (insulator), c) reactive ion etching in Ar^{+} plasma, and d) addition of CdS and ZnO buffer layers and Al:ZnO front contact.
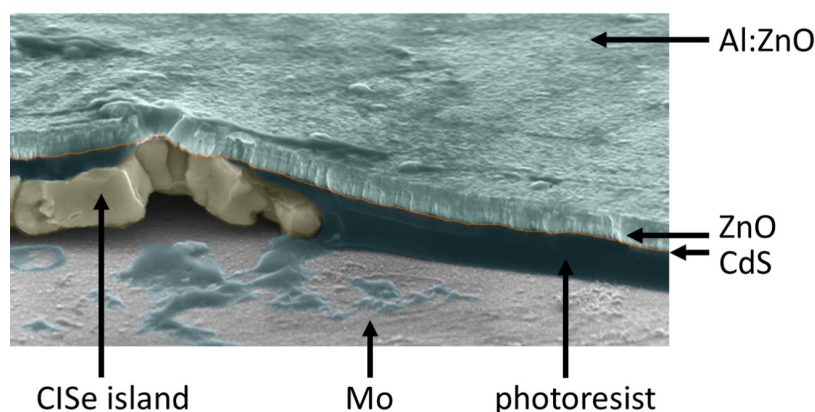
Figure 13: Cross section of a CISe micro absorber island after processing to a micro cell imaged by tilted-view SEM. Note that the different materials were artificially post-colorized to enhance their visibility. The height of the CISe absorber is ca.1 μm.

single microabsorber sizes or by optical microscope measurements. The absorber areas estimated for the different absorber fabrication approaches were (0.00125 ± 0.00007) cm^2 for CISe islands from the nucleation approach, (0.00145 ± 0.00008) cm^2 for CIGSe islands from the nucleation approach and (0.0019 ± 0.00003) cm^2 for CIGSe islands from the LIFT approach. Errors in area measurement are given and directly translate into uncertainties of the final current density and cell-efficiency values. Further errors may arise from the fact that the active absorber area may still be smaller than the measured one. For all three types of locally grown micro solar cells, working devices were obtained. Table 1 summarizes the solar cell parameters determined under 1 sun illumination. The *IV* measurements under 1 sun illumination were depicted in [24].

Astonishingly, the open-circuit voltage (V_{OC}) for the CISe microcells is more than twice as high as the one reached by the CIGSe absorbers. According to the dependence of band-gap energy on the Ga content, the opposite behavior would be expected. This observation points to the fact that the intermixing of In and Ga in the quaternary compounds has still to be improved. In contrast, the short-circuit current per active area (j_{SC}) is almost comparable for CISe and CIGSe micro solar cells from the nucleation approach, but a factor of ten lower for the

CIGSe microabsorbers fabricated via LIFT. The lower current densities achieved for the absorbers from LIFT fabrication can be attributed to a remaining lack of compactness of the absorbers leading to lower carrier generation and extraction. The fill factor (FF) is comparable for all three types of absorbers. Overall, an efficiency (η) of 2.9% for CISe islands from the nucleation approach, of 1.4% for CIGSe islands from the nucleation approach and of 0.15% for CIGSe islands from the LIFT approach was demonstrated. Planar reference cells were fabricated in a sequential process as well, and the precursor stacks were designed according to the bottom-up growth process. This means the same element sequence was chosen for direct comparison, which however, does not correspond to an optimization for planar absorbers. The corresponding efficiencies of the planar references were 5.9% for CISe by nucleation, 8.5% for CIGSe by nucleation and 8.1% for CIGSe by LIFT. The efficiencies given were obtained as an average of measurements on 16 individual solar cells with 0.5 cm^2 size each. For the CISe microcells obtained from the nucleation approach the efficiency amounts to 50% of the planar reference under 1 sun illumination. Given the facts of efficiency enhancement under light concentration and of more than 97% material saving, a relative increase in efficiency per volume by more than 46% can be expected.

Table 1: Solar-cell parameters at 1 sun illumination compared for micro cells fabricated from the different local absorbers and the corresponding planar reference cells.

	j_{SC} (mA/cm^2)	V_{OC} (mV)	FF (%)	η (%)
nucleation CISe	27.5 ± 2.3	295	36	2.9 ± 0.2
nucleation CIGSe	29.7 ± 2.3	132	36	1.4 ± 0.2
LIFT CIGSe	2.9 ± 0.2	145	36	0.15 ± 0.02
planar reference nucleation CISe	33 ± 5	406 ± 50	39 ± 5	5.9 ± 0.5
planar reference nucleation CIGSe	36 ± 4	505 ± 20	45 ± 2	8.5 ± 0.4
planar reference LIFT CIGSe	34 ± 2	425 ± 10	48 ± 4	8.1 ± 0.6

The results of measurements under enhanced illumination intensities are shown below in Figures 14–16 for CISe and CIGSe islands from the nucleation approach, and CIGSe islands from the LIFT approach, respectively. In an ideal concentrator solar cell, the current increases linearly with the concentration factor. This is, however, due to the increase in incident power upon concentration. Thus, both factors cancel each other when it comes to efficiency calculation. The net efficiency enhancement results from the fact that, in addition, the open-circuit voltages rises logartihmically with the concentration factor, which can be deduced from the diode equation:

$$ I = I_{\mathrm{L}} - I_0 \left[\exp\left((qV)/(nk_{\mathrm{B}}T) \right) - 1 \right], \qquad (1) $$

with *I* representing the total current, I_{L} the photo current, I_0 the dark current, *q* the elementary charge, k_{B} the Boltzmann constant, *n* the diode quality factor and *T* the temperature. By solving for $V_{\mathrm{OC}} = V(I = 0)$ and performing the substition of $I_{\mathrm{SC}} = I_{\mathrm{L}}$ with $I_{\mathrm{SC}} \cdot C$, where *C* is the concentration factor and I_{SC} the short-circuit current we obtain:

$$ \begin{aligned} V_{\mathrm{OC}}(C) &= (nk_{\mathrm{B}}T)/q \cdot \ln\left(I_{\mathrm{SC}} \cdot C / I_0 + 1 \right) \\ &\approx V_{\mathrm{OC}}(C=1) + (nk_{\mathrm{B}}T)/q \cdot \ln(C). \end{aligned} \qquad (2) $$

This is inserted into the expression for the efficiency:

$$ \eta = \left(j_{\mathrm{SC}} \cdot V_{\mathrm{OC}} \cdot \mathrm{FF} \right) / P_{\mathrm{in}}. \qquad (3) $$

With the incident power density $P_{\mathrm{in}} = C \cdot 1000$ W/m^2 and the enhancement in V_{OC} by $(nk_{\mathrm{B}}T)/q \cdot \ln(C)$, the efficiency under concentration for an ideal cell translates to:

$$ \eta(C) = \eta(C=1) + (nk_{\mathrm{B}}T)/q \cdot \ln(C) \cdot \left(j_{\mathrm{SC}} \cdot \mathrm{FF} \right) / P_{\mathrm{in}}. \qquad (4) $$

For the three cases of differently grown microabsorbers, we tested these expectations by investigating *IV* measurements with different values of the light concentration (*C*).

For CISe microabsorbers from the nucleation approach, Figure 14a depicts the development of *IV* characteristics from 1 to 50 suns. As Figure 14b illustrates in more detail, I_{SC} only experiences the predicted steep linear increase up to a concentration factor of three, which quickly decreases thereafter. Also FF is governed by a small peak around 3 suns before declining. V_{OC} follows a more steady increase of, in this case, logarithmic rise also at higher concentration levels, yet again with a peak at 3 suns, see Figure 14c. In consequence, the efficiency reaches its maximum at 3 suns already. The deviation from linear rise in current can be understood when looking at the development of series and shunt resistance as a function of the concentration. Both are decreasing with increasing illumination intensity, yet this happens faster for the shunt resistance as it can be deduced from the *IV* curves. A resulting effect is the drop of I_{SC} at higher concentration values.

Moving on to CIGSe microcells fabricated by the nucleation approach, we can, in contrast, observe from Figure 15b a perfectly
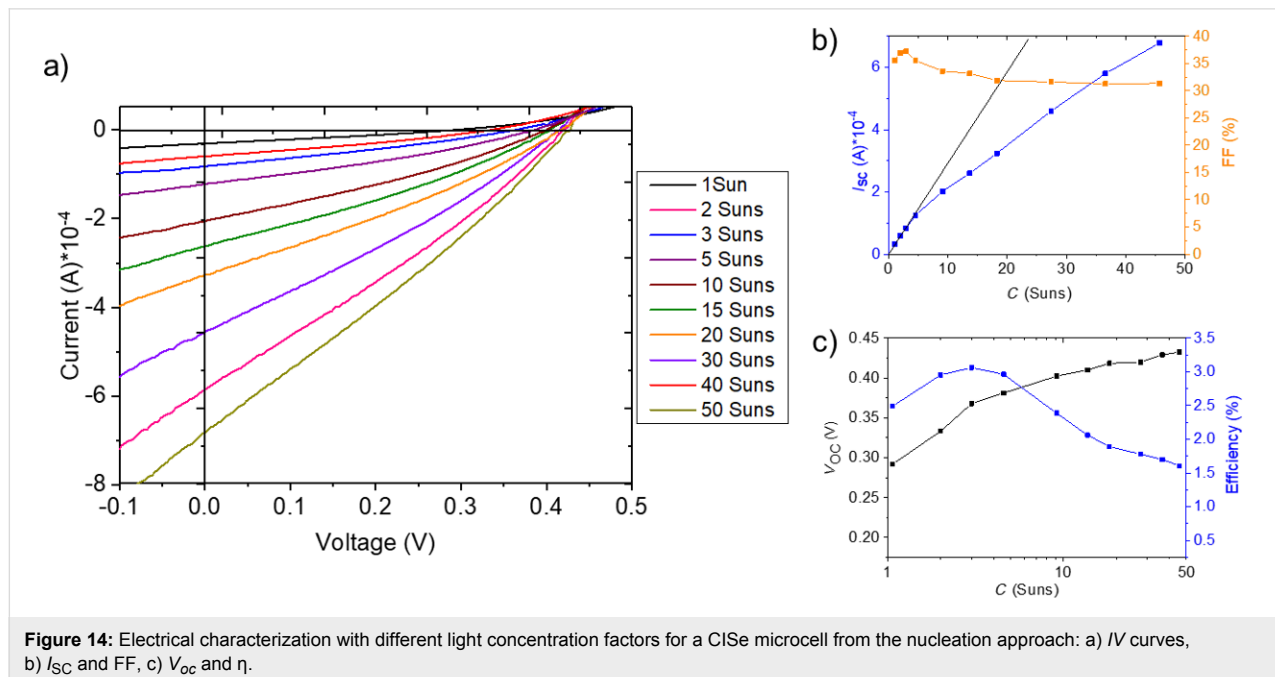
Figure 14: Electrical characterization with different light concentration factors for a CISe microcell from the nucleation approach: a) *IV* curves, b) I_{SC} and FF, c) V_{oc} and η.
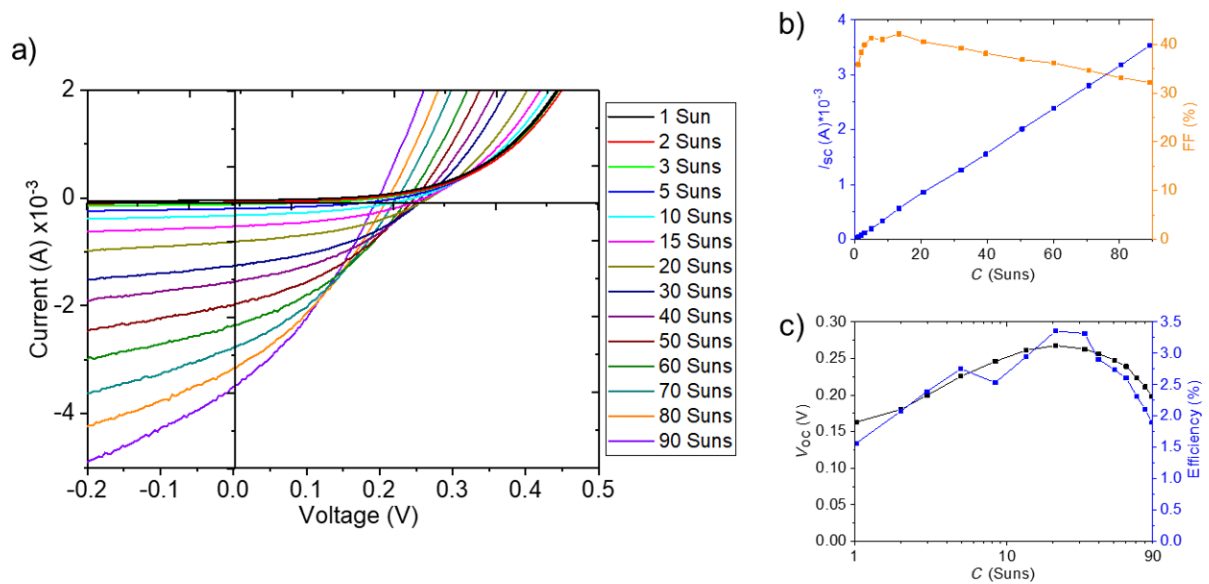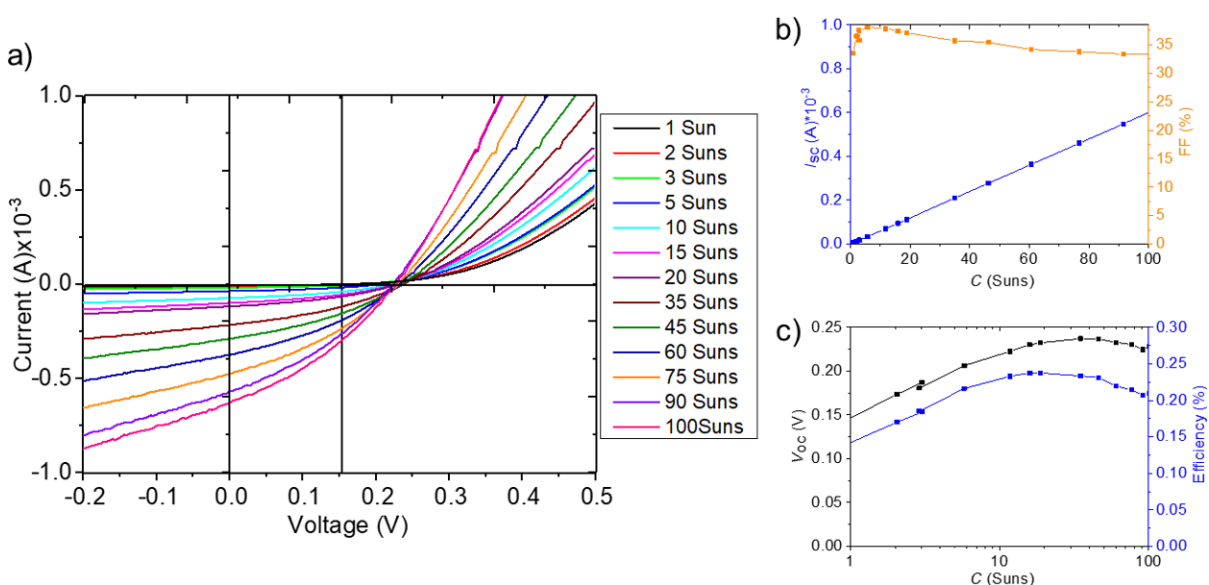
Figure 15: Electrical characterization under various light concentration factors for CIGSe micro cell from nucleation approach: a) *IV* curves, b) I_{SC} and FF, c) V_{OC} and η.

linear increase in I_{SC} with concentration up to 100 suns. Yet, V_{OC} experiences a drop above 30 suns, as it can be seen from $V_{OC}(C)$ plot in Figure 15c. In combination with an even earlier decline of FF (Figure 15b), this behavior leads to an efficiency maximum at 20 suns.

An overall very similar behavior is found for CIGSe microcells fabricated by the LIFT approach, as illustrated by the results of *IV* measurements shown in Figure 16 and in [25]. Here, I_{SC} also

increases linearly, but V_{OC} decreases above 30–40 suns, leading, together with a quick decrease in FF, to a maximum in efficiency at 20 suns.

For both cases of CIGSe microabsorbers, shunt and series resistances drop with similar slopes in a double-log plot, which, however, is more detrimental for the higher shunt resistance. This is consistent with a drop in FF but a linear increase in I_{SC}.

Figure 16: Electrical characterization under various light concentration factors for CIGSe micro cell from LIFT approach: a) *IV* curves, b) I_{SC} and FF, c) V_{OC} and η.

A remaining question is why V_{OC} starts to deviate from the expected logarithmic increase at a certain concentration level. One possible explanation is the experimental approach chosen here: The entire micro solar cell array is illuminated with enhanced light intensity, which leads to heating of the whole assembly including the non-active areas, in particular at higher light concentration levels. In a microconcentrator device, however, light will be focused on the absorber area only and the design will benefit from improved heat dissipation. A further enhancement can thus be expected in the final device. In the configuration investigated here, the highest efficiencies were 3.06% at 3 suns for CISe microcells from the nucleation approach, corresponding to a relative enhancement of 6% compared to illumination at 1 sun. An efficiency of 3.36% at 20 suns was achieved for CIGSe microcells from the nucleation approach, i.e., a relative enhancement of 138%. CIGSe microcells from the LIFT approach reached 0.237% at 20 suns and thus a relative enhancement of 60% compared to illumination at 1 sun. These enhancement factors constitute a promising starting point for future research from which efficiency maxima at elevated concentration factors and higher efficiencies can be expected.

Conclusion

The promising new solar cell concept of micro CPV was addressed in this review using CISe and CIGSe microabsorbers. A particular challenge for a material-efficient fabrication of such microcells is the local bottom-up growth of absorbers. For this purpose, two laser-based methods were applied, namely the nucleation approach and the LIFT approach. In both cases, metallic precursors were created, site-controlled via femtosecond-laser treatment, which were subsequently processed to microabsorbers. For further processing to microcells, a pathway was demonstrated, in which an isolation concept based on spin coating was applied. The advantage of this approach is that imperfections can be compensated, since the spin-coated photoresist insulates any potentially occurring irregularities such as microcavities. The microcells were connected in a parallel manner and exhibited efficiencies between 0.15% and 2.9% under 1 sun illumination. Under concentrated illumination, significant efficiency enhancements could be achieved. These results constitute a promising step towards the maturation of this cell concept.

Acknowledgements

ORCID® iDs

Jörn Bonse - https://orcid.org/0000-0003-4984-3896
Owen Ernst - https://orcid.org/0000-0003-1429-9763
Martina Schmid - https://orcid.org/0000-0001-5103-0750
Jörg Krüger - https://orcid.org/0000-0003-2632-9448

References

1. Renewables 2017 - Global Status Report.
   http://www.ren21.net/gsr-2017/ (accessed Feb 2, 2018).
2. Solar Frontier Achieves World Record Thin-Film Solar Cell Efficiency of 22.9%. http://www.solarfrontier.com/eng/news/2017/1220_press.html (accessed Dec 21, 2017).
3. Green, M. A.; Hishikawa, Y.; Warta, W.; Dunlop, E. D.; Levi, D. H.; Hohl-Ebinger, J.; Ho-Baillie, A. W. H. *Prog. Photovoltaics* **2017**, *25*, 668–676. doi:10.1002/pip.2909
4. Yin, G.; Knight, M. W.; van Lare, M.-C.; Solà Garcia, M. M.; Polman, A.; Schmid, M. *Adv. Opt. Mater.* **2017**, *5*, 1600637. doi:10.1002/adom.201600637
5. van Lare, C.; Yin, G.; Polman, A.; Schmid, M. *ACS Nano* **2015**, *9*, 9603–9613. doi:10.1021/acsnano.5b04091
6. Boeck, T.; Ringleb, F.; Bansen, R. *Cryst. Res. Technol.* **2017**, *52*, 1600239. doi:10.1002/crat.201600239
7. Sancho-Martínez, D.; Schmid, M. *J. Phys. D: Appl. Phys.* **2017**, *50*, 445501. doi:10.1088/1361-6463/aa8ac5
8. Paire, M.; Shams, A.; Lombez, L.; Péré-Laperne, N.; Collin, S.; Pelouard, J.-L.; Guillemoles, J.-F.; Lincot, D. *Energy Environ. Sci.* **2011**, *4*, 4972. doi:10.1039/c1ee01661j
9. Paire, M.; Lombez, L.; Péré-Laperne, N.; Collin, S.; Pelouard, J.-L.; Lincot, D.; Guillemoles, J.-F. *Appl. Phys. Lett.* **2011**, *98*, 264102. doi:10.1063/1.3604789
10. Price, J. S.; Grede, A. J.; Wang, B.; Lipski, M. V.; Fisher, B.; Lee, K.-T.; He, J.; Brulo, G. S.; Ma, X.; Burroughs, S.; Rahn, C. D.; Nuzzo, R. G.; Rogers, J. A.; Giebink, N. C. *Nat. Energy* **2017**, *2*, 17113. doi:10.1038/nenergy.2017.113
11. Domínguez, C.; Jost, N.; Askins, S.; Victoria, M.; Antón, I. *AIP Conf. Proc.* **2017**, *1881*, 080003. doi:10.1063/1.5001441
12. Paire, M.; Lombez, L.; Donsanti, F.; Jubault, M.; Collin, S.; Pelouard, J.-L.; Guillemoles, J.-F.; Lincot, D. *J. Renewable Sustainable Energy* **2013**, *5*, 011202. doi:10.1063/1.4791778
13. Reinhold, B.; Schmid, M.; Greiner, D.; Schüle, M.; Kieven, D.; Ennaoui, A.; Lux-Steiner, M. C. *Prog. Photovoltaics* **2015**, *23*, 1929–1939. doi:10.1002/pip.2611
14. Lotter, E.; Jackson, P.; Paetel, S.; Wischmann, W. Identification of loss mechanisms in CIGS micro-cells for concentrator applications. 32nd EU PVSEC 2016, Munich, Germany, June 20–24, 2016; . doi:10.4229/eupvsec20162016-3cv.2.19
15. Duchatelet, A.; Nguyen, K.; Grand, P.-P.; Lincot, D.; Paire, M. *Appl. Phys. Lett.* **2016**, *109*, 253901. doi:10.1063/1.4971975
16. Sadewasser, S.; Salomé, P. M. P.; Rodriguez-Alvarez, H. *Sol. Energy Mater. Sol. Cells* **2017**, *159*, 496–502. doi:10.1016/j.solmat.2016.09.041

17. Ringleb, F.; Eylers, K.; Teubner, T.; Schramm, H.-P.; Symietz, C.; Bonse, J.; Andree, S.; Heidmann, B.; Schmid, M.; Krüger, J.; Boeck, T. *Appl. Surf. Sci.* **2017,** *418,* 548–553. doi:10.1016/j.apsusc.2016.11.135

18. Ringleb, F.; Eylers, K.; Teubner, T.; Boeck, T.; Symietz, C.; Bonse, J.; Andree, S.; Krüger, J.; Heidmann, B.; Schmid, M.; Lux-Steiner, M. *Appl. Phys. Lett.* **2016,** *108,* 111904. doi:10.1063/1.4943794

19. Bonse, J.; Höhm, S.; Kirner, S. V.; Rosenfeld, A.; Krüger, J. *IEEE J. Sel. Top. Quantum Electron.* **2017,** *23,* 9000615. doi:10.1109/jstqe.2016.2614183

20. Rudenko, A.; Colombier, J.-P.; Höhm, S.; Rosenfeld, A.; Krüger, J.; Bonse, J.; Itina, T. E. *Sci. Rep.* **2017,** *7,* 12306. doi:10.1038/s41598-017-12502-4

21. Bohandy, J.; Kim, B. F.; Adrian, F. J. *J. Appl. Phys.* **1986,** *60,* 1538–1539. doi:10.1063/1.337287

22. Andree, S.; Heidmann, B.; Ringleb, F.; Eylers, K.; Bonse, J.; Boeck, T.; Schmid, M.; Krüger, J. *Appl. Phys. A: Mater. Sci. Process.* **2017,** *123,* 670. doi:10.1007/s00339-017-1282-x

23. Heidmann, B.; Ringleb, F.; Eylers, K.; Levcenco, S.; Bonse, J.; Andree, S.; Krüger, J.; Unold, T.; Boeck, T.; Lux-Steiner, M. C.; Schmid, M. *Mater. Today Energy* **2017,** *6,* 238–247. doi:10.1016/j.mtener.2017.10.010

24. Schmid, M.; Heidmann, B.; Ringleb, F.; Eylers, K.; Ernst, O.; Andree, S.; Bonse, J.; Boeck, T.; Krüger, J. *Proc. SPIE* **2018,** *10527,* 1052707. doi:10.1117/12.2288253

25. Heidmann, B.; Andree, S.; Levcenko, S.; Unold, T.; Abou-Ras, D.; Schäfer, N.; Bonse, J.; Krüger, J.; Schmid, M. *ACS Appl. Energy Mater.* **2018,** *1,* 27–31. doi:10.1021/acsaem.7b00028

Geometrical optimisation of core–shell nanowire arrays for enhanced absorption in thin crystalline silicon heterojunction solar cells

Robin Vismara[*1], Olindo Isabella[1], Andrea Ingenito[1,2], Fai Tong Si[1] and Miro Zeman[1]

Full Research Paper

Address:
[1]Photovoltaic Materials and Devices/Else Kooi Lab, Delft University of Technology, Mekelweg 4, 2628CD Delft, The Netherlands and [2]École Polytechnique Fédérale de Lausanne (EPFL), Institute of Microengineering (IMT), Photovoltaics and Thin Film Electronic Laboratory (PV-Lab), Rue de la Maladière 71b, 2002 Neuchâtel, Switzerland

Email:
Robin Vismara[*] - r.vismara@tudelft.nl; Olindo Isabella - o.isabella@tudelft.nl

* Corresponding author

Abstract

Background: Elongated nanostructures, such as nanowires, have attracted significant attention for application in silicon-based solar cells. The high aspect ratio and characteristic radial junction configuration can lead to higher device performance, by increasing light absorption and, at the same time, improving the collection efficiency of photo-generated charge carriers. This work investigates the performance of ultra-thin solar cells characterised by nanowire arrays on a crystalline silicon bulk.

Results: Proof-of-concept devices on a p-type mono-crystalline silicon wafer were manufactured and compared to flat references, showing improved absorption of light, while the final 11.8% (best-device) efficiency was hindered by sub-optimal passivation of the nanowire array. A modelling analysis of the optical performance of the proposed solar cell architecture was also carried out. Results showed that nanowires act as resonators, amplifying interference resonances and exciting additional wave-guided modes. The optimisation of the array geometrical dimensions highlighted a strong dependence of absorption on the nanowire cross section, a weaker effect of the nanowire height and good resilience for angles of incidence of light up to 60°.

Conclusion: The presence of a nanowire array increases the optical performance of ultra-thin crystalline silicon solar cells in a wide range of illumination conditions, by exciting resonances inside the absorber layer. However, passivation of nanowires is critical to further improve the efficiency of such devices.

Introduction

The implementation of effective and low-cost light trapping schemes is of paramount importance for the development of high-efficiency thin silicon solar cells. The most common approach is the texturing of interfaces, to increase the path length of light inside the absorber. This allows for the use of thinner absorbers, which can decrease manufacturing costs and, in the case of amorphous silicon alloys, reduce the effect of light-induced degradation [1-3]. An alternative approach involves the utilisation of nanostructures that are similar in size to the wavelength of light. This allows for an increase of the electromagnetic (EM) field intensity inside the device, resulting in the enhancement of light absorption [4].

Of particular interest is the employment of elongated nanostructures, such as nanowire arrays. While their nanoscale dimensions can excite various types of resonances of the EM field within the absorber, such as wave-guiding [5-8], cavity modes [5,8-11], Fabry–Perót and whispering gallery modes [12], their characteristic high aspect ratio promotes anti-reflection, allowing for more light to be coupled into the active layer of the solar cell [13-15]. In addition, radial-junction nanowires have the advantage of decoupling absorption and collection, by orthogonalising the path of light with respect to the direction of charge carrier collection [14,16,17]. This aspect allows for the use of lower-quality materials, characterised by short minority carrier diffusion length and/or low absorptivity.

Multiple studies of nanowire solar cells can be found in literature, using different materials: indium phosphide [18,19], gallium arsenide [20,21], zinc oxide [15,22], crystalline silicon [6,8,11-13,16,17,23-34], amorphous silicon alloys [35-37], and recently perovskite [38-41]. In this contribution, the performance of crystalline silicon (c-Si) nanowire arrays is investigated. The study is divided in two parts. First, a proof-of-concept device was realised, consisting of a heterojunction of amorphous silicon on a p-type c-Si nanowire array. The standard manufacturing procedure of c-Si heterojunction solar cells was followed, with the only addition of a cost-effective mask-less reactive ion etching step to create nanowires on the surface of the p-type Si wafer. The resulting 5×5 mm^2 cell exhibits a best-device efficiency of 11.8%, ensuring the feasibility of our proposed device architecture. In the second part, a geometrical study of the nanowire array is carried out, using rigorous optical modelling. An ultra-thin c-Si absorber is employed, to focus the analysis on the effect of nanowires on the propagation of light inside the solar cell. Implied photocurrent densities close to 27 mAcm^{-2} are achieved, for a 2 μm thick c-Si absorber coated with nanowires. The enhanced optical performance, with respect to a flat device, is explained by excitation of resonances both inside the nanowires and in the bulk c-Si absorber. In addi-

tion, good angular resilience is displayed, with high implied photocurrent density values (i.e., strong absorption) observed for angles of incidence of light up to 60°, making the proposed solar cell architecture attractive in a wide range of illumination conditions.

Experimental
Device manufacturing and characterisation

The nanowire array was manufactured on a p-type mono-crystalline silicon wafer by reactive ion etching (RIE) using a gaseous mixture of SF$_6$ and O$_2$, followed by standard cleaning, rinsing in de-ionised water and drying of the substrate. In particular, the SF$_6$/O$_2$ plasma provides a continuous flow of fluorine radicals (F*) and oxygen radicals O*, which feed two competing chemical reactions: F* and Si react to form SF^{4+} ions, while from the reaction of O* and Si a silicon oxyfluorine (SiO$_x$F$_y$) layer is formed. This layer acts as mask against F* etching, but is physically broken by sputtered ions bombarding the surface of the sample. Such effect occurs with higher speed on the horizontal than on the vertical plane, due to the larger angle of incidence of ions hitting the vertical side walls, which leads to a strong anisotropy of the Si etching rate. The process is made mask-less by the precipitation of SiO$_x$F$_y$ particles, which start the formation of randomly distributed etch pits [42]. These regions become deeper during the process, thanks to the strong anisotropic nature of this RIE etching.

A back-side emitter was formed by phosphorous ion implantation, with energy of 2×10^{15} cm^{-2} and dose of 20 keV. Oxidation and annealing were carried out in dry ambient at 850 °C for 90 min, resulting in a sheet resistance R_{SH} of 60 Ω/square. Before depositing the coating layers, the silicon wafer with nanowires on top was treated with diluted hydrofluoric acid, to remove the thin native oxide layer from the surface. Plasma-enhanced chemical vapour deposition (PECVD) was used for growing thin-film silicon and silicon alloys layers, to implement surface passivation and front surface field. Intrinsic hydrogenated amorphous silicon (a-Si(i):H), with a thickness equivalent to 30 nm on a flat substrate, was first coated onto the front surface of the wafer on which the nanowires were distributed. Following a hydrogen-plasma treatment, highly transparent boron-doped hydrogenated nanocrystalline silicon oxide (nc-SiO$_x$(p):H) with 30 nm equivalent thickness was deposited on a-Si:H. For the front electrode, a 100 nm thick transparent tin-doped indium oxide (In$_2$O$_3$:Sn, ITO) was deposited at low power and low temperature, using radio-frequency (RF) magnetron sputtering. The cell area was defined as 5 mm × 5 mm, using a mask during ITO deposition. The reported equivalent thickness values of thin films on the flat c-Si substrates were characterised via spectroscopic ellipsometry. Finally, using

physical vapour deposition, metal electrodes consisting of Ag/Cr/Al were deposited at the front (as patterned grids) and at the rear surfaces of the wafer (full area), with thickness values of 300/30/300 nm and 300/30/2000 nm, respectively.

A Philips XL-50 scanning electron microscope was used for the visual investigation of the nanowires. In Figure 1, pictures of the bare (Figure 1a) and coated (Figure 1b) nanowire arrays are presented. The continuous solar sun simulator Wacom WXS-156S, equipped with a vacuum mask with a 3 mm × 3 mm aperture area, was used to measure the current–voltage characteristics of the fabricated solar cells. The simulator consists of a xenon and a halogen lamp that closely reproduce the spectrum and the intensity of the AM1.5 spectrum [43], which was verified with a c-Si device calibrated at Fraunhofer ISE. For external quantum efficiency (EQE) measurements, the setup used in this work was custom-built. It comprises a Newport illuminator/monochromator, a chopper, a substrate holder (with magnetic pads to hold the probes), and a lock-in amplifier. A calibrated monocrystalline silicon diode with known spectral response was used as reference. The short-current density (J_{sc}) was determined by a convolution of the measured EQE and the photon flux of the AM1.5 spectrum ($\phi_{AM1.5}$). The internal quantum efficiency (IQE) was calculated by dividing the measured EQE by $(1 - R)$, where R is the reflectance measured by means of a Perkin Elmer LAMBDA 950 UV–vis–NIR spectrophotometer.

Modelling approach

Simulations of the radial heterojunction c-Si nanowire solar cell were carried out by means of a 3D Maxwell equation solver, based on the finite element method (FEM). The "High Frequency Structure Simulator" (HFSS) was employed [44], which allows for the modelling of thin-film optoelectronic devices with arbitrarily complex geometries [45-52]. To ensure accuracy, accurately measured optical properties (refractive index n and extinction coefficient κ) of each material of the structure were used. Simulation results consists of reflection (R) and absorption (A_i) in each layer (i) of the model, as functions of the wavelength of the incident light. A convolution of the obtained spectral data with the AM1.5 photon flux results in the implied photocurrent density ($J_{ph,i}$) generated (in the active layer) or lost (in supporting layers, or due to reflection):

$$J_{ph,i} = |q| \int_{300\,nm}^{1200\,nm} X(\lambda)\,\phi_{AM1.5}(\lambda)\,d\lambda, \qquad (1)$$

where q is the elemental charge, X can be either A_i or R, and λ is the wavelength of light. Note that only the spectral range between 300 and 1200 nm was considered. In addition, the value of electric and magnetic field inside the structure was exported, to obtain an insight into the propagation of light in the solar cell.

Results and Discussion
Device performance

Two series of devices were manufactured: nanowire heterojunction solar cells, with the procedure described in the previous section, and flat references, synthesised through the same process except for the RIE step. The nanowire array has the following (average) dimensions: height $\overline{h} \approx 2$ μm, diameter $\overline{d} \approx 200$ nm and distance $\overline{\Lambda} \approx 800$ nm. For each architecture, a total of 48 5 mm × 5 mm solar cells were fabricated, on 4 inch c-Si wafers with an initial thickness of 280 μm.

In Figure 2a, the (non-biased) EQE of both nanowire and flat devices are depicted. The nanowire solar cell performs better at
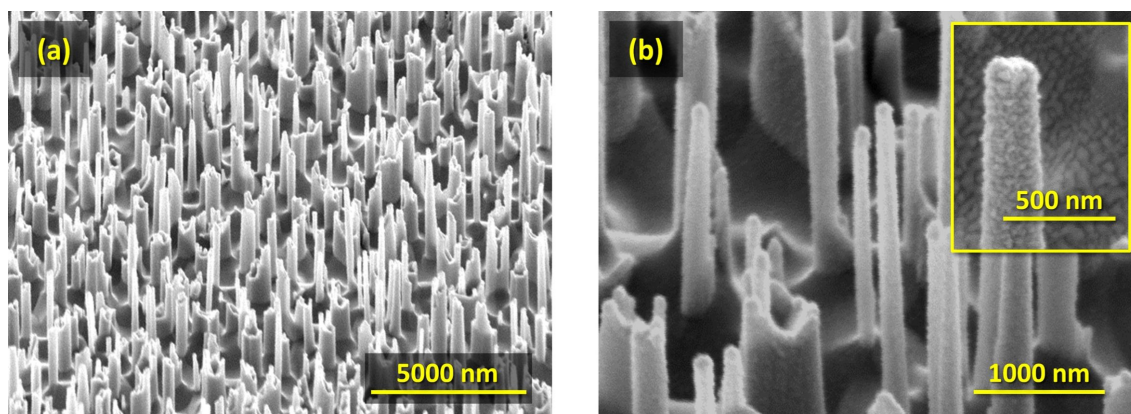
Figure 1: Scanning electron microscopy pictures of (a) bare and (b) coated nanowires on the c-Si substrate. In the inset of (b), the enlargement of a single c-Si nanowire wrapped with supporting layers is depicted, showing excellent coating uniformity.
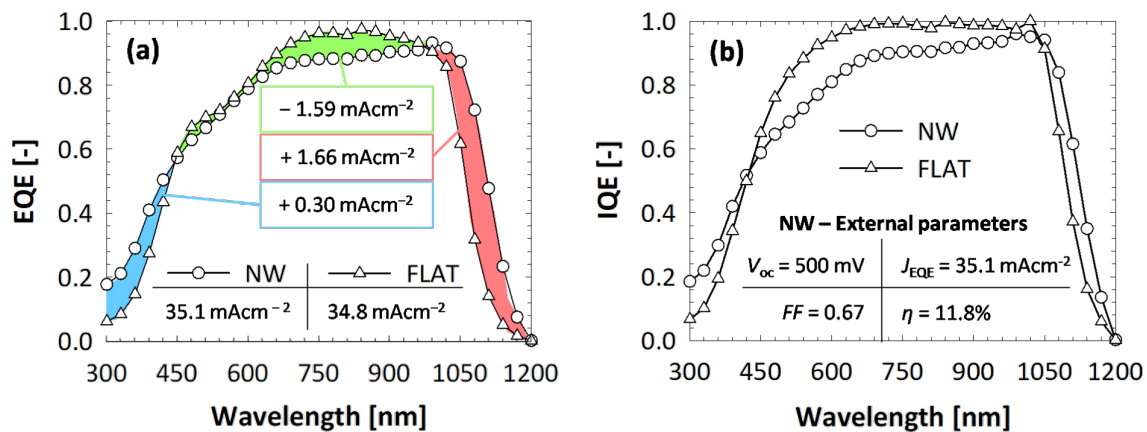
Figure 2: Measured (a) EQE and (b) IQE of the best nanowire heterojunction solar cell (NW) and of the flat heterojunction reference (FLAT). The blue and red areas in (a) indicate the net current gain of the NW structure with respect to the FLAT counterpart at short and long wavelengths, respectively, while the green area indicates the net current loss in the central region of the spectrum of the NW device with respect to FLAT device. The table in (b) reports the external parameters of the best NW device.

short and long wavelengths, while its performance suffers in the range between 450 and 950 nm. The higher EQE of the nanowire solar cell at short wavelengths (up to $\lambda = 450$ nm) can be mainly explained by a better in-coupling of light, promoted by the nanostructure array at the front side. Lower parasitic absorption at the front side can also explain the improvement. This results in a net gain in photocurrent density of 0.30 mAcm^{-2}. At longer wavelengths, scattering of photons adds to the antireflective effect, resulting in a significant performance increase (+1.66 mAcm^{-2}) with respect to the flat device. An additional explanation for the higher performance in these two spectral regions is an increased injection level, due to the same or even higher absorption taking place in less material. The higher carrier concentration results in a performance closer to the radiative limit, which is evidenced by the higher IQE observed at both short and long wavelengths.

On the other hand, the lower EQE in the spectral region of 450–950 nm can be ascribed to a higher charge-carrier recombination (i.e., lower collection efficiency), as highlighted by the IQE curves presented in Figure 2b. While recombination affects the performance across the entire spectrum, at short and long wavelengths this effect is not apparent in Figure 2 since the absorption increase promoted by the nanowires compensates the decreased collection efficiency. Across the 48 individual cells, the low average open-circuit voltage ($V_{oc} = 495 \pm 8$ mV) and fill factor (FF $= 0.66 \pm 0.01$) are evidence of high recombination, likely caused by the larger interface area with respect to the flat device. The short-circuit current density ($J_{EQE}^{(NW)} = 35.1$ mAcm^{-2}), calculated from the EQE measurements, is only slightly higher than the value obtained for the flat reference ($J_{EQE}^{(FLAT)} = 34.8$ mAcm^{-2}), since the absorption gains observed at short and long wavelengths are almost entirely
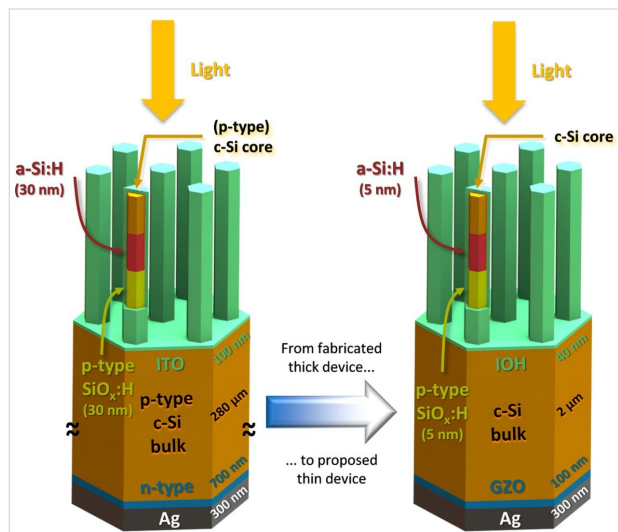
offset by higher charge-carrier recombination. The resulting conversion efficiency is $\eta = (11.5 \pm 0.4)\%$, one of the highest reported values for this type of device [29,32,33].

It can be concluded that the presence of the nanowire array improves the optical performance of the solar cell, namely by promoting very good light in-coupling at the front side and by scattering of photons in the near infrared region of the spectrum, where absorption in c-Si is weak. However, charge-collection efficiency suffers, resulting in low V_{oc} and FF and a reduced quantum efficiency, particularly in the visible part of the spectrum. This setback could be avoided by deploying a defect removal etching [53], which would dramatically improve the surface passivation.

Geometrical study of nanowire arrays

To further understand the interaction of light with nanowires, and how the presence of the NW array affects the absorption in the active silicon layer, optical simulations were used. First, a comparison of the absorption is carried out, between a flat reference and a device model endowed with nanowires. The array is assumed periodic (due to modelling constraints) and arranged in a hexagonal lattice. The hexagonal distribution was chosen after a short preliminary study (not reported here for brevity) showed that the hexagonal lattice resulted in slightly higher absorption with respect to square or rectangular ones. This effect was attributed to the larger number of diffraction modes excited by the hexagonal array. Nevertheless, differences between the different arrangements were small, and it is thus assumed that a perfectly random arrangement, such as the one of the manufactured device (Figure 1), would yield similar results. The geometrical properties of the modelled nanowires mirror the dimensions of the manufactured nanostructures: the distance (or
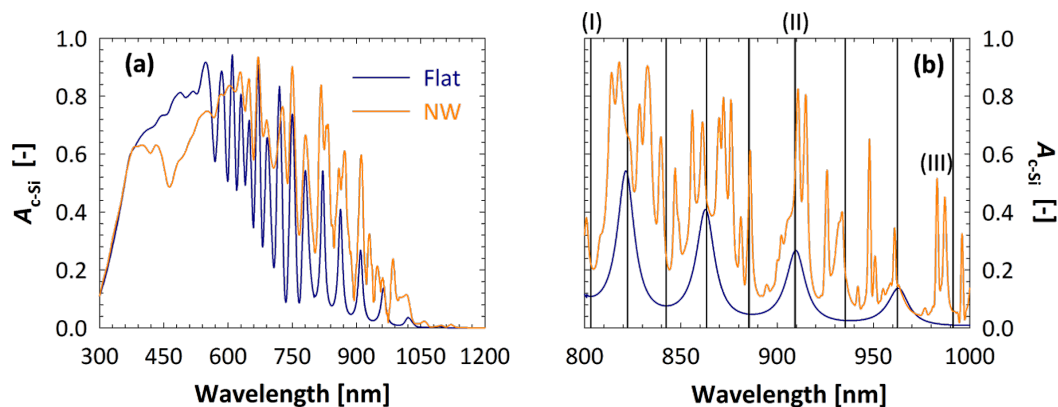
period of the array) is Λ = 800 nm, the height is *h* = 2 μm and the cross section is *d* = 200 nm. A depiction of one unit cell of the device model is presented in Figure 3. Appropriately defined periodic boundary conditions ensure the creation of a complete solar cell endowed with an hexagonal nanowire array. The crystalline silicon bulk has a thickness of only 2 μm, to better highlight the effect of the presence of nanowires. At the front side, a stack of a-Si:H (thickness of 5 nm) and p-type nc-SiO$_x$:H (5 nm) forms the hole-selective contact, followed by In$_2$O$_3$:H (IOH, 40 nm) in the role of the front transparent conductive oxide (TCO). The three layers uniformly coat both

the nanowires and the exposed portion of the bulk. At the back side, the negative contact consists of another TCO, ZnO:Ga (GZO, 100 nm) [47,54], and silver (300 nm). There are a few differences between the manufactured solar cells and the model employed (in addition to the thinner bulk and the periodicity of the nanowire array): (i) To reduce parasitic absorption at the front, the a-Si:H and p-type nc-SiO$_x$:H layers are significantly thinner, and IOH is preferred to ITO due to its higher transparency and conductivity [55,56]; (ii) at the back, GZO is introduced to improve the reflectivity of the contact. The flat reference employs the same layers (material and thickness) as the nanowire model, the only difference being the absence of the nanostructure array.

In Figure 4, the calculated absorption in the c-Si layer ($A_{c–Si}$) is depicted, for both nanowire device (NW) and flat reference (FLAT). For 400 nm < λ < 550 nm, the optical performance of the NW model is inferior to the FLAT reference. This result can be explained by the higher absorption in the front layers, particularly a-Si:H, which in the model endowed with nanowires have to cover a larger surface area. In addition, the geometry of the nanowires can result in light being trapped in the front layers and thereby being parasitically absorbed. On the other hand, $A_{c-Si}^{(NW)}$ is larger than $A_{c-Si}^{(FLAT)}$ for λ > 600 nm. In this region of the spectrum, the absorptivity of supporting layers is weaker, thus the optical performance of the active layer is not strongly affected by their presence. The difference between NW and FLAT architectures is to be ascribed to two factors: (i) The NW solar cell model exhibits lower reflectivity than the FLAT reference, due to the presence of nanowires at the front side; (ii) light propagates differently inside the absorber layer, in particular the absorption spectrum of the NW device displays more (resonance) peaks, as highlighted in Figure 4b for wavelengths between 800 and 1000 nm. In this spectrum range, $A_{c-Si}^{(FLAT)}$

Figure 3: 3D rendering of the real device (left) and of the simulation model (right). The differences are: thinner absorber (device: 280 μm, model: 2 μm), thinner and more transparent supporting layers (p-type SiO$_x$:H + a-Si:H + TCO) at the front (device: 30 nm + 30 nm + 100 nm, model: 5 nm + 5 nm + 40 nm), introduction of a TCO between silicon and metal at the back, in place of the implanted n-type doped silicon layer. The core of one nanowire (c-Si, orange) is presented in both figures, to show the layers that are coating it radially.

Figure 4: Calculated absorption in c-Si, as function of the wavelength, of the flat reference (FLAT, blue) and nanowire (NW, orange) device models. In (a), the range 300–1200 nm is considered, while (b) focuses on the spectrum between 800 and 1000 nm. Black vertical lines in (b) indicate the position of interference resonances, calculated with Equation 2. The corresponding electric field distributions are presented in Figure 5.

follows the typical profile of a Fabry–Perót interference (F-P), due to the total model thickness being of the same order of magnitude of the wavelength of light. In fact, the position (i.e., the wavelength) of peaks and valleys (black vertical lines in Figure 4b) can be accurately predicted by imposing the condition that the phase difference between primary reflection (air–IOH interface) and secondary reflection (GZO–silver interface) is an integer multiple of π:
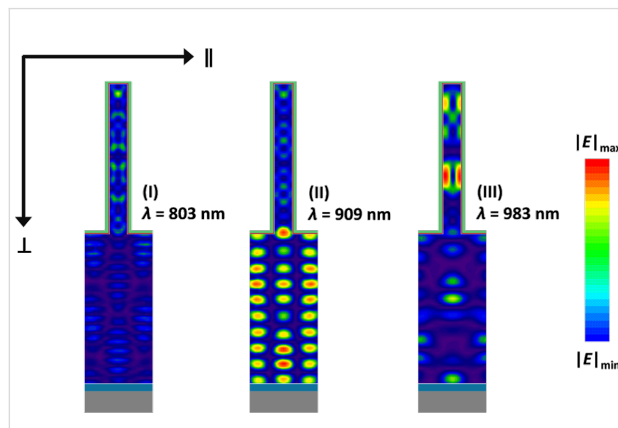
$$\lambda_{\text{F-P}} = \frac{4\pi \sum_i d_i n_i(\lambda)}{m\pi - \left[\varphi_b^{(r)}(\lambda) - \varphi_f^{(r)}(\lambda) + \sum_j \varphi_j^{(t)}(\lambda) \right]}, \quad (2)$$

where $\lambda_{\text{F-P}}$ is the wavelength (in vacuo) at which there is constructive or destructive interference between front and back reflected beams. d_i and n_i are the thickness and (wavelength-dependent) refractive index of the i-th layer, $m = 0, 1, 2, \dots,$ $\varphi_f^{(r)}$ and $\varphi_b^{(r)}$ are the (wavelength-dependent) phase shifts taking place when light is reflected at the front and back interfaces, respectively, and $\varphi_j^{(t)}(\lambda)$ is the (wavelength-dependent) phase shift happening during transmission at the j-th interface (between layer i and $i + 1$). The absorption profile of the NW model, on the other hand, presents a significantly larger number of peaks. Still the typical shape of F-P interference can be observed, only lifted to higher absorption values due to the diffraction promoted by the presence of nanowires.

The electric field (E) distribution inside the device is useful to understand how the propagation of light is affected by the presence of the nanowire array. To this purpose, $|E|$ inside the c-Si absorber layer is presented in Figure 5, for three different wavelengths. At $\lambda^{(I)} = 803$ nm, Fabry–Perót interference results in a valley in the absorption profile (see (I) in Figure 4). As expected $|E|$ is small, with some higher-intensity spots located within the nanowires. This weak guided resonance, combined with the presence of more absorber material, explains that $A_{\text{c-Si}}^{(\text{NW})} > A_{\text{c-Si}}^{(\text{FLAT})}$ for $\lambda = 803$ nm. On the other hand, at $\lambda^{(II)} = 909$ nm several high-intensity regions are observed, particularly in the c-Si bulk. In particular, resonances are excited in both the vertical direction (i.e., the direction of the incident light, $\perp$), due to F-P interference, and in the horizontal direction ($\parallel$), due to interference between diffraction modes inside the silicon layer. The two effects combine to increase the total intensity of the electric field within the absorber layer. This in turn results in a value of absorption, for the NW model, significantly enhanced with respect to the FLAT sample, as shown in (II) in Figure 4. Finally, at $\lambda^{(III)} = 983$ nm a peak in $A_{\text{c-Si}}^{(\text{NW})}$ can be seen, while $A_{\text{c-Si}}^{(\text{FLAT})}$ is very low due to being close to a Fabry-Perót minimum. At this wavelength $|E|$ is strongly enhanced within the nanowires, which appear to act as cavities for the electromagnetic field. The distribution of $|E|$ does not follow the typical F-P interference or diffraction patterns, but can still explain the boost in absorption observed at (III) in Figure 4.

The convolution of $A_{\text{c-Si}}$ with the photon flux of the solar spectrum (Equation 1) allows for the quantification of the optical performance improvement introduced by the presence of nanowires. The implied photocurrent density generated in the absorber of the NW device ($J_{\text{ph,c-Si}}^{(\text{NW})} = 21.8$ mAcm^{-2}) is significantly higher then the value computed for the FLAT reference ($J_{\text{ph,c-Si}}^{(\text{FLAT})} = 17.6$ mAcm^{-2}), but can be further increased by careful optimisation of the nanowire geometry. To this purpose, the height (h) and cross section (d) of the nanowires were varied in the ranges of 0–5 μm and 0–700 nm, respectively. The distance between individual nanowires was kept constant at $\Lambda = 800$ nm. h, d and Λ were varied or kept constant within values that are expected to be achievable with the developed RIE process.

On the left-hand side of Figure 6, the value of $J_{\text{ph,c-Si}}^{(\text{NW})}$ as a function of d and h is plotted. In Supporting Information File 1, the implied photocurrent density losses, due to reflection and parasitic absorption in supporting layers, are included. It can be observed that an increase in NW height reduces reflectance. This can be expected since (in general) taller nanostructures exhibit better anti-reflection properties. Conversely, losses in the supporting layers increase, since more material needs to cover the taller nanowires. The net result of the two opposite trends is that $J_{\text{ph,c-Si}}^{(\text{NW})}$ does not exhibit a strong dependence on h. In fact, for all values of d the difference in $J_{\text{ph,c-Si}}^{(\text{NW})}$ between the best and the worst performing architecture is smaller than 3 mAcm^{-2}.

A stronger dependence of performance on the nanowire cross section is observed. On one hand, parasitic absorption losses are
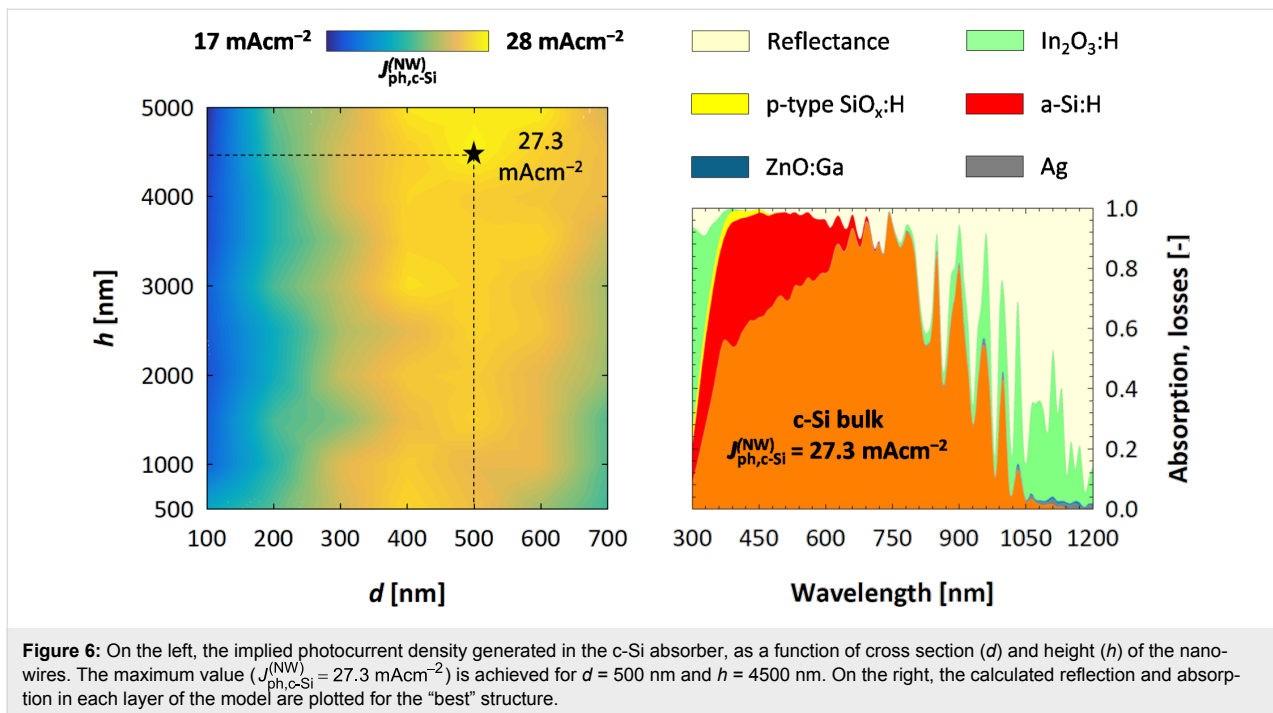

Figure 5: Distribution of the electric field inside the absorber layer of the NW device for three different wavelengths: (I) 803 nm, (II) 909 nm and (III) 983 nm.

Figure 6: On the left, the implied photocurrent density generated in the c-Si absorber, as a function of cross section (*d*) and height (*h*) of the nanowires. The maximum value ($J_{ph,c-Si}^{(NW)}$ = 27.3 mAcm^{-2}) is achieved for *d* = 500 nm and *h* = 4500 nm. On the right, the calculated reflection and absorption in each layer of the model are plotted for the "best" structure.
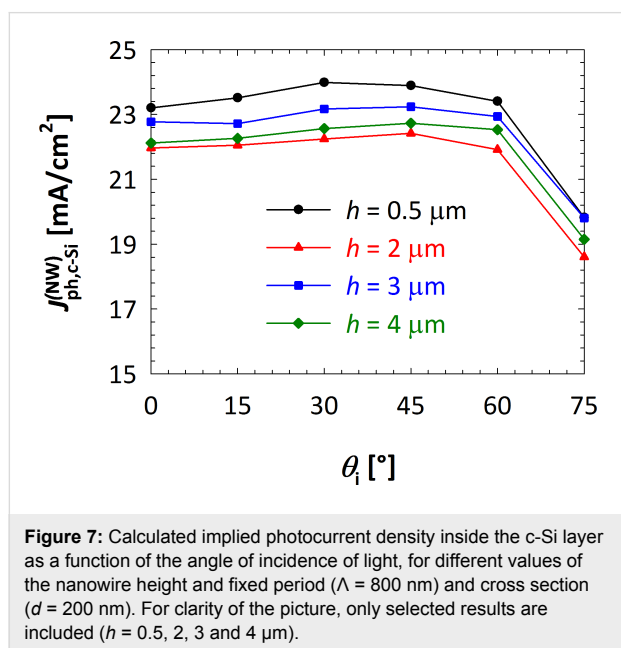
(almost) independent on the value of *d*, because the amount of material used in supporting layers does not depend on the NW lateral size. On the other hand, reflectance losses are significant for narrow nanowires (*d* < 200 nm), decreasing sharply until reaching a minimum between 400 and 500 nm. For larger values of the cross section (*d* > 500 nm), reflection losses become larger again. This behaviour can be explained as follows: When *d* is too small the space between individual wires is wide, reducing the amount of light that hits the NWs and can be absorbed. By increasing the cross section, a larger portion of the incident radiation will hit the nanostructures and thereby be absorbed. If *d* becomes too large, however, more and more light is reflected by the top surface of the nanowire, thus increasing total reflection. Anttu et al. suggest another possible explanation for the optimal cross section value [19]. In their work on III–V semiconductors nanowire arrays, they observed the presence of optimum, bandgap-dependent nanowire diameter values. They associate the calculated optima with specific, diameter-tunable nanophotonic resonances, implying that for a specific semiconductor material an optimal value of the diameter can be found that maximises absorption owing to the excitation of resonant modes at specific wavelengths.

The final result is that the $J_{ph,c-Si}^{(NW)}$ achieves its maximum when reflection is at a minimum (i.e., for *d* = 400–500 nm). The highest performance is achieved for a solar cell model with *d* = 500 nm and *h* = 4500 nm, reaching an implied photocurrent density value of 27.3 mAcm^{-2}. Further analysis of the optical losses of the "best" structure (Figure 6, right) reveal that a sig-

nificant amount of light is parasitically absorbed in the intrinsic a-Si:H layer. On the other hand, it is well known that a-Si:H layers in heterojunction devices do contribute to the charge generation, thus adding to the short-circuit current density [57]. This effect can be noted in Figure 2a, where the EQE is higher than the absorption depicted in Figure 6, and could be quantified with a rigorous electrical simulation, which is beyond the scope of this work. Nevertheless, the choice of a more transparent passivating layer could result in significant increase of absorption, particularly at short wavelengths (λ < 600 nm), and in an increase of $J_{ph,c-Si}^{(NW)}$ up to 4 mAcm^{-2}. It must be noted that the best implied photocurrent density value achieved ($J_{ph,c-Si}^{(NW)}$ = 27.3 mAcm^{-2}) is significantly smaller than what was measured for the manufactured NW device ($J_{EQE}^{(NW)}$ = 35.1 mAcm^{-2}). This can only be ascribed to the significant difference in thickness, which in the case of the modelled structures is more than 100 times smaller (2 μm) than that of the nanowire solar cell (280 μm).

Finally, the effect of the angle of incidence of the light (θ$_i$) was studied. For different heights and constant values of the period (Λ = 800 nm) and cross section (*d* = 200 nm), θ$_i$ was varied between 0° and 75°. Results (expressed in terms of $J_{ph,c-Si}^{(NW)}$) are presented in Figure 7. The optical performance remains fairly constant over a wide range of the angle of incidence. Only for very large angles (θ$_i$ > 60°) a decrease in $J_{ph,c-Si}$ is observed. Device models with different nanowire heights all follow this trend, showing that nanowire solar cells can efficiently absorb light over a wide range of illumination conditions, independent

on the size of the NWs. In addition, the performance for different values of *h* is similar within the entire range of angles of incidence (0° < θ_i < 60°). These results are consistent with the findings of the height sweep in the case of perpendicular incidence (Figure 6a) for which it was shown that *h* has little to no effect of the calculated implied photocurrent density of the absorber.

Figure 7: Calculated implied photocurrent density inside the c-Si layer as a function of the angle of incidence of light, for different values of the nanowire height and fixed period (Λ = 800 nm) and cross section (*d* = 200 nm). For clarity of the picture, only selected results are included (*h* = 0.5, 2, 3 and 4 μm).

Conclusion

Nanowires have the potential for improving the optical performance of ultra-thin (ca. 2 μm) c-Si solar cells. The fabricated heterojunction c-Si NW-based solar cell displayed enhanced absorption of light. However, the electrical performance suffered, limiting the final conversion efficiency to (11.5 ± 0.4)%. The optical simulation of NW-based solar cells demonstrated that NWs amplify Fabry–Perót resonances and, at the same time, excite wave-guided modes inside the thin absorber layers. A study of the effect of the NW geometrical parameters on light absorption was carried out. For a given periodicity (Λ = 800 nm) of the NW array and thickness of supporting layers, the optimal NW dimensions were determined resulting in $J_{\text{ph,c-Si}}^{(\text{NW})} = 27.3$ mAcm^{-2}. It should be noted that an optimisation of the array periodicity could further improve the optical performance, particularly by choosing a value of Λ closer to the band-gap wavelength of c-Si (λ_{BG} = 1107 nm) [52,58,59]. However, the manufacturing of such device would require abandoning the proposed mask-less approach in favour of a (potentially) more expensive lithography process and was thus not investigated in this work. Finally, it was observed that NW-based solar cells maintain high performance over a wide range of angles of the incidence light, up to 60°.

Supporting Information

Supporting information includes: (i) measured reflection of the FLAT and NW devices, to complement the data presented in Figure 2; (ii) the implied photocurrent density losses, due to reflection and parasitic absorption, as function of height and cross section of the nanowires. The two pictures are complementary to the data presented in Figure 6 of this manuscript.

Supporting Information File 1
Additional experimental data.
[https://www.beilstein-journals.org/bjnano/content/supplementary/2190-4286-10-31-S1.pdf]

ORCID® iDs
Robin Vismara - https://orcid.org/0000-0001-5347-5112

References

1. Staebler, D. L.; Wronski, C. R. *Appl. Phys. Lett.* **1977,** *31,* 292–294. doi:10.1063/1.89674
2. Staebler, D. L.; Wronski, C. R. *J. Appl. Phys.* **1980,** *51,* 3262–3268. doi:10.1063/1.328084
3. Kakinuma, H.; Nishikawa, S.; Watanabe, T. *J. Non-Cryst. Solids* **1983,** *59–60,* 421–424. doi:10.1016/0022-3093(83)90610-5
4. Santbergen, R.; Tan, H.; Zeman, M.; Smets, A. H. M. *Opt. Express* **2014,** *22* (Suppl. 4), A1023–A1028. doi:10.1364/oe.22.0a1023
5. Lin, C.; Povinelli, M. L. *Opt. Express* **2009,** *17,* 19371–19381. doi:10.1364/oe.17.019371
6. Demésy, G.; John, S. *J. Appl. Phys.* **2012,** *112,* 074326. doi:10.1063/1.4752775
7. Narasimhan, V. K.; Cui, Y. *Nanophotonics* **2013,** *2,* 187. doi:10.1515/nanoph-2013-0001
8. Yoo, J.; Nguyen, B.-M.; Campbell, I. H.; Dayeh, S. A.; Schuele, P.; Evans, D.; Picraux, S. T. *ACS Nano* **2015,** *9,* 5154–5163. doi:10.1021/acsnano.5b00500
9. Cao, L.; White, J. S.; Park, J.-S.; Schuller, J. A.; Clemens, B. M.; Brongersma, M. L. *Nat. Mater.* **2009,** *8,* 643–647. doi:10.1038/nmat2477
10. Cao, L.; Fan, P.; Vasudev, A. P.; White, J. S.; Yu, Z.; Cai, W.; Schuller, J. A.; Fan, S.; Brongersma, M. L. *Nano Lett.* **2010,** *10,* 439–445. doi:10.1021/nl9036627
11. Kim, S.-K.; Song, K.-D.; Kempa, T. J.; Day, R. W.; Lieber, C. M.; Park, H.-G. *ACS Nano* **2014,** *8,* 3707–3714. doi:10.1021/nn5003776
12. Kim, S.-K.; Day, R. W.; Cahoon, J. F.; Kempa, T. J.; Song, K.-D.; Park, H.-G.; Lieber, C. M. *Nano Lett.* **2012,** *12,* 4971–4976. doi:10.1021/nl302578z
13. Adachi, M. M.; Anantram, M. P.; Karim, K. S. *Sci. Rep.* **2013,** *3,* 1546. doi:10.1038/srep01546
14. Kuang, Y.; Di Vece, M.; Rath, J. K.; van Dijk, L.; Schropp, R. E. I. *Rep. Prog. Phys.* **2013,** *76,* 106502. doi:10.1088/0034-4885/76/10/106502
15. Nowak, R.-E.; Vehse, M.; Sergeev, O.; Voss, T.; Seyfried, M.; von Maydell, K.; Agert, C. *Adv. Opt. Mater.* **2014,** *2,* 94–99. doi:10.1002/adom.201300455

16. Tsakalakos, L.; Balch, J.; Fronheiser, J.; Korevaar, B. A.; Sulima, O.; Rand, J. *Appl. Phys. Lett.* **2007,** *91,* 233117. doi:10.1063/1.2821113

17. Garnett, E.; Yang, P. *Nano Lett.* **2010,** *10,* 1082–1087. doi:10.1021/nl100161z

18. Bakkers, E. P. A. M.; van Dam, J. A.; De Franceschi, S.; Kouwenhoven, L. P.; Kaiser, M.; Verheijen, M.; Wondergem, H.; van der Sluis, P. *Nat. Mater.* **2004,** *3,* 769–773. doi:10.1038/nmat1235

19. Anttu, N.; Xu, H. Q. *Opt. Express* **2013,** *21* (Suppl. 3), A558–A575. doi:10.1364/oe.21.00a558

20. Colombo, C.; Heiß, M.; Grätzel, M.; Fontcuberta i Morral, A. *Appl. Phys. Lett.* **2009,** *94,* 173108. doi:10.1063/1.3125435

21. Krogstrup, P.; Jørgensen, H. I.; Heiss, M.; Demichel, O.; Holm, J. V.; Aagesen, M.; Nygard, J.; Fontcuberta i Morral, A. *Nat. Photonics* **2013,** *7,* 306–310. doi:10.1038/nphoton.2013.32

22. Geißendörfer, S.; Vehse, M.; Voss, T.; Richters, J.-P.; Hanke, B.; von Maydell, K.; Agert, C. *Sol. Energy Mater. Sol. Cells* **2013,** *111,* 153–159. doi:10.1016/j.solmat.2012.12.042

23. Fontcuberta i Morral, A.; Arbiol, J.; Prades, J. D.; Cirera, A.; Morante, J. R. *Adv. Mater. (Weinheim, Ger.)* **2007,** *19,* 1347–1351. doi:10.1002/adma.200602318

24. Tian, B.; Zheng, X.; Kempa, T. J.; Fang, Y.; Yu, N.; Yu, G.; Huang, J.; Lieber, C. M. *Nature* **2007,** *449,* 885–889. doi:10.1038/nature06181

25. Garnett, E. C.; Yang, P. *J. Am. Chem. Soc.* **2008,** *130,* 9224–9225. doi:10.1021/ja8032907

26. Stelzner, T.; Pietsch, M.; Andrä, G.; Falk, F.; Ose, E.; Christiansen, S. *Nanotechnology* **2008,** *19,* 295203. doi:10.1088/0957-4484/19/29/295203

27. Sivakov, V.; Andrä, G.; Gawlik, A.; Berger, A.; Plentz, J.; Falk, F.; Christiansen, S. H. *Nano Lett.* **2009,** *9,* 1549–1554. doi:10.1021/nl803641f

28. Garnett, E. C.; Brongersma, M. L.; Cui, Y.; McGehee, M. D. *Annu. Rev. Mater. Res.* **2011,** *41,* 269–295. doi:10.1146/annurev-matsci-062910-100434

29. Jia, G.; Steglich, M.; Sill, I.; Falk, F. *Sol. Energy Mater. Sol. Cells* **2012,** *96,* 226–230. doi:10.1016/j.solmat.2011.09.062

30. Kim, D. R.; Lee, C. H.; Rao, P. M.; Cho, I. S.; Zheng, X. *Nano Lett.* **2011,** *11,* 2704–2708. doi:10.1021/nl2009636

31. Peng, K.-Q.; Lee, S.-T. *Adv. Mater. (Weinheim, Ger.)* **2011,** *23,* 198–215. doi:10.1002/adma.201002410

32. Gharghi, M.; Fathi, E.; Kante, B.; Sivoththaman, S.; Zhang, X. *Nano Lett.* **2012,** *12,* 6278–6282. doi:10.1021/nl3033813

33. Jia, G.; Eisenhawer, B.; Dellith, J.; Falk, F.; Thøgersen, A.; Ulyashin, A. *J. Phys. Chem. C* **2013,** *117,* 1091–1096. doi:10.1021/jp311047k

34. Li, K.; Wang, X.; Lu, P.; Ding, J.; Yuan, N. *Nanoscale Res. Lett.* **2013,** *8,* 396. doi:10.1186/1556-276x-8-396

35. Zhu, J.; Yu, Z.; Burkhard, G. F.; Hsu, C.-M.; Connor, S. T.; Xu, Y.; Wang, Q.; McGehee, M.; Fan, S.; Cui, Y. *Nano Lett.* **2009,** *9,* 279–282. doi:10.1021/nl802886y

36. Cho, J.; O'Donnell, B.; Yu, L.; Kim, K.-H.; Ngo, I.; Roca i Cabarrocas, P. *Prog. Photovoltaics* **2013,** *21,* 77–81. doi:10.1002/pip.1245

37. Veldhuizen, L. W.; Kuang, Y.; Schropp, R. E. I. *Sol. Energy Mater. Sol. Cells* **2016,** *158,* 209–213. doi:10.1016/j.solmat.2016.03.041

38. Ashley, M. J.; O'Brien, M. N.; Hedderick, K. R.; Mason, J. A.; Ross, M. B.; Mirkin, C. A. *J. Am. Chem. Soc.* **2016,** *138,* 10096–10099. doi:10.1021/jacs.6b05901

39. Lafalce, E.; Zhang, C.; Zhai, Y.; Sun, D.; Vardeny, Z. V. *J. Appl. Phys.* **2016,** *120,* 143101. doi:10.1063/1.4964417

40. Oener, S. Z.; Khoram, P.; Brittman, S.; Mann, S. A.; Zhang, Q.; Fan, Z.; Boettcher, S. W.; Garnett, E. C. *Nano Lett.* **2017,** *17,* 6557–6563. doi:10.1021/acs.nanolett.7b02213

41. Waleed, A.; Tavakoli, M. M.; Gu, L.; Wang, Z.; Zhang, D.; Manikandan, A.; Zhang, Q.; Zhang, R.; Chueh, Y.-L.; Fan, Z. *Nano Lett.* **2017,** *17,* 523–530. doi:10.1021/acs.nanolett.6b04587

42. Ingenito, A. Opto-Electrical Surface Engineering of Wafer Based c-Si Solar Cells. Ph.D. Thesis, Delft University of Technology, , Delft, Netherlands, 2016.

43. Reference Solar Spectral Irradiance: Air Mass 1.5. https://rredc.nrel.gov/solar/spectra/am1.5/ (accessed July 23, 2018).

44. ANSYS HFSS White papers. https://www.ansys.com/Products/Electronics/ANSYS-HFSS (accessed July 23, 2018).

45. Isabella, O. Light management in thin-film siliocn solar cells. Ph.D. Thesis, Delft University of Technology, Delft, Netherlands, 2013.

46. Zeman, M.; Isabella, O.; Solntsev, S.; Jäger, K. *Sol. Energy Mater. Sol. Cells* **2013,** *119,* 94–111. doi:10.1016/j.solmat.2013.05.037

47. Isabella, O.; Sai, H.; Kondo, M.; Zeman, M. *Prog. Photovoltaics* **2014,** *22,* 671–689. doi:10.1002/pip.2314

48. Isabella, O.; Vismara, R.; Ingenito, A.; Rezaei, N.; Zeman, M. *Opt. Express* **2016,** *24,* A708–A719. doi:10.1364/oe.24.00a708

49. Onwudinanti, C.; Vismara, R.; Isabella, O.; Grenet, L.; Emieux, F.; Zeman, M. *Opt. Express* **2016,** *24,* A693–A707. doi:10.1364/oe.24.00a693

50. Vismara, R.; Isabella, O.; Zeman, M. *Proc. SPIE* **2016,** *9898,* 98980J. doi:10.1117/12.2227174

51. Vismara, R.; Isabella, O.; Zeman, M. *Opt. Express* **2017,** *25,* A402–A408. doi:10.1364/oe.25.00a402

52. Isabella, O.; Vismara, R.; Linssen, D. N. P.; Wang, K. X.; Fan, S.; Zeman, M. *Sol. Energy* **2018,** *162,* 344–356. doi:10.1016/j.solener.2018.01.040

53. Ingenito, A.; Isabella, O.; Zeman, M. *Prog. Photovoltaics* **2015,** *23,* 1649–1659. doi:10.1002/pip.2606

54. Fujiwara, H.; Kondo, M. *Phys. Rev. B* **2005,** *71,* 075109. doi:10.1103/physrevb.71.075109

55. Koida, T.; Fujiwara, H.; Kondo, M. *Jpn. J. Appl. Phys., Part 2* **2007,** *46,* L685–L687. doi:10.1143/jjap.46.l685

56. Koida, T.; Fujiwara, H.; Kondo, M. *Appl. Phys. Express* **2008,** *1,* 041501. doi:10.1143/apex.1.041501

57. Paduthol, A.; Juhl, M. K.; Nogay, G.; Löper, P.; Trupke, T. *Prog. Photovoltaics* **2018,** *26,* 968–973. doi:10.1002/pip.3042

58. Yu, Z.; Raman, A.; Fan, S. *Proc. Natl. Acad. Sci. U. S. A.* **2010,** *107,* 17491–17496. doi:10.1073/pnas.1008296107

59. Yu, Z.; Raman, A.; Fan, S. *Opt. Express* **2010,** *18* (Suppl. 3), A366–A380. doi:10.1364/oe.18.00a366